SINGLE-MOLECULE METHODS FOR AN IMPROVED UNDERSTANDING OF BIOPHYSICAL INTERACTIONS: FROM FUNDAMENTAL BIOLOGY TO APPLIED NANOTECHNOLOGY

BY

MARKITA PATRICIA LANDRY

DISSERTATION

Submitted in partial fulfillment of the requirements
for the degree of Doctor of Philosophy in Chemical Physics
in the Graduate College of the
University of Illinois at Urbana-Champaign, 2012

Urbana, Illinois

Doctoral Committee:

Assistant Professor Yann R Chemla, Director of research, Chair
Professor Taekjip Ha
Professor Paul Selvin
Professor Scott K. Silverman

Abstract

The advent of single-molecule methods has greatly extended the scale at which we are able to probe natural systems. The information that can be gained by studying biological systems on a single-molecule scale, in the absence of ensemble averaging, provides an unprecedented amount of detail about molecular interactions in real-time. Single-molecule biophysical techniques have provided unique insights into the nature of protein-DNA interactions, and have allowed for the development of novel platforms to study nano-bio interactions. In this thesis, we will describe two main sets of experiments to explore molecular interactions at the single-molecule scale. We will focus on the study of protein-DNA interactions and also the interactions between biological molecules and synthetic nanoparticles, using a variety of single-molecule techniques.

Protein-DNA interactions are essential to cellular processes, many of which require proteins to recognize a specific DNA target-site. This search process is well-documented for monomeric proteins, but not as well understood for systems that require dimerization or oligomerization at the target site for activity. We present a single-molecule study of the target-search mechanism of Protelomerase TelK, a recombinase-like protein that is only active as a dimer. Interestingly, we observe that TelK undergoes 1D diffusion on non-target DNA as a monomer, as expected, but becomes immobile on DNA as a dimer or oligomer despite the absence of its target site. We further show that TelK condenses non-target DNA upon dimerization, forming a tightly bound nucleo-protein complex. Together with simulations of dimer-active protein search, our results suggest a search model whereby monomers diffuse along DNA, and subsequently dimerize to form an active complex on target DNA. These results show that target-finding occurs faster than nonspecific dimerization at biologically relevant protein

concentrations. This model may provide insights into the search mechanisms of proteins that are active as multimeric complexes for a more accurate and comprehensive model for the target-search process by sequence specific proteins (SSPs).

In addition to studying the target-search process of protelomerase TelK, we have also studied the molecular mechanism of TelK activity at the target site. We attempt to capture the dynamics responsible for DNA hairpin formation by TelK, and we discuss the unique features of TelK-DNA interactions that contribute to the complexity of this process.

Nanomaterials have unique optical, chemical and mechanical properties that make them useful in biological applications, acting as drug and gene delivery agents, electrical and optical sensors, and cell-signaling components. Although many tools exist to characterize both biomolecules and nanomaterials, these methods are currently unable to give a detailed picture of biomolecular structure at the nano-bio interface. As a result, local electronic properties, bioavailability, toxicological effects, and basic molecular structure and conformation of biomolecules on nanoparticles remain unclear.

Single-Walled Nanotubes (SWNTs) are allotropes of carbon with a cylindrical nanostructure. Though SWNTs tend to form insoluble aggregates, sonicating SWNTs with DNA forms a DNA-SWNT complex that is soluble in water. Single-stranded DNA (ssDNA) is believed to form a helical structure on the SWNT surface. This DNA-SWNT complex is not only soluble in water and does not appear to be toxic to mammalian cells, but it is also uptaken by mammalian cells via endocytosis. Therefore, there is significant interest in understanding the mechanism of SWNT encapsulation by ssDNA. However, current experimental tools have been unable to probe the structure of biomolecules on the surface of nanomaterials. Consequently,

little is known about the mechanism by which ssDNA wraps SWNT, and how biomolecules interact with the resulting DNA-SWNT structure.

In order to extend the range of biochemical interactions that can be detected on a SWNT surface, we have developed a variety of experimental platforms to study biological interactions on SWNT surfaces by extending several well-established single-molecule biophysics techniques to the study of nano-bio interactions. By applying single-molecule techniques to the study of the nano-bio interface, we uncover changes in the expected behavior of biomolecules. These effects include cooperative DNA hybridization, changes in the accessibility of DNA to nuclease proteins, and protein deactivation on a SWNT surface. We also uncover details of the mechanism by which ssDNA wraps SWNT to form a biologically-compatible nanoparticle-biomolecule conjugate.

To my mother

Acknowledgements

First and foremost, I would like to thank my research advisor, Yann Chemla, for his support and guidance throughout my graduate studies. Yann encouraged and supported my various research interests, which led to the many fruitful collaborations I've had the good fortune of cultivating over the past 5 years. Yann's role as a mentor and research director has enabled me to become the scientist I am today.

I am grateful for the detailed feelback provided by my preliminary exam committee members: My advisor Yann Chemla, and Taekjip Ha, Paul Selvin, Scott Silverman, and Karin Dahmen. This feedback helped steer my thesis project to completion. Along the same lines, I thank my doctoral thesis committee – Yann Chemla, Taekjip Ha, Paul Selvin, and Scott Silverman – for their continued support of my work, and their helpful feedback.

My fellow group members, both past and present, have been instrumental in the continued progress of my work. Each has been quick to provide help, feedback, or assistance whenever I've encountered a stall in the progress of my research. Chemla group members Matt Comstock, Kiran Girdhar, Rustem Khafizov, Vishal Kottadiel, Patrick Mears, Lance Min, Tanya Perlova, Barbara Stekas, Sukrit Suksombat, Zhi Qi, Kevin Whitley, and undergraduate researchers Patrick McCall, Brian Silvers, Elana Urbach have made my graduate studies both productive and fun.

Much of this work could not have been possible without the numerous collaborations with several outstanding research groups and individual researchers. Our collaborator at the University of Utah, Professor Wai Mun Huang, has always been quick to provide us with samples of TelK protein, but has also provided helpful criticism of our work from the onset of collaboration in 2007. Fluorescence microscopy studies of TelK were initiated in Professor

Toshio Yanagida's research group at Osaka University. With the generous guidance of several Yanagida group members, particularly Thomas Martin and Komori Tomotaka, we developed several experimental approaches to the study of TelK, including the "DNA bridge" assay that provided us with a significantly better understanding of our protein-DNA system. Professor Paul Selvin was generous in allowing the fluorescence studies developed in the Yanagida group to continue in his research group upon my return to the University of Illinois. Several Selvin group members, namely Hannah Deberg, Eli Rothenberg, Dylan Reid, and Marco Tjioe, were particularly helpful in teaching me microscopic and analysis techniques. I would like to thank Professor Klaus Schulten and his theoretical and computational biology group. They were accommodating in having me present at their group meetings, and were subsequently welcoming of my ideas and enthusiastic about pursuing several research collaborations. I would particularly like to thank Lei Wang and Xueqing Zou, who carried out the molecular dynamics simulations that became an integral part of the work herein. I am grateful for my early friendship with Dan Heller, who was a friend and mentor since my first semester of graduate school, and who has since shaped many of my career endeavors. Dan introduced me to the field of nanomaterials and facilitated my collaboration with Ankur Jain and Prarkit Jena in Professor Haekjip Ha's group. Both Ankur and Prakrit welcomed me into the DNA-SWNT microscopy project, and provided me with endless opportunities to contribute its progress and completion. I would also like to thank Professor Michael Strano for his generous input as we completed this project. Several additional members of the Ha group generously assisted my TelK FRET project: Reza Vafabakhsh, Prakrit Jena, and Michael Schlierf.

Thanks for the financial support provided by my funding sources: The NSF Graduate Research Fellowship under Grant No. 0913128, the NSF East Asia and Pacific Summer Institute

Fellowship under Award ID OISE-0913128, the Japan Society for the Promotion of Science, the Center for the Physics of Living Cells, the Hispanic Scholarship Fund, the Society of Hispanic Engineers, the Burroughs Wellcome Fund under award ID 1011264, and numerous conference travel awards through the Physics and Chemistry departments. I gladly acknowledge supercomputer time provided by the Texas Advanced Computing Center and the National Center for Supercomputing Applications via TeraGrid Resource Allocation Committee grant MCA93S028 for the molecular dynamics work presented herein.

I am thankful for the numerous sources of support external to my academic connections: the Society for the Advancement of Chicanos and Native Americans in Science UIUC chapter, the C-U tango dance community, and all my friends on campus who have been at the finish line of half-marathons and triathlons, and at this finish line too. My friends in the 'Infinite Paradigm' happy hour group were always quick to offer a hug or a beer in trying times.

Above all, I thank my family, who never let me lose sight of who I am and what I strive for. My Landry family in Canada, and Del Carpio family in Mexico, Venezuela, and Bolivia have supported me incessantly despite our geographical distance. I thank my father for teaching me the importance of hard work, persistence, and reminding me that nothing worth having comes easy. My father was always subtle but generous with his love but cleverly thrifty with his praise, and as such has been a primary source of my motivation to achieve both happiness and success in life. My mother has been and will always be my role model. It is my mother's strong character and commitment to academic success that led me to discover my academic passions. In every respect, I look up to her and do my best to face each day with the kindness, determination, wit, and love-of-life that she irradiates. Finally, I want to thank my best friend, my sister. Despite being nearly 5 years my junior, she is one of the sharpest people I know and has been a

fundamental source of advice and wisdom, particularly during my time in graduate school. There is nothing that a phone call to her couldn't fix. Nothing in life makes me happier than the friendship I've developed with my sister Allie, and there is nothing in life that I look forward to more than its continuation and progression in years to come.

Table of contents

List of abbreviations

Chapter 1

Total Internal Reflection Fluorescence (TIRF) microscopy

Atomic Force Microscopy (AFM)

Molecular dynamics (MD)

Sequence-specific proteins (SSPs)

Single-wall carbon nanotube (SWNT)

Near-infrared (nIR)

Protelomerase TelK protein (TelK)

Fluorescence Resonance Energy Transfer (FRET)

Chapter 2

Lowest electronic state available (S_0)

Vibrational levels (V_n)

First and second excited electronic states (S_1, S_2)

Fluorescence resonance energy transfer (FRET)

Stimulated emission depletion microscopy (STED)

Stochastic optical reconstruction microscopy (STORM)

Total internal reflection fluorescence (TIRF) microscopy

Bovine Serum Albumin (BSA)

Polyethylene Glycol (PEG)

Signal-to-noise ratio (SNR)

DNA-wrapped carbon nanotubes (DNA-SWNT)

Near-infrared (nIR)

Quadrant photodiode (QPD)

Polarizing beam splitter (PBS)

Quadrant photodiode (QPD)

Molecular dynamics (MD)

Single-stranded DNA (ssDNA)

Chapter 3

Near-infrared (NIR)

Reactive oxygen species (ROS)

Double-stranded DNA (dsDNA)

Kilobase (kb)

Streptavidin (SA)

Anti-digoxigenin (AD)

Biotin (BT)

Protocatechuic acid-protocatechate 3,4-dioxygenase (PCA/PCD)

Glucose oxidase-catalase (GODCAT)

3-(10-(2-carboxy-ethyl)-anthracen-9-yl)-propinoic acid (CEAPA)

Electrospray ionization-mass spectrometry (ESI-MS)

Singlet-oxygen sensor green (SOSG)

Chapter 4

Sequence-specific proteins (SSPs)

Protelomerase TelK (TelK)

Single-stranded DNA (ssDNA)

Total internal reflection fluorescence microscopy (TIRFM)

Molecular dynamics (MD)

Quantum-dot (QD)

Mean squared displacement (MSD)

Fluorescence imaging with one nanometer accuracy (FIONA)

Tyrosine recombinases (Y-recombinases)

Molecular dynamics (MD)

Center of mass (CoM)

IB topoisomerases (IB topos)

Chapter 5

Protelomerases TelK (TelK)

Total internal reflection fluorescence (TIRF) microscopy

Tethered particle microscopy (TPM)

Anti-digoxygenin (AD)

Bovine serum albumin (BSA)

Fluorescence resonance energy transfer (FRET)

Single-stranded DNA (ssDNA)

Polyethylene Glycol (PEG)

Protein-induced fluorescence enhancement (PIFE)

Protein-induced fluorescence depression (PIFD)

Tyrosine recombinase (Y-recombinase)

Chapter 6

Single-wall carbon nanotubes (SWNT)

Near-infrared (nIR)

Single-stranded DNA (ssDNA)

Sodium dodecyl sulfate (SDS)

ssDNA-solubilized SWNT (DNA-SWNT)

Single-molecule total internal reflection fluorescence microscopy (sm-TIRF)

Atomic force microscope (AFM)

Polyethylene Glycol (PEG)

S1 Nuclease (S1)

DdeI Nuclease (DdeI)

Chapter 7

Single-wall carbon nanotubes (SWNT)

Single-stranded DNA (ssDNA)

ssDNA-solubilized SWNT (DNA-SWNT)

Atomic Force Microscopy (AFM)

Scanning Tunneling Microscope (STM)

Double-stranded DNA (dsDNA)

Anti-digoxigenin (AD)

Steered molecular dynamics (SMD)

Chapter 8

Fluorescence resonance energy transfer (FRET)

Total internal reflection fluorescence (TIRF) microscopy

Stimulated Emission Depletion (STED) microscopy

Fluorescence correlation spectroscopy (FCS)

Molecular dynamics (MD)

Tyrosine recombinases (Y-recombinases)

Single-walled carbon nanotubes (SWNTs)

Single-stranded DNA (ssDNA)

Steered molecular dynamics (SMD)

Chapter 1. Introduction

Life takes on unique characteristics at the nano-scale. We are accustomed to making observations and predictions for the behavior of living systems on a scale that is intuitive for the time and size scales of our day-to-day lives. Recent advances in single-molecule techniques have enabled researchers to probe the behavior of living systems at the scale of the biological building blocks of which living systems are comprised. Methods such as single-molecule fluorescence microscopy, optical traps, and molecular dynamics provide a comprehensive set of tools with which to uncover single-molecule biological interactions. This chapter presents a brief overview of the single-molecule methods that allow us to probe living systems at a wide range of size and time scales, using experimental, theoretical, and computational approaches.

1.1 Life at the nanoscale

For centuries, scientific advancements have been on a size-scale that is familiar to us: distances in meters, times in seconds, masses in kilograms, and volumes in liters. When we hike up a mountain, we are at 1000 *meters* above sea level. If we run a sprint, we finish in 15 *seconds*. When we step on the bathroom scale, we weigh 60 *kilos*, and if we order a medium cola at a restaurant, we expect half a liter. However, the building blocks of life: proteins, nucleic acids, cells, all live at a very different scale. When we zoom into life down to the molecular level, the scales used to describe distances, times, masses, and volumes shrink to a level that is not intuitive to one accustomed to living life at the macro-scale. Within a protein, neighboring atoms can be mere Ångstroms (10^{-10} meters) away from each other, and the molecular interactions between neighboring protein subunits can occur on a nanosecond (10^{-9} seconds) time scale. This single protein will have a mass of roughly 10 kilodaltons (10^{-22} kilograms) and will occupy a volume of 100 cubic nanometers (10^{-22} liters).

In recent years, there have been significant efforts in accessing the information stored at the nano-scale. Single-molecule biophysical techniques and instruments have allowed us to study molecules at their own size scales, giving us an unprecedented amount of information about the way single biological molecules behave in the absence of ensemble averaging. Similarly, nanotechnology has focused on the study of the unique properties materials acquire when their electrons are confined to the nano-scale. Both fields have focused on the study of nano-scale interactions, and have shown much potential to uncover new behaviors at these unintuitive size and time scales.

1.2 Single-molecule methods

Single-molecule methods have transformed our ability to measure physical phenomena of molecules in real-time. Particularly in the case of biological molecules, traditional experimental methods rely on data acquired from bulk biological samples whose quantitative outputs reflect the mean behavior of the sample under study. This phenomenon of ensemble averaging masks any fluctuations undergone by individual molecules in the bulk sample, and inhibits the direct measurement of any sub-population behaviors. In contrast, the information that can be gained by studying biological systems on a single-molecule scale supersedes the level of detail that can be measured by studying biological systems being studied in bulk. Single-molecule techniques enable biological molecules to be studied one-by-one in the absence of ensemble averaging, and provide unprecedented detail about bimolecular interactions at the length and force scales of the molecules themselves [2].

Different single-molecule techniques have been optimized to study different phenomena. For example, certain techniques such as Total Internal Reflection Fluorescence (TIRF)

microscopy visually track the position and dynamics of single-molecules in real-time [3]. Other techniques, such as Atomic Force Microscopy (AFM) or optical trapping, are often referred to as force microscopy approaches and monitor the forces associated with single-molecule bio-molecular processes [4, 5]. An entire subset of single-molecule studies are approached through atomic-scale theoretical calculations of molecular processes. Molecular dynamics (MD) simulations are a good example of such approaches, which apply computer simulations to study the interactions of individual atoms within or between single bio-molecules based on numerical solutions of Newton's equations of motion for each atomic interaction.

Each of these techniques alone provides specific information about the behavior of single molecules. However, biological processes occur on a broad range of timescales, and a single-molecule technique will only be able to access a certain spatial and temporal resolution (**Figure**

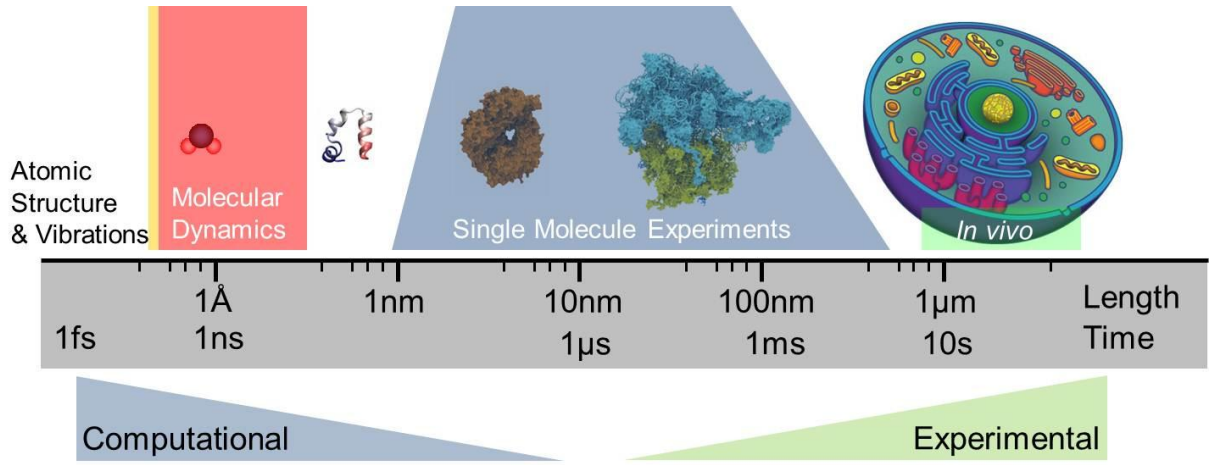

Figure 1-1. Probing life at all scales. Life operates on multiple scales. Organisms are comprised of atoms, which make up DNA and protein polymers, of which cells are comprised. Each of these biological entities span a wide range of length scales, and their functions occur on a similarly wide range of timescales. Single-molecule biophysical techniques can probe these molecules and their processes at different time and size windows, yet often times several experimental and theoretical techniques are combined to decipher biological function of the living cell.

1-1). As such, each individual single-molecule technique provides a space and time window within which we are able to gather information about bio-molecular interactions. This window is limited by instrumental data-gathering capabilities in the case of experimental single-molecule techniques, which limits the level of detail we can observe experimentally. On the other hand, MD simulations are limited at the opposite end of the time-space ruler: MD simulations are able to provide a much more detailed look at small-scale interactions, yet computational power has not yet enabled these simulations to extend to experimentally accessible time- scales.

1.3 Applications of single-molecule techniques

The large variety of single-molecule techniques often complement each other to provide a comprehensive picture of the molecules under study. As is the case in this thesis, a combination of several single-molecule experimental and theoretical techniques can be applied to supplement each other to gain a more complete understanding of a biological system. We employ a variety of techniques to decipher the mechanism by which proteins and DNA molecules interact to find DNA target sequences.

Within the cell, an important set of molecular interactions occurs between proteins and DNA. Protein-DNA interactions are fundamental to cellular processes such as transcription and translation, which are crucial for cellular viability. Many essential cellular processes involve protein-DNA interactions at specific sequences in the genome. Sequence-specific proteins (SSPs) must quickly and reliably locate DNA target sites typically only a few base pairs in length amongst kilobases of nonspecific genomic DNA. Moreover, the rates for target localization are often orders of magnitude larger than those predicted by bimolecular reaction rates driven by 3D diffusion of proteins through a volume [6]. To expedite the search process, proteins have been

shown to bind non-specifically to DNA in order to scan DNA in 1-D, with intermittent 3D "hops" to distant DNA sites. Proteins undergo this facilitated diffusion mechanism until the protein identifies its target sequence along the DNA backbone [7]. Once the target site has been identified, the electrostatic interactions are maximized between the protein surface and the DNA nucleotides, the protein adopts a "tightly" bound state on the DNA in order to undergo its designated biochemical activity on the DNA substrate [6]. However, studies to-date have focused on the target search mechanism for proteins that are active-site functional as monomers [8-10]. This search process is well-documented for monomeric proteins, but not as well understood for systems that require dimerization or oligomerization at the target site for activity. Many protein systems rely on dimerization or oligomerization for proper activity [11]. The complexity of target-search mechanisms for dimer- or oligomer- active proteins makes it difficult to decipher using a single approach, because protein-protein interactions must be considered *in addition to* protein-DNA interactions. Therefore, target-search mechanisms of dimer- and oligomer- active proteins are a prime example of a biological system that is best studied through a combination of single-molecule techniques that give us access to multiple time and size information windows.

1.4 Biomolecules meet nanoparticles

The development of single-molecule techniques has occurred parallel to advancements in nanotechnology. In the past few decades, the discovery and use of synthetic nanomaterials has occurred across many fields. Nanomaterials are defined as materials having at least one physical dimension measuring on the nanometer length scale [12]. As we approach these small scales, competing processes such as electron movements within atoms have a more noticeable effect than they do on their macro-scale counterparts. As a result, nanomaterials exhibit many unique

properties that did not exist when that same material is scaled up to the macro-scale. For instance, in the case of semiconductors, quantum confinement of the electron creates an electron/electron-hole pair instead of creating current, thereby giving that material luminescent properties that did not exist at the macro-scale, and these tiny semiconductors are called quantum dots or semiconducting nanocrystals [13]. Since their development, they have been used widely in a variety of different fields, including single-molecule fluorescence imaging [14]. Another good example of a material that has shown unique properties at the nano-scale is carbon. Carbon has many allotropes, the most common being graphite. Macroscopic quantities of graphite exhibit conductive properties of semimetals, whereas a single layer of graphite is a one-atom-thick sheet of carbon atoms arranged in a hexagonal lattice called graphene which was once presumed not to exist. Graphene has a remarkably high electron mobility that is temperature-independent, and also has one of the lowest electrical resistivities of any known material at room temperature [15]. If a sheet of graphene is conceptually rolled-up into a tube, a new nanomaterial emerges known as a single-wall carbon nanotube (SWNT). SWNTs come with their own collection of unique properties, such as high tensile strengths, remarkable aspect ratios, and near-infrared (nIR) fluorescence [16, 17].

Of the many fields that can benefit from advances in nanotechnology, biology and medicine stand out. Organisms are made up of micro- and nano-sized building blocks such as proteins and DNA that interact on the molecular level to bring about a living organism. These fundamental interactions maintain homeostatic balances within an organism, but when things go awry at the organismal level, it is fundamentally due to imbalances at the molecular level. Therefore, the field of clinically applied nanomaterials has grown substantially in recent years, in an effort to diagnose, control, and rectify biological processes on a small scale using

nanomaterial-based drugs and therapeutics [1]. The similarity in size between life's building blocks and nanomaterials has been instrumental in enabling the field of nanomedicine (**Figure 1-2**). However, physical properties of nanomaterials have a strong dependence on the

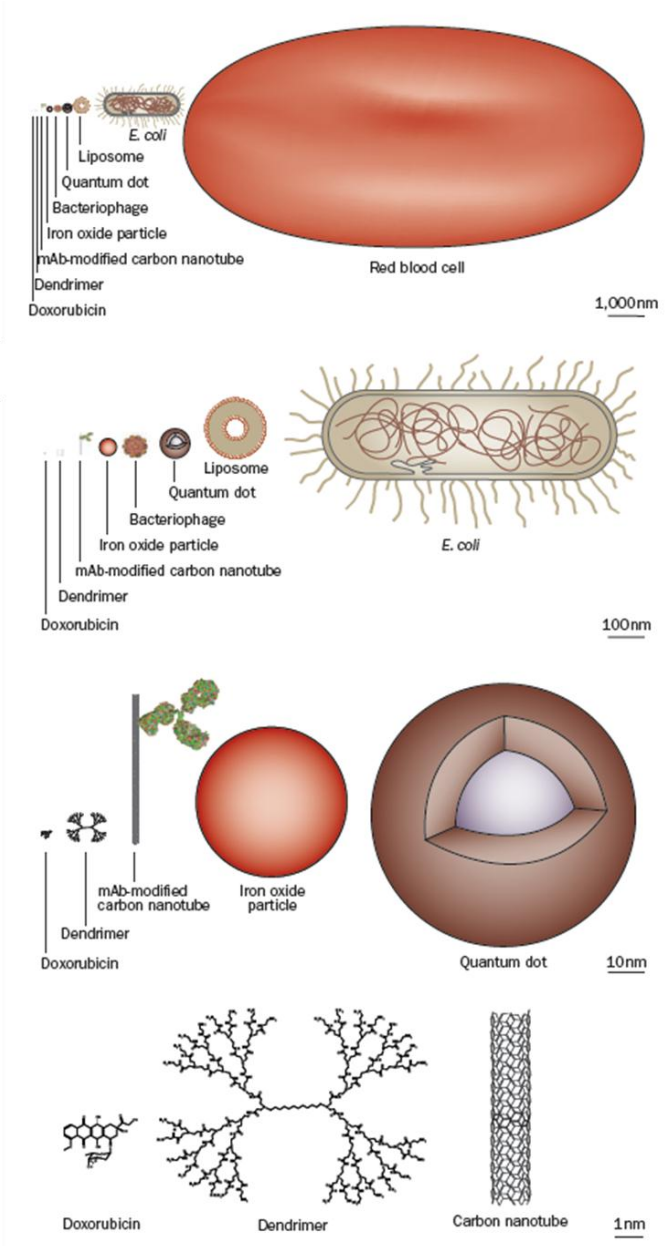

Figure 1-2. To-scale representation of nanomaterials and biological molecules. Biological molecules and nanoparticles fall on a similar length scale, making them ideal to study concurrently. However, their fundamental physical characteristics – aspect ratios, charge, size-to-surface-area ratios – give them distinct properties. Figure adapted from Scheinberg et al. [1].

nanomaterials' surface area, shape, charge, and surface patterning. Consequently, a small change in any of these parameters can drastically influence the resulting interactive behavior between the nanoparticle and a biological molecule.

The variability in nano-bio interactions makes it difficult to predict the behavior of biological molecules in the vicinity of nanoparticles. As is the case with most emerging fields, there is an incomplete understanding of biomolecule-nanoparticle interactions, which makes it difficult to predict the interactions of nanomaterials with live cells and tissues for downstream applications such as nanomedicine.

1.5 Thesis outline

In this thesis we present a study of biological systems with a variety of single-molecule instruments that we describe in detail in **Chapter 2**, primarily fluorescence microscopy and optical traps. In **Chapter 3**, we address the precautions that must be taken when working with certain single-molecule instruments, such as optical traps, that can produce reactive oxygen species at the sample plane thereby exposing the biological molecules to highly reactive electronically excited species [18]. Next, in **Chapter 4**, we present a comprehensive study of Protelomerase TelK protein (TelK), a phage protein responsible for the formation of DNA hairpins at the end of linear chromosomes. We study the target-search mechanism of TelK to uncover the details of how this dimer-active protein finds its target site, using a variety of single-molecule techniques including TIRF microscopy, optical trapping, and MD simulations. In **Chapter 6**, we perform a separate study of TelK to address its behavior at the target site, and to probe the DNA substrate's structural fluctuations during the course of hairpin formation using

another single-molecule technique, Fluorescence Resonance Energy Transfer (FRET). Lastly, we extend the use of these single-molecule methods to the study of nanoparticles and their interactions with biological molecules. In **Chapter 6**, we employ TIRF microscopy to develop platforms to probe bio-nano interactions with unprecedented spatial and temporal resolution, and in **Chapter 7**, we use dual optical traps to probe the unraveling and unbinding mechanism of ssDNA from a SWNT surface. Overall, we demonstrate the capability of single-molecule techniques to probe small-scale systems, and the added benefits of combining several single-molecule techniques to decipher the complex mechanisms of biological processes.

1.6 Chapter references

1. Scheinberg, D.A., et al., *Conscripts of the infinite armada: systemic cancer therapy using nanomaterials.* Nat Rev Clin Oncol, 2010. **7**(5): p. 266-76.
2. Weiss, S., *Fluorescence spectroscopy of single biomolecules.* Science, 1999. **283**(5408): p. 1676-1683.
3. Yildiz, A., et al., *Myosin V walks hand-over-hand: Single fluorophore imaging with 1.5-nm localization.* Science, 2003. **300**(5628): p. 2061-2065.
4. McAllister, C., et al., *Protein interactions and misfolding analyzed by AFM force spectroscopy.* Journal of Molecular Biology, 2005. **354**(5): p. 1028-1042.
5. Moffitt, J.R., et al., *Recent advances in optical tweezers.* Annual Review of Biochemistry, 2008. **77**: p. 205-228.
6. Halford, S.E. and J.F. Marko, *How do site-specific DNA-binding proteins find their targets?* Nucleic Acids Research, 2004. **32**(10): p. 3040-3052.
7. Gowers, D.M., G.G. Wilson, and S.E. Halford, *Measurement of the contributions of 1D and 3D pathways to the translocation of a protein along DNA.* Proc Natl Acad Sci U S A, 2005. **102**(44): p. 15883-8.
8. Coppey, M., et al., *Kinetics of target site localization of a protein on DNA: a stochastic approach.* Biophys J, 2004. **87**(3): p. 1640-9.
9. de la Rosa, M.A., et al., *Dynamic strategies for target-site search by DNA-binding proteins.* Biophys J, 2010. **98**(12): p. 2943-53.
10. Gorman, J. and E.C. Greene, *Visualizing one-dimensional diffusion of proteins along DNA.* Nat Struct Mol Biol, 2008. **15**(8): p. 768-74.
11. Marianayagam, N.J., M. Sunde, and J.M. Matthews, *The power of two: protein dimerization in biology.* Trends Biochem Sci, 2004. **29**(11): p. 618-25.
12. Langer, R. and D.A. Tirrell, *Designing materials for biology and medicine.* Nature, 2004. **428**(6982): p. 487-92.
13. Alivisatos, A.P., *Semiconductor clusters, nanocrystals, and quantum dots.* Science, 1996. **271**(5251): p. 933-937.
14. Zhou, M. and I. Ghosh, *Current trends in peptide science. Quantum dots and peptides: a bright future together.* PeptideScience, 2006. **88**(3).
15. Chen, J.H., et al., *Intrinsic and extrinsic performance limits of graphene devices on SiO2.* Nature Nanotechnology, 2008. **3**(4): p. 206-209.
16. Wang, X.S., et al., *Fabrication of Ultralong and Electrically Uniform Single-Walled Carbon Nanotubes on Clean Substrates.* Nano Letters, 2009. **9**(9): p. 3137-3141.
17. Welsher, K., et al., *A route to brightly fluorescent carbon nanotubes for near-infrared imaging in mice.* Nature Nanotechnology, 2009. **4**(11): p. 773-780.
18. Landry, M.P., et al., *Characterization of Photoactivated Singlet Oxygen Damage in Single-Molecule Optical Trap Experiments.* Biophysical Journal, 2009. **97**(8): p. 2128-2136.

Chapter 2. Instrument design and data acquisition

Single-molecule techniques are powerful tools to study molecular interactions at their fundamental length and time scales. This chapter describes the tools used throughout the course of this thesis: Prism- and objective-type TIRF microscopy, FRET, optical trapping, molecular dynamics, and a brief introduction to nanoparticles and graphene-based nanotechnology.

2.1 Introduction to single-molecule techniques

It is not easy to observe interactions at the size scale of biological molecules. Most proteins, for example, measure only a few tens of nanometers, making it difficult to study them one-by-one. However, the information that can be gained by studying biological systems on a single-molecule scale provides a higher level of detail than bulk studies. This is simply because, when biological molecules are studied on a single-molecule scale, we are able to extract specific details about their molecular interactions, details that are obscured by averaging in bulk. Recent advances in physics and optics have made it possible to isolate these bio-molecules individually and study their properties on a single-molecule scale.

2.2 Fluorescence microscopy

Fluorescence microscopy techniques rely on basic photo-physical principles that govern the phenomenon of luminescence. Certain molecules, such as organic fluorophores, will emit photons with wavelengths in the visible range (λ = ~400nm – 800nm) via specific electronic transitions that occur within and between the molecule's vibrational levels [2]. At room

temperature, organic fluorophores are in their lowest energy state, and the molecule's electrons occupy the lowest electronic state available (S_0) in each electron's orbital. However, upon photoexcitation via absorption of a photon of a specific wavelength λ_1, the fluorophore can absorb this photon and excite one of its electrons into one of many vibrational levels (V_n) within an excited electronic state (S_1 or S_2). From the molecule's S_1 excited electronic state, it can decay via vibrational energy dissipation to the lowest vibrational level within the S_1 electronic state. From the molecule's S_2 excited electronic state, it must first undergo internal conversion into the S_1 electronic state, followed by vibrational relaxation to the lowest S_1 vibrational state. From the S_1 electronic state, the molecule may then undergo fluorescence by emitting a photon with wavelength λ_2, in the process of transitioning between electronic states S_1 and S_0 where $\lambda_1 < \lambda_2$.

The process of releasing a photon via electronic state transitions makes molecules with λ_1 and λ_2 in the visible-wavelength range optimal for use in visible fluorescence microscopy experiments. As such, many organic fluorophores have been used for visible microscopy

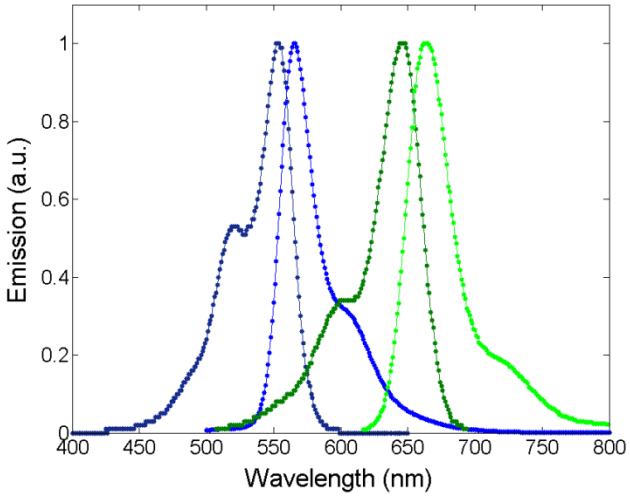

Figure 2-1. Cy3 and Cy5 fluorescence spectra. Excitation and emission spectra for Cy3 (dark blue, light blue) and Cy5 (dark green, light green), respectively. Spectral data from Jena Bioscience [1].

experiments. Two of the most common dyes used for this purpose and throughout this thesis are Cy3 and Cy5. Both dyes have well-documented excitation and emission spectra with peak excitation/emission wavelength values of 550nm/570nm and 643nm/667nm, respectively (**Figure 2-1**).

By tagging a molecule of interest with a fluorescent tag such as Cy3 and/or Cy5, one can detect photons at that fluorophore's characteristic emission wavelength and monitor changes in the behavior of the molecule to which it is attached. Tagging biological molecules with organic dyes is a commonly-used method to study the dynamics of individual biomolecules. An alternate method to tag biological molecules is by using semiconducting nanocrystals, or quantum dots [3]. Quantum dots exploit the fact that a material's fundamental properties will change as a function of that material's size. For semiconducting materials such as CdS, a nanometer-scale sample size can lead to quantum confinement of the electrons in that material [4]. Quantum dots rely on different fundamental photophysical phenomena for their fluorescence than do organic fluorophores, enabling longer lifetimes – (30-100 ns), compared to ~0.15ns for Cy3 – and a much higher quantum yield than organic dyes [5], making them an attractive alternative for single-molecule fluorescence experiments. Briefly, quantum dots force their electrons into quantum confinement via the creation of an electron/hole. With light irradiation, an electron in the quantum dot's valence band will transition into the quantum dot's conduction band to create an exciton (a bound electron and electron-hole pair). Once the electron and electron hole recombine, light is emitted at a characteristic wavelength that is tunable as a function of the quantum dot's band gap size. In this thesis, we use both cyanine dyes and quantum dots for different fluorescence-based single-molecule assays.

Once the biomolecule of interest has been tagged with a nanometer-scale source of fluorescence, many microscopy techniques are available to study that molecule including: Fluorescence resonance energy transfer (FRET), stimulated emission depletion microscopy (STED), stochastic optical reconstruction microscopy (STORM), confocal microscopy, and total internal reflection fluorescence (TIRF) microscopy [6-10]. In this thesis, we focus on the use of TIRF microscopy and FRET. It is important to note that we apply two types of TIRF microscopy (objective type and prism type) to study single biomolecules, with several microfluidic chamber designs and surface passivation techniques.

2.3 TIRF microscopy

TIRF microscopy has been used to study many biological molecules in motion, including but not limited to biological motors along cytoskeletal filaments and proteins along DNA [11, 12]. TIRF microscopy holds many advantages over other forms of fluorescence microscopy, most notably in reducing the area of fluorescent excitation to a thin region of the specimen plane, typically less than ~150 nm in depth within a sample chamber. This excitation method drastically reduces the fluorescent background, and enables high-resolution observation of dynamic single-biomolecule behavior. Coupled with mathematical peak-fitting algorithms to localize the position of single fluorophores [13], TIRF enables tracking of fluorescent particles in motion to below the diffraction limit of light, which is roughly defined as $\lambda/2 \approx 250$nm.

2.3.1 Microfluidic chamber preparation

TIRF microscopy, which is most commonly used for the study of surface-immobilized and fluorescently-tagged biomolecules, often requires surface-passivated sample chambers to

reduce non-specific binding and interaction of molecules. Proteins and DNA readily bind to glass and quartz slides, which are most commonly used for TIRF microscopy. This nonspecific binding can create false signals due to nonspecific adherence of fluorescently-tagged biological molecules to the microfluidic chamber surface, particularly when the desired signal comes from the *specific* adhesion between a surface-immobilized substrate and a fluorescent target. For this reason, several different surface-passivation techniques are used, such as surface passivation with Bovine Serum Albumin (BSA) or Polyethylene Glycol (PEG) [14]. Both surface passivation techniques, previously described elsewhere [15, 16], reduce nonspecific biomolecule adhesion to the surface of microfluidic sample chambers, yet PEGylation is a more intricate procedure but superior at reducing such nonspecific interactions. Both surface passivation techniques are used in this thesis for different assays, depending mainly on whether the biological molecules studied in that particular assay are surface-immobilized (requiring PEGylation), or not tethered to the surface (only requiring BSA-passivation). An example of PEG-surface passivation for the construction of TIRF microfluidic chambers is outlined in **Figure 2-2**.

Microfluidic chambers for TIRF experiments were prepared in several varieties to suit each experiment. For surface-tethered assays, PEGylation of microfluidic channels is typically required, since the biomolecule(s) of interest that are tagged with fluorophores will approach the slide surface. For these chambers, PEGylation of the surface of a glass or quartz slide and a glass coverslip is first performed [16], followed by the formation of microfluidic flow channels by cutting several channels out of double-sided tape and sealing the tape between the quartz slide and the coverslip (**Figure 2-2a**). For flow experiments, a micropipette tip is introduced at the flow inlet of a diagonal microfluidic channel, and a syringe is coupled into the flow outlet to

change buffer conditions of the experimental chamber (**Figure 2-2b**). Both surfaces of the microfluidic chamber are coated with a 1:100 ratio of PEG:Biotin-PEG (**Figure 2-2c**).

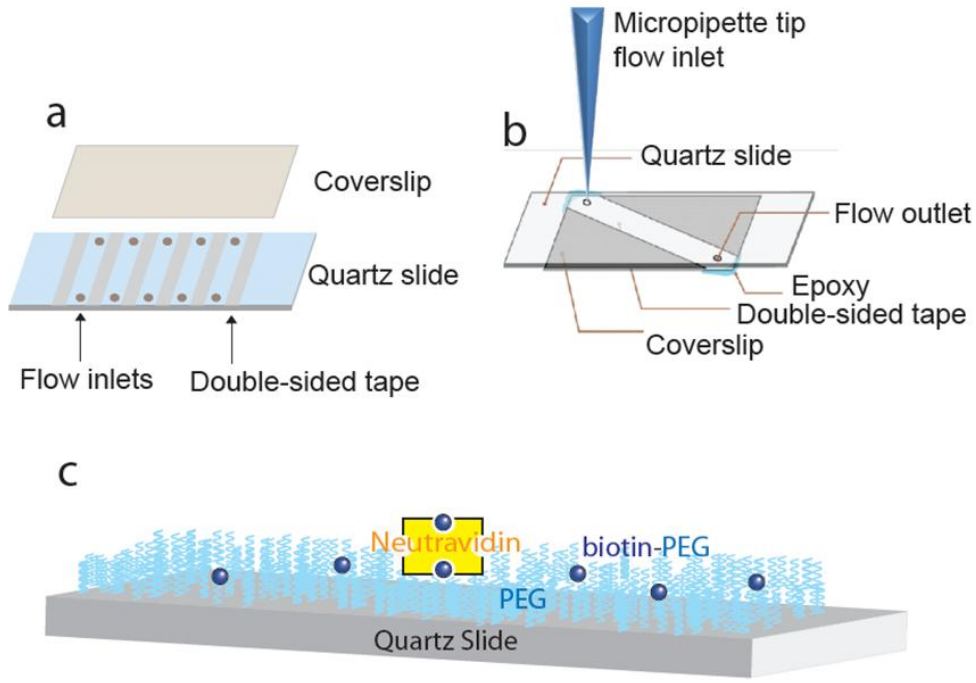

Figure 2-2. Microfluidic channel preparation for surface-tethered biomolecules. (a) Microfluidic channels are formed by coupling a coverslip to a quartz slide with double-sided tape. (b) For experiments requiring real-time buffer exchange, a single-channel flow cell is coupled to a micropipette tip and a flow outlet. Input buffer is placed in the micropipette inlet, and is drawn into the channel via syringe-induced flow in the flow outlet. (c) The microfluidic chamber surface is coated with a 1:100 ratio of PEG: Biotin-PEG, and Neutravidin is subsequently flowed into the chamber to adhere to the biotinylated PEG, creating a surface binding site for a biotinylated substrate protein or DNA molecule.

For TIRF experiments in which the biomolecule(s) under study are not tethered to the surface, BSA surface-passivation often suffices to eliminate surface effects. In this thesis, we use one particular variation of a BSA-passivized surface for the study of protein-DNA interactions, where the proteins are interacting with DNA bridges at dozens of nanometers from the closest surface, as described in more detail in **Chapter 4**. In this assay, DNA is tethered across micron-

scale glass etches serves as a substrate for the study of protein-DNA interactions, and BSA suffices to greatly reduce sticking of labeled protein on the glass surface (**Figure 2-3**).

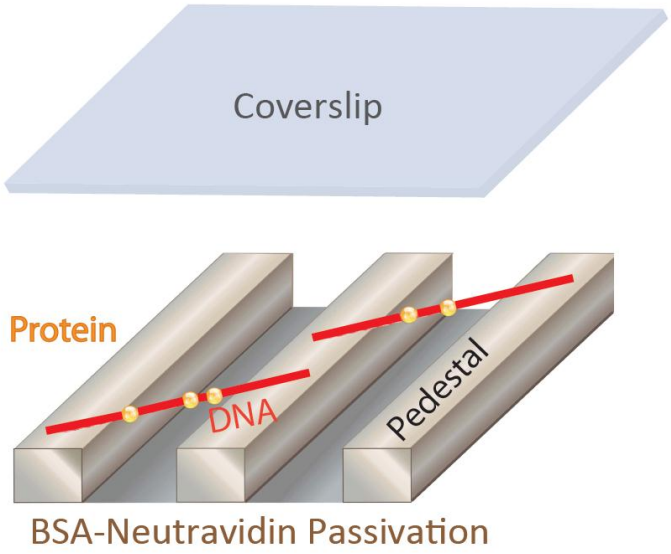

Figure 2-3. Microfluidic channel preparation for DNA-bridge assay. An etched glass slide with 1x1 µm pedestals separated by 7-µm etches is coated with Neutravidin and BSA, which both adhere to the glass surface nonspecifically. A dual-biotinylated substrate such as DNA is flowed in to form DNA bridges. Protein is subsequently added to the flow cell, and a coverslip is sealed onto the etched glass slide prior to imaging.

2.3.2 Objective and Prism TIR fluorescence microscopy

Both objective- and prism- type TIRF microscopy techniques rely on the same principles to obtain high spatial and temporal resolution of the biomolecules under study. By introducing the imaging light at an angle at which light is fully reflected from the imaging surface, only surface molecules are illuminated, thereby reducing fluorescence background from the entire volume of the sample chamber. TIR occurs when coherent light at an angle of incidence greater than the critical angle (Θc) is directed onto the surface of the sample chamber from a high index of refraction medium into a lower index of refraction medium based on the following equation:

$$\Theta c = \arcsin\left(\frac{n_2}{n_1}\right)$$

Here, n_2 is the index of refraction of the sample buffer (typically water at $n_2 \approx 1.3$), and n_1 is the index of refraction of the sample chamber's glass ($n_1 \approx 1.5$). When $\Theta = \Theta c$, all of the incident light is reflected from the surface of the glass-water interface, and an evanescent wave of exponentially-decaying light will penetrate the sample chamber ~100nm and will therefore only illuminate molecules within this limited field of view. The depth and intensity profile of this evanescent wave follows the following relation:

$$I(z) = I(0)e^{-\frac{z}{d}}$$

where

$$d = \frac{\lambda}{4\pi}\left(n_{sample}^2 \sin^2\Theta - n_{oil}^2\right)^{-\frac{z}{d}}$$

The method by which TIR is achieved varies in two ways. One can use a plano-convex lens termed a TIR lens to modify the angle of incidence, coupled to a high- numerical aperture oil-immersion objective as in objective-type TIR fluorescence microscopy. Alternatively, a mirror can be adjusted to introduce laser light into a quartz prism that passes through immersion oil with an index of refraction identical to that of the quartz prism, such that the beam is introduced into the lower index of refraction medium at the critical angle needed to undergo TIR. This latter method, called prism-type TIR fluorescence microscopy, uses a water immersion objective opposite of the imaging surface of the microfluidic chamber to achieve TIR. In prism-type TIRF, a prism is used to couple a laser into the microfluidic chamber slide, and emission is collected from the opposite glass surface of the microfluidic channel. In objective-type TIRF, the

excitation laser enters and leaves via the objective, and imaging is achieved on the same side of the microfluidic chamber.

Each TIRF method comes with advantages and disadvantages, and the choice of using either approach depends mostly on the type of experiment being performed. Prism TIRF can have a slightly lower signal-to-noise ratio (SNR) because emission collection is accomplished through the buffer. Therefore, experiments requiring better localization of individual fluorophores are best accomplished with objective TIRF. On the other hand, prism TIRF requires less table space to direct the laser into the sample, since the beam does not need to be expanded as in objective TIRF. The type of TIRF microscopy used can also depend on the samples one wishes to image. Larger and denser samples such as cells or tissues are best imaged with objective-TIRF, since appending them to the top surface of a microfluidic slide can be difficult. Smaller samples such as DNA or proteins can more easily be immobilized on either surface of the microfluidic chamber. Lastly, objective TIR provides the option to direct several different laser lines into the objective via different TIR lenses, which allows for independent control of each excitation line. In this thesis, we use objective-TIRF to study protein-DNA interactions, but we use prism-TIRF to study DNA-wrapped carbon nanotubes (DNA-SWNT). Both methods of TIR fluorescence imaging are outlined briefly in below.

2.3.3 Prism TIRF: Instrument design

For a 2-excitation laser prism-type total internal reflection fluorescence microscope with dual channel imaging, two excitation lasers, 532nm and 633nm, are relayed through various optics into a prism at a critical angle necessary for TIR (**Figure 2-4)**. The angle of incidence for TIR is formed by mirror 1 (M_1). An evanescent wave is created at the sample-coverslip interface

and fluorescence from the sample is collected through an objective through the microfluidic chamber slide. A 60x objective collects emitted light which is split into two emission wavelengths specific to the fluorophores being imaged. Individual molecules are monitored at these two wavelengths on a 512 x 512 pixel CCD, where each channel images one wavelength on half of the CCD – a 512 x 256 pixel – area. Objective-type total internal reflection

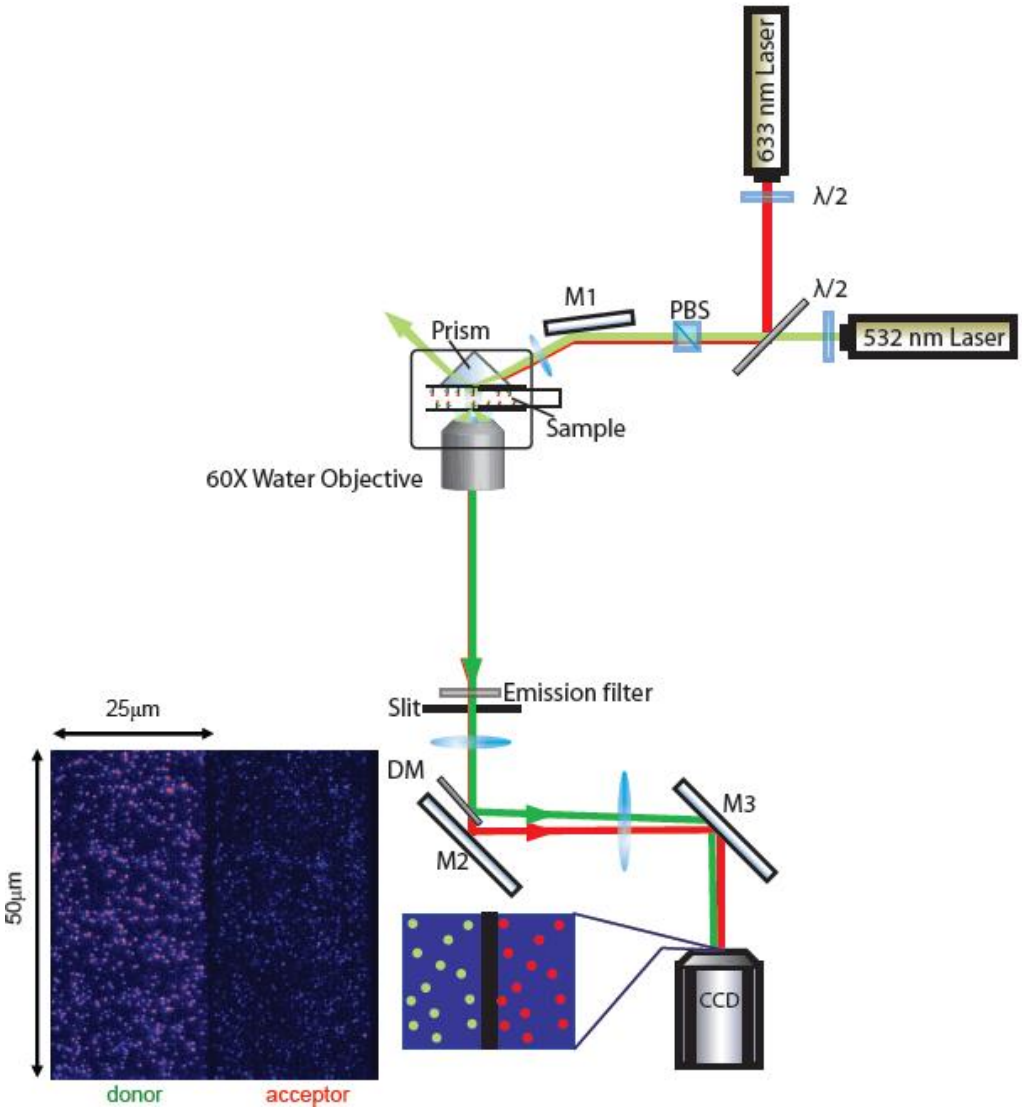

Figure 2-4. Prism TIRF setup. Optical path for prism-type TIRF microscope with two-channel imaging.

fluorescence microscopes are similarly constructed with a few notable differences. A standard 2-excitation laser objective-type TIRF microscope will have its lasers relayed through several conditioning optics, including a 10x beam expansion telescope (**Figure 2-5**). Unlike prism-type TIRF, objective TIRF beams must overfill the objective to achieve maximal excitation area of the sample, requiring a beam of approximately 1.5 cm in diameter. The expanded beam is directed into a plano-convex focusing lens (TIR lens), which is mounted on a 3-axis translational stage. Movement of the TIR lens in the plane perpendicular to beam propagation will change the angle of beam incidence at the interface of the sample chamber, and will steer the beam from epifluorescence mode when the angle of incidence is zero with respect to the beam propagation vector, into TIR mode when this angle reaches the critical angle. In this thesis, we use an objective-type TIRF microscope with a CCD camera coupled to the exit port of the microscope to capture a 512 x 512 pixel field of view for single-color imaging.

The emission path of the prism-TIRF microscope begins with the collection of the emission from the sample by the objective. This emission passes through a notch filter that reflects the excitation laser light but transmits the fluorescence emission wavelength(s). A slit crops the emission field of view into a 2:1 sided rectangle to be projected onto a 512 x 256 pixel field of view. A pair of doublet lenses expand the 75 μm x 75 μm) image to fill the (8.2 mm x 8.2 mm) CCD sensor, and relays the emission through a dichroic mirror that separates the emission from each fluorophore. Each emission path is then relayed separately by mirrors M2 and M3onto the EM-CCD camera, to monitor each channel simultaneously. Both channels are spatially separated on the CCD and are considered as 2 distinct images during image analysis. We use a mapping algorithm to determine which molecules are located at the same location in each channel.

2.3.4 Objective TIRF: Instrument design

The theory for the formation of TIRF illumination in an objective-type TIRF microscope is essentially the same as that described for a prism-type TIRF microscope. However, the

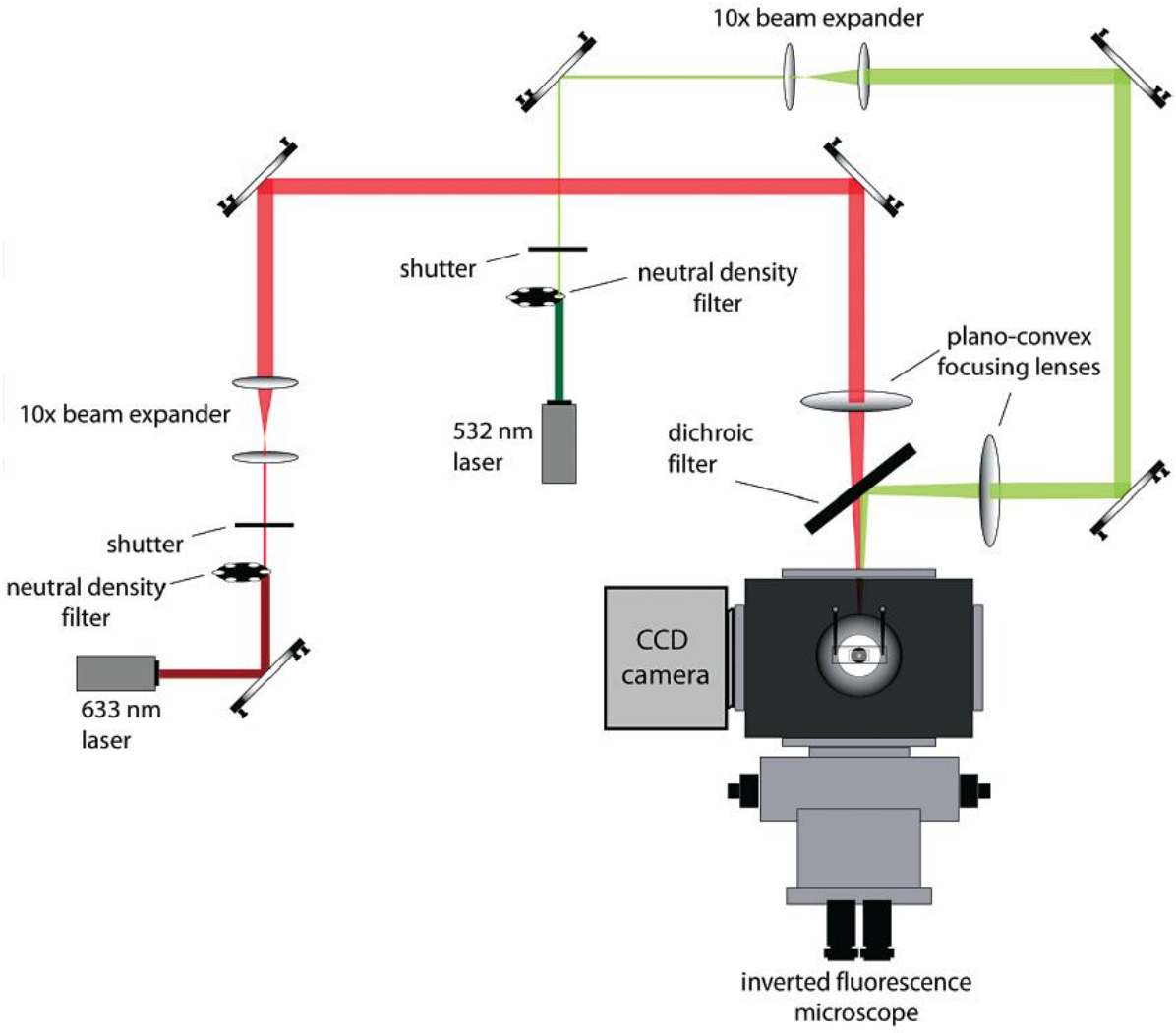

Figure 2-5. Objective TIRF setup. Optical path for objective-type TIRF microscopy with single-channel emission imaging. Figure adapted from [10].

excitation path for objective TIR differs substantially. In our objective-type TIRF setup, a 633 nm laser and a 532 nm laser are each attenuated with a neutral density filter and expanded by a 10x beam expander. A set of mirrors directs the expanded beams through a plano-convex TIR

lens and into the back port of the microscope body into the objective (**Figure 2-5**). The emission is also collected through the objective, and is filtered using a dichroic filter set appropriate for the dyes used. The emission is relayed onto an EM-CCD camera in a single channel 512 x 512 pixel imaging area. This instrument is described in greater detail elsewhere [10].

2.3.5 Fluorescence resonance energy transfer

Fluorescence resonance energy transfer (FRET) is a subset of fluorescence imaging that captures nanometer-scale inter- and intra-molecular motions [17]. Resonance energy transfer occurs between two weakly coupled molecules with the capacity to communicate via non-radiative energy transfer. This phenomenon is observed when two organic fluorophores such as Cy3 and Cy5 are brought within ~80 angstroms from each other, and the higher-energy fluorophore (donor fluorophore) is excited with an external excitation source such as the excitation laser used for TIRF. Within this ~80 angstrom distance, the donor can transfer energy to the acceptor fluorophore with an efficiency of energy transfer that depends on the ratio of intensities of the donor and acceptor fluorophores, as a measure of their distance from each other via the following formula:

$$E(t) = \frac{I_{acceptor}}{I_{acceptor} + I_{donor}} = \frac{1}{1 + (r/R_o)^6}$$

Where $I_{acceptor}$ and I_{donor} are the acceptor and donor intensities, respectively, r is the distance between the two dyes, and R_0 is the distance at which transfer and spontaneous decay of the excited donor are equally likely, also known as the Förster radius. The effectiveness of FRET as

a molecular ruler stems from its 6th power dependence on (r/R_0). For a ~40 angstrom range in inter-dye distance, a small change in r leads to a large and easily observed and quantified change in FRET for the dye pair (**Figure 2-6**). By tagging one or more molecule(s) of interest with a FRET dye pair, we can experimentally monitor both inter- and intra-molecular processes in real-time and at the nanometer scale.

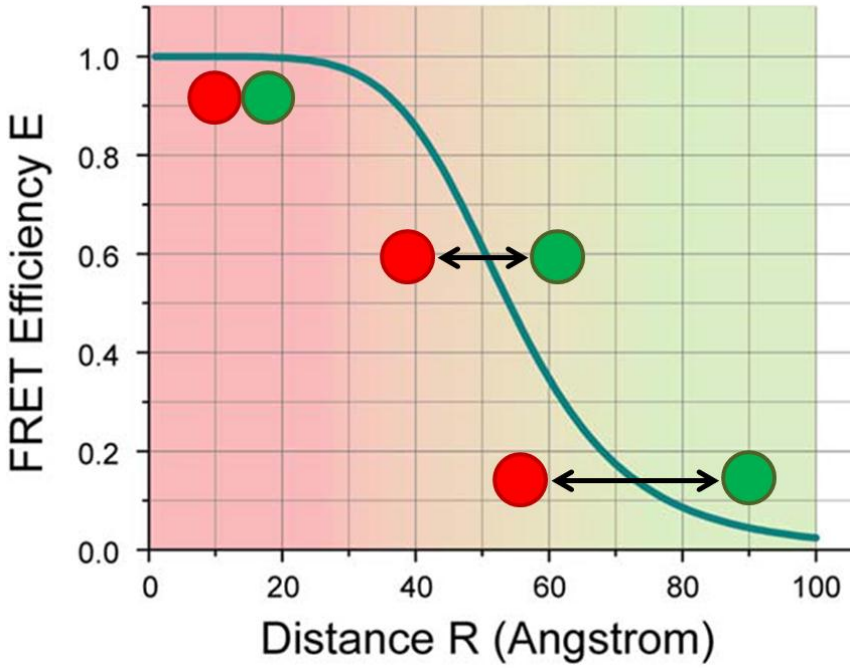

Figure 2-6. FRET efficiency as a function of dye distance. FRET efficiency between a donor (green) and an acceptor (red) molecule depends on the inter-dye distance. Optimal experimental FRET is achieved when a small change in inter-dye distance results in the greatest possible change in FRET efficiency, namely in the ~30-70 angstrom range.

FRET has been used to study a variety of molecular processes. Certain experimental approaches incorporate both the donor and acceptor dyes onto DNA or RNA, to monitor the

dynamics of the DNA or RNA molecule in the presence of different substrates such as g-quadruplex DNA bound by different synthetic ligands [18]. Another common approach to FRET is to tag two separate parts of a protein to monitor intermolecular transitions between protein domains. This approach was used to monitor the movement of different domains in the ribosome [19].

2.4 Optical trapping

Since the development of a stable three-dimensional optical trap in 1986 by Ashkin et al., optical traps have been used to manipulate micrometer-sized dielectric particles using forces from focused laser beams [20]. Optical traps function on basic principles governed by focused light scattering in the direction of the laser beam, and a gradient force in the direction of the beam's photon intensity gradient. By carefully positioning a focused coherent light source, such as a laser, one can stably trap neutral dielectric particles on the same length scale (0.1-1.0 λ) as the wavelength of the trapping light.

Recent advances in optical tweezers have enabled unprecedented applications of optical traps for small particle manipulation, from angstrom-scale measurements of bio-molecular motion, to manipulation of live cells [21]. Today, numerous applications of optical traps have revealed details of polymer elasticity, protein-DNA interactions, motor protein motion along cytoskeletons, and bacterial behaviors [22-25].

2.4.1 Optical trapping principles

The principles of optical trapping can be described through a ray optics model based on the refraction of light at the interface of a trapped particle. When light such as the near-infrared (nIR) laser used to form our optical traps hits a dielectric interface such as a polystyrene microsphere, the refraction of light at the dielectric particle interface causes a change in the momentum of the light. Because our trapping laser has a Gaussian beam profile, a microsphere will experience a gradient in the intensity of trapping light that depends on its position with respect to the beam profile. As shown in **Figure 2-7**, a microsphere positioned off-center from the beam profile will interact with light proportional to the beam intensity at that point. The two rays of light represented by bold and thin black lines represent the different light intensities hitting the microspheres at that particular point. The resulting refraction of the rays due to their interaction with the microspheres changes the direction of the trapping laser photons, resulting in

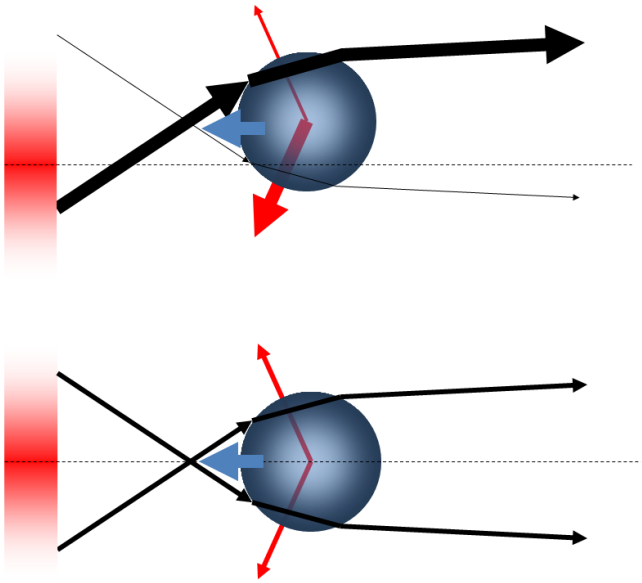

Figure 2-7. Optical trapping forces. An interplay between the scattering force (black arrow) and the gradient force (blue arrow) holds a dielectric microsphere in the center of the optical trap. A microsphere positioned away from the trap center, as depicted above, will create an imbalance in the forces experienced by the microsphere until the microsphere becomes stably trapped in all three dimensions as depicted below.

a change in the momentum of those photons. Since momentum is conserved, the microsphere experiences an equal and opposite change in momentum. The net sum of the resulting forces, represented by the red arrows of differing intensities in **Figure 2-7**,redirect the microsphere into the center of the beam where it becomes stably trapped in all 3 dimensions with the help of the scattering force that pushes the microsphere in the direction of beam propagation (not depicted).

Subsequently, this optical trap can be used to hold and manipulate biological molecules such as cells and large organelles, but is also commonly used to trap microspheres that are used as 'handles' to manipulate smaller biological systems, such as DNA. The work presented in this thesis hinges mostly on the latter application of optical traps, so further explanation of optical trapping principles will hinge upon the trapping of dielectric microspheres for manipulation of DNA.

A trapped spherical particle such as a micron-sized sphere (microsphere) can be manipulated by moving the position of the optical trap. Furthermore, the optical trap itself can also be used to obtain quantitative information about the trapped microsphere. Detection of a trapped particle's position is accomplished through an interferometry technique based on the interference pattern produced by the interaction of the laser light with the microsphere, and its subsequent detection at the back focal plane of the optical trap setup. This technique, called back focal plane interferometry, detects changes in the interference pattern formed between light that is undeflected by the trapped microsphere and forward-scattered light from the microsphere surface. Calibration of the system allows the position and subsequently the force on the microsphere to be determined by the interference pattern projected onto a quadrant photodiode (QPD) downstream of the optical trap, as detailed in the **optical trap layout** section below. As

such, micron-sized particles can be both manipulated and quantitatively monitored with optical traps.

2.4.2 Optical trap layout

Several varieties of optical traps exist in the field of single-molecule biophysics. Single optical traps were amongst the first to be used in single-molecule biological applications, sometimes in conjunction with other techniques, and other times aided by a micropipette to serve as a second attachment point for biomolecules in lieu of a second optical trap [26, 27]. Recent advances in optical "tweezers" have made it possible to resolve motions on the scale of a single base pair of DNA, 3.4Å [28]. High-resolution optical traps attain base-pair resolution due to several key design features that together enable a SNR suitable for base-pair detection. Firstly, single optical traps are limited by stage drift introduced into the instrument from environmental sources of noise such as temperature changes and acoustic noise that couples into the instrument through the stage relative to the optical trap. The high-resolution optical trap design greatly reduces this noise by decoupling the experimental components from the stage by using a second optical trap in lieu of an attachment to the stage. The introduction of a second optical trap is accomplished by forming two separate optical traps from a single laser for differential motion detection [28]. Differential detection is accomplished by considering only the anti-correlated signal from the two microspheres by taking the difference between the two bead signals. It is differential detection, which enables the measurement of only anti-correlated motion, which contributes primarily to the high SNR of dual optical traps.

Our instrument consists of two optical traps generated by two orthogonally polarized beams from a single 5-W, 1064-nm fiber coupled laser (YLR-5-1064-LP; IPG Photonics,

Oxford, Massachusetts). The beam path first encounters conditioning optics, including a first telescope (T_1) that expands the beam, and the first polarizing beam splitter (P_1) that splits the laser into two beams with orthogonal polarizations. The position of one trap relative to the other is controlled by a piezoactuated mirror stage, (M_1) (Nano-MTA-2; Mad City Labs, Madison, Wisconsin, and the second beam forms the stationary trap and is reflected by a second stationary mirror (M_2). Both beams are recombined by a second polarizing beam splitter (P_2) before being

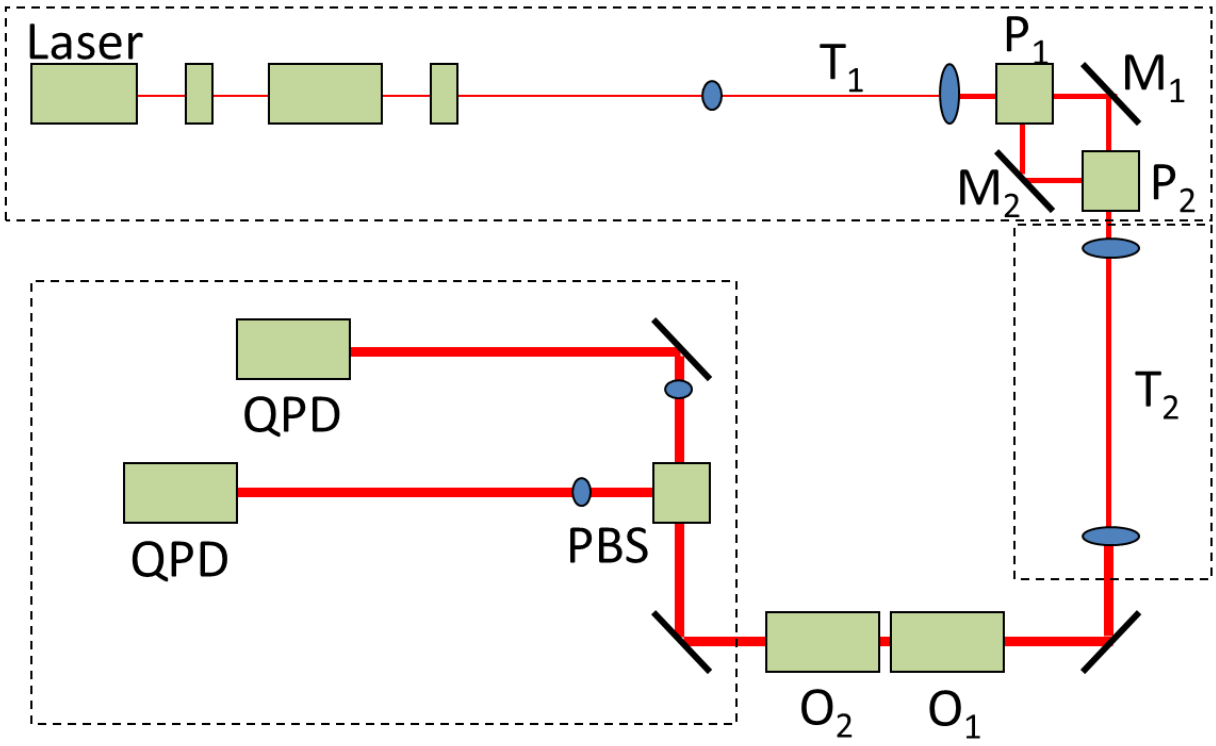

Figure 2-8. Optical trap layout. A 1064-nm laser beam is directed through an optical path consisting of a beam-expanding telescope (T_1), a polarizing beam splitter (P_1) that splits the beam into two orthogonal polarizations and directs each one into a fixed (M_2) or movable (M_1) mirror before recombining each beam with a second polarizing beam splitter (P_2). A second telescope expands the beam to an ~8mm diameter to overfill the back aperture of the first objective (O_1). Light is collected through the second objective (O_2) and directed into the emission path of the optical trap. Emission optics consists of a polarizing beam splitter cube (PBS) that separates the traps based on polarization and directs them into quadrant photodiodes (QPDs) to monitor the interference pattern of the scattered trapping light.

expanded to an ~8mm beam diameter by a second telescope (T_2). A high numerical aperture objective (O_1) (Nikon CFI Plan Apo VC 60x/1.2 Water Immersion objective, Fryer Inc.) focuses both beams to create two optical traps. Light is collected by a second objective O_2), and separated by a polarizing beam splitter (PBS) in the emission path, which relays light from each optical trap into a separate quadrant photodiode (QPD) (**Figure 2-8**). The setup contains three conjugate planes at which steering of the trap via angular displacement of the movable mirror will not affect the position of the beam. These conjugate planes are located at the back focal plane of the first objective and the QPD detectors, relative to the movable mirror, and serve to ensure that any change in position of the movable trap will not cause clipping of the beam at downstream optics. A custom flow cell is typically used as the experimental environment, and can be displaced relative to the two traps in all directions by a three-axis translational stage (ESP300; Newport, Irvine, CA). Data acquisition was accomplished through hardware located outside of the optical trapping room to avoid noise interference of the computers with the optical trap setup.

These high-resolution optical traps have enabled many advances in our understanding of mechano-chemical coupling of biochemical and biophysical systems, particularly in the resolution of DNA responses to interactions with proteins [29]. In later chapters, we demonstrate several examples of applications of our high-resolution optical trap.

2.5 Molecular dynamics

Molecular dynamics (MD) is an important biophysical tool that probes the dynamics of atomic-scale biological systems at time-scales that are inaccessible by standard experimental

methods. MD simulations are based on crystallographic data from biological systems – such as proteins and DNA – that have been crystalized such that the positions of the system's atoms are known at the angstrom scale. MD simulations take into consideration the positions of these atoms, and simulate their interactions in (typically) aqueous environments at nanosecond to microsecond timescales [30]. Newton's equations of motion are then applied to each of these atoms and their interactions with neighboring atoms within a certain radius, typically of a few angstroms. The numerical solution to each of these equations' of motion is then solved for all interacting particles for an integer number of timesteps, where each timestep is limited by the femtosecond timescale at which the molecular interactions naturally occur in complex biological systems. The length of a given MD simulation depends on how quickly each femtosecond timestep can be calculated for the entire system. This depends on computational power, as well as the size of the system. A typical MD simulation between an average-sized protein of ~50 kDa can expect to be run for tens to hundreds of nanoseconds over the course of a few days.

MD simulations can provide and abundance of information on biological systems, as long as there is a crystal structure of the system available to serve as a blueprint for the MD simulation. Often times, MD simulations and single-molecule experiments will be performed in parallel to complement each other and provide information about the system at the timescales at which each system is limited: MD simulations can provide information on the fast, atomic-scale interactions that occur and can be useful in predicting behavior at longer timescales which are observable experimentally [31]. A variety of different systems can be probed in this manner. We collaborate with Klaus Schulten's group to prove a variety of different systems including protein-DNA interactions [32], and DNA-SWNT interactions, both of which will be addressed through MD simulations in this thesis.

2.6 Nanotechnology – Single wall carbon nanotubes (SWNT)

The past decade has seen a rapid emergence in the use of nanomaterials for biomedical applications including drug development, sensing, catalysis, diagnostics, and drug delivery [33]. Nanomaterials are defined as materials with at least one physical dimension measuring on the nanometer length-scale [34]. These unique dimensions lend unique optical, chemical, and mechanical properties to nanomaterials that make them useful for various biological applications such as drug delivery and small-molecule sensing [34, 35]. Toward these ends, nanomaterials are often functionalized with organic ligands and polymers such as proteins and nucleic acids [36]. Unfortunately, interactions between nanomaterials and other molecules are often unpredictable, since these interactions depend greatly on the nanomaterial's size, surface area, aspect ratio, charge, and the like [36]. In this thesis, we collaborate with Taekjip Ha and Michael Strano's research groups to probe the interactions of DNA and proteins with single wall carbon nanotubes (SWNT).

2.6.1 Nanomaterial-biomolecule interactions

Although many tools exist to characterize both biomolecules and nanomaterials [37, 38], these methods are currently unable to give a detailed picture of biomolecular structure at the nanomaterial-biomoclecule (nano-bio) interface, which is becoming increasingly necessary to advance fields of research that hinge on nano-bio interactions [39]. Existing methods often focus on a detailed understanding of either biomolecules or nanomaterials, but have insufficient overlap to study both simultaneously. As a result, local electronic properties, bioavailability, toxicological effects, and basic molecular structure and conformation of biomolecules on nanoparticles remain unclear [40]. This hampers our ability to predict relevant biological activity

on nanoparticles, and leaves us ill-equipped to design sensors, biocatalysts, and medical diagnostic tools [41]. Understanding these interactions is crucial for the advancement of the field in creating functional biomedical or sensing tools from nanomaterials based on a firm understanding of nanomaterial behavior and toxicity.

In this thesis, we focus on two main studies involving nanomaterial-biomolecule interactions, both based on SWNT. The first study involves the development of a fluorescence microscopy-based platform to study the interaction of proteins and nucleic acids on the surface of a SWNT at the single-molecule level. The second study uses a high-resolution optical trap to characterize the nanometer-scale wrapping mechanism of single-stranded DNA (ssDNA) on a SWNT, and characterizes the piconewton-scale forces at which these interactions occur.

2.6.2 Single wall carbon nanotubes

SWNTs can be envisioned as hollow tubes formed of an infinite sheet of graphene [42], which can have different configurations, or chiralities, depending on the direction the tube has been rolled. SWNTs can be classified as either metallic or semiconducting depending on their chirality [43], which is determined by the chiral vector of the nanotube, C, where

$$C = na_1 + ma_2.$$

In this formula, $0 \leq m \leq n$ and are integers defined by the intersection of the chiral vector with the tube axis, and a_1 and a_2 represent the unit vectors of graphene in real space. As such, n and m represent the nanotube's electrical properties: if n = m, the nanotube is a metal, if n – m is a multiple of 3, the nanotube is a semiconductor, and all other nanotubes are moderate semiconductors (**Figure 2-9**).

SWNT are typically synthesized via chemical vapor deposition, and variations on this method are used to produce different SWNT samples. In this thesis, high-pressure carbon monoxide (HiPCO) nanotubes are used which are commercially procured from Rice University's Smalley Institute for Nanoscale Science and Technology. These SWNT have diameters ranging from 0.8 – 1.2 nm, and lengths from ~100 – 1500 nm.

SWNTs have numerous applications and potential uses in a variety of fields, yet the application for which we will focus is their potential use in biomedical and biological sensing applications. Biological applications focus on the potential implementation of SWNT in medical care as diagnostics or drug delivery agents [34]. In addition, SWNT-based x-ray devices, chemical/biological sensors, probes, and nanotweezers (for manipulation of objects within a cell)

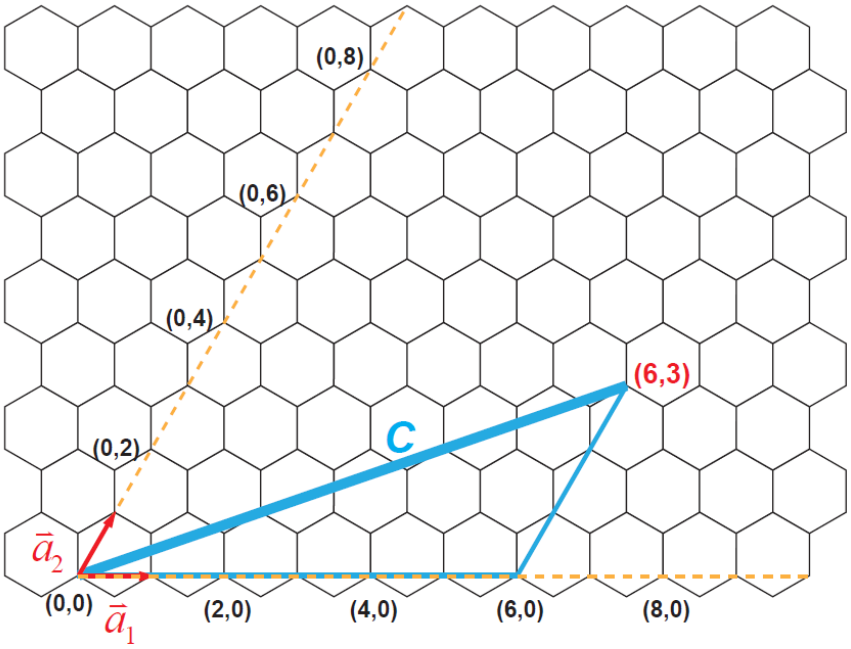

Figure 2-9. Structure and nomenclature of graphene. SWNTs have many different chiralities that are characterized by the structure and orientation of the graphene sheet that comprises them. The chiral vector (C) defines the vector along which a sheet of graphene is theoretically rolled-up to form a SWNT. This chiral vector is defined by the integers n and mas depicted above.

are devices which have been considered [44]. The main reason SWNT are an attractive material to use for developments in biomedical applications is due to their unique photoluminescent properties that enable them to emit light in the near-infrared, where tissues and cells are most transparent. SWNT emit in the 800-1600 nm range, tissue-transparent region of the electromagnetic spectrum overlaps very well with this emission range. Blood, for example, has a wavelength range of 900-1400 nm in which light can penetrate between 3-5 cm [45].This reduces interference of the biological tool (SWNT-based technology) with the biological entity being probed or visualized. There is a lack of sensors that emit strongly in this window of the electromagnetic spectrum, particularly ones that are as photophysically stable and long-lived as SWNT [46]. For these reasons, the use of SWNT in applied biotechnology, sensing, diagnostics, and therapeutics is very promising. However, concurrent with the development of SWNT-based biological applications, studies must be performed to understand the unique interactions of biological molecules with nanoparticles, to ensure optimal implementation of SWNT in these fields while reducing nanoparticle-induced toxicity. Many nanoparticles such as SWNT are hydrophobic, which makes them incompatible with the aqueous environment of biological samples. SWNT are also toxic to biological samples. While both of these biologically-incompatible properties of SWNT are overcome when SWNT are functionalized with biomolecules such as DNA, the nature of these interactions is not well understood. In chapters 6 and 7, we study the behaviors of several different biological molecules in the vicinity of SWNT using several different single-molecule techniques.

2.7 Acknowledgements

We would like to highlight the significant contributions made by our collaborators to the work introduced in this chapter. Toshio Yanagida's group was instrumental in helping us develop TIRF-based assays to probe protein-DNA interactions, and graciously allowed us to perform experiments on the Yanagida lab objective-type TIRF microscope described herein. Many of the experiments initiated in the Yanagida lab were continued in Paul Selvin's group with assistance from Selvin group members who were generous with their time, advice, and flexibility in using the Selvin lab objective-type TIRF setups which are also described in this chapter. Several of our prism-type TIRF experiments were performed in Taekjip Ha's group with useful guidance from several Ha group members. Lastly, our studies of biomolecule interactions with SWNT were the product of a collaboration with Michael Strano's research group, which was essential for the success of these projects.

2.8 Chapter references

1. JenaBioscience, *Data Sheet Cy3-dUTP-PCR and Cy5 dUTP-PCR*, JenaBioscience.
2. Valeur, B., *Molecular Fluorescence: Principles and Applications*. 2002, Weinheim:: Wiley-VCH.
3. Jaiswal, J.K. and S.M. Simon, *Potentials and pitfalls of fluorescent quantum dots for biological imaging.* Trends in Cell Biology, 2004. **14**(9): p. 497-504.
4. Alivisatos, A.P., *Semiconductor clusters, nanocrystals, and quantum dots.* Science, 1996. **271**(5251): p. 933-937.
5. Zhou, M. and I. Ghosh, *Current trends in peptide science. Quantum dots and peptides: a bright future together.* PeptideScience, 2006. **88**(3).
6. Joo, C., et al., *Advances in single-molecule fluorescence methods for molecular biology.* Annual Review of Biochemistry, 2008. **77**: p. 51-76.
7. Nie, S.M. and S.R. Emery, *Probing single molecules and single nanoparticles by surface-enhanced Raman scattering.* Science, 1997. **275**(5303): p. 1102-1106.
8. Fernandez-Suarez, M. and A.Y. Ting, *Fluorescent probes for super-resolution imaging in living cells.* Nature Reviews Molecular Cell Biology, 2008. **9**(12): p. 929-943.
9. Rust, M.J., M. Bates, and X.W. Zhuang, *Sub-diffraction-limit imaging by stochastic optical reconstruction microscopy (STORM).* Nature Methods, 2006. **3**(10): p. 793-795.
10. Selvin, P.R. and T. Ha, *Single-molecule techniques: a laboratory manual*. 2008, Cold Spring Harbor, New York: John Inglis.
11. Graneli, A., et al., *Long-distance lateral diffusion of human Rad51 on double-stranded DNA.* Proceedings of the National Academy of Sciences of the United States of America, 2006. **103**(5): p. 1221-1226.
12. Yildiz, A., et al., *Myosin V walks hand-over-hand: Single fluorophore imaging with 1.5-nm localization.* Science, 2003. **300**(5628): p. 2061-2065.
13. Selvin, P.R., et al., *In Vitro and In Vivo FIONA and Other Acronyms for Watching Molecular Motors Walk*, in *Single-Molecule Techniques, A Laboratory Manual*, T. Ha and P.R. Selvin, Editors. 2008, Cold Spring Harbor Laboratory Press: Cold Spring Harbor. p. 37-71.
14. Lamichhane, R., et al., *Single-molecule FRET of protein-nucleic acid and protein-protein complexes: surface passivation and immobilization.* Methods, 2010. **52**(2): p. 192-200.
15. Ha, T., *Single-molecule fluorescence resonance energy transfer.* Methods, 2001. **25**(1): p. 78-86.
16. Roy, R., S. Hohng, and T. Ha, *A practical guide to single-molecule FRET.* Nat Methods, 2008. **5**(6): p. 507-16.
17. Roy, R., S. Hohng, and T. Ha, *A practical guide to single-molecule FRET.* Nature Methods, 2008. **5**(6): p. 507-16.
18. Jena, P.V., et al., *G-quadruplex DNA bound by a synthetic ligand is highly dynamic.* J Am Chem Soc, 2009. **131**(35): p. 12522-3.
19. Cornish, P.V., et al., *Following movement of the L1 stalk between three functional states in single ribosomes.* Proc Natl Acad Sci U S A, 2009. **106**(8): p. 2571-6.
20. Ashkin, A., et al., *Observation of a single-beam gradient force optical trap for dielectric particles.* Opt Lett, 1986. **11**(5): p. 288.
21. Moffitt, J.R., et al., *Recent advances in optical tweezers.* Annu Rev Biochem, 2008. **77**: p. 205-28.
22. Wang, M.D., et al., *Stretching DNA with optical tweezers.* Biophys J, 1997. **72**(3): p. 1335-46.
23. Bustamante, C., et al., *Single-molecule studies of DNA mechanics.* Curr Opin Struct Biol, 2000. **10**(3): p. 279-85.
24. Guydosh, N.R. and S.M. Block, *Direct observation of the binding state of the kinesin head to the microtubule.* Nature, 2009. **461**(7260): p. 125-8.

25. Min, T.L., et al., *Chemotactic adaptation kinetics of individual Escherichia coli cells.* Proc Natl Acad Sci U S A, 2012. **109**(25): p. 9869-74.
26. Bennink, M.L., et al., *Unfolding individual nucleosomes by stretching single chromatin fibers with optical tweezers.* Nat Struct Biol, 2001. **8**(7): p. 606-10.
27. Kellermayer, M.S., et al., *Folding-unfolding transitions in single titin molecules characterized with laser tweezers.* Science, 1997. **276**(5315): p. 1112-6.
28. Moffitt, J.R., et al., *Differential detection of dual traps improves the spatial resolution of optical tweezers.* Proc Natl Acad Sci U S A, 2006. **103**(24): p. 9006-11.
29. Hilario, J. and S.C. Kowalczykowski, *Visualizing protein-DNA interactions at the single-molecule level.* Curr Opin Chem Biol, 2010. **14**(1): p. 15-22.
30. Lee, E.H., et al., *Discovery Through the Computational Microscope.* Structure, 2009. **17**(10): p. 1295-1306.
31. Klepeis, J.L., et al., *Long-timescale molecular dynamics simulations of protein structure and function.* Curr Opin Struct Biol, 2009. **19**(2): p. 120-7.
32. Husby, J., et al., *Molecular dynamics studies of the STAT3 homodimer:DNA complex: relationships between STAT3 mutations and protein-DNA recognition.* J Chem Inf Model, 2012. **52**(5): p. 1179-92.
33. Duncan, R. and R. Gaspar, *Nanomedicine(s) under the microscope.* Mol Pharm, 2011. **8**(6): p. 2101-41.
34. Langer, R. and D.A. Tirrell, *Designing materials for biology and medicine.* Nature, 2004. **428**(6982): p. 487-92.
35. Rosi, N.L., et al., *Oligonucleotide-modified gold nanoparticles for intracellular gene regulation.* Science, 2006. **312**(5776): p. 1027-1030.
36. Aillon, K.L., et al., *Effects of nanomaterial physicochemical properties on in vivo toxicity.* Adv Drug Deliv Rev, 2009. **61**(6): p. 457-66.
37. Campbell, J.F., et al., *Atomic force microscopy studies of DNA-wrapped carbon nanotube structure and binding to quantum dots.* J Am Chem Soc, 2008. **130**(32): p. 10648-55.
38. Sapsford, K.E., et al., *Analyzing nanomaterial bioconjugates: a review of current and emerging purification and characterization techniques.* Anal Chem, 2011. **83**(12): p. 4453-88.
39. Nel, A.E., et al., *Understanding biophysicochemical interactions at the nano-bio interface.* Nat Mater, 2009. **8**(7): p. 543-57.
40. Shvedova, A.A., V.E. Kagan, and B. Fadeel, *Close encounters of the small kind: adverse effects of man-made materials interfacing with the nano-cosmos of biological systems.* Annu Rev Pharmacol Toxicol, 2010. **50**: p. 63-88.
41. Hauck, T.S., A.A. Ghazani, and W.C. Chan, *Assessing the effect of surface chemistry on gold nanorod uptake, toxicity, and gene expression in mammalian cells.* Small, 2008. **4**(1): p. 153-9.
42. Manohar, S., *DNA--Carbon Nanotube Interactions.* 2010.
43. Zheng, M., et al., *Structure-based carbon nanotube sorting by sequence-dependent DNA assembly.* Science, 2003. **302**(5650): p. 1545-8.
44. Sinha, N. and J.T. Yeow, *Carbon nanotubes for biomedical applications.* IEEE Trans Nanobioscience, 2005. **4**(2): p. 180-95.
45. Wray, S., et al., *Characterization of the near infrared absorption spectra of cytochrome aa3 and haemoglobin for the non-invasive monitoring of cerebral oxygenation.* Biochim Biophys Acta, 1988. **933**(1): p. 184-92.
46. Smith, A.M. and S. Nie, *Chemical analysis and cellular imaging with quantum dots.* Analyst, 2004. **129**(8): p. 672-7.

Chapter 3. Photodamage in single-molecule systems†

Optical traps use high-power, near-infrared lasers to manipulate and apply forces to biological systems, ranging from individual molecules to cells. Although previous studies have established that optical tweezers induce photodamage in live cells, the effects of trap irradiation have yet to be examined in vitro, at the single-molecule level. In this chapter, we investigate trap-induced damage in a simple system consisting of DNA molecules tethered between optically trapped polystyrene microspheres. We show that exposure to the trapping light affects the lifetime of the tethers, the efficiency with which they can be formed, and their structure. Moreover, we establish that these irreversible effects are caused by oxidative damage from singlet oxygen. This reactive state of molecular oxygen is generated locally by the optical traps in the presence of a sensitizer, which we identify as the trapped polystyrene microspheres. Trap-induced oxidative damage can be reduced greatly by working under anaerobic conditions, using additives that quench singlet oxygen, or trapping microspheres lacking the sensitizers necessary for singlet state photoexcitation. Our findings are relevant to a broad range of trap-based single-molecule experiments—the most common biological application of optical tweezers—and may guide the development of more robust experimental protocols.

---

† This work in this chapter has been published as:

[1] Landry, M.P., et al., *Characterization of Photoactivated Singlet Oxygen Damage in Single-Molecule Optical Trap Experiments*. Biophysical Journal, 2009. **97**(8): p. 2128-2136.

3.1 Background

Single molecule techniques such as optical trapping have emerged as powerful tools in molecular biology, biochemistry, and biophysics. Optical traps have been instrumental in addressing fundamental biological problems. For example, optical tweezers have been used to understand the mechanical properties of nucleic acid structures and proteins, sensitively probe

protein-nucleic acid interactions, and decipher the mechanisms of many cytoskeletal and nucleic acid molecular motors [2-4]. In this thesis, optical traps are employed for a variety of applications ranging from the study of protein target-search mechanisms, to the interaction of DNA with nanoparticles. Typical measurements occur over the course of many tens of seconds, if not minutes. Therefore, proper characterization of such processes requires an experimental setup that is stable at these timescales, or longer. This requires optical trap-based experiments involving DNA tethering to withstand the high photon flux required to form optical traps. This high photon flux increases the risk of photodamage to our biological stamples induced by the optical trap. Otherwise, our experimental time window will be limited to the timescale of optical trap-induced photodamage. Furthermore, DNA tether instability also raises the question about the cause of this instability, and whether the processes responsible for tether breakage also adversely affect the integrity of our biological samples.

Generation of the large optical forces necessary to efficiently trap microscopic objects [5] and to counteract the forces exerted by biological systems (typically in the 1-100pN range) requires both a high photon flux and tight focus of light to a diffraction limited spot [6]. The high light intensity at the optical trap (>1 MW/cm^2) thus poses a risk for optical damage to the biological systems of interest. An early finding in the development of this technique was that near-infrared (nIR) wavelengths (800-1100nm) were more biocompatible compared to those in the visible spectrum, due to decreased absorption by cellular molecules and proteins in the nIR [7]. nIR light is now exclusively used in biological applications of optical tweezers, with 1064 nm the most common wavelength in the field in large part due to the availability of high-power YAG lasers at this wavelength [8]. Despite these findings and widespread use of nIR optical traps, it is well-documented that nIR wavelengths can still cause photodamage in irradiated *E.*

coli, HeLa, and CHO cells [8-10] as deduced from reduced motility and cloning efficiency. Although the exact mechanism for this process has not been well established, evidence suggests excitation of molecular oxygen into reactive oxygen species (ROS) by the nIR light via sensitizer molecules in the cell. Studies of trap-induced optical damage have so far been limited to cells, yet the most common biological applications of optical traps involve single molecules studied *in vitro*. This chapter investigates the potential for photodamage in the most widespread application of optical tweezers.

3.2 Quantification of tether breakage

To investigate the effect of nIR traps in vitro, we developed a simple assay that captures essential features common to a large class of optical tweezers experiments. Optical trap measurements of nucleic acids and the proteins with which they interact usually involve tethering a molecule between two attachment points: either an optically trapped microsphere and the surface of a fluidic chamber or micropipette, or two optically trapped microspheres [2, 11, 12]. Typically, this is achieved by modifying the ends of the DNA molecule with different chemical moieties that can make specific linkages with the functionalized microsphere or surface. Biotin, which interacts tightly with streptavidin, and a small molecule like the hapten digoxigenin, which binds to its antibody, are common approaches to forming specific linkages [13].

In this work, we measured the properties of single DNA tethers with a 1064-nm dual trap optical tweezers [14]. Double-stranded DNA (dsDNA) molecules of 3.4-kilobase (kb) contour length were synthesized with a single 5'-biotin and 5'-digoxigenin modification at each end

(**Section 3.7 - Materials and methods**). Inside a custom flow cell, these bi-functional molecules were tethered (**Section 3.7 - Materials and Methods**) to 0.79-μm streptavidin (SA) and 0.86-μm anti-digoxigenin (AD) antibody-coated microspheres each held in an optical trap, as shown schematically in **Figure 3-1 a**. Measurements were carried out in an experimental buffer of 50 mM Tris with 150 mM NaCl, selected based on studies indicating tethers were formed most efficiently under this salt concentration [13]. In our first experiment, we measured the longevity of these tethers under a constant range of tensions (14 ± 3 pN; mean ± SD) as a function of the intensity of 1064-nm light in both traps. In **Figure 3-1 b**, the average tether lifetime is seen to be strongly affected by increasing trap power in the trap holding the AD microsphere (measured at the sample plane; **Section 3.7 - Materials and methods**), decreasing as a power law with an exponent of -1.66 ± 0.12 ($\chi 2$ = 13.7, p-value = 0.06). Tether breakage was probably irreversible, based on the limited success in reforming tethers once broken. At all tested trap powers, lifetimes were exponentially distributed, in agreement with previous reports [13], and were independent of the tether history—whether the molecule was held at different tensions or exposed to different light intensities prior to lifetime measurement (data not shown)—indicative of a process determined by a single rate-limiting step. Lifetimes also exhibited a weak dependence on tension, as reported previously [13], which was identical across the range of trap powers investigated (lifetimes were well-fit to an exponential $\exp\left(-F\Delta x/k_BT\right)$, with $\Delta x = 0.30 \pm 0.1$ nm; data not shown).

3.3 Identification of tether breakage point

To determine which component of the tethers were most prone to breakage, we performed two tests of the attachment moieties. In the first, we applied asymmetrical light intensities to the dual traps (120 mW in one versus 230 mW in the other) and measured the tether lifetimes in the two possible geometries: SA microspheres in the strong trap and AD microspheres in the weak trap, or vice versa. As shown in **Figure 3-1 b** (red and orange data points), the tether lifetimes correlated strongly with the light intensity in the trap holding the AD microsphere, corresponding to the abscissa in that plot. In contrast, lifetimes correlated only weakly with the intensity in the trap holding the SA microsphere (**Figure 3-1 b**, inset) or the total intensity (data not shown). In the second test, DNA molecules with 5'-biotin modifications at both ends were tethered to two SA microspheres in traps of equal power (**Section 3.7 - Materials and methods**). In comparison to bi-functional molecules exposed to the same trapping light intensity, the lifetimes of dual-biotin tethers were enhanced by a factor of >20 (**Figure 3-1 b**, green diamond). These two results establish that the digoxigenin-anti-digoxigenin linkage is prone to breakage, and responsible for the tether lifetime. This is consistent with the many-fold slower dissociation rate of streptavidin-biotin in comparison to that of digoxigenin-anti-digoxigenin observed in bulk studies [15, 16].

The strong power law dependence of tether lifetime with trapping light intensity is suggestive of photodamage. Although the 1064-nm light of the traps is absorbed by the aqueous buffer in the experimental flow cell, leading to heating, the temperature increase with trap power is small (~1.0-1.45°C per 100 mW [9, 17]) and unlikely to elicit the dramatic effect on tether lifetime observed. Fits to the data in **Figure 3-1 b** with the Arrhenius equation, as expected for a temperature-dependent effect, are poor compared to a power law (χ^2 = 1005, p-value = 0; data not shown). Moreover, as demonstrated previously [18], heating by optical traps is not localized

to the laser focus, but extends spatially in a weak, logarithmic decay. It follows that the temperature of the region surrounding the dual traps in these experiments (which are separated by at most ~2 μm) is approximately uniform, and determined by the total light intensity in the two traps. However, our measurements indicate that trap-mediated tether breakage is a highly local effect as demonstrated by the fact that tethers under identical total trap power exhibit such disparate lifetimes depending on whether the SA or AD microsphere is exposed to more light (open symbol points, **Figure 3-1 b**). This point is further corroborated by the observation that the lifetimes of tethers attached to two large, 2.1-μm microspheres are 6-fold longer than those of tethers on smaller microspheres at identical trap powers (110 ± 31 s compared to 20 ± 3.5 s; mean ± SE. magenta circle, **Figure 3-1 b**). In addition, tethers held between a small, 0.79-μm SA microsphere and a large, 2.1-μm AD microsphere lasted as long as those attached to two large microspheres (110 ± 32 s; mean ± SE. blue X, **Figure 3-1 b**), corroborating the view that tether lifetime is determined by the digoxigenin-AD linkage. Thus, although we cannot rule out that temperature may play a minor role, our data are more consistent with local optical damage as the primary cause of tether breakage, a claim further confirmed by additional studies detailed below.

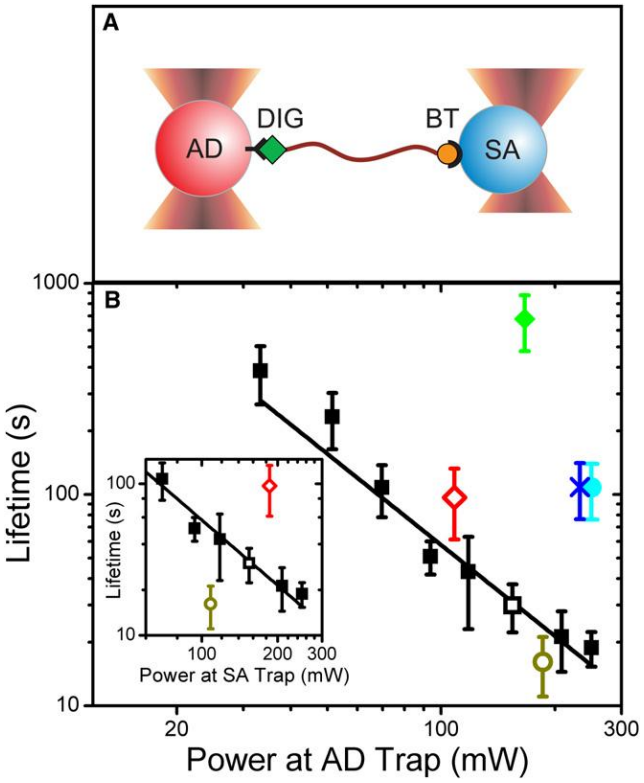

Figure 3-1. Dependence of tether lifetime on trap power. (a) Schematic representation of a dsDNA tether with 50-digoxigenin (labeled DIG) and 50-biotin (BT) modifications held between an anti-digoxigenin (AD, red) and a streptavidin (SA, blue) microsphere. (b) Tether lifetime versus laser power measured at the AD microsphere. Average lifetimes of tethers formed between 0.86-mm AD and 0.79-mm SA microspheres in traps of identical power (black squares, N = 18–55), and asymmetric power, with the AD microsphere in the low-power trap (open red diamond, N = 23) and high power trap (open dark yellow circle, N = 22). Open symbols represent tethers under identical total trap power. Average lifetime of tethers formed between 2.1-mm AD and SA microspheres (cyan circle, N = 29), between a 2.1-mm AD microsphere and a 0.79-mm SA microsphere (blue X, N = 16) and between two 0.79-mm SA microspheres through dual biotin-streptavidin linkages (green diamond, N = 8). Inset: Above data plotted as a function of laser power measured at the SA microsphere. All tethers were held at tensions of 10–20 pN (1453 pN; mean ± SD, N = 268). Error bars ¼ SE. Power-law fit to tether lifetime versus trap power measured at the AD microsphere yields the equation $t = A \times P^B$ with $A = (3.95 \pm 2.0) \times 10^5$ s/mW and $B = -1.66 \pm 0.12$, ($\chi^2 = 13.7$).

3.4 Tethering efficiency decreases with exposure to trapping light

We characterized the ability of trapped microspheres to form DNA tethers as a function of exposure to trapping light. To determine if one linkage was more sensitive than the other, we

tested two configurations: one in which the SA microsphere was coated with DNA and the AD microsphere was bare, and vice versa. An attempt was made to form a tether for each microsphere in the two configurations independently by bringing its complementary microsphere in contact using the optical traps (**Section 3.7 - Materials and methods**). For each type of microsphere we determined the tethering efficiency—defined as the fraction of trials that formed tethers—at low laser power (100 mW; power measured at each trap unless otherwise noted) and after 10 min of exposure to high-intensity (350 mW) light. To isolate the effect of nIR irradiation to one microsphere, we used a new, unexposed complementary microsphere for each time point. Moreover, each attempt to form a tether was made at the same low laser power (100 mW).

As shown in **Figure 3-2**, while the initial tethering efficiencies were high for all microsphere types (SA with DNA, blue bar 1 and AD, blue bar 4; SA, red bar 1 and AD with DNA, red bar 4), they significantly decreased upon microsphere exposure to 350-mW light in some cases. DNA-coated SA microspheres, for instance, exhibited much lower tethering efficiencies compared to bare AD microspheres after irradiation (**Figure 3-2**, compare blue bars 2 to 5). In controls experiments with 10 min irradiation with low light intensities (100 mW; blue bars 3 and 6), the efficiencies were indistinguishable from their initial values. Interestingly, irradiating the SA or AD microsphere for a longer time in proportion to the light intensity (~40 min for 100 mW light) eventually reduced the tethering efficiency to 0 (data not shown), suggesting that rate of decay is determined by the total dosage of photons. When bare SA microspheres were irradiated, the decrease in tethering efficiency was much more dramatic (red bar 2); no tethers were formed in a set of 16 microspheres. Here, moreover, controls at low power (red bar 3) also exhibited a reduced efficiency. Experiments on DNA-coated AD

microspheres displayed a similar pattern (red bar 5 and 6), though less severe. In these experiments, tether lifetimes in instances when tethers were formed (27.3 ± 3.7 s; mean ± SE) were comparable, within standard error, to those of unexposed microsphere pairs (26.3 ± 4.5 s; mean ± SE), suggesting that this fraction of molecules was not affected by trap irradiation.

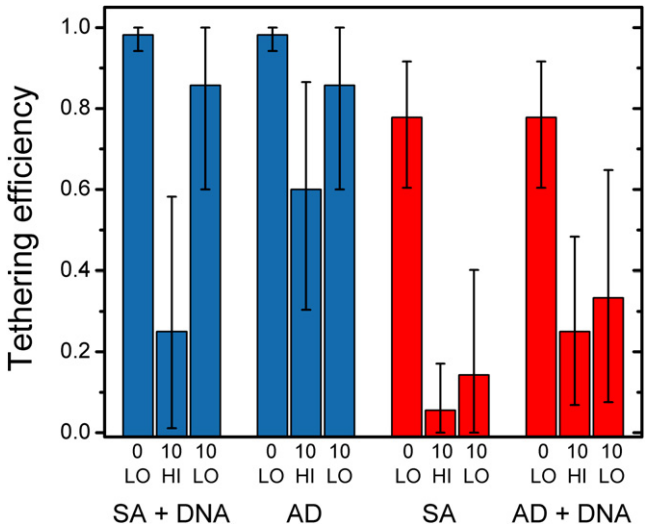

Figure 3-2. Dependence of tether forming efficiencies on trap irradiation. Tether formation was attempted in microsphere pairs in two configurations: 0.79-μm DNA-coated SA with 0.86-μm bare AD microspheres (*blue bars*; ~20 mol/microsphere), or DNA-coated AD with bare SA microspheres (*red bars*; ~30 mol/microsphere). Tethering efficiencies were measured for DNA-coated SA (*blue bars 1–3*), AD (*blue bars 4–6*), SA (*red bars 1–3*), and DNA-coated AD (*red bars 4–6*) microspheres under the following conditions: after initial trapping at low, 100 mW laser power (denoted 0 LO), after 10 min of exposure to high, 350 mW power (10 HI), or after 10 min of exposure to low, 100 mW power (10 LO). Each trial involved a tethering attempt with a new, unexposed complementary microsphere. Tethering efficiencies were calculated using the Laplace best estimator $(S + 1)/(N + 2)$, where S is the number of successes and N is the number of trials. This estimator is considered better than the maximum-likelihood S/N, when N is small. Error bars = 95% confidence intervals from the adjusted Wald method.

In the two cases where bare SA (blue bars 4-6) and AD (red bars 1-3) microspheres were exposed, the data clearly indicate that the SA microspheres were prone to rapid, irreversible

photodamage even at modest laser powers, whereas the AD microspheres were relatively insensitive to irradiation by nIR light. The results for DNA-coated SA (blue bars 1-3) and AD (red bars 1-3) microspheres are more difficult to interpret. Based on our experiments on tether lifetime implicating tether breakage at the microsphere-DNA linkage, one possible interpretation for the data is that the DNA detached from the microspheres. Alternatively, there may have been irreversible damage to the DNA or the microsphere attachment moieties, resulting in lowered tethering efficiency.

To test these possible interpretations, we developed a novel assay to monitor the amount of DNA on trapped microspheres in real time. Microspheres undergoing random Brownian motion in the harmonic potential of an optical trap normally exhibit a characteristic Lorentzian noise power spectrum [19]. We discovered that microspheres coated with DNA displayed excess noise at low frequencies (<100 Hz) that increased with the amount of DNA (**Figure 3-3 a**). Presumably, this excess noise is caused by hydrodynamic interactions of the DNA molecules with the surrounding solvent. As shown in **Figure 3-3 b**, this excess noise can be calibrated against the amount of DNA coating the microspheres (**Section 3.7 - Materials and methods**); thus, by periodically monitoring the noise characteristics of DNA-coated microspheres, we determined the amount of DNA on the microspheres as a function of time.

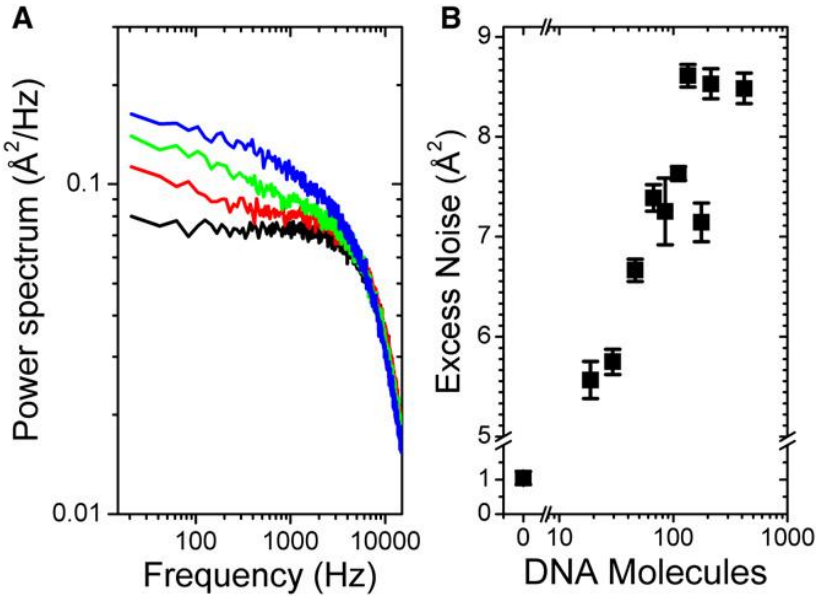

Figure 3-3. Dependence of tether forming efficiencies on trap irradiation. Low frequency noise as a function of DNA on microspheres. (*a*) Power spectra for a SA microsphere coated with 0 (*black*), ~30 (*red*), ~80 (*green*), and ~400 molecules (*blue*) of DNA exposed to 300 mW laser power. (*b*) Excess integrated noise between 0 and 100 Hz as a function of the number DNA molecules on the microsphere. Each data point represents the average from nine power spectra from three separate microspheres. Error bars = SE.

Figure 3-4 a and **b** demonstrate that DNA indeed dissociates with exposure to high trap light intensities (350 mW). Not surprisingly, given that the digoxigenin-AD linkage was more prone to breakage in the tether longevity measurements, DNA molecules detached from the AD microspheres more rapidly than from SA microspheres (red and blue data points, **Figure 3-4 b**).

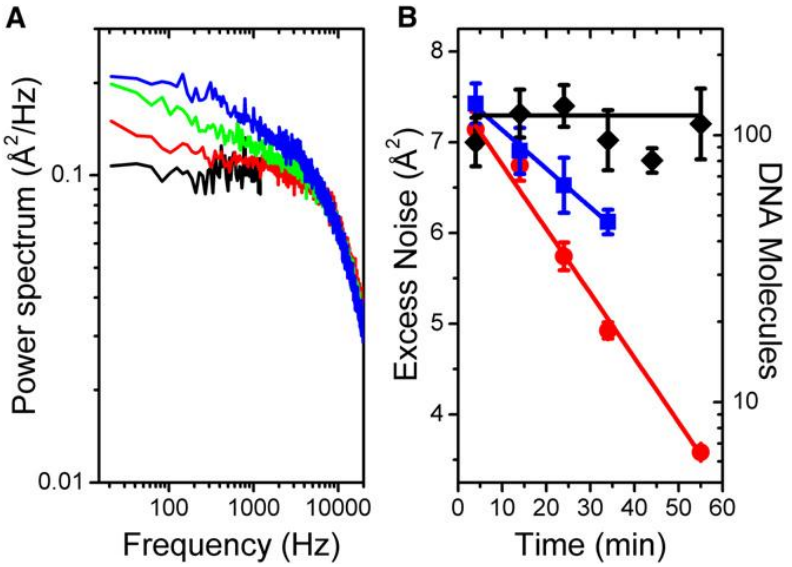

Figure 3-4. DNA dissociation from microspheres. (*a*) Power spectra of a heavily DNA-coated AD microsphere (~230 mol/ microsphere) at t = 4 min (*blue*), 14 min (*green*), and 34 min (*red*) and an AD microsphere with no DNA (*black*). (*b*) Excess integrated noise between 0 and 100 Hz as a function of time for 0.79-μm SA (*blue squares*), 0.86-μm AD (*red circles*), and 0.97-μm SA silica (*black diamonds*) DNA-coated microspheres exposed to 350 mW of laser power. Error bars = SE from five power spectra. Red, blue, and black lines are trend lines to guide the eye.

These data suggest that dissociation of DNA from AD microspheres may explain the decrease in tethering efficiency in DNA-coated AD microspheres (red bars 4-6, **Figure 3-2**), since they occur on similar time scales. However, DNA detaches from SA microspheres much too slowly to account for the rapid decay in efficiency in DNA-coated SA microspheres (blue bars 1-3, **Figure 3-2**); it takes >30 min for half the molecules to detach from SA microspheres compared to 10 min to completely abolish tethering efficiency. This result indicates that the DNA itself—most likely the digoxigenin linkage moiety—is being photodamaged with irradiation. These measurements taken together thus highlight which components of the two-microsphere DNA-tether system are most affected by the optical traps. Damage to digoxigenin likely accounts for several observed behaviors: reduced tether lifetime (**Figure 3-1 b**), decreased tethering efficiency in exposed DNA-coated SA microspheres (blue bar 2, **Figure 3-2**), and

dissociation of DNA from AD microspheres (red points, **Figure 3-4**). Streptavidin is also prone to damage, as attested by the dramatic and rapid decrease in tethering efficiency with irradiation (red bars 2-3, **Figure 3-2**). However, in contrast to digoxigenin, photodamage to SA does not lead to fast dissociation of DNA (blue points, **Figure 3-4**), suggesting that SA may be protected if bound to a complementary biotin.

Our measurements therefore pinpoint two likely areas of damage to the microsphere-DNA linkages: digoxigenin and streptavidin. Oxidative damage of digoxigenin is likely responsible for the observed decrease in tether lifetimes (and tethering efficiency) with irradiation, while damage to streptavidin dramatically reduces the efficiency but surprisingly does not lead to DNA dissociation. This result suggests that while streptavidin may be prone to damage, its binding sites are protected if bound to a complementary biotin.

3.5 Chemical cause of photodamage

The observed decrease in tether longevity and efficiency with exposure to nIR trapping light points to damage of the attachment moieties in the DNA tethers. In studies of trap-induced optical damage in cells, the underlying mechanism is believed to entail generation of ROS by the nIR trapping light [8-10]. To determine if a similar mechanism is involved, we repeated the above experiments under anaerobic conditions, using two different oxygen scavenging systems: the protocatechuic acid-protocatechate 3,4-dioxygenase (PCA/PCD) system and the glucose oxidase-catalase (GODCAT) coupled enzyme system [20] (**Section 3.7 - Materials and methods**). In the absence of oxygen, the detrimental effects of the nIR trapping light are dramatically reduced, indicating an analogous mechanism at play in this simplified, in vitro assay. Dissociation of the digoxigenin-anti-digoxigenin linkage is reduced, leading to longer

tether lifetimes (350 ± 110 s with PCA/PCD compared to 21 ± 10 s without; mean ± SE) and improved tethering efficiency in experiments where DNA coats the AD microsphere, and irreversible damage to the SA microspheres is all but eliminated (the tethering efficiency for SA and DNA-coated SA microspheres remained high after over 1 hr of exposure at 350 mW; data not shown). Table 3-1 summarizes the relative benefits of the PCA/PCD and GODCAT oxygen scavenging systems, as measured by the improvement in tether longevity at a high trap power; the concentrations of enzymes and substrates used in both systems reflect standardized conditions from the literature [20]. Interestingly, the PCA/PCD system appears to elicit a larger improvement in tether longevity compared to GODCAT, consistent with its reported higher efficiency of oxygen depletion [20].

Method	Concentration	Relative Lifetime
*PCA/PCD	100 mM PCA; 10 nM PCD	17.0
*GODCAT	100 nM glucose oxidase; 1.5 mM catalase; 56 mM glucose	7.6
†Ascorbic Acid	12.5 mM	5.2
†Sodium Azide	100 mM	3.8
†Lipoic Acid	3.1 mM	2.1
‡Tris-Cl	200 mM	1.1
‡Manitol	200 mM	1.0

Table 3-1. Increase in tether lifetime upon addition of oxygen scavengers (denoted by *, N=28 and 21), singlet oxygen quenchers (†, N=41, 31, and 18), and hydroxyl radical quenchers (‡, N=25 and 35). Tether lifetimes with additive were measured relative to that in standard TS buffer at the same trap power (a range of 150-300 mW).

The above results indicate that, as observed in vivo, trap-mediated damage occurs through the excitation of molecular oxygen into ROS, leading to oxidative damage of the DNA linkages. Several kinds of ROS can in principle be generated from molecular oxygen: superoxide anion, hydrogen peroxide, hydroxyl radicals, and singlet oxygen [21] to name a few examples. Studies carried out in vivo indicate that hydroxyl radicals and singlet oxygen are two ROS generated by laser irradiation [10]. To determine which ROS is the dominant source of damage in our assays, we performed two tests. In the first, we measured the improvement in tether longevity at high trap power upon addition of known singlet oxygen quenchers—the antioxidants ascorbic acid, lipoic acid, and sodium azide [22-24]—and hydroxyl radical quenchers Tris and manitol [25]. Table 3-1 summarizes the results; concentrations reflect the maximum amount of additive that did not adversely affect our tethering efficiency (**Section 3.7 - Materials and methods**). While all three singlet oxygen quenchers increased tether lifetimes, with ascorbic acid (12.5mM) eliciting the largest improvement comparable to that of GODCAT (a ~6-fold improvement), the hydroxyl radical quenchers had little effect, implicating singlet oxygen as the ROS generated by the optical traps.

This conclusion is further confirmed by our second test, in which singlet oxygen was directly detected with 3-(10-(2-carboxy-ethyl)-anthracen-9-yl)-propinoic acid (CEAPA). This anthracene derivative exhibits specific reactivity for singlet oxygen by forming a stable epoxide derivative via a Diels-Alder cycloaddition across its middle ring [26]. CEAPA dissolved in methanol was flowed into a custom sample chamber, exposed to a high intensity of our trapping light (1.6 W; total power) for a period of 360 min, collected, and tested by electrospray ionization-mass spectrometry (ESI-MS) (**Section 3.7 - Materials and methods**). After exposure to the trapping light, ESI-MS of CEAPA revealed a peak at a mass-to-charge (m/z) value of

355.1, corresponding to a molecular mass of 354.1 g/mol, precisely one O_2 molecule more than that of unexposed CEAPA, providing direct evidence for photoexcitation of singlet oxygen by the optical traps.

While the energy required to excite ground state molecular oxygen into its singlet excited state (E = 0.98 eV; λ = 1270 nm) is consistent with the energy provided by the nIR trapping light (E = 1.17 eV; λ = 1064 nm), this transition is strictly forbidden by spin, symmetry, and Laporte selection rule [27]. As a result, singlet oxygen can only be produced by energy transfer to molecular oxygen through a triplet sensitizer [28]. This sensitizer molecule must be present to accept energy, store it in the form of vibrations, and transfer it to ground state oxygen exciting the molecule to its singlet state. Molecules capable of storing energy in vibrational form are typically rich in π-bonded electrons and highly aromatic. Inside the cellular environment, molecules of this character are likely plentiful, facilitating the generation of singlet oxygen in cells exposed to nIR trapping light. In the case of our in vitro tether assays, however, the only likely sensitizer exhibiting significant π-bond character and aromaticity are the polystyrene microspheres. (In the experiments with CEAPA, the anthracene derivative itself acted as a sensitizer.) To test this hypothesis, we developed a hybrid fluorescence-optical tweezers assay, using the singlet-oxygen sensor green (SOSG) fluorescent probe, which emits light at 525 nm in the presence of singlet oxygen [29]. Our apparatus could switch between brightfield images of trapped microspheres and fluorescence images of the specimen plane (excitation, 488 nm; emission, 525 nm; **Section 3.7 - Materials and methods**), allowing us to localize singlet oxygen generation at the optical traps and determine precisely the conditions for its generation.

The results are summarized in **Figure 3-5 a-e**. In control experiments, optically trapped 0.79-μm polystyrene microspheres in the absence of SOSG produced the expected brightfield microsphere images but no fluorescence (**Figure 3-5 a**). In the presence of SOSG, the optical trap itself (not trapping a microsphere) produced no fluorescence signal (**Figure 3-5 b**). Only when a polystyrene microsphere was trapped in buffer containing SOSG did we detect significant fluorescence localized at the trapped microsphere position (**Figure 3-5 c** and **3-5 d**), in support of our conjecture that the microspheres provide the sensitizers required for singlet oxygen generation. Interestingly, the intensity profiles of the SOSG fluorescence for two microspheres of different sizes (compare 0.79-μm microsphere in **Figure 3-5 c** with 2.1-μm microsphere in **Figure 3-5 d**) correlate well with the microsphere diameter and suggest that fluorescence is localized at the surface. Moreover, the total fluorescence intensity from the larger 2.1-μm microsphere, normalized by the microsphere surface area, is consistent with the higher tether lifetimes observed with larger microspheres (**Figure 3-1 b**). The ratio of fluorescence intensity per unit area is 5.6 (small microsphere : large microsphere) whereas the ratio of the tether lifetimes (large microsphere : small microsphere) is 5.7. Finally, when trapping a comparably-sized (0.78 μm) small microsphere made of silica—a material lacking the aromaticity of polystyrene—SOSG fluorescence was not observed (**Figure 3-5 e**).

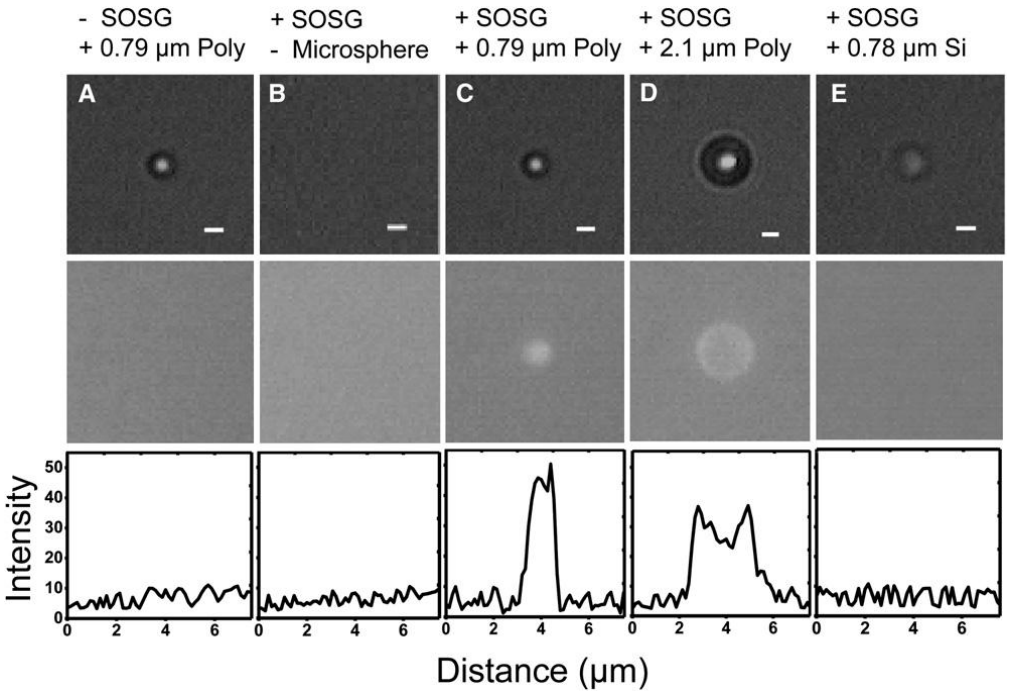

Figure 3-5. SOSG fluorescence in optically trapped microspheres. (*Top*) Brightfield images. (*Center*) Fluorescence images at 535 nm. (*Bottom*) Fluorescence image line scans. (*a*) 0.79-μm SA polystyrene microsphere without SOSG. (*b*) No microsphere with SOSG. (*c*) 0.79-μm SA polystyrene microsphere with SOSG. (*d*) 2.1-μm SA polystyrene microsphere with SOSG. (*e*) 0.78-μm silica microsphere with SOSG. Scale bar = 1 μm. A trap power of 390 mW was used in all the images.

This observation would suggest that oxidative damage is reduced in silica microspheres. Indeed, DNA-coated SA silica microspheres of a similar size (0.97 µm) exhibited dramatically reduced levels of photodamage. There was no detectable dissociation of DNA from the microspheres over an hour of exposure to high laser power (310 mW; black data points, **Figure 3-4 b**). These results demonstrate that the generation of singlet oxygen is mediated by the polystyrene microspheres, which act as a triplet sensitizer.

Our SOSG fluorescence images and controls with silica microspheres demonstrate that generation of singlet oxygen is mediated by the polystyrene microspheres. Though they appear to act as sensitizers, polystyrene is not known to absorb in the nIR [30]. One possibility is that impurities in the microspheres play a role. Alternatively, sensitization may occur through a two-

photon process; it has been demonstrated that polystyrene microspheres do absorb at visible wavelengths [30]. The observed exponent of -1.66 ± 0.12 in the power-law dependence of tether lifetime on trapping light intensity could indicate that photodamage involves one- and two-photon absorption processes. It is also conceivable that the two-photon mechanism corresponds to excitation of molecular oxygen to its second excited triplet state (E = 6.9eV; λ = 757.1nm) which is known to decay rapidly to the longer-lived reactive singlet state [31]. It is interesting to note that in studies of trap photodamage in *E. coli* cells [8], a smaller exponent (albeit larger than one) was measured. The fact that the sensitizers involved in singlet state generation in cells are undoubtedly different than in our in vitro assay may account for the discrepancies in the two measurements, however.

3.6 Photodamage to nucleic acids

The results detailed above indicate that trap-mediated oxidative damage is local and targets the biotin-SA and digoxigenin-AD linkages in the tethered molecule. However, singlet oxygen is also known to oxidize certain nucleic acids (guanine, thymine, and uracil) irreversibly [32]. Moreover, many studies have reported singlet oxygen-induced damage to single- and double-stranded DNA [33-38]. To investigate the effect of trapping light on nucleic acids more directly, we performed experiments on a 3.1-kb DNA molecule containing an 89-bp hairpin sequence (**Section 3.7 - Materials and methods**). This construct allowed us to expose its bases at will by unwinding the hairpin with tension, and probe changes to its secondary structure through its force-extension behavior.

Figures 3-6 a and **3-6 b** display typical hairpin force-extension curves taken in our standard tether assay buffer and in a buffer depleted of oxygen by the GODCAT coupled enzyme system, respectively. Other than the presence or absence of oxygen, the measurements were taken under identical conditions (140 mW, 2 pN/s pulling rate). Under aerobic conditions, where generation of singlet oxygen by the traps is possible, the force-extension curves exhibit hysteresis that grows with time (**Figure 3-6 a**). Interestingly, while the unfolding curves of the hairpin (where tension is increased) are the same, the refolding curves (where tension is decreased) display a progressively lower refolding force, suggesting that the folded hairpin configurations are identical, but that energetic barriers to refolding become progressively larger over time with continued exposure. In contrast, all force-extension curves are reversible under anaerobic conditions, displaying no hysteresis for extended periods of time (**Figure 3-6 b**), demonstrating a mechanism that also involves oxygen-dependent damage.

Plotting the hysteresis area—the difference between the unfolding and refolding force-extension areas—as a function of time summarizes these results. In **Figure 3-6 c**, the hysteresis area increases linearly (black line) with time under aerobic conditions, but remains low under anaerobic conditions (red line). These results indicate that bases are far more prone to oxidative damage when exposed to the surrounding buffer, and suggest that DNA is somewhat protected from damage in its duplex form.

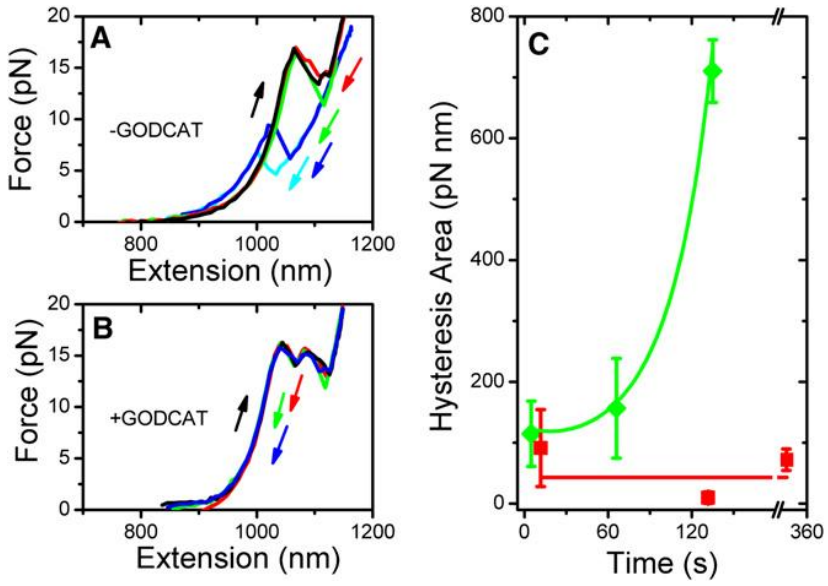

Figure 3-6. Oxidative damage to DNA hairpin. (*a*) Hairpin force-extension behavior under aerobic conditions (without GODCAT): stretching curves (*black*), relaxation curves after holding the hairpin folded at t = 0 s (*red*), 75 s (*green*), 200 s (*blue*), and 220 s (*cyan*). (*b)* Hairpin force-extension behavior under anaerobic conditions (with GODCAT): stretching curves (*black*), and relaxation curves at t = 0 s (*red*), 150 s (*green*), and 330 s (*blue*). All force-extension curves obtained at a pulling rate of 2 pN/s. (*c*) Increase in hysteresis area as a function of time for a DNA hairpin stretched under anaerobic condition (*red squares*), and aerobic conditions (*green diamonds*). Error bars = SE from 49 force-extension curves of two tethers. Red line and green curve are trend lines to guide the eye.

Several results indicate that trap-mediated photodamage is a local effect: the dependence of tether lifetime on which microsphere is exposed to high light intensities, the increased tether lifetime when using larger microspheres, and the localization of SOSG fluorescence to the microspheres. Given the diffusion constant of molecular O_2 in water (2x10-5 cm^2/s [39]) and the lifetime of singlet oxygen in water (2 μs [40]), we estimate that this ROS should be localized to ~100-nm surrounding the trapped microspheres, consistent with this picture. This likely explains why oxidative damage appears manifested most at the microsphere-DNA linkages of our dsDNA tethers. However, the DNA hairpin construct also exhibits signs of photodamage despite not being localized to the microsphere surfaces (the hairpin is separated from both microspheres by two 1.5-kb, or 510-nm, dsDNA spacer "handles"). It is possible that in cases of high sensitivity

to oxidation such as with exposed bases, damage need not be limited to the region surrounding the microsphere surfaces.

Our findings are relevant to a large class of in vitro DNA-based optical trap experiments. First, short tether lifetimes severely limit the duration and throughput of an experiment. More importantly, trap-mediated photodamage requires that an excess of DNA be placed on microspheres in order to form tethers with a reasonable efficiency. As we have shown in the microsphere power spectra, however, excess DNA coating the microspheres also leads to increased noise. Recent advances in optical tweezers design have led to new high-resolution instruments capable of detecting conformational motion on the scale of one basepair of DNA [14, 41, 42]. Excess noise from DNA-coated microspheres may thus be an important consideration in measurements requiring high resolution. Finally, although we have limited the scope of our study to DNA tethers, ROS may have significant effects on the activity and structure of other biomolecules such as RNA, lipids, and, in particular, proteins [43]. In many experiments probing protein-nucleic acid interactions or molecular motors translocating along nucleic acid, the proteins are either linked directly or are in close proximity to the trapped microspheres, and thus subject to the same conditions that lead to photodamage of our DNA tethers. Proteins can undergo conformational changes, experience changes in refolding rates, exhibit reduced activity, and form cross-linked aggregates when exposed to singlet oxygen [44, 45]. Histidine, tyrosine, methionine, and cysteine are particularly vulnerable to oxidation by singlet oxygen [44].

As we have shown, oxidative damage can be mitigated largely by working under anaerobic conditions by using the appropriate oxygen scavenging systems. In certain cases, it may not be permissive to operate under oxygen free conditions (for example in applications

where trapping is attempted in vivo [46, 47], and we have demonstrated that certain antioxidant additives that quench the singlet state can reduce the effect almost as efficiently. The microsphere composition can also have a large effect on oxidative damage. A promising direction for the future will be the examination of alternative microsphere compositions and the development of less sensitive attachment moieties—for example covalent linkages using amide, carboxyl, and sulfhydril chemistry [13] - that completely abolish trap-mediated oxidative damage in optical tweezers assays. Finally, the choice of trapping wavelength may have a strong effect on the degree of damage, as observed in studies of photodamage in vivo [8]. Although we limited our studies to a single wavelength, 1064 nm, due to its common usage in the field, optical traps at other IR wavelengths have also been in use. Singlet oxygen production decreases away from the peak in the oxygen absorption band (1270nm) [48]. However, two-photon excitation of the short-lived triplet excited state by short IR wavelengths (590-880 nm) is also possible, depending on the sensitizer [49]. Future work will be necessary to determine if the observed effects are as severe at other wavelengths. It is unfortunate that, decades after the implementation of optical traps for biological studies, discoveries about the effects of photodamage have come to light only in recent years. Hopefully, in the future, the development of novel scientific techniques and instrumentation will always be carried out in parallel to efforts which ensure that the implementation of these techniques will produce reliable results.

3.7 Materials and methods

Optical trap

The dual trap optical tweezers has been described in detail previously [50, 51]. Briefly, the instrument consisted of two optical traps generated by two orthogonally polarized beams

from a single 5-W, 1064-nm diode-pumped solid-state laser (J20I-BL-106C; Spectra Physics, Mountain View, California). The position of one trap relative to the other was controlled by a piezo-actuated mirror stage (Nano-MTA-2; Mad City Labs, Madison, Wisconsin). A custom flow cell served as the experimental trap chamber, and could be displaced relative to the two traps in all directions by a three-axis translational stage (ESP300; Newport, Irvine, California). To visualize the specimen plane, Köhler illumination from a white light-emitting diode (LED) was used. Brightfield images were collected on a charge-coupled device (CCD) camera (902-C; Watec, Orangeburg, New York). The total and relative laser trap intensities were controlled by two independent motorized halfwave plates (Model 8401; New Focus, San Jose, California), as described in Bustamante et al. [4]. Laser power at the sample plane was determined by taking the geometric mean of the light intensity before the trap-forming objective and after the condenser objective. In the text, laser powers are reported throughout as power at the sample plane for each optical trap.

Fluorescence-optical trap setup. Fluorescence excitation of SOSG was provided by a 488-nm 50 mW laser (Sapphire 488-50; Coherent, Santa Clara, California) aligned for Köhler illumination at the sample plane. The apparatus could switch from brightfield to fluorescence imaging of the specimen plane by reflecting the excitation light with a 488-nm dichroic flip-mount mirror (bandpass 450-515 nm; z488rdc, Chroma, Rockingham, Vermont). Fluorescence images were monitored through a 525-nm bandpass filter (bandpass 500-550 nm; HQ525/50m, Chroma) by a CCD camera (902-C; Watec, Orangeburg, New York).

DNA preparation

Our dsDNA tethers were synthesized using a 5'-mono-biotinylated forward and a 5'-mono-digoxigenated reverse PCR primer (Integrated DNA Technologies, Coralville, Iowa) to amplify the desired 3.4 kb sequence of the pBR322 *E. coli* plasmid (Fermentas, Glen Burnie, Maryland). A high fidelity Phusion PCR kit (F-513S, Finnzymes, Woburn, Massachusetts) was used to carry out the PCR amplification. Subsequent DNA purification was performed with a Qiagen PCR purification kit with a 50-µl DNA elution volume. An identical protocol was followed for the synthesis of dual-biotinylated DNA tethers, replacing the reverse primer above with a 5'-mono-biotinylated PCR primer with the same sequence.

The DNA hairpin construct was synthesized adapting a protocol by Woodside et al. [52]. Briefly, the 3131-nt construct consisted of an 89-bp DNA hairpin flanked by two ~1.5-kb dsDNA functionalized "handles". One handle was synthesized from a 1.5-kb PCR-amplified section of the pBR322 plasmid (New England Biolabs, Ipswich, Massachusetts) using a 5'-mono-digoxigeninated primer (Integrated DNA Technologies); the other handle was also PCR-amplified from a different 1.55-kb section of the same plasmid using a 5'-mono-biotinylated primer.

Microsphere preparation

The following microspheres were used in our experiments: 0.79-µm streptavidin (SA) polystyrene particles, 1.0% w/v (SVP-08-10, Spherotech, Lake Forest, Illinois); 0.86-µm protein-G polystyrene particles, 1.0% w/v (PGP-08-5, Spherotech); 2.1-µm SA polystyrene particles, 0.5% w/v (SVP-20-5, Spherotech); 2.1-µm protein-G polystyrene particles, 0.5% w/v (PGP-20-5, Spherotech); 0.78-µm silica microspheres, 10% solids (SS03N, Bangs Laboratories, Fishers, IN), 0.97-µm SA silica microspheres, 1% solids (CS01N, Bangs Laboratories). All microsphere samples were prepared as follows: a 30-µl aliquot of microspheres was washed in

1X phosphate buffered saline (PBS) twice to exchange the microsphere storage buffer by alternating centrifugation and resuspension. To prepare AD microspheres, 10 µl of anti-digoxigenin polyclonal antibody (11 333 089 001, Roche, Indianapolis, Indiana) was added to the protein-G microsphere aliquot after the final wash. These microspheres were shaken with the antibody for 30 min at low vortex speed and washed again three times in PBS. In all cases the final pellet was resuspended and stored in 200 µl PBS.

Tethering protocol

To attach DNA onto microspheres, 5 µl SA or AD microspheres were vortexed for 5 seconds, and sonicated for 20 seconds to dissemble microsphere aggregates. Subsequently, varying amounts of biotin- and digoxigenin-labeled DNA (typically 5 ng) was incubated with the microsphere aliquot, for one hour at room temperature unless otherwise noted. DNA-microsphere particles were then resuspended in 5 ml TS buffer (50 mM Tris-HCl, 150 mM NaCl, pH 7.6). TS buffer was used for all assays unless otherwise noted. The salt concentration was chosen due to previous studies that determined 150 mM to be the ideal ionic condition for the formation of DNA tethers [13]. Tethers were formed and tested in our custom flow cells. These consisted of three separate chambers cut from Nescofilm sealing film (N-1040; Karlan, Cottonwood, Arizona) one to contain AD microspheres, another to contain SA microspheres, the third to contain pure buffer for tether formation. Individual chambers were shunted together by glass capillaries (P0147447; Garner Glass, Claremont, California). First, an AD microsphere was trapped in the stationary optical trap. A SA microsphere was subsequently trapped in the second (movable) optical trap. The microspheres were brought into contact until a tether formed between them, as determined by the observation of force on the microspheres as they were moved apart from each other. Only tethers formed with a single DNA molecule were considered

as determined by the observation of tether breakage in a single step. Tethers with two biotin-streptavidin linkages were formed as described by Wuite et al. [53].

Quantification of DNA on microspheres

To determine the exact number of DNA molecules on the DNA-microsphere aliquots used in the assay described above, DNA quantization by agarose gel electrophoresis was employed. DNA was incubated with SA and AD microspheres in ratios of 0, 1, 10, 20, 40, 70, 100, 500, and 1000 ng per µl microspheres in a total volume of 47.6 µl. Each aliquot was incubated for 2.5 hours at room temperature. The aliquots were then spun down at 13,000 rpm for 5 min, and a 15-µl aliquot of the supernatant was run on a 1% agarose gel with ethidium bromide staining, along with a 15-µl control sample corresponding to the amount of DNA incubated with the microspheres. Band intensities were analyzed on a Kodak image station gel scanner (864 2985; Carestream Health, Rochester, NY) to determine the amount of DNA on the microspheres.

The number of DNA molecules per microsphere was calculated using the following expression

$$DNA_{bead} = \left(I_{cont} - I_{bead}\right) / I_{cont} \times DNA_{in} \qquad (3\text{-}1)$$

where I_{bead} is the band intensity in lanes containing the supernatant of DNA-incubated microspheres, I_{cont} is the band intensity in the corresponding control lanes containing only DNA, DNA_{bead} is the amount of DNA per microspheres in ng/µl, and DNA_{in} is the

concentration of DNA in ng/µl in the control lanes. To convert DNA_{bead} into number of DNA molecules per microsphere, we used the molecular weight of our 3.4-kb construct, 2.1×106 g/mol / 6.022×1023 molecules/mol, and the microsphere number density 3.7×107 or 3.0x107 microspheres/µl (corresponding to 1% w/v SA and AD microspheres, respectively).

Quantification of DNA on beads

To determine the exact number of DNA molecules on the DNA-microsphere aliquots used in the assay described above, DNA quantization by agarose gel electrophoresis was employed. DNA was incubated with SA and AD microspheres in ratios of 0, 1, 10, 20, 40, 70, 100, 500, and 1000 ng per µl microspheres, and the total volume for each sample was brought up to 47.6 µl. Each aliquot was incubated for 2.5 hours at room temperature. The aliquots were then spun down at 13,000 rpm for 5 min, and a 15-µl aliquot of the supernatant was run on a 1% agarose gel with ethidium bromide staining, along with a 15-µl control sample corresponding to the amount of DNA incubated with the bead. Band intensities were analyzed on a Kodak image station gel scanner (864 2985; Carestream Health, Rochester, NY) to determine the amount of DNA on the beads.

The number of DNA molecules per microsphere was calculated as follows where:

DNA_{ng} = ng DNA per µl microspheres

DNA_{mol} = Moles DNA per µl microspheres

DNA_{micro} = Molecules DNA per microsphere

DNA_i = Initial ng DNA used to incubate microspheres

I_M = Intensity of band in lane of DNA + Microspheres

I_{DNA} = Intensity of band in lane of DNA only

$$DNA_{ng} = \frac{I_M - I_{DNA}}{I_{DNA}} * DNA_i \tag{3-2}$$

$$DNA_{mol} = \frac{DNA_{ng} \times 10^{-9}\ g/ng}{1049170.6\ g/mol \times 6.022 \times 10^{23}\ molecules/mol} \tag{3-3}$$

$$DNA_{micro} = \frac{DNA_{mol}}{3.7 \times 10^{7}\ microspheres/\mu l} \tag{3-4}$$

Oxygen scavengers and ROS quenchers

Oxygen scavengers. Two enzymatic oxygen scavenging systems were assayed: the glucose oxidase/catalase oxygen scavenging system (GODCAT), and the protocatechuic acid/protocatechate 3,4-dioxygenase oxygen scavenging system (PCA/PCD). GODCAT was prepared by dissolving 20 mg of glucose oxidase and 4 mg of catalase into 200 µl of T50 buffer (10 mM Tris, 1 mM EDTA, 50 mM NaCl, pH 7). The solution was then centrifuged twice at 13,000 rpm for 5 min, and the supernatant was subsequently centrifuge filtered twice at 11,000 rpm for one min to remove undissolved protein [54]. For each GODCAT tethering assay, 1 µl of GODCAT and 0.4% glucose was added to the standard TS buffer. PCA/PCD was prepared by adding 1 mg of PCA and 71.4 µl of 100% glycerol to 71.4 µl KET buffer (100 mM KCl, 2 mM EDTA, 200 mM Tris-Cl, pH 8.0) [55]. For each PCA/PCD tethering assay, a buffer composed of

TS buffer and 10 nM PCD and 100 mM PCA was used. Tether longevity assays in PCA/PCD and GODCAT were performed as previously described.

ROS quenchers

Three singlet oxygen quenchers were assayed: ascorbic acid, lipoic acid, and sodium azide. Each of these was assayed at the maximum quencher concentration that would allow tether formation. Ascorbic acid and lipoic acid both abolish tether formation at concentrations higher than 12.5 mM and 3.1 mM, respectively. Tether longevity assays in the presence of these three singlet oxygen quenchers were thus performed by making 12.5-mM, 3.1-mM, and 100-mM solutions of ascorbic acid, lipoic acid, and sodium azide (concentration chosen arbitrarily) in TS buffer, respectively. Two hydroxyl radical quenchers were assayed: Tris-Cl and manitol. 200-mM solutions of each of these quenchers were made in TS buffer. Tether longevity assays were performed in these solutions as described previously.

Singlet oxygen sensors

Anthracene assay. A 13.6-μM solution of 3-(10-(2-carboxy-ethyl)-anthracen-9-yl)-propinoic acid (CEAPA) in methanol was prepared. Both optical traps were set such that the total power at the sample plane was 1.6 W. The CEAPA/MeOH solution was flowed through a sample chamber at a rate of 10 μl/hr, using a remote-controlled syringe pump (70-2100 PHD 2000; Harvard Apparatus, Holliston, Massachusetts). The laser-exposed solution, in addition to non-exposed solution of CEAPA, was analyzed by electrospray ionization mass spectrometry (ESI-MS).

SOSG Assay. Singlet oxygen sensor green (S36002, Invitrogen) was prepared by dissolving the contents of one 100-µg vial in 33 µl methanol (~5 mM). 1 µl of this solution was dissolved into 100 µl water for all SOSG assays.

3.8 Chapter references

1. Landry, M.P., et al., *Characterization of Photoactivated Singlet Oxygen Damage in Single-Molecule Optical Trap Experiments.* Biophysical Journal, 2009. **97**(8): p. 2128-2136.
2. Bustamante, C., Z. Bryant, and S.B. Smith, *Ten years of tension: single-molecule DNA mechanics.* Nature, 2003. **421**(6921): p. 423-427.
3. Mehta, A.D., et al., *Single-molecule biomechanics with optical methods.* Science, 1999. **283**(5408): p. 1689-1695.
4. Moffitt, J.R., et al., *Recent advances in optical tweezers.* Annual Review of Biochemistry, 2008. **77**: p. 205-228.
5. Ashkin, A., et al., *Observation of a Single-Beam Gradient Force Optical Trap for Dielectric Particles.* Optics Letters, 1986. **11**(5): p. 288-290.
6. Neuman, K.C. and S.M. Block, *Optical trapping.* Rev Sci Instrum, 2004. **75**(9): p. 2787-809.
7. Ashkin, A., J.M. Dziedzic, and T. Yamane, *Optical trapping and manipulation of single cells using infrared laser beams.* Nature, 1987. **330**(6150): p. 769-71.
8. Neuman, K.C., et al., *Characterization of photodamage to Escherichia coli in optical traps.* Biophys J, 1999. **77**(5): p. 2856-63.
9. Liu, Y., et al., *Physiological monitoring of optically trapped cells: assessing the effects of confinement by 1064-nm laser tweezers using microfluorometry.* Biophys J, 1996. **71**(4): p. 2158-67.
10. Mohanty, S.K., M. Sharma, and P.K. Gupta, *Generation of ROS in cells on exposure to CW and pulsed near-infrared laser tweezers.* Photochem Photobiol Sci, 2006. **5**(1): p. 134-9.
11. Bustamante, C., J.C. Macosko, and G.J. Wuite, *Grabbing the cat by the tail: manipulating molecules one by one.* Nat Rev Mol Cell Biol, 2000. **1**(2): p. 130-6.
12. Greenleaf, W.J., M.T. Woodside, and S.M. Block, *High-resolution, single-molecule measurements of biomolecular motion.* Annu Rev Biophys Biomol Struct, 2007. **36**: p. 171-90.
13. Fuller, D.N., et al., *A general method for manipulating DNA sequences from any organism with optical tweezers.* Nucleic Acids Res, 2006. **34**(2): p. e15.
14. Moffitt, J.R., et al., *Differential detection of dual traps improves the spatial resolution of optical tweezers.* Proc Natl Acad Sci U S A, 2006. **103**(24): p. 9006-11.
15. Chen, G., et al., *In vitro scanning saturation mutagenesis of all the specificity determining residues in an antibody binding site.* Protein Engineering, 1999. **12**(4): p. 349-356.
16. Piran, U. and W.J. Riordan, *Dissociation Rate-Constant of the Biotin-Streptavidin Complex.* Journal of Immunological Methods, 1990. **133**(1): p. 141-143.
17. Gross, S.P., *Application of optical traps in vivo.* Methods Enzymol, 2003. **361**: p. 162-74.
18. Mao, H.B., et al., *Temperature control methods in a laser tweezers system.* Biophysical Journal, 2005. **89**(2): p. 1308-1316.
19. Visscher, K., S.P. Gross, and S.M. Block, *Construction of multiple-beam optical traps with nanometer-resolution position sensing.* Ieee Journal of Selected Topics in Quantum Electronics, 1996. **2**(4): p. 1066-1076.
20. Aitken, C.E., R.A. Marshall, and J.D. Pulglisi, *An oxygen scavenging system for improvement of dye stability in single-molecule fluorescence experiments.* Biophysical Journal, 2008. **94**(5): p. 1826-1835.
21. Sies, H., *Oxidative stress: oxidants and antioxidants.* Exp Physiol, 1997. **82**(2): p. 291-5.
22. Devasagayam, T.P.A., et al., *Activity of Thiols as Singlet Molecular-Oxygen Quenchers.* Journal of Photochemistry and Photobiology B-Biology, 1991. **9**(1): p. 105-116.

23. Machlin, L.J. and A. Bendich, *Free-Radical Tissue-Damage - Protective Role of Antioxidant Nutrients.* Faseb Journal, 1987. **1**(6): p. 441-445.
24. Packer, L., E.H. Witt, and H.J. Tritschler, *Alpha-Lipoic Acid as a Biological Antioxidant.* Free Radical Biology and Medicine, 1995. **19**(2): p. 227-250.
25. Frati, E., et al., *Degradation of hyaluronic acid by photosensitized riboflavin in vitro. Modulation of the effect by transition metals, radical quenchers, and metal chelators.* Free Radical Biology and Medicine, 1997. **22**(7): p. 1139-1144.
26. Trabanco, A.A., et al., *A seco-porphyrazine: Superb sensitizer for singlet oxygen generation and endoperoxide synthesis.* Synlett, 2000(7): p. 1010-1012.
27. Herzberg, G. and T.J. Hugo, *Forbidden Transitions in Diatomic Molecules .4. The Alpha+3-Sigma+]-Chi-1-Sigma+ and Epsilon-3-Sigma-]-Chi-1-Sigma+ Absorption Bands of Carbon Monoxide.* Canadian Journal of Physics, 1955. **33**(12): p. 757-772.
28. Foote, C.S., et al., *Quenching of Singlet Oxygen.* Annals of the New York Academy of Sciences, 1970. **171**(1): p. 139-&.
29. Flors, C., et al., *Imaging the production of singlet oxygen in vivo using a new fluorescent sensor, Singlet Oxygen Sensor Green.* J Exp Bot, 2006. **57**(8): p. 1725-34.
30. Wittmershaus, B.P., et al., *Excitation energy transfer from polystyrene to dye in 40-nm diameter microspheres.* Journal of Luminescence, 2002. **96**(2-4): p. 107-118.
31. Herzberg, G. and T.J. Hugo, *Molecular Spectra and Molecular Structure I: Spectra of Diatomic Molecules* 2ed. 1950, New York: VonNostrand.
32. Hallett, F.R., B.P. Hallett, and W. Snipes, *Reactions between Singlet Oxygen and Constituents of Nucleic Acids - Importance of Reactions in Photodynamic Processes.* Biophysical Journal, 1970. **10**(4): p. 305-&.
33. Boegheim, J.P.J., et al., *Damaging Action of Photodynamic Treatment in Combination with Hyperthermia on Transmembrane Transport in Murine L929 Fibroblasts.* Biochimica Et Biophysica Acta, 1989. **979**(2): p. 215-220.
34. Decuyper-Debergh, D., J. Piette, and A. Van de Vorst, *Singlet oxygen-induced mutations in M13 lacZ phage DNA.* EMBO J, 1987. **6**(10): p. 3155-61.
35. Ravanat, J.L., et al., *Singlet oxygen induces oxidation of cellular DNA.* J Biol Chem, 2000. **275**(51): p. 40601-4.
36. Ribeiro, D.T., et al., *Singlet oxygen induces predominantly G to T transversions on a single-stranded shuttle vector replicated in monkey cells.* Free Radic Res, 1994. **21**(2): p. 75-83.
37. Ribeiro, D.T., et al., *Singlet oxygen induced DNA damage and mutagenicity in a single-stranded SV40-based shuttle vector.* Photochem Photobiol, 1992. **55**(1): p. 39-45.
38. Sies, H. and C.F. Menck, *Singlet oxygen induced DNA damage.* Mutat Res, 1992. **275**(3-6): p. 367-75.
39. Bird, R.B., W.E. Stewart, and E.N. Lightfoot, *Transport Phenomena*. 1960, New York: John Wiley & Sons.
40. Merkel, P.B. and D.R. Kearns, *An Experimental and Theoretical Study of Electronic-to-Vibrational Energy Transfer.* Proc Natl Acad Sci U S A, 1972. **94**(21): p. 7244-7253.
41. Abbondanzieri, E.A., et al., *Direct observation of base-pair stepping by RNA polymerase.* Nature, 2005. **438**(7067): p. 460-5.
42. Carter, A.R., Y. Seol, and T.T. Perkins, *Precision surface-coupled optical-trapping assay with one-basepair resolution.* Biophys J, 2009. **96**(7): p. 2926-34.
43. Davies, M.J., *Singlet oxygen-mediated damage to proteins and its consequences.* Biochem Biophys Res Commun, 2003. **305**(3): p. 761-70.
44. Davies, M.J., *Reactive species formed on proteins exposed to singlet oxygen.* Photochem Photobiol Sci, 2004. **3**(1): p. 17-25.

45. Prinsze, C., T.M. Dubbelman, and J. Van Steveninck, *Protein damage, induced by small amounts of photodynamically generated singlet oxygen or hydroxyl radicals.* Biochimica Et Biophysica Acta, 1990. **1038**(2): p. 152-7.
46. Chattopadhyay, S., et al., *Swimming efficiency of bacterium Escherichia coli.* Proc Natl Acad Sci U S A, 2006. **103**(37): p. 13712-7.
47. Shubeita, G.T., et al., *Consequences of motor copy number on the intracellular transport of kinesin-1-driven lipid droplets.* Cell, 2008. **135**(6): p. 1098-107.
48. Krasnovsky, A.A., et al., *Activation of molecular oxygen by infrared laser radiation in pigment-free aerobic systems.* Biochemistry-Moscow, 2003. **68**(9): p. 963-966.
49. Frederiksen, P.K., M. Jorgensen, and P.R. Ogilby, *Two-photon photosensitized production of singlet oxygen.* Journal of the American Chemical Society, 2001. **123**(6): p. 1215-1221.
50. Bustamante, C., Y.R. Chemla, and J.R. Moffitt, *Single-Molecule Techniques: A Laboratory Manual*, C.S. Harbor, Editor. 2008: New York.
51. Moffitt, J.R., et al., *Differential detection of dual traps improves the spatial resolution of optical tweezers.* Proceedings of the National Academy of Sciences of the United States of America, 2006. **103**(24): p. 9006-9011.
52. Woodside, M.T., et al., *Nanomechanical measurements of the sequence-dependent folding landscapes of single nucleic acid hairpins.* Proc Natl Acad Sci U S A, 2006. **103**(16): p. 6190-5.
53. Wuite, G.J., et al., *An integrated laser trap/flow control video microscope for the study of single biomolecules.* Biophys J, 2000. **79**(2): p. 1155-67.
54. Selvin, P.R., et al., *In Vitro and In Vivo FIONA and Other Acronyms for Watching Molecular Motors Walk*. 2008, Cold Spring Harbor: Cold Spring Harbor Press.
55. Aitken, C.E., R.A. Marshall, and J.D. Puglisi, *An oxygen scavenging system for improvement of dye stability in single-molecule fluorescence experiments.* Biophys J, 2008. **94**(5): p. 1826-35.

Chapter 4. Target search of dimer-active proteins

Sequence-specific DNA-binding proteins (SSPs) must quickly and reliably localize specific target sites on DNA. This search process has been well characterized for monomeric proteins, but remains poorly understood for systems that require assembly into dimers or oligomers at the target site. We present a single-molecule study of the target-search mechanism of protelomerase TelK, a recombinase-like protein that is only active as a dimer. We show that TelK undergoes 1D diffusion on non-target DNA as a monomer, and immobilizes upon dimerization even in the absence of a DNA target site. We further show that dimeric TelK condenses non-target DNA, forming a tightly bound nucleoprotein complex. Together with theoretical calculations and molecular dynamics simulations, we present a novel target-search model for TelK, which may be generalizable to other dimer and oligomer-active proteins.

4.1 Introduction to protein-DNA target search mechanisms

Single-molecule techniques are powerful in their ability to monitor biological processes in real-time. One particular biological sub-field which has benefitted greatly from single-molecule techniques is protein-DNA target search mechanisms. A long-standing question in biology involves understanding how a protein can identify a target site amongst kilobases of non-target DNA in the short time-frames required by most protein-DNA dependent biological processes. The theoretical amount of time it should take for a protein to identify a target site amongst kilobases of non-target DNA via 3D Brownian diffusion does not explain the kinetics of protein-DNA interactions in bulk studies. Single-molecule techniques enabled direct confirmation of the mechanisms responsible for protein-DNA target search kinetics, and confirmed many of the theories that had been proposed via earlier bulk studies. In this chapter, we extend our understanding of protein-DNA target search mechanisms using a variety of single-molecule experimental and theoretical approaches.

Many essential cellular processes depend on protein-DNA interactions at specific sequences in the genome. Sequence-specific proteins (SSPs) must quickly and reliably localize target sites that are typically only a few base pairs in length amongst kilobases of non-target genomic DNA. Several studies of the interaction of SSPs along DNA have revealed some aspects of the mechanism by which target-finding occurs [2-5]. According to current models, a protein binds and scans non-target regions of DNA by 1D diffusion facilitated by 3D hopping, until the protein identifies its target sequence [6-8].

Most studies to-date have focused on the target search mechanism of a particular class of sequence-specific proteins. Experimental and theoretical studies of target search have mainly considered proteins that are either monomeric (ex: certain restriction enzymes such as FokI and mismatch repair proteins such as MutH and T4 endonuclease V, DNA repair protein hOgg1 [9-12]), or when oligomeric, pre-assembled in solution (ex: BbvCl, LacI repressor, EcoRV, EcoRI, Msh2-Msh6, MutS, Mlh1-Pms1 [13-18]). These examples bind DNA and locate a target site as a single functional unit. Many proteins, however, function exclusively as dimers or oligomers at a target site, but are monomeric in solution, only assembling into higher-order complexes on DNA. Such proteins are ubiquitous in the cell, and are involved in a range of cellular functions including DNA repair, replication, transcription, and translation [19-21]. Common examples of such proteins include certain recombinases, select type II and III restriction enzymes, transcription factors, integrases, DNA-repair proteins, and signal transducers [21-24]. Despite the abundance of cellular proteins that must dimerize or oligomerize onto DNA in addition to identifying a target site, little work has been done to understand the complete mechanism by which they localize both their target sequence and protein partner(s). An exception is type III restriction endonucleases [5, 25], in which two distinct protein monomers find two separate

target sites by a facilitated 1D diffusion and then use sliding to assemble a higher-order complex on the DNA.

Proteins that must assemble higher-order complexes on single target sites must not only locate their DNA target sites but must also find their protein partner(s). This added complexity gives rise to new questions: How do two protein monomers find each other? Is dimerization required for target-site specificity, or do individual monomers hold the capacity to identify a target sequence? Do protein monomers or dimers undergo 1D diffusion? If proteins diffuse in 1D as monomers, what happens if two proteins encounter each other along non-target DNA? Answers to these questions may provide a comprehensive model for the target-search process of dimer-active proteins.

4.2 Protelomerase TelK

In the prokaryotic organism *Klebsiella oxytoca*, protelomerase TelK is a protein that is encoded by the lysogenic phage K02 upon infection. Unlike the other well-known lysogenic λ phages, whose DNA is integrated into the *E. coli* chromosome, the phage K02 DNA instead forms a linear plasmid with hairpin ends. Replication of this linear plasmid generates catenated genomes that are resolved by TelK [1]. The protein localizes two 56-bp target sequences at opposite poles of the DNA circle replication intermediate, and generates hairpin-capped ends via site-specific excision, strand exchange, and re-ligation. TelK-induced DNA hairpin formation occurs independently of ATP or other cofactors such as Mg^{2+}, and TelK is a single-turnover protein [1]. TelK shares sequence and structural homology to tyrosine recombinases (Y-recombinases) and type IB topoisomerases [26]. The crystal structure of TelK538, a truncation mutant of wild-type TelK, complexed with a 44-mer target-DNA substrate shows two tightly

bound TelK monomers that form the active dimer oriented head-to-head on the dyad symmetric DNA target site. Dimerization induces a sharp 73° bend in the DNA substrate [26]. While TelK is known to be a monomer in solution, target-sequence activity requires TelK to dimerize at its target site in the correct head-to-head orientation [1], making it an ideal protein for the study of target-search by monomer-to-dimer SSPs.

To understand the target-site search mechanism for this protein, we studied the interaction of TelK with both DNA lacking and containing the target sequence. Through a combination of single-molecule experiments—including total internal reflection fluorescence microscopy (TIRFM) and optical trapping [27, 28]—and theoretical analysis in the form of molecular dynamics (MD) simulations [29] and stochastic simulations, we determined the novel search mechanism TelK uses to identify its DNA target site. As a monomer, TelK undergoes 1D diffusion along nonspecific DNA, and is able to bind to the target site preferentially. There, the target-immobilized monomer waits for a second binding partner to form an active protein complex. Surprisingly, if two monomers coalesce on non-target DNA, they also immobilize and condense DNA. This transient tight-binding is reversible; non-target bound dimers will eventually dissociate into monomers along DNA or into solution. We propose this target-search model for TelK may be applicable to other proteins that are active as dimers or oligomers at DNA target sites.

4.3 TIR fluorescence microscopy of TelK on non-target DNA bridges

We first investigated the interaction between TelK and *non-target* DNA. We used TIRF microscopy to image individual quantum-dot (QD) labeled proteins on linearly extended DNA that lacked the TelK target sequence. This was achieved by depositing 48.5-kb, end-biotinylated

λ-DNA across neutravidin-coated pedestals etched in a glass surface (**Materials and Methods**; **Figure 4-1 a**). These formed extended DNA "bridges" with which QD-TelK interacted. The etched glass chamber was then sealed with a glass cover slip, and TIRF imaging was achieved by creating an evanescent light field through this cover slip. TelK640 (the full-length wild-type 640 amino acid protein henceforth referred to as TelK) was labeled with anti-histidine conjugated QDs with an ~84% labeling efficiency (**Figure 4-16**). Control assays showed that QD-labeled TelK displayed comparable activity to unlabeled TelK in bulk (**Figure 4-16**). Prior to a typical measurement, QD-labeled TelK was flowed into the chamber and left to incubate with the DNA bridges for 5 minutes to allow TelK to bind to the DNA bridges. Unbound TelK and free QD were subsequently rinsed away with a small volume (50 μL) of imaging buffer (20 mM Tris-HCl, 50 mM potassium glutamate, 1mM DTT, 0.1 mM EDTA, 100 nM glucose oxidase; 1.5 mM catalase; 56 mM glucose; **Materials and Methods**) to reduce the fluorescence background. A low background concentration of TelK remained in solution throughout the experiment due to unbound protein not removed during rinsing and from dissociation of bound protein from DNA.

The positions of individual protein units on DNA were tracked by Gaussian-fitting the fluorescent intensity [30].

4.3.1 TelK motion along non-target DNA

In **Figure 4-1 b**, a kymograph of TelK's motion along DNA shows Brownian 1D diffusional motion along the DNA backbone as TelK searches for a target site. However, we also observed a stationary mode of TelK interaction with non-target DNA. The same fluorescent spot is observed to switch abruptly from a "mobile" mode undergoing rapid 1D diffusion to a clearly distinguishable "stationary" mode. Intensity analysis of the mobile and stationary part of the

trace reveals that the mobile part of the trace is roughly half as bright as the stationary part of the trace (**Figure 4-1 c**). Also, QDs are known to exhibit "blinking" behavior, where the QD fluorescence intensity stochastically switches on and off [31]. In our image analysis, we defined blinking spots as those whose intensity dropped to zero for at least one frame (0.1s). In **Figure 4-1 c**, the mobile part of the trace shows on/off QD behavior, whereas the stationary part of the trace does not blink off. Based on their intensity and on/off behavior, we deduced that the mobile part of the trace represents the motion of a single labeled TelK monomer, whereas the stationary and non-blinking part of the trace represents two TelK proteins within a diffraction limited spot, presumably from binding of a second TelK monomer in solution.

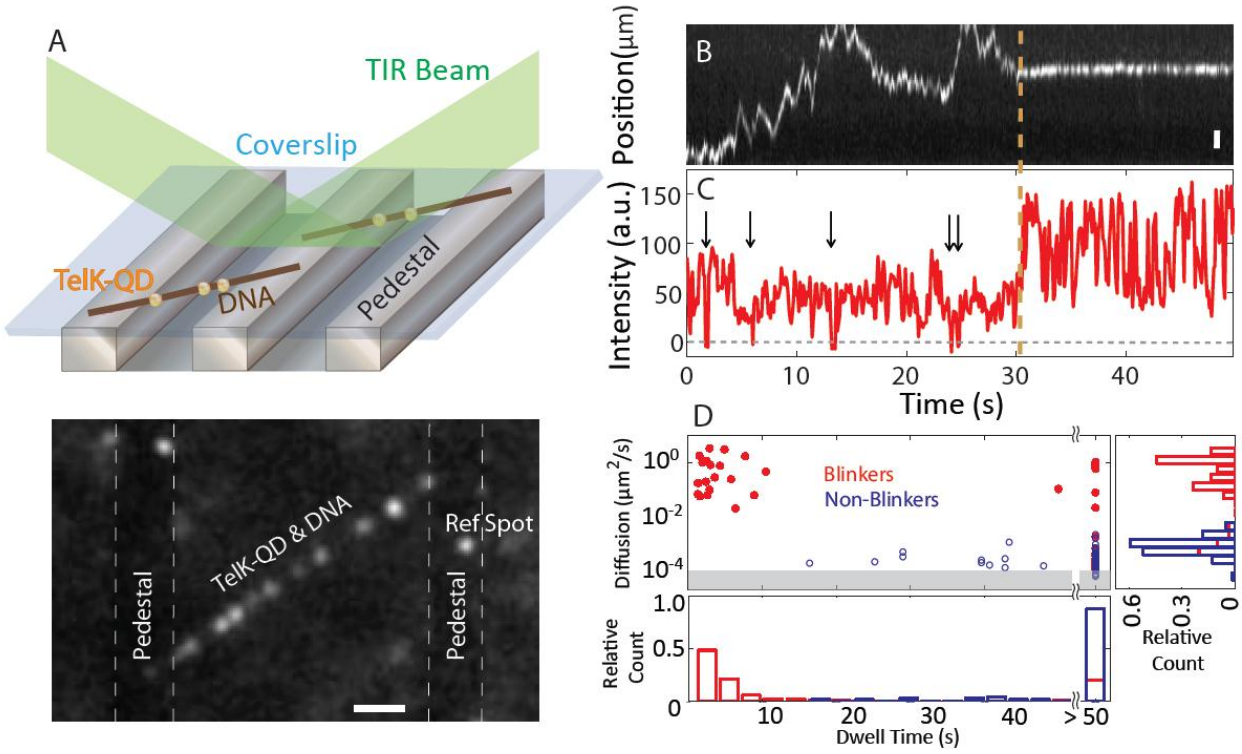

Figure 4-1. TelK monomers diffuse along non-target DNA whereas dimers immobilize.

(a) Schematic of TIRFM experimental setup and representative fluorescence image. An etched glass slide with 1x1 μm pedestals separated by 7-μm etches was coated with neutravidin. Dual-biotinylated λ-DNA was flowed in to form DNA bridges, and the chamber was subsequently incubated with quantum-dot labeled TelK monomers (here, 340 nM). QDs stuck to the glass surface were used as reference spots to ensure that drift and background motion were minimal. TelK concentrations used in all TIRF experiments ranged from 70 to 1350 nM.

(b) Kymograph of QD-labeled TelK on λ-DNA showing mobile (1 – 31 s) and stationary (32 – 50 s) states after analysis and background subtraction with Gaussian fitting of spots.

(c) Fluorescence intensity corresponding to the kymograph. The intensity of the mobile TelK doubles as it becomes immobile along the λ-DNA bridge. QD blinking events (arrows), known to occur for single QDs, are observed only prior to TelK immobilization.

(d) Diffusion coefficient and lifetime for blinking fluorescence spots (N = 114, red) and non-blinking spots (N = 81, blue). The shaded area represents the limit of sensitivity of our assay. The distribution of diffusion coefficients (right panel) is bimodal, with blinkers diffusing approximately four orders of magnitude faster than non-blinkers. As shown in the lifetime distributions (bottom panel), blinking spots also remained DNA-bound for shorter times (4.2 s) than non-blinkers (>50 s).

4.3.2 TelK mobility at different concentrations

We performed this TIRFM assay over a range of TelK concentrations from 70 to 1350 nM. Analysis over many DNA bridges revealed a clear bimodal distribution in the population of fluorescently labeled protein, showing species of mobile and immobile spots (**Figure 4-1 d**). Mobile spots diffused rapidly along DNA with an average diffusion coefficient D = 0.74 ± 0.1 $\mu m^2/s$ (mean ± s.e.m.) whereas stationary spots had a diffusion coefficient of (3.0 ± 0.4) × 10^{-4} $\mu m^2/s$ (mean ± s.e.m.). Diffusion coefficients were calculated by fitting the linear part of the fluorescent protein's mean squared displacement (MSD) dependence on time (**Materials and Methods** and **Figure 4-17**). Based on the bimodal distribution of diffusion coefficients (**Figure 4-1 d**), a cutoff of $D \sim 0.01$ $\mu m^2/s$ was used to classify spots as mobile or stationary. In a subset of movies, we observed stationary fluorescent spots stuck to the glass pedestals. When available, these reference spots were also tracked. The mean diffusion coefficient from reference spots was $D \sim 1 \times 10^{-4}$ $\mu m^2/s$, providing an estimate of the instrument noise and of the sensitivity limit of our measurements. Subtracting the reference spot motion from the DNA-bound TelK positions had only a negligible effect on our estimates of the diffusion coefficients. Beyond differences in mobility on DNA, mobile spots dissociated from the DNA at a rate of k_{off} = 0.24 ± 0.07 s^{-1} (mean ± s.e.m.), whereas most (88%) stationary spots remained stably bound for the duration of the TIRFM experiments (typically 50 sec.; i.e. $k_{off} < 0.02$ s^{-1}) (**Figure 4-1d**). On occasions, stationary spots were observed to dissociate from DNA (12%) or separate into two mobile spots (2%), and a small fraction of mobile spots were observed to coalesce into an immobile spot (2%) (**Figure 4-2**).

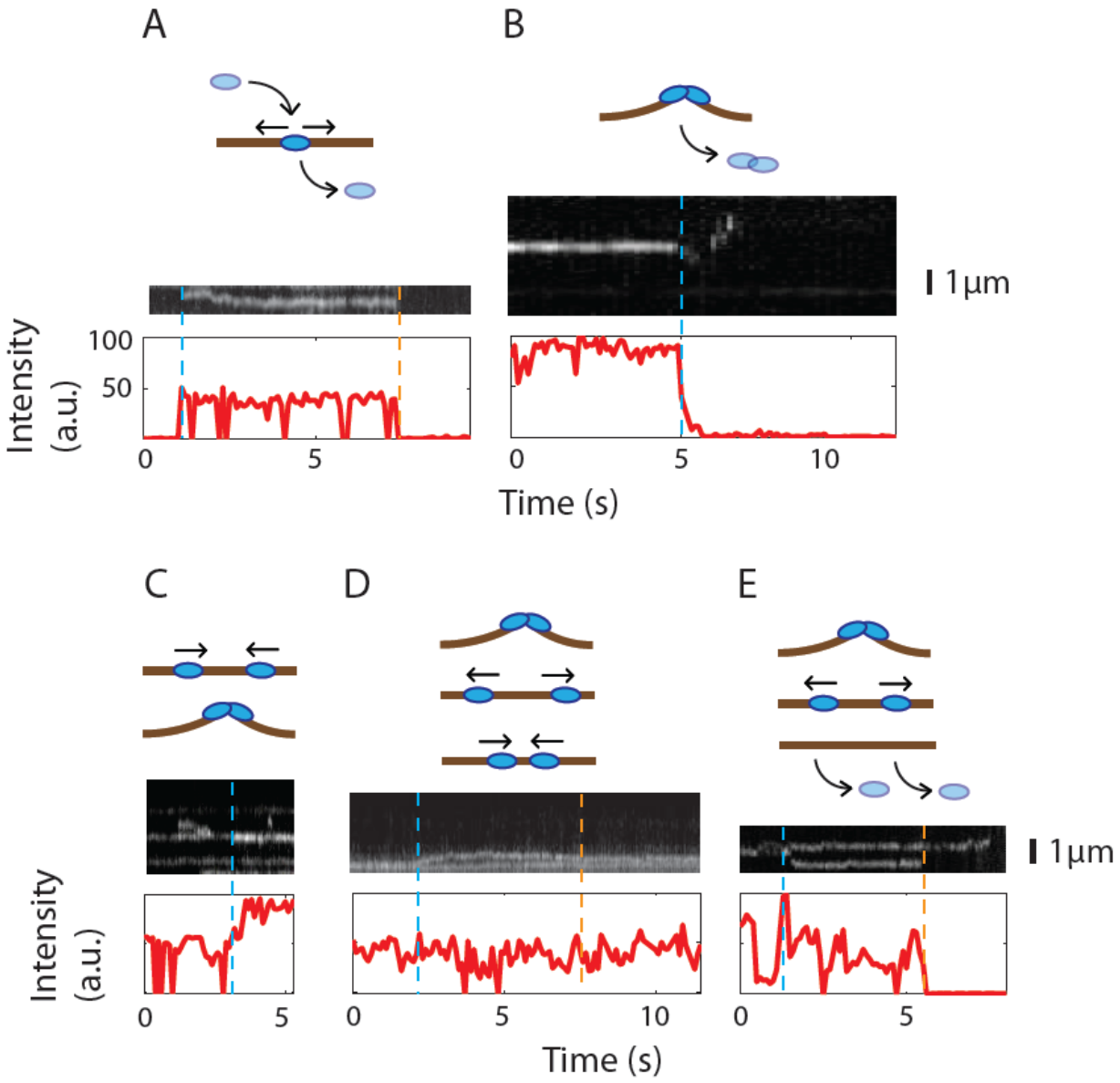

Figure 4-2. Representative data traces of TelK behavior on non-target DNA.
Schematics of various TelK behavior with corresponding kymographs and fluorescence intensity are shown.
(a) A TelK monomer binds to DNA (blue dashed line), diffuses, and dissociates (orange dashed line).
(b) An immobile spot dissociates from the DNA (blue dashed line).
(c) Two mobile TelK coalesce on DNA as intensity doubles (blue dashed line).
(d) An immobile spot separates into two mobile spots (blue dashed line) and re-joins downstream (orange dashed line).
(e) An immobile spot separates into two spots (blue dashed line), one of which dissociates from the DNA (orange dashed line). In c-e, the intensity of only one fluorescent spot is shown.

As in **Figure 4-1b**, overall protein mobilities displayed a distinct correlation between TelK diffusion coefficient and QD fluorescence behavior. All mobile diffraction-limited fluorescent spots showed blinking behavior, compared to only ~14% stationary spots (**Figure 4-1d**). This analysis strongly suggests that TelK monomers are able to exhibit the characteristic 1D diffusion of SSPs with non-target DNA, but that dimerization (or oligomerization) between TelK monomers causes 1D diffusion to cease. We attribute the small 14% fraction of blinking spots belonging to the stationary population to the ~16% unlabeled "dark" protein from our QD labeling (**Figure 4-16**).

Trajectories such as that shown in **Figure 4-1b** demonstrate that a minimum of two TelK proteins are sufficient to cause the protein immobilization on the λ-DNA bridges. In most cases, we were not able to observe directly a switch from the mobile to stationary state. However, most of the stationary spots observed under low TelK concentration (0–200 nM) exhibited the same characteristic fluctuating pattern in fluorescence intensity as the dimer in **Figure 4-1b** and **c** (81%). As TelK concentration was increased (>400 nM), we observed an increasing number of trajectories (~85%) exhibiting multiple plateaus in fluorescence intensity, which we attributed to higher-order (>2) TelK assemblies within a diffraction-limited spot. We believe these results are consistent with monomeric TelK being mobile and dimers being stationary, though larger aggregates are possible and may also lead to immobilization. Because TelK is functional as a dimer, our results strongly suggest that the active state of the protein is not competent to search for the target site.

4.4 Optical trap studies of TelK with non-target DNA

The TIRF measurements above demonstrate that dimers (and higher order oligomers) of TelK immobilize on DNA, surprisingly even in the absence of the target sequence. What is the mechanism for the observed dimer immobilization? Crystal structures of the TelK dimer in complex with target DNA indicate a conformation in which monomer-monomer contacts and a tight interaction to the target sequence kink the DNA by an angle of 73° [26]. Dimer immobilization observed in our TIRF measurements suggests that similar monomer-monomer contacts may also be responsible for dimer immobilization on non-target DNA. To test this hypothesis, we next utilized an optical trap to probe the TelK-DNA conformation on an extended DNA molecule.

4.4.1 Optical trap experimental approach

Using a previously established protocol (**Materials and Methods**), a 3.4-kb DNA molecule lacking the target sequence was tethered between two microspheres held in two optical traps.

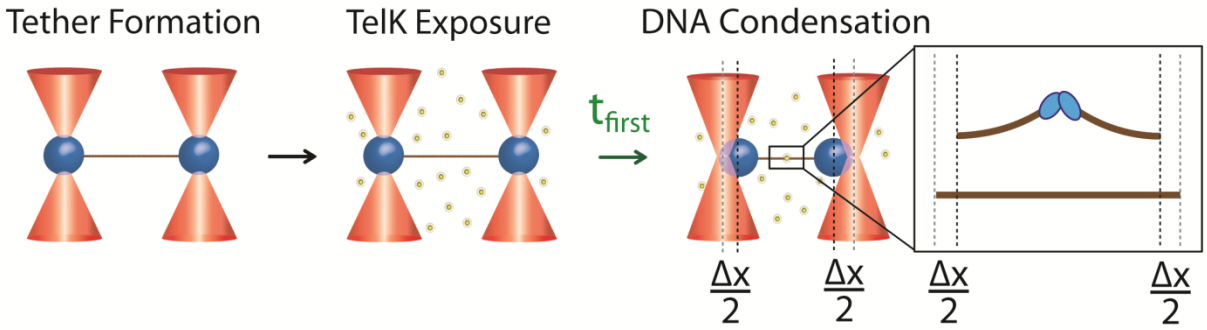

Figure 4-3. Optical trap experimental setup.
Schematic of optical trap experimental setup. A DNA tether was formed in a stream containing buffer only, and subsequently moved into a stream with buffer containing TelK. TelK binding to the DNA tether causes DNA condensation. The first passage time, t_{first}, is defined as the time between TelK exposure and the first condensation event.

The DNA tether was held at a low force (5.2 ± 1.3 pN, mean ± SD) comparable to that experienced by the extended DNA bridges in the TIRF assay (3.1 ± 2.7 pN, mean ± SD.; **Materials and Methods**; **Figure 4-18**). For our optical trap assay, we designed a sample chamber that allowed us to control when a DNA tether was exposed to TelK (**Figure 4-18**). Chambers were designed with two main parallel channels, one containing protein-free buffer, the other with a fixed concentration of TelK (**Materials and Methods**). A laminar flow of 100 μm/s created a ~200-μm boundary between the two channels. This design allowed us to move a DNA tether from the flow channel containing protein-free buffer through the buffer boundary into the second channel containing TelK within 2 seconds. This allowed for control of the timing of DNA tether exposure to TelK (**Figure 4-3**).

4.4.2 Non-target DNA condensation by TelK

Despite the absence of the TelK target site on the DNA, we repeatedly observed the DNA end-to-end extension to decrease by a few nanometers upon exposure to TelK (blue traces, **Figure 4-4 a**). These condensation events were transient with an average dwell time of 22 ± 6 s (mean ± s.e.m.) and occurred repeatedly at TelK concentrations ranging from 40 to 270 nM. In contrast, control experiments performed in buffer lacking TelK showed no DNA condensation (gray trace, **Figure 4-4 a**). Our ability to control when DNA was first exposed to TelK allowed us to measure accurately the time to the first condensation event. As expected, this first condensation time was strongly dependent on TelK concentration (red data points, **Figure 4-4 b**), indicating binding of one or multiple TelK to the DNA. In contrast, the average condensed state lifetime and the time between subsequent condensation events were independent of TelK concentration (blue data points, **Figure 4-4 b**), indicating that the same individual TelK complex

was responsible for those condensation events. At high (>200 nM) concentrations of TelK, we mostly observed multiple simultaneous condensation events that were indistinguishable from each other. Therefore we restricted our analysis to tethers showing individual separate condensation steps.

The size of these individual condensation events was determined with a step-finding algorithm [32]. The step-size distribution for DNA condensation by TelK is displayed in **Figure 4-4 c**. Condensation behavior is expected as a result of TelK dimer formation at the DNA target site, as the 73° bend of the target DNA observed in crystal structures condenses the DNA,

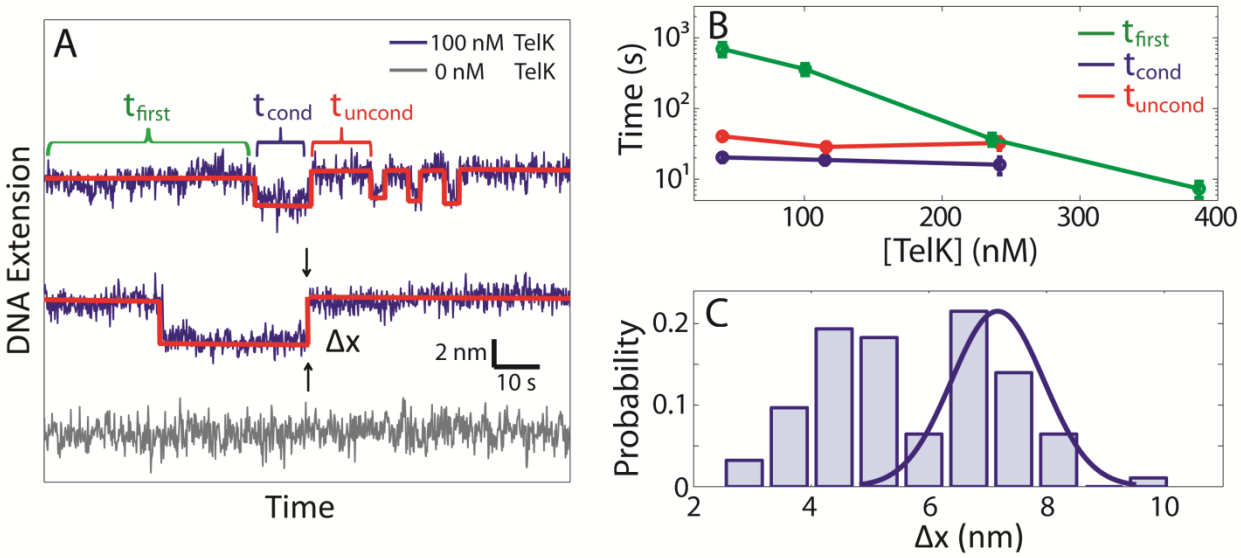

Figure 4-4. TelK dimers condense non-target DNA.

(a) Time traces showing single DNA condensation events for tethers exposed to 100 nM TelK (blue) fit with a step-finder algorithm (red), and protein-free control trace (grey). Three characteristic times are highlighted in a sample trace: the time to first condensation, the condensed state lifetime, and uncondensed state time. Traces offset for clarity.

(b) The time for first TelK-induced condensation (green) is strongly dependent on [TelK], whereas the dwell time of the condensed state (blue) and the time between condensation events (red) do not depend on [TelK].

(c) Normalized histogram of step size (Δx) for all observed condensation events (N = 93) due to DNA-induced TelK bending, with Gaussian fit to the condensation step size expected from the TelK dimer-DNA crystal structure.

reducing its end-to-end extension. However, DNA condensation in the absence of the target site is not expected. The observed condensation in the optical trap measurements suggests that the same dimer-DNA conformation may be adopted on non-target DNA.

4.4.3 Small DNA condensation step size

Our optical trap studies show that TelK dimerizes non-target DNA. Two distinct condensation step sizes are observed from the optical trap data, one of which matches what would be expected from the TelK-DNA crystal structure. However, the second condensation step size (which accounts for 51% of all condensation events) remains puzzling. We propose that the small step size is due to the interaction of two misoriented TelK monomers on DNA.

Previous work has proposed that the high degree of cooperative electrostatic binding between protein monomers in dimer- or oligomer-active protein families may lead to different modes of nonspecific binding that depend on protein orientation on the DNA. For example, in the process of site-specific recombination, the two different modes of binding between two recombinase monomers determine which DNA strand is cut first, and determine the product of recombination [33]. Correct orientation of two monomers in dimer-active Y-recombinases has also been proposed to be a control mechanism that ensures correct protein-DNA interactions prior to catalysis [34, 35]. As a member of the Y-recombinase protein family, TelK must correctly orient itself along the DNA target site in order to form a functional unit. The TelK crystal structure shows that the active dimer must be oriented head-to-head on the dyad symmetric DNA target site, and shows that this protein-DNA interaction causes a sharp 73° bend in the target DNA [26]. However, due to the random orientation of TelK monomers along DNA, we speculate that half of the stochastic monomer encounters along DNA will involve dimers that are incorrectly

oriented in a head-to-tail or tail-to-tail orientation. These dimerization events may explain the bimodal distribution of condensation step size, with the large DNA condensation corresponding to correctly oriented TelK monomers, and the small DNA condensation corresponding to incorrectly oriented molecules.

4.4.4 Target-DNA condensation behavior

Repeating the optical trap experiments with DNA containing the TelK target site, we again observed repeated condensation of the DNA. The average condensation dwell time was 21 ± 2 s (mean ± s.e.m.), with an average step-size of 7.7 ± 0.2 nm (mean ± s.e.m.; **Figure 4-5 a** and **b**), in good agreement with the value measured with non-target DNA. Interestingly, we observed less of the 4.5-nm condensation events, which we attributed to misoriented dimers. We speculate that the presence of the target site may bias dimer formation into the more "proper" configuration consistent with crystal structures.

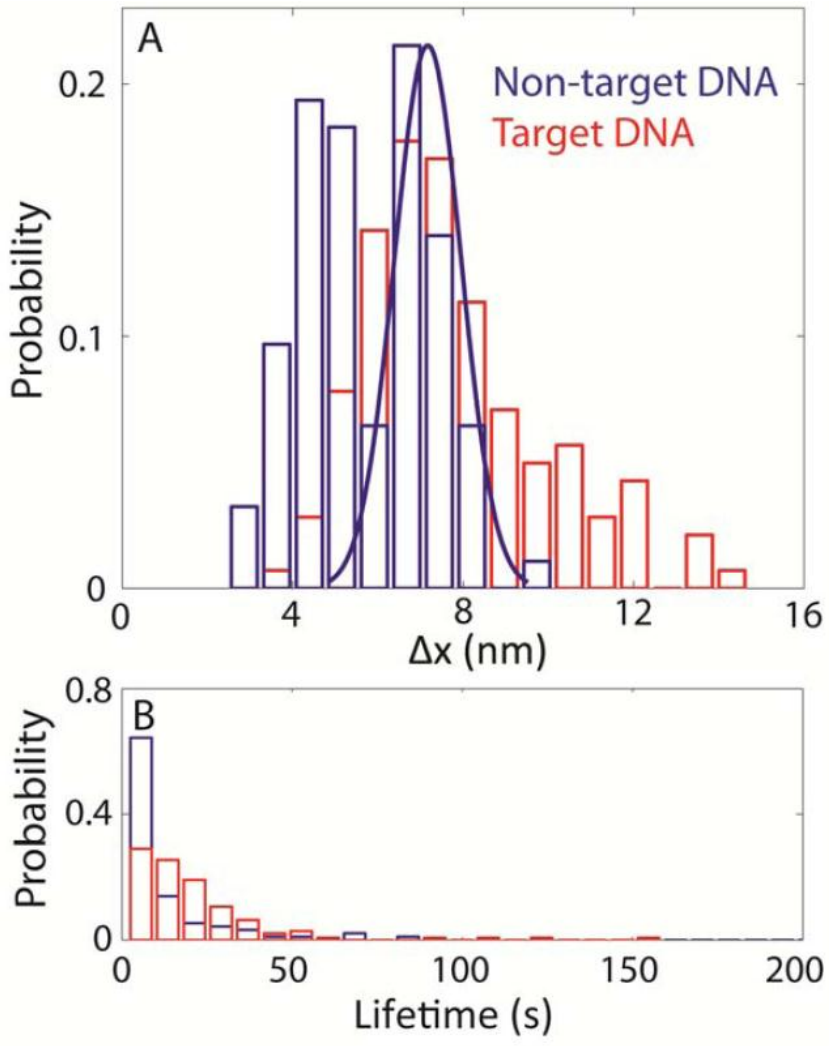

Figure 4-5. Condensation behavior of target vs. non-target DNA.

(a) Step-size distributions for target (red) and non-target (blue) DNA yield a single peaked distribution with an average condensation stepsize of 7.75 ± 0.2 nm, and a doubly-peaked distribution with peak condensation step-sizes of 7.2 ± 0.1nm and 4.5 ± 0.1 nm, respectively.

(b) Mean condensed state lifetime distributions for target DNA (red) and for non-target DNA (blue). Mean lifetimes are 22 ± 6 s and 21 ± 2 s, respectively (mean ± s.e.m.).

4.5 Molecular Dynamics simulations of TelK with DNA

The nature of the non-target DNA condensation in the optical trap is unclear. Are TelK monomers or dimers responsible for the condensation observed in the optical trap? To test this question, we performed a series of MD simulations to study the interaction of 1) a TelK538 dimer bound to target DNA; 2) a TelK538 dimer bound to non-target DNA; 3) a TelK538 monomer bound to target DNA; 4) a TelK538 monomer bound to non-target DNA; 5) a TelK538 dimer without DNA. Non-target DNA was simulated by mutating nucleotides that make contacts with TelK538 in the crystal structure; the mutated sites are shown in (**Figure 4-6**).

4.5.1 TelK bends target and non-target DNA

The simulations reveal that near identical bend angles (~70°) are induced onto DNA with and without the target sequence (**Figure 4-6**). MD simulations show that TelK maintains a sharp bend angle on a DNA substrate regardless of whether the DNA substrate contains the TelK target

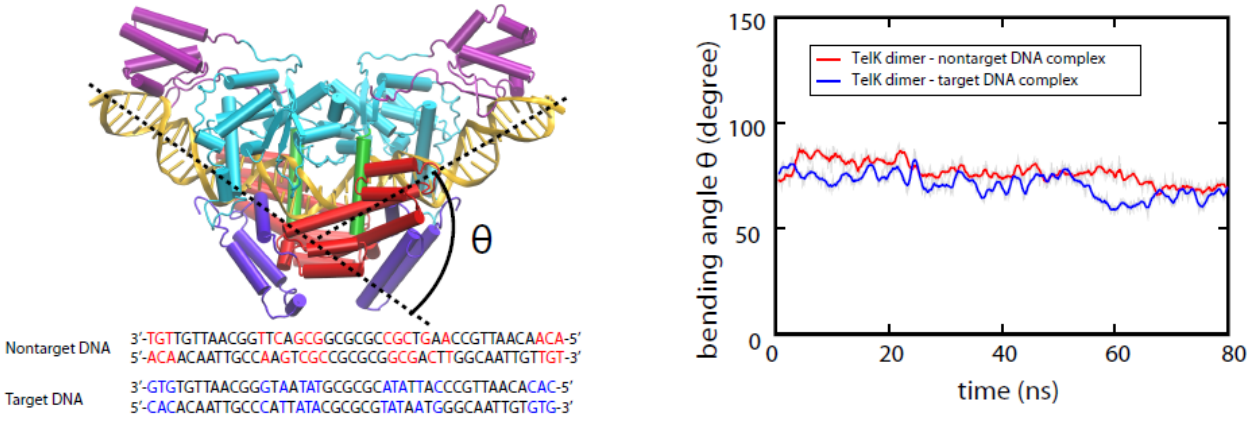

Figure 4-6. TelK dimer bends target and nontarget DNA.
MD simulation of TelK dimer complexed with either non-target (red) or target (blue) DNA. Mutations made to target DNA to produce non-target DNA are highlighted in red (mutated base) and blue (wild-type base). Non-target (red) and target (blue) DNA is bent by similar angles during an 80-ns simulation.

sequence, as observed in our experimental data. We used the bend angle observed in these MD simulations to estimate the change in DNA end-to-end extension as a result of TelK dimerization on the non-target DNA substrate used in our optical trap assays. Besides the DNA bend angle observed in the MD simulation, this calculation takes into consideration the DNA persistence length (50 nm), the force at which DNA is held in the optical trap, and the resulting extension is compared to that of linearly extended DNA as shown in **Figure 4-7** [36] (see **Methods**). Based on this calculation, we expect a condensation step size of 7.5 nm at a tension of 5.2 pN. As

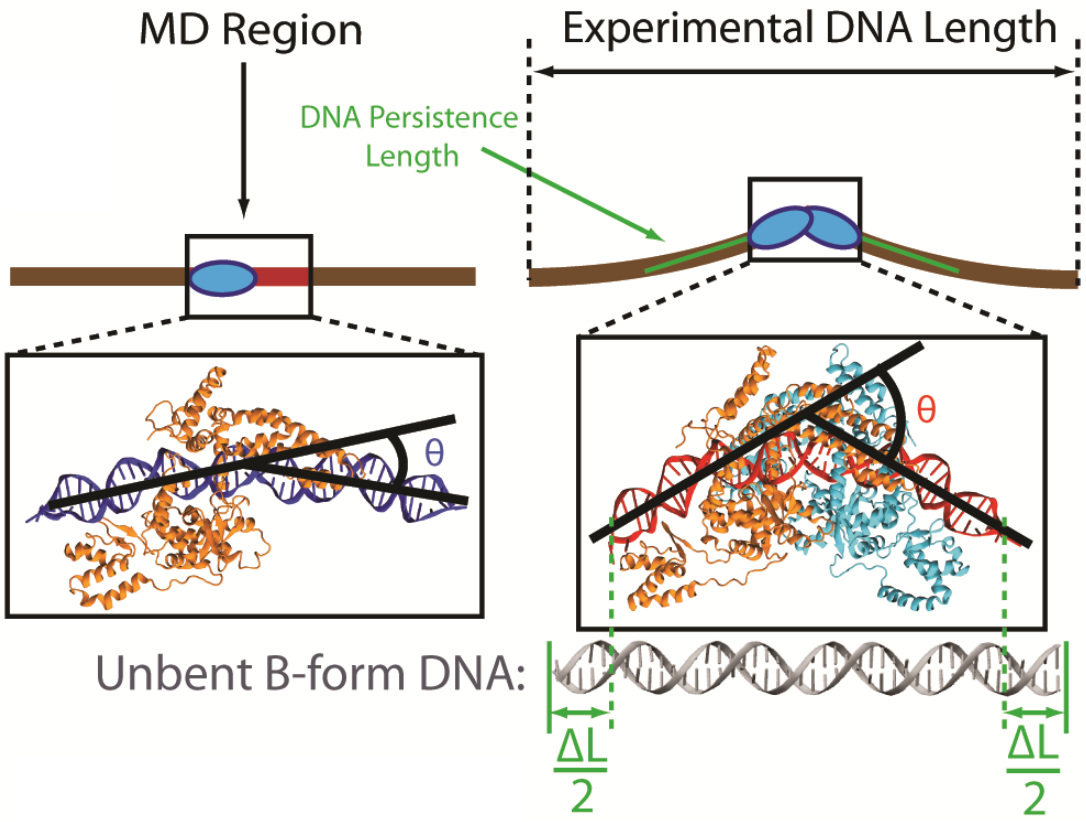

Figure 4-7. MD simulation setup of monomer vs. dimer non-target DNA bend angle. Schematic representation of DNA condensation as would be measured in optical trap experiments (brown line) and MD simulations (boxed region). Δ*L* is defined as the difference between the contour length and the end-to-end distance of the 44-bp DNA substrate. MD snapshots of a TelK dimer-DNA complex and a TelK monomer-DNA complex are shown. DNA adopts a bent conformation in interaction with the TelK dimer, but not with the TelK monomer.

shown in **Figure 4-4 c**, the observed step-size distribution is bimodal, with one peak at 7.2 nm, in excellent agreement with the prediction. This suggests that a significant fraction of condensation events observed correspond to formation of DNA-TelK dimer complexes similar to those seen in crystal structures. As shown in **Figure 4-4 c**, the condensation step-size distribution displays a second peak at 4.8 nm, corresponding to 51% of all observed condensation events. This suggests that TelK condensation may have two distinct tight-binding conformations on non-target DNA. Unfortunately, MD simulations do not reproduce this feature within the simulation time frame, instead producing only a single condensed conformation. We speculate that the smaller step may result from misoriented dimers that meet along the DNA. Such a conformation would not be observable with MD simulations, which start from the correctly oriented DNA-TelK crystal structure (**Materials and Methods**).

4.5.2 Ability of TelK monomer or dimer to bend non-target DNA

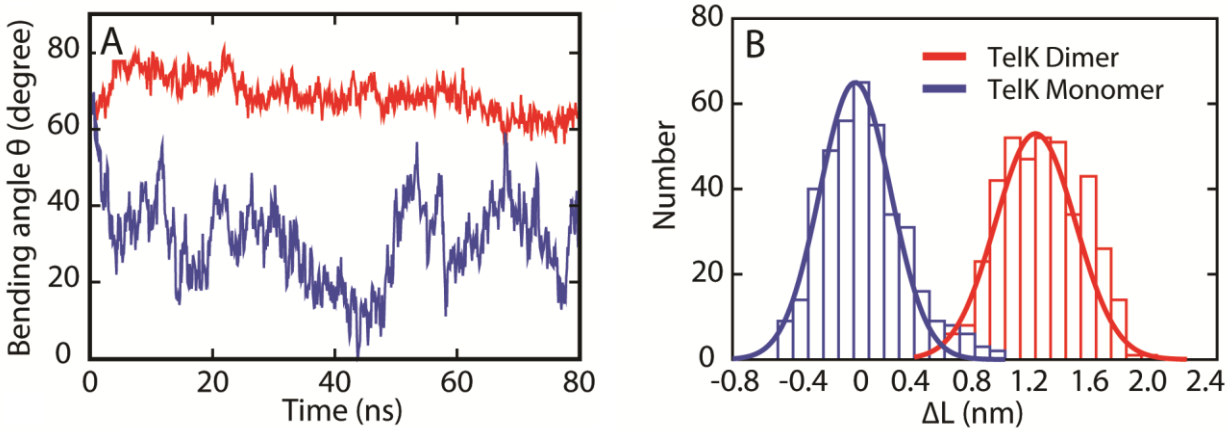

Figure 4-8. MD simulations confirm that Telk dimers bend non-target DNA whereas monomers cannot.
(a) DNA bend angle induced by a TelK dimer (red) and a TelK monomer (blue).
(b**)** Distribution of the change in end-to-end distance in the 44-bp MD DNA substrate (ΔL) induced by a TelK dimer and monomer in MD simulations.

We next performed a set of MD simulations to explore the DNA-bending ability of a TelK monomer versus a TelK dimer, both on non-target DNA. These simulations present a snapshot of the TelK-binding region of our experiments (**Figure 4-7**). Simulations of a TelK monomer binding to non-target DNA further showed that the monomeric form of TelK is unable to bend DNA as a dimer does. Instead, monomeric TelK interaction with DNA results in a large decrease in the bend angle (**Figure 4-8 a**). A histogram of the end-to-end distance of the DNA substrate shows significant condensation in the case of the TelK dimer, but on average no condensation for a TelK monomer on non-target DNA (**Figure 4-8 b**). Furthermore, MD simulations showed that

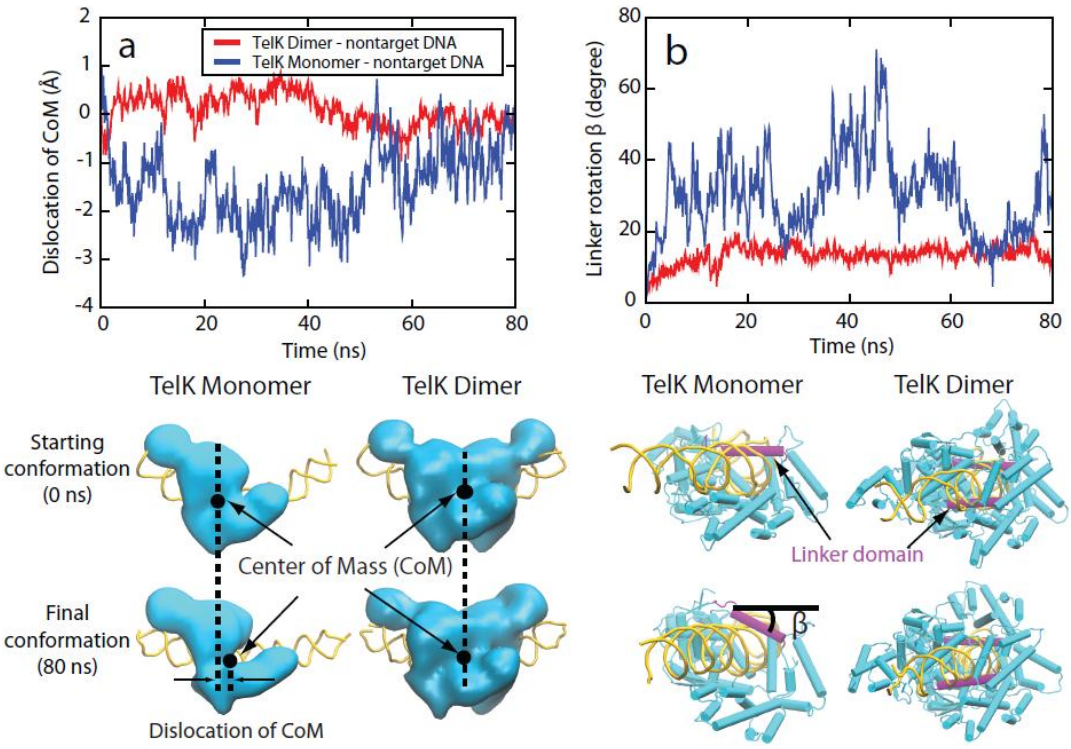

Figure 4-9. TelK monomers (blue) are more mobile on non-target DNA compared to dimers (red).
(a) Dislocation of TelK dimer and monomer along non-target DNA axis based on MD simulations.
(b) Rotation of TelK linker domain (SER208-ASN229). The snapshots show the starting and final positions of the linker domain (magenta) in TelK monomer and dimer after 80 ns. DNA is shown in yellow and TelK is shown in cyan.

the TelK center of mass (CoM) dislocation along the axis of non-target DNA is greater for monomeric TelK than for dimeric TelK (**Figure 4-9 a**). A similar mobility discrepancy is observed for the rotational motion of TelK around the DNA axis; the TelK monomer is able to rotate around DNA freely, whereas a TelK dimer does not rotate (**Figure 4-9 b**). These results suggest that TelK dimers exhibit tight-binding behavior on DNA (consistent with the optical trap measurements) resulting in limited translocation along the DNA backbone (consistent with the TIRFM measurements), in contrast to TelK monomers, which exhibit higher mobility along DNA due to weaker binding interactions.

4.5.3 TelK dimer may act as a hinge

Subsequent MD simulations performed without DNA (a TelK dimer only) show that the TelK dimer adopts a sharper bend angle than the dimer interacting with target or non-target DNA (**Figure 4-10**). Therefore, it is likely that TelK acts as a hinge, and DNA acts as an electrostatic scaffold that wedges the TelK dimer into a more obtuse bend angle. This result highlights the importance of protein-protein electrostatic interactions that must be taken into account for dimer-active protein systems, which are notably absent in monomer-active sequence-specific proteins. This result also suggests that protein-protein interactions may contribute to nonspecific DNA condensation that can be observed for dimer-active protein systems.

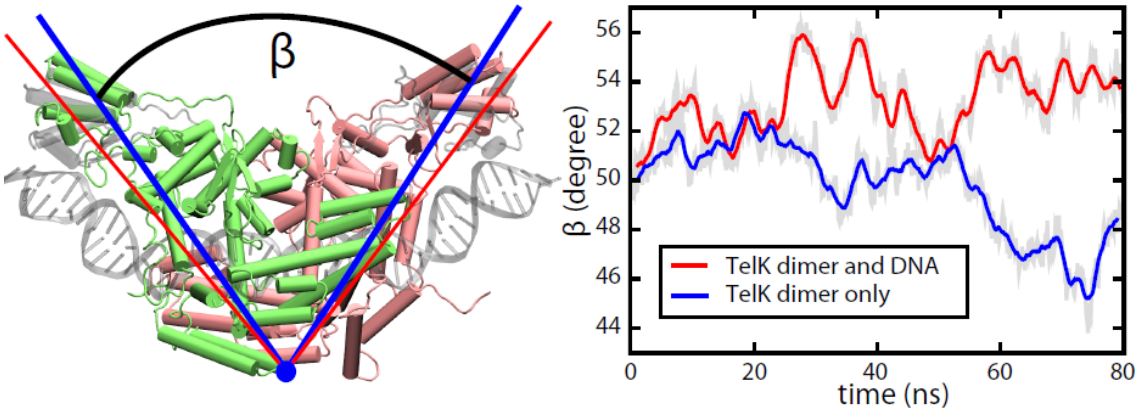

Figure 4-10. Influence of DNA on TelK dimer conformation.
(a) Superposition of MD simulations of a TelK dimer-DNA complex (transparent grey) and a TelK dimer without DNA (color) shows different TelK-dimer bend angles, β.
(b) The angle β formed by a TelK dimer complexed with a target-DNA substrate (red) is more obtuse than the bend angle formed by a TelK dimer alone (blue).

4.6 TIRF: TelK interactions with target DNA

The experiments and simulations above establish that TelK dimers become immobilized on non-target DNA, yet likely form complexes that are close to those depicted in crystal structures of TelK on target DNA. If dimers form tightly-bound and immobile complexes on non-target DNA, how is target search accomplished?

4.6.1 TIRF assay with target DNA

To answer this question, we performed TIRF assays with 12.8-kb DNA bridges containing a single TelK target site located near the center of the molecule (**Materials and Methods**). The concentration of TelK was varied from 70 to 1350 nM as for the TIRF assay with λ-DNA bridges. (Despite the presence of a target sequence, we did not observe cutting of the DNA bridges by TelK. We attribute this to an inhibitory effect due to the tension applied on the DNA

molecule when stretched over the TIRF chamber glass pedestals. Across all assayed TelK concentrations, we observed a preference for TelK binding to the center of the target DNA substrate, compared to random TelK binding along non-target λ-DNA (**Figure 4-11 a & b**). We also observed mostly dimers (non-blinking spots) at the target site (78%). To determine whether dimers or monomers confer target-site specificity, we considered a subset of our data by comparing only DNA tethers that showed one single blinking fluorescent spot per molecule of extended target or non-target DNA. For all singly-occupied DNA bridges containing the target sequence, all observed blinking fluorescent spots were located at the target site, indicating that monomeric TelK have a binding preference for the target site. Based on the TelK-QD labeling

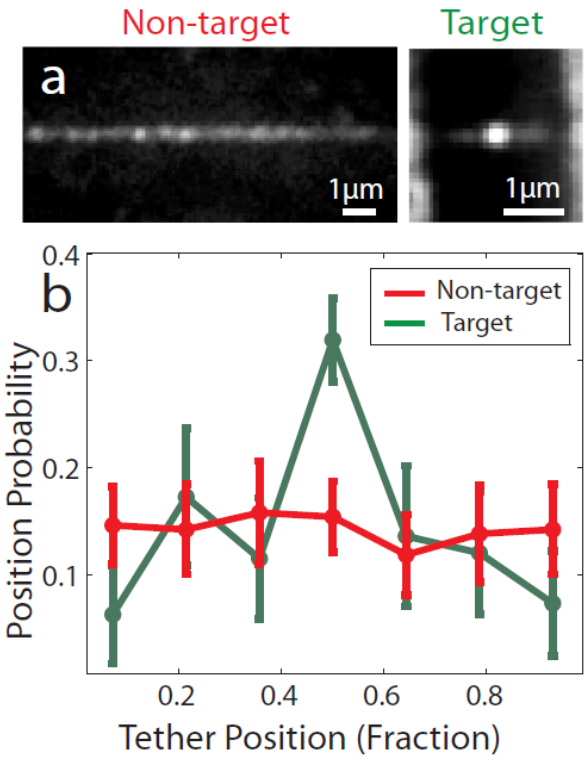

Figure 4-11. TelK binds preferentially to target DNA.
(a) Average TelK fluorescent spot positions along target (green, N = 182) and non-target (red, N = 253) DNA, obtained by aligning and overlapping fluorescence images. TelK concentration range used in all TIRF experiments ranges from 70 nM to 1350 nM.
(b) Position probability distribution of TelK along target (green) and non-target (red) DNA.

efficiency, we are confident that at least 84% of these spots are monomers. Importantly, none of these blinking spots at the target site underwent 1D diffusion (D = (3.8 ± 0.4) × 10^{-5} $\mu m^2/s$; mean ± s.e.m.). In contrast, blinking, singly-occupied λ-DNA bridges lacking the target sequence did not display a binding site-preference along the DNA, and the single QD-TelK underwent 1D diffusion (0.88 ± 0.10 $\mu m^2/s$; mean ± s.e.m., comparable to that obtained for all mobile spots on non-target DNA). The tensions experienced by the TIRF bridges (3.1 ± 2.7 pN, mean ± SD.; **Methods and Figure 4-18**) inhibited TelK cutting at the target site. TelK cutting could be recovered when tensions on the DNA were removed and the DNA was allowed to take on a globular conformation in a tethered particle assay (**Chapter 5**).

4.6.2 MD simulations with target DNA

Our TIRF results are supported by MD simulations of a single TelK monomer on target and non-target DNA substrates. We performed a set of MD simulations to probe the molecular basis for target-site specificity. Monomers along target DNA exhibited greater stability than monomers along non-target DNA. We compared the trajectories of a TelK monomer and target DNA versus a TelK monomer and non-target DNA. As shown in **Figure 4-12**, the contact area and number of hydrogen bonds between a TelK monomer and target DNA remain constant during simulations, while both decrease in simulations of TelK monomer-non-target DNA complexes. A comparison of the contact area (**Figure 4-12 a**) number of hydrogen bonds (**Figure 4-12 b**) show that TelK monomer binding to target DNA is more stable than binding to non-target DNA; there is an increase in contact area and hydrogen bonds between TelK monomer and target DNA compared to between TelK monomer and non-target DNA). We show that GUA23 forms two stable hydrogen bonds with ARG492 (**Figure 4-12 c**), both of which are lost after mutating

GUA23 to a thymine. Additionally, while CYT38 forms one stable hydrogen bond with ALA358 at the start of the simulation, the distance between these increased gradually, indicating the instability of that hydrogen bond. MD simulation results comparing the stability of a TelK monomer on target vs non-target DNA suggest that TelK monomers have an increased affinity for the target sequence.

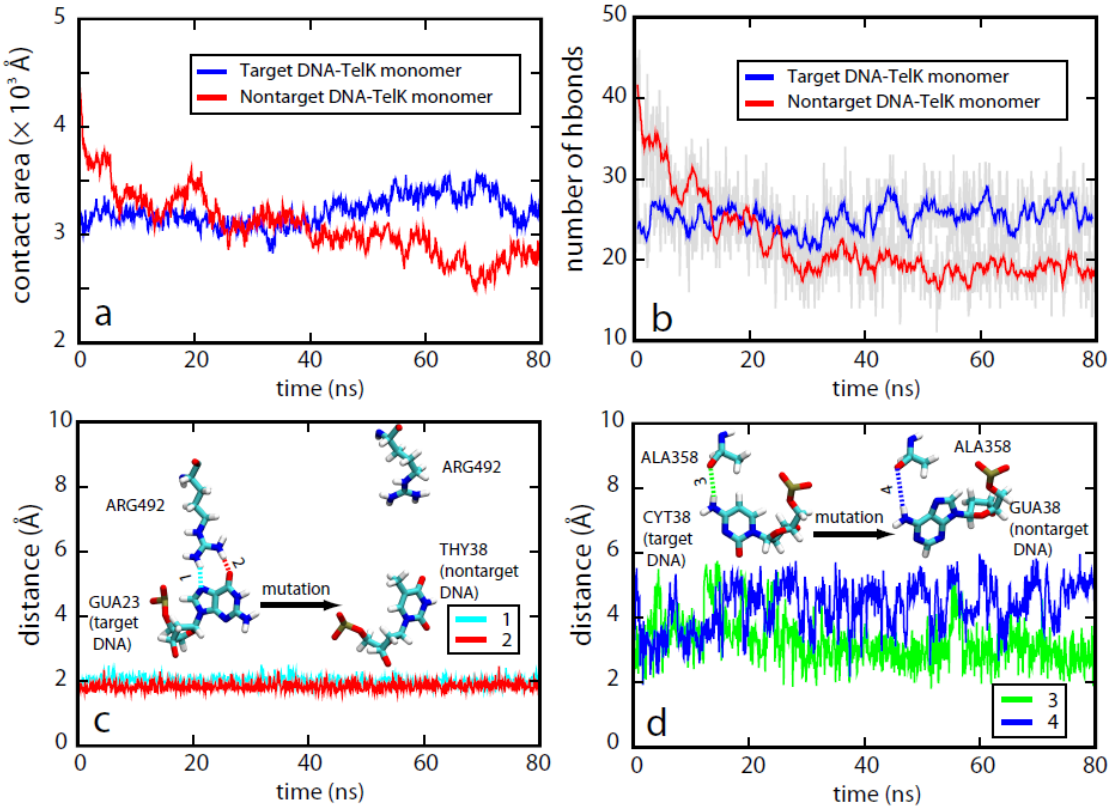

Figure 4-12. Interaction between TelK monomer and target/nontarget DNA.
(a) Comparison of contact area between TelK monomer and target DNA (blue) and that between TelK monomer and non-target DNA (red) in MD simulations.
(b) Comparison of number of hydrogen bonds between TelK monomer and target DNA (blue) and that between TelK monomer and non-target DNA (red).
(c) and
(d) show two examples of how target DNA mutation affects TelK-DNA interaction. DNA mutations were made based on residues within the TelK footprint as determined in previous studies [1].

4.7 TelK target search model

Based on our results, we propose a mechanism for dimer-active TelK that involves: 1) protein monomer diffusion to the target and 2) preferential binding to the target sequence, followed by 3) dimerization at the target site. Our TIRF studies demonstrate that TelK diffuses in 1D as a monomer along non-target DNA, yet becomes immobile as it encounters its target sequence. Therefore, monomer target-site immobilization confers specificity for TelK dimerization at the target site. MD simulations confirm experimental observations of monomer target-site specificity, and provide molecular details of TelK's interactions with target versus non-target DNA (**Figure 4-12**).

However, protein immobilization on non-target DNA is intuitively counter-productive for the localization of the DNA target site as it truncates the search process prematurely. Similarly, non-target DNA condensation is unexpected for a protein requiring sequence specificity for activity, because condensation is usually predicted to occur at the target site prior to catalytic activity [37]. Condensation and immobilization may be essential target-search features for dimer-active protein complexes that require more complex mechanisms for target-site identification.

We suspect condensation and immobilization may be essential target-search features for proteins that must assemble into oligomeric complexes on DNA and that require more complex mechanisms for target-site identification than monomeric or pre-assembled SSPs. DNA bending has been thought to occur exclusively at target sites for sequence-specific protein-DNA systems. Only at the target-site do protein-DNA electrostatic interactions become maximized, and catalysis occurs hand-in-hand with DNA topological distortions [36]. However, as has been previously suggested for certain SSPs [38], a protein's ability to bend DNA indiscriminately may aid target-site identification. Erie et al. suggest that dimer-active proteins may bend DNA to

"test" their compatibility with that particular DNA sequence via protein-DNA and protein-protein interactions [39]. Transcription factor HoxD9 has also been shown by Clore et al. [40, 41] to bind non-target DNA with the same affinity and in the same binding mode as target-DNA as a means of enhancing the rate of target identification. Dimer-active proteins such as TelK may use this mechanism to maximize their electrostatic contacts with the DNA during their "sampling" state, not only during site-specific catalysis.

Our optical trap data may provide some support for a "sampling" mechanism in TelK. The mean dwell time of the condensation events (22 ± 6 s; mean ± s.e.m.) in the trap measurements is noticeably shorter than the immobilized-state lifetime observed in our TIRF experiments, which spanned minutes (**Figure 4-4 b & 4-1 d**). However, the time between condensation events was independent of TelK concentration, suggesting that a single intra-molecular dimerization event was responsible for multiple sequential condensation and de-condensation events. We suspect this indicates that a TelK dimer may repeatedly attempt to bend its DNA substrate.

4.8 Competition of target-localization versus dimerization

If non-target DNA condensation occurs too readily, it may significantly slow or inhibit target-finding and substrate formation. At first glance, it may appear that two monomers will find each other more quickly on DNA abundantly coated with protein, when in direct competition with the process of finding a target site. We analyzed the expected scaling of each process based on our model of target-finding for dimer-active proteins.

Our dimer-active model predicts a power-law dependence of protein activity on protein concentration. Stochastic simulations of two kinetic processes—dimerization and target localization—over a large range of protein concentrations show a difference in the power-law

dependence for each of these processes. This can be understood from a simple scaling argument, considering a finite length of DNA coated with N protein monomers when the process of target-finding and dimerization are both diffusion limited (and not protein binding-limited). On average, the distance between the protein closest to the target site is inversely proportional to the number of proteins on the DNA ($\langle d_{min} \rangle \sim 1/N$). Conversely, the average shortest inter-protein distance varies inversely with the square of the number of proteins ($\langle x_{min} \rangle \sim 1/N^2$) . Thus, the rates for target localization and for dimerization are given by the protein diffusion rate over these distances, and will depend differently on protein occupancy:

$$k_{\text{target}} \sim {}^{D}/_{\langle d_{min} \rangle^2} \sim N^2$$

and

$$k_{\text{dimer}} \sim {}^{D}/_{\langle x_{min} \rangle^2} \sim N^4.$$

Through stochastic simulations of our dimer-active protein target-search model (**Materials and Methods**), we show there is a range of parameters for which target localization occurs much more quickly than dimerization. Our simulations take into account experimentally measured kinetic parameters for TelK unbinding (k_{off} = 0.2392 s^{-1}) and monomer diffusion (D = 1.8 $\mu m^2/s$) to calculate the rate of dimerization k_{dimer} on non-target DNA versus the target-finding rate k_{target}.

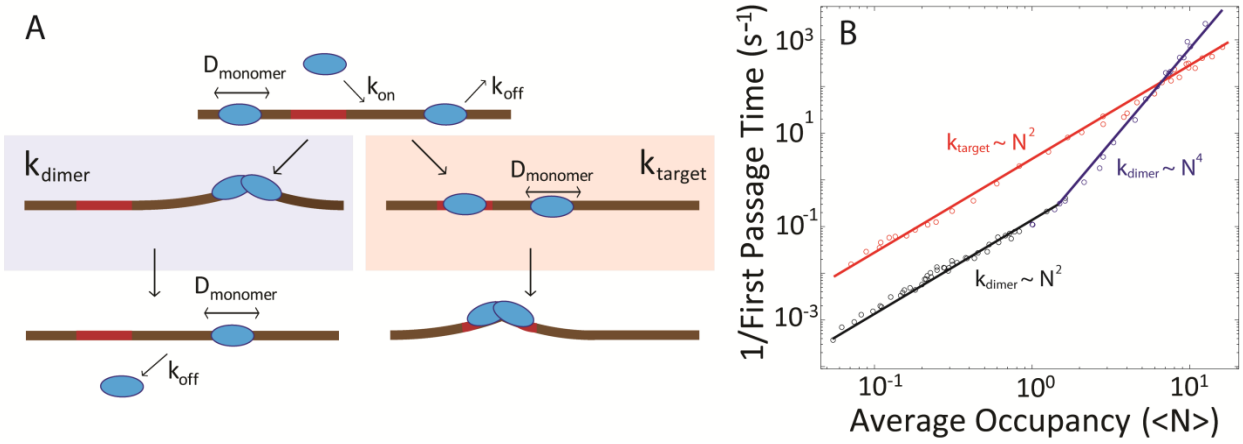

Figure 4-13. Kinetics of TelK-induced dimerization and target search.

(a) Model of TelK target search. TelK monomers in solution bind DNA with rate k_{on} and scan rapidly along non-target DNA with mean diffusion coefficient $D_{monomer}$ = 1.8 $\mu m^2/s$. Monomers localize the target site with rate k_{target} and bind tightly, or dissociate from non-target DNA with average rate k_{off} = 0.24 s^{-1}. Preferential and stable binding of a TelK monomer allows a second monomer to dimerize at the target site and form a kinked DNA-TelK complex primed for catalysis. Occasionally, mobile monomers encounter each other on non-target DNA with rate k_{dimer} and form stable, immobile dimers (D_{dimer} < 1x10^{-4} $\mu m^2/s$) that "test" their substrate by condensing the DNA transiently. Eventually dimers on non-target DNA dissociate or separate into mobile monomers again (rate < 0.01 s^{-1}).

(b) Implementation of kinetic model in (a) via stochastic simulations using experimentally derived kinetic parameters. Average rates for first dimerization k_{dimer} (blue, black), and first target localization k_{target} (red) as a function of average protein occupancy, <N>, on DNA. For mean occupancies > 1, target-finding and dimerization rates obey simple scaling laws of N^2 and N^4, respectively. For mean occupancies < 1, dimerization follows of N^2 scaling. Provided TelK occupancy is reasonably small, target localization consistently occurs faster than dimerization. Simulated rates are in good agreement with experimentally derived rates of first dimerization.

We vary the average protein occupancy (N per DNA strand) by varying the kinetic parameter k_{on} from 0.06 – 4 s^{-1} (**Figure 4-13 a**). The dependence of k_{target} scales as N^2 for all simulated protein average occupancies, as expected by the scaling laws for the target-finding kinetics based on protein occupancy described above. On the other hand, the dependence of k_{dimer} on average protein occupancy has two distinct regimes: a low-protein density regime in which k_{dimer} scales as N^2, and a high-protein density regime in which k_{dimer} scales as N^4. The two distinct kinetic regimes observed for protein dimerization can be explained by considering the dimerization process as a protein binding-limited process at low protein occupancies, and a diffusion-limited process at high protein occupancies. We observe the transition from diffusion-limited to binding-limited dimerization kinetics to occur roughly when the average protein occupancy drops below 1 as shown in **Figure 4-13 b**. At average occupancies below ~1, the process of protein dimerization is limited by the long timescales of protein binding when the effective protein on-rate is low, but at average occupancies above ~1, the protein on-rate reaches a critical value at which the protein diffusion coefficient dominates the dimerization process.

In comparing the two competing processes of protein dimerization versus protein target-finding, two regimes are observed in this simulation: at low TelK occupancies, the rate for target-site identification is significantly higher than for dimerization. However, at high occupancies, dimerization occurs faster than target-finding. This can be conceptualized by considering two competing processes: a monomer finding a target site versus a monomer finding another monomer. For a DNA molecule coated with N monomers, we show that, on average, the minimum inter-monomer distance varies as $1/N^2$. Conversely, on average the distance between a target site and the closest monomer varies as $1/N$. As a result, the rates of dimerization vs. target finding depend differently on the occupancy of protein on DNA for diffusion-limited regimes.

Nonetheless, at low protein concentrations, the chance of a protein diffusing into a target site is much higher than a protein diffusing into another protein. The protein-target site distance dependence on N allows target-finding to occur faster than protein dimerization, despite both rates having an N^2 dependence on protein occupancy. At high protein concentrations, where the occupancy of protein along DNA is large, dimerization is faster than target localization as it takes on an N^4 dependence due to diffusion-limited protein dimerization. These relationships are observed in our simulations for binding-limited k_{dimer} ($\sim N^{2.2}$; $R^2 = 0.99$), diffusion-limited k_{dimer} ($\sim N^{4.4}$; $R^2 = 0.98$), and k_{target} ($\sim N^{2.0}$; $R^2 = 0.97$).

Our simulations would thus predict that the activity of the protein should decrease at high concentrations due to inhibition of target finding. This is consistent with our observation of TelK inhibition at high TelK concentrations in bulk (**Figure 4-14**). TelK's host organism, *Klebsiella oxytoca*, is known to maintain a cellular TelK copy number below 20 for a ~52-kb genome, or less than one dimer per 5 kb of DNA (data not published). These estimates are firmly placed in the low-occupancy regime predicted in our simulations. Therefore, it is likely that target-site localization occurs faster than dimerization at biologically relevant TelK concentrations, allowing non-target DNA condensation to provide site-specificity in dimer-active proteins without hindering the kinetics of product formation. A target-search mechanism in which protein dimers immobilize along non-target DNA is thus viable.

The results of kinetic simulations can be compared to our optical trap data. Since DNA is exposed to TelK at a well-defined time in our optical trap assay, we can measure directly the time for the first DNA condensation event (the first passage time) as a function of TelK concentration. To compare our theoretical and experimental rates, we first need to compare TelK occupancies across our experimental data and our simulations. To do so, we calibrated the number of TelK units observed per DNA bridge in our TIRF assay as a function of TelK concentration, and use this relationship to correlate TelK occupancies in our optical trap

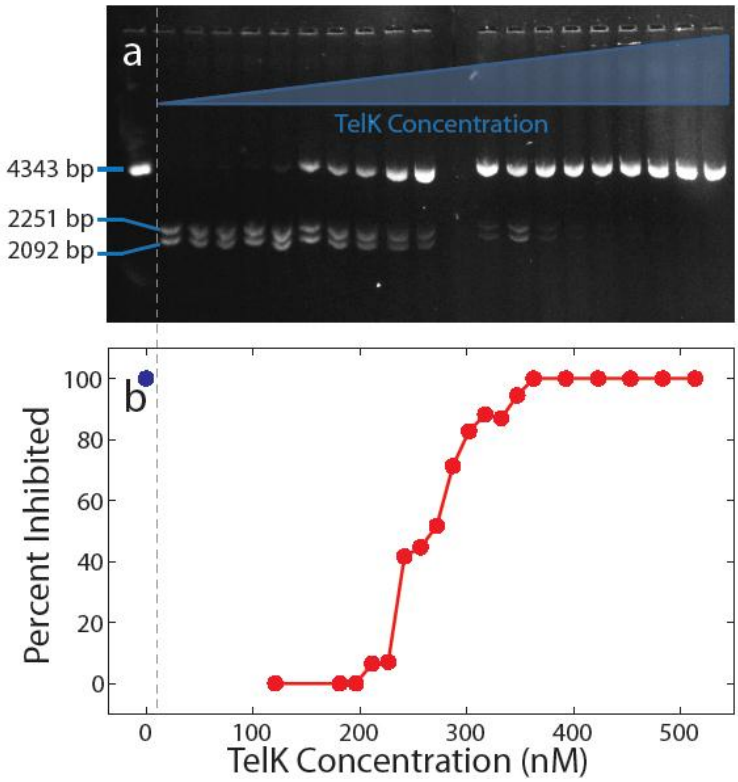

Figure 4-14. TelK cutting inhibition increases with TelK concentration.
(a) 50 ng of pSKN DNA substrate containing the TelK target sequence slightly off-center wassynthesized as described in **Materials and Methods.** This DNA was incubated with 0 nM TelK (DNA-only control) and a range between 120 nM to 513 nM TelK visualized on a 1% agarose gel stained with EtBr. The DNA substrate runs at its full length when uncut, but TelK-cut DNA is observed as 2 cut products at 2092- and 2251-bp.

(b) Intensities of each band are measured and used to determine percent inhibition of DNA cutting by TelK via the following relationship: $\%Inhibition = \frac{I_{uncut}}{\sum I_{band}}$.

experiments to our simulations (**Materials and Methods**). We find that the measured first passage times in our optical trap match the rates for protein binding-limited dimerization in our simulations. Therefore, we suggest that the condensation events we observe in our optical trap assay correspond to protein dimerization, further supporting our dimer-active protein model for target search.

4.9 How universal is this target-search mechanism?

The literature to-date suggests an all-encompassing model for protein target-search in which proteins scan non-target DNA in their fully functional form [6, 13]. However, our studies of protelomerase TelK, a protein that is functional only as a dimer, reveal that additional variables must be taken into consideration when describing target-search mechanisms for proteins that assemble into dimer-active complexes on DNA. Previous studies have reported different binding behaviors of SSPs to non-target DNA: some SSPs bind loosely; others bend both their target and non-target DNA sites by similar angles. However, the underlying assumption is that both loosely and tightly-bound SSPs will scan non-target DNA via 1D sliding with different amounts of protein-DNA friction [13]. We show that, for the dimer-active protein TelK, scanning only occurs as a monomer, and immobilization occurs when it forms a tightly-bound dimer on DNA. We speculate that the target-search mechanism proposed as a result of this work is extendable to several different protein families that share characteristics with TelK, such as dimer functional units.

In a single-molecule study of Cro protein, a transcription regulatory protein that is active as a dimer, it was shown that Cro distorts both non-target and target DNA substrates as a dimer by similar bend angles [39]. Erie et al. proposed that non-target DNA distortion helps increase Cro specificity for target sites. In contrast, proteins requiring DNA bending for site-specific catalysis—such as the endonuclease EcoRV—would not induce DNA distortions on non-target DNA. Our studies of EcoRV in the optical trap confirm this prediction and show no DNA condensation, even at high EcoRV concentrations (**Figure 4-15**) although we do observe EcoRV cutting of its DNA target site. Conversely, proteins in the TelK recombinase family—Y-recombinase Cre and protelomerase TelAg—both display DNA condensation in our optical trap assay and dimer immobilization in our TIRFM assay.

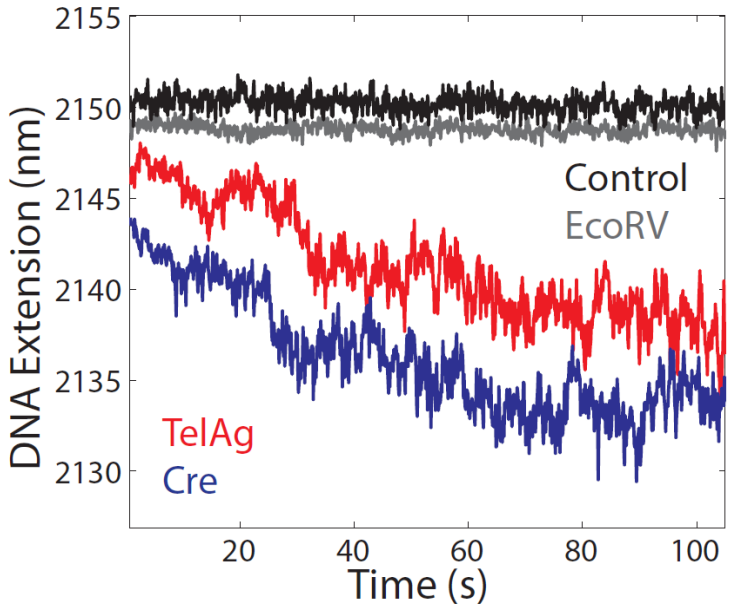

Figure 4-15. DNA tether condensation behavior of EcoRV, TelAg, and Cre protein in the optical trap.
150 nM EcoRV (grey) in the optical trap shows no DNA condensation. Conversely, 150 nM Y-recombinase Cre protein (blue) and 150 nM protelomerase TelAg (red) both show DNA condensation in the optical trap. Traces offset for clarity.

Our studies of EcoRV, Cre, and TelAg proteins confirm predictions made in previous work regarding the binding behavior of proteins to non-target DNA [39]. EcoRV shows no DNA condensation, even at high concentrations (150 nM). Unlike the TelK immobilization observed on non-target DNA, single-molecule studies of QD-labeled EcoRV show 1D diffusion along nontarget DNA with no discernible immobilization events of protein units on non-target DNA [42]. Conversely, proteins that are more structurally and functionally related to TelK, the Y-recombinase Cre protein and protelomerase TelAg, both show DNA condensation in the optical trap (**Figure 4-15**). Cre also showed immobilization in our TIRFM assay at concentrations above 125 nM ($D = 4.2 \pm 0.5 \times 10^{-5}$ $\mu m^2/s$ (mean ± s.e.m.)). Therefore, we suggest that dimer-induced nonspecific DNA condensation may be a target-search characteristic shared by several protein families with structural and functional similarities to TelK. We speculate that our results may be applicable to particular protein families. Future studies of other members of the recombinase protein family will further our understanding of this novel target search mechanism, and its applicability to dimer and oligomer SSPs.

4.10 Absence of hairpin formation on linearly extended DNA

When using a DNA substrate containing the TelK target sequence in our single-molecule assays, it was expected that TelK would cut the DNA at the target site and form DNA hairpins. However, no DNA cutting or hairpin formation was observed with DNA containing the TelK target site in either the TIRFM or optical trap assay, despite control cutting assays showing full activity in bulk (**Materials and methods**). We attribute the lack of TelK activity on our DNA substrates to the extended conformation to which our DNA substrates are confined in either assay. In both assays, the behavior of TelK is studied on DNA substrates that are linearly

extended, either in the form of DNA bridges in TIRFM or DNA tethers in the optical trap. These observations strongly suggest that TelK activity may be inhibited on linear DNA substrates extended by applied low tensions. We explore this hypothesis in **Chapter 5**, which studies the process of hairpin formation using a fluorescent tethered particle microscopy assay, and FRET.

4.11 Role of nonspecific DNA condensation

For TelK, the processes of target sequence identification, DNA cutting, rearrangement, re-ligation, and finally hairpin formation is performed without the aid of high-energy cofactors such as ATP. Much ambiguity exists about how ATP-independent proteins manage to perform these sterically arduous DNA transformations and obtain 100% conversion of substrate to product, particularly when theory would predict a 50-50 ratio of substrate and product due in the absence of a driving factor such as ATP.

It has been previously noted that proteins similar to TelK, such as IB topos and Y-recombinases have highly charged DNA binding sites, thereby maximizing electrostatic interactions between the protein surface and the DNA substrate [43]. These highly positively charged protein surfaces could induce tight binding of the protein onto the negatively charged DNA backbone, causing DNA distortions regardless of nucleotide sequence. However, these electrostatic distortions could also serve as a substitute for high-energy cofactors such as ATP. It is possible that electrostatically induced DNA twisting or bending at the DNA target site may help stabilize the protein-DNA complex and drive the overall reaction forward. In essence, the energy of DNA distortion through protein-DNA electrostatics could be translated into a potential energy that is mechanically induced onto DNA. This could be the added driving force that makes the formation of DNA hairpins by TelK unidirectional, despite the predicted 50-50 ratio of

reactant and product due to the reactant and product being isoenergetic. In this way, TelK, and possibly other ATP-independent proteins such as Y-recombinases, could come "spring-loaded" with a structural form of potential energy for the eventual energy-expensive catalysis of DNA hairpin formation. This mechanism may explain the unidirectionality of the TelK DNA-hairpin formation reaction despite the absence of high-energy cofactors.

4.12 Materials and methods

DNA synthesis

TIRFM non-target DNA substrate. A 48-kb DNA molecule with biotin at both ends was synthesized by filling in the *cos* ends of λ-DNA with biotinylated dNTPs. Briefly, 1 μg of λ-DNA (D1501, Promega, Madison, WI, USA) was incubated at room temperature for 10 minutes with 1 unit of DNA Polymerase I Large Klenow Fragment (M0210S, NEB, Ipswich, MA, USA) and 40 μM of dATP, dGTP, dTTP (R0141, R0171, and R0161, respectively; Fermentas, Glen Burnie, MD), and biotinylated dCTP (19518-018, Invitrogen, Carlsbad, CA). The reaction was stopped by heating to 10 minutes at 75°C and run through a Qiagen PCR purification kit (28104, Qiagen, Valencia, CA, USA) with a 50-μl DNA elution volume.

TIRFM target DNA substrate. The target DNA substrate for use in our TIRFM assays was synthesized based on the 2.9-kbp origin pSKN plasmid harboring the TelK target site, and the 6.9-kbp integration vector of *B. subtilis*, pKSV7 [44], plus an unrelated 4-kbp fragment from phage G of *B. megaterium* [45]. These plasmids were built by enlarging the parent pSKN [1] with non-*E. coli* sequences to 12.9-kbp length to span across the TIRFM glass pedestals.

Optical trap non-target DNA substrate. A 3.4-kb DNA molecule with a single biotin and digoxigenin at each end was synthesized by amplifying a segment of the pBR322 DNA plasmid (Fermentas, Glen Burnie, Maryland). A 5'-biotinylated forward and a 5'-digoxigenated reverse PCR primer (Integrated DNA Technologies, Coralville, IA) was used for amplification along with a high fidelity Phusion PCR kit (F-513S, Finnzymes, Woburn, MA). Subsequent DNA purification was performed with a Qiagen PCR purification kit (28104, Qiagen, Valencia, CA, USA) with a 50-µl DNA elution volume. The purity of the DNA product was confirmed by running an agarose gel.

TIRF Microscopy

TIRFM instrument. We utilized a total internal reflection fluorescence microscope as previously described [46]. A spot-fitting algorithm allowed for nanometer-scale localization of the fluorescent spot position, as previously detailed [30].

QD labeling of TelK. Full-length TelK 640 (henceforth referred to as TelK) was purified using a previously established protocol [1]. This full-length wild-type TelK was used for all TIRF and optical trap experiments. TelK contained a 6-amino acid N-terminal His tag. To label TelK, we incubated the protein with a 10x excess of Anti-His QDs (Qdot 565 Antibody Conjugation Kit, Invitrogen, Carlsbad, CA, USA, Q22032MP) on ice for 2 hours and re-suspended the solution in a total volume of 20 µL of 1x TelK buffer (20 mM Tris-HCl, 50 mM potassium glutamate, 1mM DTT, 0.1 mM EDTA). We estimated a QD labeling efficiency of ~80%, measured by an agarose gel-shift assay comparing the mobility of DNA, DNA + TelK, and DNA + QD-TelK (**Methods Figure 4-16 a**). The activity of QD-labeled TelK was shown to

be unaffected by QD labeling when compared to unlabeled protein, as shown by agarose gel electrophoresis (**Methods Figure 4-16 b**).

QD labeling efficiency. TelK QD labeling efficiency was estimated using a gel-shift assay. A non-cutting mutant of full-length TelK was used, TelK-YF, for which the active site tyrosine was mutated to a phenylalanine. TelK-YF binds to target-site DNA as efficiently as wild-type TelK, but does not cut the substrate [26]. A 66-bp DNA duplex containing the TelK target site and labeled with a single 5'-Alexa647 dye (Integrated DNA Technologies, Coralville, IA) served as a substrate. 10 ng of Alexa-labeled DNA was incubated with 50 nM unlabeled TelK-YF and separately with 50 nM QD-labeled TelK-YF for 1 hour at room temperature.

The Alexa-DNA substrate by itself, the substrate with unlabeled TelK-YF, and the substrate with QD-labeled TelK-YF were run on a 0.5% agarose gel for 1 hour at 100 V. This gel was imaged at 650ex/680em to visualize the Alexa-DNA (**Methods Figure 4-16 a)** and at 525ex/550em to visualize the QDs (**Methods Figure 4-16 b)**. The DNA band shifted slightly with unlabeled TelK-YF (**Methods Figure 4-16 a**, lane 2), and more significantly with QD-TelK-YF (lane 3). QD emission was only observed at the DNA + QD-TelK shifted band position (**Methods Figure 4-16 b**, lane 3). We defined the labeling efficiency as the percentage of Alexa-DNA bound by QD-TelK, as determined by the ratio of the DNA + QD-TelK shifted band intensity to the total DNA intensity:

$$\text{Labeling efficiency} = \frac{I_{\text{shifted DNA+QD TelK band}}}{\sum I_{\text{lane}}}$$

This procedure yielded a labeling efficiency of ~80%.

QD labeled TelK activity. QD-labeled TelK cutting activity was tested to ensure that modification of TelK via the noncovalent attachment of Anti-His QDs did not affect its function. Wild-type TelK was labeled with QDs as described in **Materials and Methods**. Both QD-labeled and unlabeled 50-nm TelK samples were incubated with 50 ng of 4.3 kb pSKN DNA, synthesized as described in **Materials and Methods** to contain the TelK target sequence slightly off-center at position 2092. QD-TelK and pSKN DNA were incubated for 15 minutes at room temperature, and subsequently run on an agarose gel as detailed in [1]. The activity was determined from the ratio of the cut DNA band intensity to that of the input DNA

$$\text{Activity} = \frac{I_{\text{cut DNA}}}{\sum I_{\text{lane}}}$$

where *I* is the band intensity at 535 nm measured with a gel scanner (Kodak 4000mm). Both lanes showed complete cutting of DNA by TelK (**Methods Figure 4-16 c**). Therefore, the activity of labeled TelK was determined to be unaffected by the QD, as compared to unlabeled TelK.

This assay does not determine directly the rates of target localization for the QD-labeled

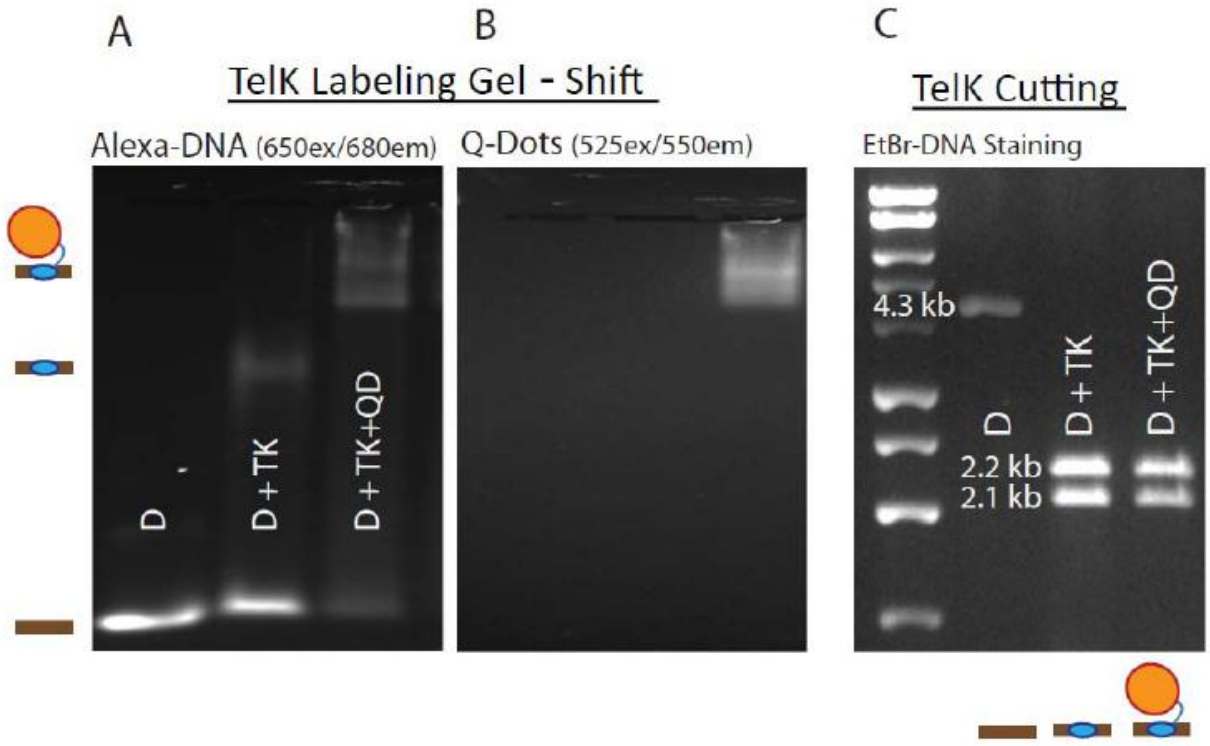

Figure 4-16. Quantification of TelK Quantum Dot labeling efficiency, and labeled TelK activity.
Gel shift quantification of TelK-bound DNA.
(a) Imaged at 650ex/680em to visualize Alexa-DNA: Lanes, from left to right: Alexa-DNA only, Alexa-DNA with TelK, and Alexa-DNA with QD-labeled TelK.
(b) Same gel imaged at 525ex/550em to visualize QDs. Intensity analysis shows an 84% labeling efficiency.
(c) Quantification of TelK cutting activity. Lanes, from left to right: Promega 1-kb DNA ladder, pSKN DNA only, with TelK, and with QD-labeled TelK. Both TelK and QD-labeled TelK cut DNA substrate with the same efficiency, as determined by intensity of DNA bands on a1% agarose gel.

TelK. Though previous studies using QD-labeled proteins have shown a slight decrease in the protein diffusion coefficient due to QD size, motion of the labeled protein has been shown to remain representative of the unlabeled protein behavior [42].

TIRF chamber design. DNA bridges were formed on an etched glass surface with glass pedestals measuring 1 μm in height and separated by 7 μm (Institute of Microchemical Technology, Kanagawa, Japan) using a modification of a previous design [47]. A circular glass coverslip (26022, Ted Pella, Redding, CA) was placed on two 50-μm thick plastic spacers flanking the glass grating such that a 50-μm wide channel was formed over the glass surface. The channel was filled with buffer using a pipette from one end, and a kimwipe (Kimberly-Clark, Irving, TX, USA) on the opposite end to create fluid flow through the channel. A solution of 33 μM neutravidin in water (Thermo Scientific, Waltham, MA, USA) was flowed in, and allowed to adsorb onto the glass surface for 5 minutes. The neutravidin was rinsed with phosphate buffered saline (PBS) buffer. 20 μL of a 80 nM solution of biotinylated λ-DNA (see DNA synthesis, **Materials and Methods**) was flowed in, and subsequently rinsed with PBS. A predetermined concentration of QD-labeled TelK was flowed in and incubated for 5 minutes with the DNA bridges. The unbound labeled TelK was rinsed from the channel with deoxygenated TelK buffer. Deoxygenation was achieved by adding an oxygen scavenging system (100 nM glucose oxidase, 1.5 mM catalase, 56 mM glucose) to TelK buffer. The 50-μm plastic spacers were removed, leaving behind ~50 nm of fluid between the glass pedestals and the coverslip surface to allow TIRF illumination. The coverslip was then sealed to the etched glass slide using nail polish prior to imaging.

MSD and Diffusion Coefficient Analysis. Continuous image sequences were acquired for up to 50 seconds at 100 ms per frame. For each trajectory, the mean square displacement (MSD) of the spot was calculated. The diffusion coefficient (D) for each TelK spot was determined by fitting the first 0.6 s of the MSD versus time plot to a line through the following relation: $\mathrm{MSD} = \langle|x(t) - x(0)|^2\rangle = 2Dt$, as in previous studies [16, 48-50]. Mobile spots showed linear MSD vs. time traces (**Figure 4-17 a**) characteristic of Brownian 1D diffusion. An offset at t = 0 due to the small thermally-driven longitudinal motion of the DNA bridges was most apparent for stationary spots (**Figure 4-17 b**), which exhibited far smaller MSDs than mobile spots. Stationary spots showed a linear MSD vs. time regime but also exhibited deviations from linearity after ~1 s consistent with confined diffusion [51].

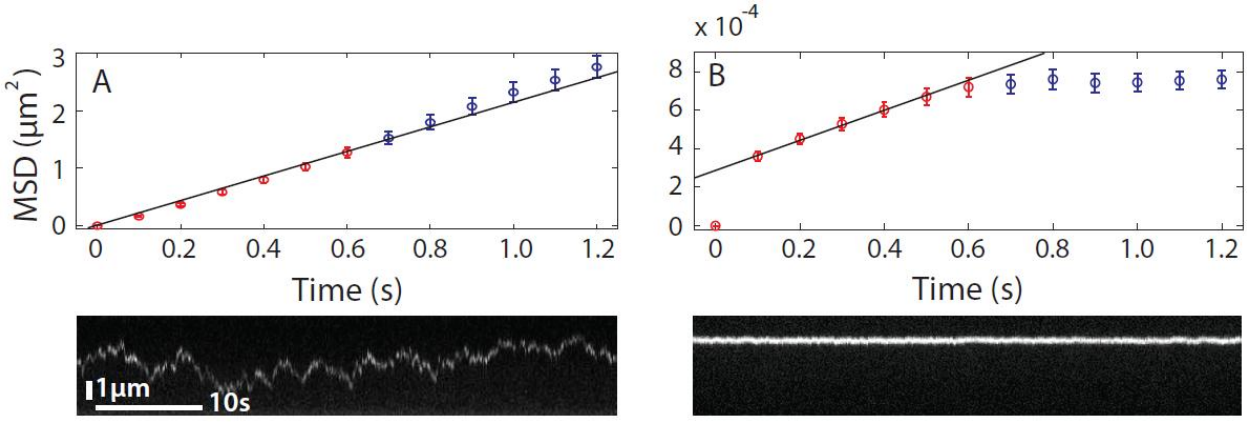

Figure 4-17. Determination of QD-labeled TelK diffusion coefficients
Representative trajectories and corresponding MSD vs. time plots for mobile
(a) and immobile
(b) spots are shown. Diffusion coefficients are determined from fitting the first 0.6 s (red data points) of the MSD to a line (**Materials and Methods**). Fits yield diffusion coefficients of $D_{mobile} = 1.1\ \mu m^2/s$ and $D_{immobile} = 4.6 \times 10^{-4}\ \mu m^2/s$, respectively. Error bars represent s.e.m.

Determination of tether tension. Tensions experienced by the DNA bridges in the TIRFM assay were estimated from the transverse fluctuations of the DNA, based on the positions of 6 highlighted stationary quantum dot-labeled TelK units, each of a different color (**Figure 4-18 a**). These thermally driven fluctuations are related to the force at which the bridge is extended from the relation $\langle y_{DNA}^2 \rangle = \frac{k_B T}{F} \sqrt{\frac{l(l_{tot}-l)}{l_{tot}}}$, where y_{DNA} is the motion of the protein spot perpendicular

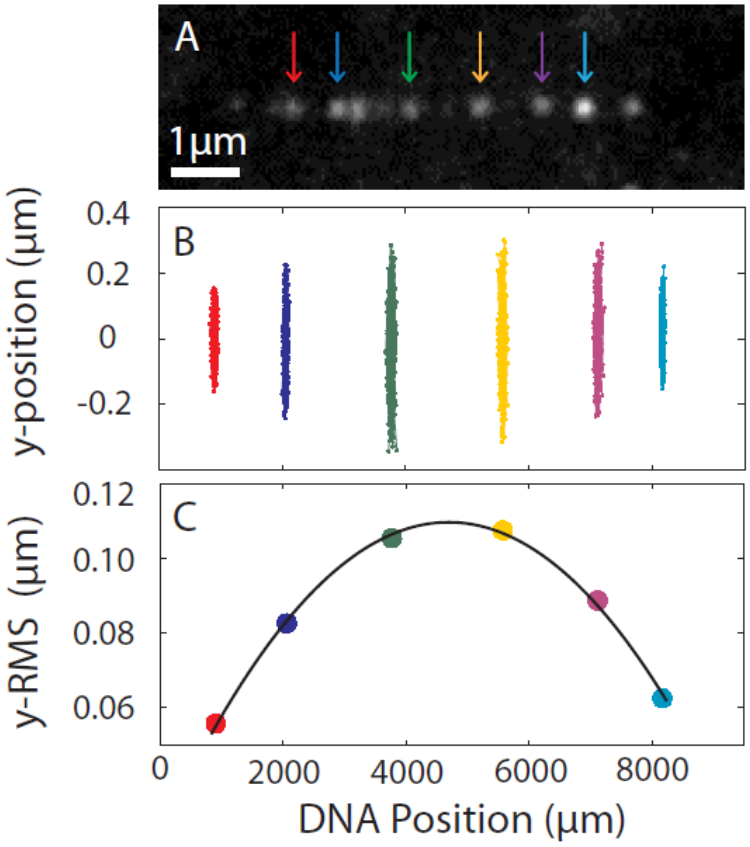

Figure 4-18. Determination of tether tension in TIRFM assay.

(a) TIRFM image of six immobile spots on a DNA bridge (colored arrows). Tensions experienced by the DNA bridges in the TIRFM assay were estimated from the transverse fluctuations of the DNA by monitoring the y-fluctuations of highlighted spots.

(b) (b) The x-and y-position trajectories of the siximmobile spots are shown, each of a different color.

(c) Corresponding fit of the variance in transverse Brownian fluctuations used todetermine the tension on the DNA tether. The transverse positions from individual stationary QD-TelK

to the DNA bridge axis, k_B is Boltzmann's constant, T is room temperature, F is the force, l is the position of the protein spot, and l_{tot} is the total length of the DNA bridge (**Figure 4-18 b)**. A fit of the variance of transverse Brownian fluctuations used to determine the tension on the DNA tether. The transverse positions from individual stationary QD-TelK were fit to the above formula using as fitting parameters F, l_{tot}, and a position offset along the glass pedestals (black line). Fits yielded an average tension of 3.1 ± 0.2 pN (mean ± SE) for all DNA bridges (**Figure 4-18 c**).

Calibration of tether occupancy vs. TelK concentration. From our TIRFM assay, the average number of fluorescent spots visualized on a single DNA bridge is linearly dependent on TelK concentration at which it was incubated (blue, mean ± SE; with linear fit in red; **Figure 4-19**). To obtain the best estimate of protein number (which we define as TelK occupancy) based on fluorescent spot counts, we used an occupation correction factor that counts non-blinking TelK spots as 2 monomers instead of 1 ($\mathrm{N_{mon}} = 1;\ \mathrm{N_{dim}} = 2$). To extrapolate from the occupancy observed in our TIRFM assay to that expected in our optical trap assay, we accounted for the DNA length difference between TIRFM λ-DNA and optical trap (OT) assay substrates with a length conversion factor, $\xi = \frac{\mathrm{l_{OT}}}{\mathrm{l_{\lambda}}}$. This approximation is valid based on the observed uniform binding affinity by TelK on non-target DNA. Thus, for each TelK concentration, the occupancy for optical trap measurements was estimated from the observed TIRFM occupancies by the following relation: $\mathrm{N_{OT}} = \mathrm{N_{TIRFM}}\ \mathrm{N_{mon/dim}}\xi$.

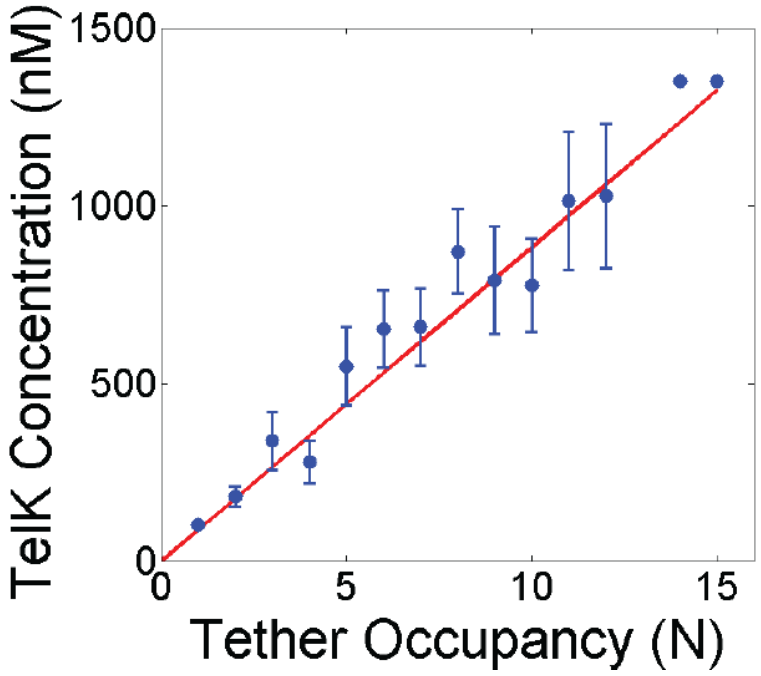

Figure 4-19. Determination of TelK occupancy on DNA as a function of TelK concentration.
Average occupancy of DNA bridges as a function of TelK incubation concentration results in a linear relationship which can be used to determine an estimate of TelK occupancy in optical trap experiments.

Optical Trap

The dual trap optical tweezers setup has been described in detail previously [52]. Briefly, the instrument consisted of two optical traps generated by two orthogonally polarized beams from a single 5-W, 1064-nm fiber coupled laser (YLR-5-1064-LP; IPG Photonics, Oxford, Massachusetts). The position of one trap relative to the other was controlled by a piezoactuated mirror stage (Nano-MTA-2; Mad City Labs, Madison, Wisconsin). A custom flow cell served as the experimental trap chamber, and could be displaced relative to the two traps in all directions by a three-axis translational stage (ESP300; Newport, Irvine, CA). Optical trap microspheres were prepared according to previously published protocols [53]. Deoxygenated TelK buffer,

prepared as described in the TIRFM **Materials and Methods** section, was used for all optical trap experiments. Optical trap experiments were performed in a 4-channel laminar flow microfluidic chamber, made by cutting flow channels into parafilm which is then melted between two glass coverslips. This chamber is designed to enable control of DNA tether exposure to a set concentration of protein. Two streams, one containing buffer only, the other containing a pre-determined concentration of TelK, were flowed side-by-side at 100 μm/s using a syringe pump (702000; Harvard Apparatus, Holliston, Massachusetts). A ~200 μm boundary between the two streams was thus created. Tethers were formed in the protein-free buffer stream and subsequently moved to the TelK stream within 2 seconds.

Calculation of expected TelK-induced DNA condensation step size.

We calculated the expected condensation step size of the DNA substrate in our optical trap assays based on a previously described model [36]. This model takes into account three contributions to the change in free energy when DNA-binding proteins bend DNA: (1) increase in distance between adjacent base pairs due to applied tension F, (2) DNA kinking by angle θ induced by the protein, and (3) DNA bending and end-to-end shortening beyond the protein-binding site:

$$E_{tot} = E_1 + E_2 + E_3 = l \cdot a\left(\frac{F}{K}\right) \cdot F + l \cdot a\left(1 - \cos\frac{\theta}{2}\right) \cdot F + \frac{\theta}{2}\sqrt{L_p k_B T}\sqrt{F}$$

where $(l \cdot a)$ = 56 x 0.34 nm = 19.04 nm represents the length of DNA contacted by TelK, θ = 73° is the kink angle, L_p = 50 nm and K = 1100 pN are the persistence length and the stretch modulus of DNA under optical trap conditions (deoxygenated TelK buffer), k_B is Boltzmann's constant, and T is the absolute temperature. The expected change in DNA extension as a function

of tension was determined from the derivative of the free energy with respect to force. For the average tension at which tethers are held in the optical trap of 5.2 ± 1.3 pN, the expected DNA condensation is 7.5 ± 0.4 nm, in excellent agreement with our average observed large step size of 7.2 nm.

Molecular Dynamics Simulations.

An active but c-terminally truncated TelK mutant, TelK538 which was used for crystal structures, was used for all molecular dynamics simulations, complexed to a 44-bp DNA substrate containing the TelK target sequence. Five atomic models of TelK-DNA were built based on a crystal structure of a TelK538 dimer complexed with double-stranded DNA (Protein Data Bank entry code 2V6E): The topology file of DNA and protein along with the missing hydrogen atoms was generated using the psfgen plug-in of VMD [54]. Each complex was placed in a water box with 0.15 mol/L NaCl. The total size of the simulated systems lies in the 270,000–350,000 atom range.

Simulations were carried out using the program NAMD 2.8 [55] with the CHARMM27 force field for DNA [56], the CHARMM22 force field for proteins with CMAP corrections [57] and the TIP3P water model [58]. Periodic boundary conditions were applied and the Particle Mesh Ewald method [59] was used to calculate full electrostatic interactions. The van der Waals (vdW) energy was calculated using a smooth cutoff of 12 Å. The system temperature was maintained at 295 K using a Langevin thermostat which was applied only to the oxygen atoms of water with a damping coefficient of 0.1 ps^{-1} [60].

All systems were energy minimized for 8000 steps and heated to ~295 K in ~4 ps. After that, systems were subjected to a ~500 ps isothermal-isobaric (NPT) equilibration with the protein

backbone constrained and a ~2 ns canonical ensemble (NVT) equilibration without constraint before production runs. Finally, an ~80 ns production run in an NVT ensemble was performed for each system (**Table 4-1** lists all simulations). Data analysis of MD trajectories and snapshots of the molecular structures were realized with VMD [54].

Name	Protein	DNA	Number of atoms	Time (ns)
SimuA	TelK dimer	Target DNA	347,912	80
SimuB	TelK dimer	Non-target DNA	343,306	80
SimuC	TelK monomer	Target DNA	281,097	80
SimuD	TelK monomer	Non-target DNA	276,057	80
SimuE	TelK dimer	None	280,741	80

Table 4-1: List of performed simulations

Stochastic Simulations

Stochastic simulations were performed to determine the first passage times for TelK dimerization and target-finding as a function of occupancy of TelK on DNA. Custom MATLAB code was used to implement the simulations. We assumed an L = 3.4-kb (1.156-μm) long molecule of DNA—the same length as that used in the optical trap measurements—which contained the target sequence at its center. Reflecting boundary conditions were applied. TelK monomers were modeled as point particles, and randomly assigned uniformly along the DNA. Particles were allowed to diffuse in 1D with coefficient D = 1.8 $\mu m^2/s$ and dissociate with rate constant k_{off} = 0.24 s^{-1}, average values corresponding to those determined from the TIRFM experiments for TelK monomers. New particles could also bind to the DNA with a preset rate

constant k_{on}. Binding and dissociation established a steady-state occupancy of TelK on DNA determined by

$$\langle N_{sim} \rangle = \frac{k_{on}}{k_{off}}$$

During the simulations, particles were advanced incrementally until two particles came into contact anywhere along the DNA and dimerized (defining the first-passage time t_{dimer}) or until a protein monomer came into contact with the target site (defining t_{target}). Dimers were assumed to be immobile and not to dissociate. Each simulation was run 100 times for 100000 x 0.1s time steps, for each of several DNA occupancies, which was achieved by varying k_{on} over the range 0.0015 – 4 s^{-1} to cover experimentally-observed occupancies. The DNA occupancies were normalized by the DNA length to represent the occupancy of TelK monomers along DNA.

4.13 Chapter references

1. Huang, W.M., et al., *Protelomerase uses a topoisomerase IB/Y-recombinase type mechanism to generate DNA hairpin ends.* Journal of Molecular Biology, 2004. **337**(1): p. 77-92.
2. Koslover, E.F., M.A. Diaz de la Rosa, and A.J. Spakowitz, *Theoretical and computational modeling of target-site search kinetics in vitro and in vivo.* Biophys J, 2011. **101**(4): p. 856-65.
3. van den Broek, B., et al., *How DNA coiling enhances target localization by proteins.* Proceedings of the National Academy of Sciences of the United States of America, 2008. **105**(41): p. 15738-15742.
4. Gowers, D.M., G.G. Wilson, and S.E. Halford, *Measurement of the contributions of 1D and 3D pathways to the translocation of a protein along DNA.* Proc Natl Acad Sci U S A, 2005. **102**(44): p. 15883-8.
5. Ramanathan, S.P., et al., *Type III restriction enzymes communicate in 1D without looping between their target sites.* Proc Natl Acad Sci U S A, 2009. **106**(6): p. 1748-53.
6. Halford, S.E. and J.F. Marko, *How do site-specific DNA-binding proteins find their targets?* Nucleic Acids Research, 2004. **32**(10): p. 3040-3052.
7. Kolomeisky, A.B., *Physics of protein-DNA interactions: mechanisms of facilitated target search.* Phys Chem Chem Phys, 2011. **13**(6): p. 2088-95.
8. Sudhanshu, B., et al., *Tension-dependent structural deformation alters single-molecule transition kinetics.* Proceedings of the National Academy of Sciences of the United States of America, 2011. **108**(5): p. 1885-1890.
9. Bitinaite, J., et al., *FokI dimerization is required for DNA cleavage.* Proc Natl Acad Sci U S A, 1998. **95**(18): p. 10570-5.
10. Ban, C. and W. Yang, *Structural basis for MutH activation in E.coli mismatch repair and relationship of MutH to restriction endonucleases.* EMBO J, 1998. **17**(5): p. 1526-34.
11. Dowd, D.R. and R.S. Lloyd, *Biological significance of facilitated diffusion in protein-DNA interactions. Applications to T4 endonuclease V-initiated DNA repair.* J Biol Chem, 1990. **265**(6): p. 3424-31.
12. Blainey, P.C., et al., *A base-excision DNA-repair protein finds intrahelical lesion bases by fast sliding in contact with DNA.* Proceedings of the National Academy of Sciences of the United States of America, 2006. **103**(15): p. 5752-5757.
13. Widom, J., *Target site localization by site-specific, DNA-binding proteins.* Proc Natl Acad Sci U S A, 2005. **102**(47): p. 16909-10.
14. van den Broek, B., M.C. Noom, and G.J. Wuite, *DNA-tension dependence of restriction enzyme activity reveals mechanochemical properties of the reaction pathway.* Nucleic Acids Res, 2005. **33**(8): p. 2676-84.
15. Langowski, J., et al., *Does the Specific Recognition of DNA by the Restriction Endonuclease Ecori Involve a Linear Diffusion Step - Investigation of the Processivity of the Ecori Endonuclease.* Nucleic Acids Research, 1983. **11**(2): p. 501-513.
16. Gorman, J., et al., *Dynamic basis for one-dimensional DNA scanning by the mismatch repair complex Msh2-Msh6.* Mol Cell, 2007. **28**(3): p. 359-70.
17. Mendillo, M.L., D.J. Mazur, and R.D. Kolodner, *Analysis of the interaction between the Saccharomyces cerevisiae MSH2-MSH6 and MLH1-PMS1 complexes with DNA using a*

reversible DNA end-blocking system. Journal of Biological Chemistry, 2005. **280**(23): p. 22245-22257.
18. Gorman, J. and E.C. Greene, *Visualizing one-dimensional diffusion of proteins along DNA*. Nature Structural & Molecular Biology, 2008. **15**(8): p. 768-774.
19. Singh, V., M.K. Ekka, and S. Kumaran, *Second Monomer Binding Is the Rate-Limiting Step in the Formation of the Dimeric PhoP-DNA Complex*. Biochemistry, 2012. **51**(7): p. 1346-1356.
20. Erie, D.A., et al., *DNA bending by Cro protein in specific and nonspecific complexes: implications for protein site recognition and specificity*. Science, 1994. **266**(5190): p. 1562-6.
21. Marianayagam, N.J., M. Sunde, and J.M. Matthews, *The power of two: protein dimerization in biology*. Trends Biochem Sci, 2004. **29**(11): p. 618-25.
22. Vangent, D.C., et al., *Complementation between Hiv Integrase Proteins Mutated in Different Domains*. Embo Journal, 1993. **12**(8): p. 3261-3267.
23. Hai, T. and T. Curran, *Cross-Family Dimerization of Transcription Factors Fos Jun and Atf Creb Alters DNA-Binding Specificity*. Proceedings of the National Academy of Sciences of the United States of America, 1991. **88**(9): p. 3720-3724.
24. Shuai, K., et al., *Interferon activation of the transcription factor Stat91 involves dimerization through SH2-phosphotyrosyl peptide interactions*. Cell, 1994. **76**(5): p. 821-8.
25. van Aelst, K., et al., *Type III restriction enzymes cleave DNA by long-range interaction between sites in both head-to-head and tail-to-tail inverted repeat*. Proc Natl Acad Sci U S A, 2010. **107**(20): p. 9123-8.
26. Aihara, H., W.M. Huang, and T. Ellenberger, *An interlocked dimer of the protelomerase TelK distorts DNA structure for the formation of hairpin telomeres*. Molecular Cell, 2007. **27**(6): p. 901-913.
27. Moffitt, J.R., et al., *Recent advances in optical tweezers*. Annual Review of Biochemistry, 2008. **77**: p. 205-228.
28. Selvin, P.R. and T. Ha, *Single-molecule techniques: a laboratory manual*. 2008, Cold Spring Harbor, New York: John Inglis.
29. Klepeis, J.L., et al., *Long-timescale molecular dynamics simulations of protein structure and function*. Curr Opin Struct Biol, 2009. **19**(2): p. 120-7.
30. Yildiz, A., et al., *Myosin V walks hand-over-hand: Single fluorophore imaging with 1.5-nm localization*. Science, 2003. **300**(5628): p. 2061-2065.
31. Nirmal, M., et al., *Fluorescence intermittency in single cadmium selenide nanocrystals*. Nature, 1996. **383**(6603): p. 802-804.
32. Dogterom, M., et al., *Assembly dynamics of microtubules at molecular resolution*. Nature, 2006. **442**(7103): p. 709-712.
33. Grindley, N.D., K.L. Whiteson, and P.A. Rice, *Mechanisms of site-specific recombination*. Annual Review of Biochemistry, 2006. **75**: p. 567-605.
34. Grainge, I. and M. Jayaram, *The integrase family of recombinase: organization and function of the active site*. Mol Microbiol, 1999. **33**(3): p. 449-56.
35. Lee, L. and P.D. Sadowski, *Strand selection by the tyrosine recombinases*. Prog Nucleic Acid Res Mol Biol, 2005. **80**: p. 1-42.

36. van den Broek, B., M.C. Noom, and G.J. Wuite, *DNA-tension dependence of restriction enzyme activity reveals mechanochemical properties of the reaction pathway.* Nucleic Acids Research, 2005. **33**(8): p. 2676-84.
37. Slutsky, M. and L.A. Mirny, *Kinetics of protein-DNA interaction: facilitated target location in sequence-dependent potential.* Biophysical Journal, 2004. **87**(6): p. 4021-35.
38. Grove, A., et al., *Localized DNA flexibility contributes to target site selection by DNA-bending proteins.* Journal of Molecular Biology, 1996. **260**(2): p. 120-5.
39. Erie, D.A., et al., *DNA Bending by Cro Protein in Specific and Nonspecific Complexes - Implications for Protein Site Recognition and Specificity.* Science, 1994. **266**(5190): p. 1562-1566.
40. Iwahara, J. and G.M. Clore, *Detecting transient intermediates in macromolecular binding by paramagnetic NMR.* Nature, 2006. **440**(7088): p. 1227-30.
41. Iwahara, J., M. Zweckstetter, and G.M. Clore, *NMR structural and kinetic characterization of a homeodomain diffusing and hopping on nonspecific DNA.* Proc Natl Acad Sci U S A, 2006. **103**(41): p. 15062-7.
42. Biebricher, A., et al., *Tracking of Single Quantum Dot Labeled EcoRV Sliding along DNA Manipulated by Double Optical Tweezers.* Biophysical Journal, 2009. **96**(8): p. L50-L52.
43. Redinbo, M.R., et al., *Crystal structures of human topoisomerase I in covalent and noncovalent complexes with DNA.* Science, 1998. **279**(5356): p. 1504-13.
44. Smith, K. and P. Youngman, *Use of a New Integrational Vector to Investigate Compartment-Specific Expression of the Bacillus-Subtilis Spoiim Gene.* Biochimie, 1992. **74**(7-8): p. 705-711.
45. Sun, M. and P. Serwer, *The conformation of DNA packaged in bacteriophage G.* Biophys J, 1997. **72**(2 Pt 1): p. 958-63.
46. Selvin, P.R., et al., *In Vitro and In Vivo FIONA and Other Acronyms for Watching Molecular Motors Walk*, in *Single-molecule techniques: a laboratory manual*, T. Ha, Editor. 2008, Cold Spring Harbor Books: Cold Spring Harbor, NY.
47. Iwaki, M., et al., *Brownian search-and-catch mechanism for myosin-VI steps.* Nat Chem Biol, 2009. **5**(6): p. 403-5.
48. Dahan, M., et al., *Diffusion dynamics of glycine receptors revealed by single-quantum dot tracking.* Science, 2003. **302**(5644): p. 442-5.
49. Bouzigues, C., et al., *Asymmetric redistribution of GABA receptors during GABA gradient sensing by nerve growth cones analyzed by single quantum dot imaging.* Proc Natl Acad Sci U S A, 2007. **104**(27): p. 11251-6.
50. Courty, S., et al., *Tracking individual kinesin motors in living cells using single quantum-dot imaging.* Nano Lett, 2006. **6**(7): p. 1491-5.
51. Bannai, H., et al., *Imaging the lateral diffusion of membrane molecules with quantum dots.* Nature Protocols, 2007. **1**: p. 2628-2634.
52. Bustamante, C., Y.R. Chemla, and J.R. Moffitt, *Single-Molecule Techniques: A Laboratory Manual*, C.S. Harbor, Editor. 2008: New York.
53. Landry, M.P., et al., *Characterization of Photoactivated Singlet Oxygen Damage in Single-Molecule Optical Trap Experiments.* Biophysical Journal, 2009. **97**(8): p. 2128-2136.
54. Humphrey, W., A. Dalke, and K. Schulten, *VMD: visual molecular dynamics.* J Mol Graph, 1996. **14**(1): p. 33-8, 27-8.

55. Phillips, J.C., et al., *Scalable molecular dynamics with NAMD.* Journal of Computational Chemistry, 2005. **26**(16): p. 1781-1802.
56. Foloppe, N. and A.D. MacKerell, *All-atom empirical force field for nucleic acids: I. Parameter optimization based on small molecule and condensed phase macromolecular target data.* Journal of Computational Chemistry, 2000. **21**(2): p. 86-104.
57. MacKerell, A.D., et al., *All-atom empirical potential for molecular modeling and dynamics studies of proteins.* Journal of Physical Chemistry B, 1998. **102**(18): p. 3586-3616.
58. Mackerell, A.D., M. Feig, and C.L. Brooks, *Extending the treatment of backbone energetics in protein force fields: Limitations of gas-phase quantum mechanics in reproducing protein conformational distributions in molecular dynamics simulations.* Journal of Computational Chemistry, 2004. **25**(11): p. 1400-1415.
59. Jorgensen, W.L., et al., *Comparison of Simple Potential Functions for Simulating Liquid Water.* Journal of Chemical Physics, 1983. **79**(2): p. 926-935.
60. Martyna, G.J., D.J. Tobias, and M.L. Klein, *Constant-Pressure Molecular-Dynamics Algorithms.* Journal of Chemical Physics, 1994. **101**(5): p. 4177-4189.

Chapter 5. TelK cutting with FRET

Certain protein systems are sensitive to tensions experienced by their DNA substrates. In this chapter, we explore an alternate approach to probing the process of DNA hairpin formation by TelK. We design a DNA substrate with a Cy3 and Cy5 FRET pair flanking the TelK target site and use a combination of PIFE and FRET to survey the conformation of target DNA with TelK in the absence of applied tension. Though cyanine dye labeling of the DNA substrate abolishes the hairpin-forming ability of TelK, we are able to observe PIFE and PIFD due to TelK binding proximal to the dye-labeled DNA. Furthermore, we observe a few rare occurrences of FRET that match the FRET signal expected from a cruciform DNA transition state. We hypothesize as to why TelK may be sensitive to externally applied tensions and DNA labeling in the context of its resemblance to other tension-dependent protein families.

5.1 TelK cutting inactivation in linear DNA conformations

The non-specific DNA condensation and immobilization behavior of protelomerases TelK (TelK) lends itself well to the study of dimer-active protein systems, particularly because it provides a clear signal (via immobilization or DNA condensation) for non-specific protein-DNA-protein interactions. These interactions played a fundamental role in deciphering the model of dimer-active proteins, as it enabled us to experimentally measure the first passage rates for dimerization in **Chapter 4**. However, the behavior of TelK at the target sequence, and the proposed mechanism through which TelK accomplished hairpin formation in the absence of external energy cofactors such as ATP, remains elusive. Because there is no net loss or gain of nucleotides during the modification of DNA structure or topology, it is unclear how TelK drives the isoenergetic process of hairpin formation unidirectionally when theory would predict a 50-50 ratio of substrate and product in the absence of a driving factor such as ATP [1]. It is possible

that electrostatically induced DNA twisting or bending at the DNA target site may help stabilize the protein-DNA complex and drive the overall reaction forward. It has also been hypothesized that protein-protein interactions may play a crucial role in making catalysis unidirectional [1].

One possible mechanism used by TelK for catalysis regulation may be DNA conformation. Whether DNA is free to take on a globular conformation, or whether it is held linearly under tension could affect the energy landscape of the biochemical processes for which DNA is a substrate. As noted in both the total internal reflection fluorescence (TIRF) microscopy and optical trap experiments, no DNA cutting was observed in either experiment, even when replacing the nonspecific DNA substrate with target site-containing DNA. In both experiments, the DNA substrate was extended linearly and held at a low force (3.1 ± 2.7 pN, and 5.2 ± 1.3 pN, mean ± SD pN for TIRF and optical trap DNA, respectively). To confirm the hairpin-forming ability of TelK at the single-molecule level, we performed a single-molecule assay that enables DNA to take on a globular, instead of a linear, conformation.

5.2 Tethered particle microscopy assay

Tethered particle microscopy (TPM) assays allow for the visualization of protein activity upon a DNA substrate that is tethered to a class surface on one end, and to a fluorescent microsphere on the other end. In this manner, a single molecule of DNA is immobilized at the surface of a microfluidic channel. This DNA is not under tension as in our optical trap or DNA bridge TIRF assays, and is free to take on a globular conformation which more closely resembles the conformation of DNA in a living cell. We used this TPM assay to test the single-molecule activity of TelK on our DNA substrates in a globular instead of a linearly extended conformation. We incubated fluorescent anti-digoxygenin (AD) microspheres with DNA

containing the TelK target site in the center, a biotin on the 5' end, and a digoxigenin at the 3' end. We then flowed the DNA-coated microspheres into a microfluidic chamber passivated with bovine serum albumin (BSA) and 1% neutravidin, as described in **Materials and methods**. We then imaged these surface-immobilized DNA-microsphere complexes using an objective-type TIRF microscope as described in **Chapter 2**. Next, we flowed in 100nM of unlabeled TelK, and recorded the disappearance of fluorescence as a marker for TelK hairpin formation activity at a given DNA molecule position (**Figure 5-1**).

We observed that TelK cut a 4.5-kb globular target DNA substrate at a rate of one cut per 41.6 ± 71.4 s (mean ± SE). Control experiments using DNA lacking the TelK target site did not exhibit any dissociation of the fluorescent AD microspheres over the duration of the experiment, 7 minutes. This confirms that TelK only causes dissociation of the fluorescent microspheres via hairpin formation at the target site. We confirm that, while TelK is able to search for, find, and preferentially bind to its target site on linearly extended DNA substrates, it is unable to catalyze the formation of DNA hairpins on extended DNA. This suggests that the process of DNA cutting and hairpin formation is very sensitive to DNA conformation, and that even applications of low force (3.1 ± 0.2 pN for TIRF DNA, 5.2 ± 0.1

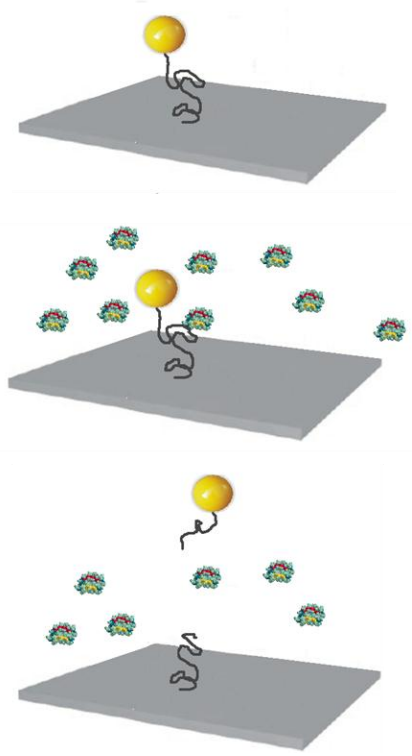

Figure 5-1. Tethered particle microscopy.
DNA containing the TelK target site is immobilized on a glass slide, and tagged with a fluorescent microsphere. Introduction of TelK causes hairpin formation at the target site, and subsequent release of the fluorescent microsphere.

pN optical trap DNA; mean ± SE) inhibit TelK activity. This strongly suggests that TelK activity can be modulated by DNA linear vs. globular conformation and base its target-site catalysis of hairpin formation based on the local DNA conformation. Certain studies have suggested that topology-sensitive proteins such as topoisomerases have increased affinities for globular DNA substrates [3]. It follows that TelK, which condenses nonspecific DNA, could catalyze substrates such as globular DNA more readily than linearly extended DNA. In order to probe the process of hairpin formation at the target sequence without the application of tension on the DNA substrate, we developed a fluorescence resonance energy transfer (FRET)-based assay.

5.3 TelK DNA hairpin formation: proposed reaction mechanisms

The mechanism by which TelK accomplishes hairpin formation remains poorly understood. This process entails substantial DNA distortion and rearrangement including DNA bending, backbone cleavage, folding, and annealing (**Figure 5-2**). This process involves the

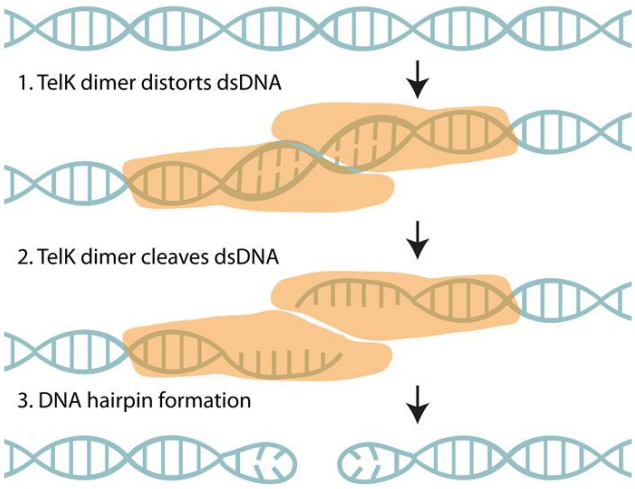

Figure 5-2. TelK hairpin formation.
The process of hairpin formation by TelK involves a dimer binding to the TelK target site, cleavage of the DNA backbone to create a 6-bp staggered cut, and rearrangement of the DNA followed by reannealing to form the DNA hairpin products.

introduction of single-stranded DNA (ssDNA) nicks on its DNA substrate through phosphoryl transfer instead of hydrolysis, and subsequent structural rearrangement of DNA through topological rearrangement and re-ligation without a net loss or gain of nucleotides. The ability of TelK to accomplish these processes without the aid of external sources of energy such as ATP leaves the mechanism of hairpin formation in the hands of electrostatic interactions between the

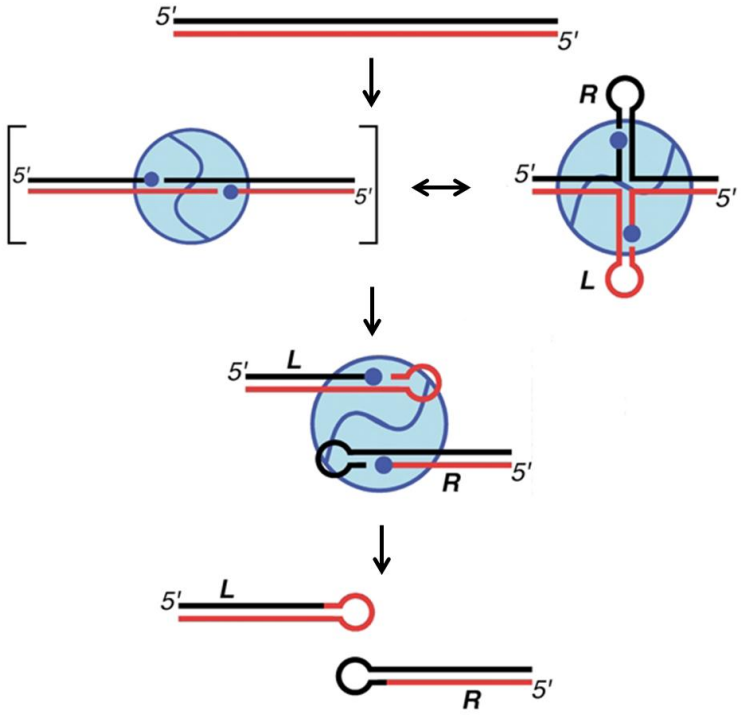

Figure 5-3. Proposed mechanism for protelomerases activity.
Protelomerases such as TelK bind as a dimer to the inverted repeat DNA dyad symmetrical target site to produce left (L) and right (R) DNA hairpin products. It is proposed that TelK may cause its DNA substrate to adopt a cruciform transition state as part of its reaction intermediate, due to the inverted repeat sequence of the target site. Whether the DNA remains in a linear conformation prior to hairpin formation and release, or whether DNA adopts a cruciform intermediate remains to be determined. Figure adapted from [2].

TelK protein dimer and the DNA. It is also important to note that TelK is a single-turnover protein, indicating that a TelK dimer self-contains the ability to undergo one round of DNA hairpin formation, but not more [2]. All of these features of the TelK-DNA reaction pathway suggest that the process of DNA hairpin formation will involve structurally distorted DNA intermediates. Furthermore, the TelK target site contains a 22-base pair inverted repeat sequence

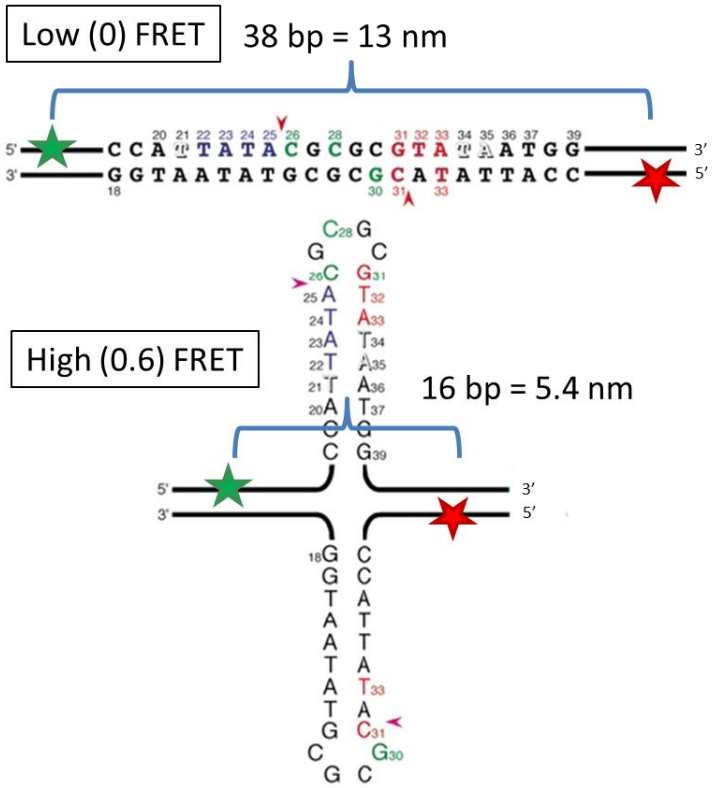

Figure 5-4. Suggested DNA cruciform transition state.
A schematic representation of the 22-bp DNA substrate that forms the inverted repeat of the TelK target sequence. Previous studies have shown that introducing singular nicks into the DNA substrate leads to different degrees of DNA hairpin formation. Nicks can lead to full hairpin products (black filled), only the downstream product (blue), only the upstream product (red), only protein-DNA linked intermediates (green), or none (shadowed). This long-range dependence on phosphate backbone intactness suggests that a cruciform intermediate may form as an essential part of TelK hairpin formation. Red arrows represent the location where TelK cleaves DNA for hairpin formation. We suggest the synthesis of a similar substrate with a Cy3 (green star) and Cy5 (red star) label to probe the DNA transition state during TelK hairpin formation. Figure adapted from [2].

which can self-anneal to form a cruciform structure, possibly as a necessary intermediate during the course of hairprin formation (**Figure 5-3**). Previous studies have argued that this cruciform intermediate is the most likely DNA transition structure for the process of DNA hairpin formation [2]. By nicking the DNA backbone of a DNA strand containing the TelK inverted repeat site, it was found that several backbone nick locations severely impaired the formation of hairpins, beyond the 6-bp location of the hairpin forming overhang region. Therefore, it is likely that a DNA structural intermediate requiring intactness of the DNA backbone at a long range (within the inverted repeat sequence) is an essential part of the hairpin-forming process. However, a more recent crystal structure of TelK complexed with its target DNA shows that there is little room in the protein binding pocket to accommodate a DNA structure as large as a DNA cruciform [4].

To better understand the mechanism by which TelK forms DNA hairpins, we designed a FRET-based assay to measure the nanometer-scale changes in DNA conformation throughout the course of the TelK-DNA reaction pathway. We considered the proposed cruciform transition state as a starting point to design our FRET pair-labeled DNA substrate. In its extended conformation, the inverted repeat sequence hypothesized to undergo structural rearrangement into a DNA cruciform is 22-bp in length (**Figure 5-4**). The change in DNA length caused by such a structural rearrangement should therefore measure approximately 7.4 nm, the length of the 22-bp inverted repeat sequence, which is within the length regime observable by FRET.

5.4 Probing DNA dynamics during TelK hairpin formation

5.4.1 DNA FRET substrate design

Our goal is to design a DNA substrate within the FRET-sensitive distance of 3-8 nm [5] to observe any structural DNA rearrangement that may occur in the inverted repeat of the TelK DNA substrate. Using a combined annealing and ligation protocol as described in **Materials and methods**, we designed a 159-bp DNA substrate with pair of FRET dyes, Cy3 and Cy5. These dyes were incorporated into the DNA substrate 38 base pairs (~13 nm) apart flanking the 22-bp TelK inverted repeat site (**Figure 5-5a**). This design ensured that zero FRET would be observed when the DNA substrate is fully-extended, but 0.6 FRET would be observed if the 22-bp inverted repeat site forms into the expected cruciform structure throughout the course of hairpin formation. This DNA substrate has the TelK target site in the center of the construct, and a biotin on one end for surface-attachment (**Figure 5-5b**). The synthesis protocol for this DNA substrate left a backbone nick at the 5' position of each dye. However, previous studies have confirmed that a backbone nick at these positions does not impede hairpin formation [2]. A terminal biotin was also incorporated into the substrate to enable biotin-neutravidin mediated surface immobilization of our DNA substrate. We ensured our DNA product had the expected length and contained both Cy3 and Cy5 dyes by running our substrate on a 3% agarose gel as described in

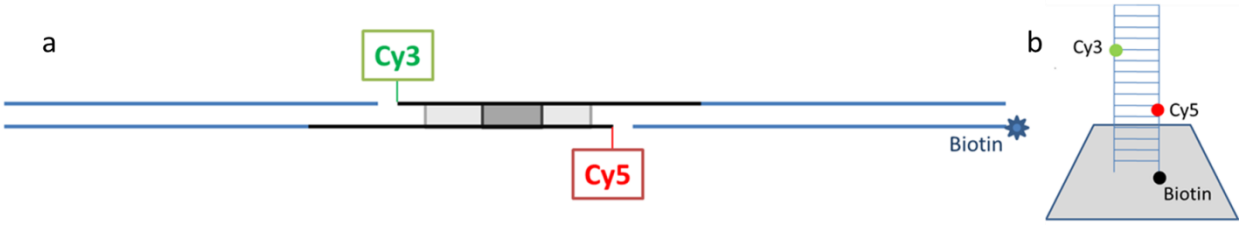

Figure 5-5. DNA substrate for TelK FRET. (a) A 159-bp substrate contains the inverted repeat target site (dark grey) flanked by the TelK crystal structure target site (light grey). Cy3 and Cy5 dyes are placed 38 base pairs (~13 nm) apart. (b) A terminal biotin proximal to the Cy5 dye is used to incorporate this DNA substrate onto a microfluidic chamber surface via biotin-neutravidin interactions.

Materials and Methods. The length of the DNA substrate approximates the persistence length of double-stranded DNA. Therefore, our DNA substrate is expected to hold a roughly linear shape at the microfluidic chamber surface, such that the TelK target site remains at a suitable distance from the chamber surface to reduce the risk of surface-effects.

Our microfluidic chamber design is a single-channel flow cell with PEG passivation to be used in a prism-TIRF microscope. Surface passivation, chamber design, and prism-TIRF are described in more detail in **Chapter 2**. Briefly, a quartz slide had a flow inlet and flow outlet hole drilled into opposite slides of the slide, prior to surface passivation with Polyethylene Glycol (PEG). Double-sided tape was used to create a single flow channel across the flow inlet and outlet, by sticking a PEGylated coverslip to the quartz slide. A micropipette tip served as a reservoir for incoming flow via the flow inlet, and a syringe was coupled to the flow outlet to draw in sample from the inlet (**Figure 5-6a**). A series of sequential flows enabled the incorporation of the TelK DNA substrate onto the surface of the channel, as detailed in **Materials and methods**.

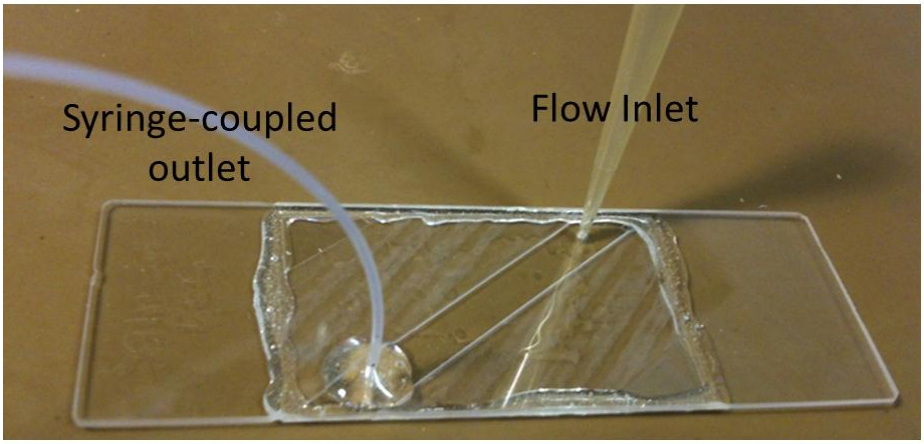

Figure 5-6. TelK FRET microfluidic flow cell setup. (a) A PEGylated flow cell is constructed from a quartz slide and a glass coverslip held together by double-sided tape. A micropipette tip served as a reservoir for the flow inlet, and flow is modulated via a syringe-coupled outlet.

5.4.2 DNA fluorescence colocalization

We next tested our DNA substrate at the single-molecule level for proper colocalization of the Cy3 and Cy5 FRET pair. A 50 pM concentration of our DNA substrate was deposited onto the microfluidic chamber surface such that each DNA strand is at least a diffraction-limited distance apart and could be individually localized. The same protocol was repeated for 50 pM control biotinylated DNA substrates that only contained a single Cy3 or a single Cy5 dye. An equimolar ratio of singly-labeled Cy3 and Cy5 control DNA substrates were deposited onto a separate microfluidic chamber surface. For both samples, we quantified the fraction of Cy3 dyes that colocalized with a Cy5 dye, and the fraction of Cy5 dyes that colocalized with a Cy3 dye for a given inter-dye pixel distance. This was accomplished using the spot-mapping algorithm described in **Chapter 2**. For both Cy3 and Cy5, our TelK DNA substrate showed a high degree of colocalization: 73 ± 1% of the surface immobilized sample has both a Cy3 and a Cy5

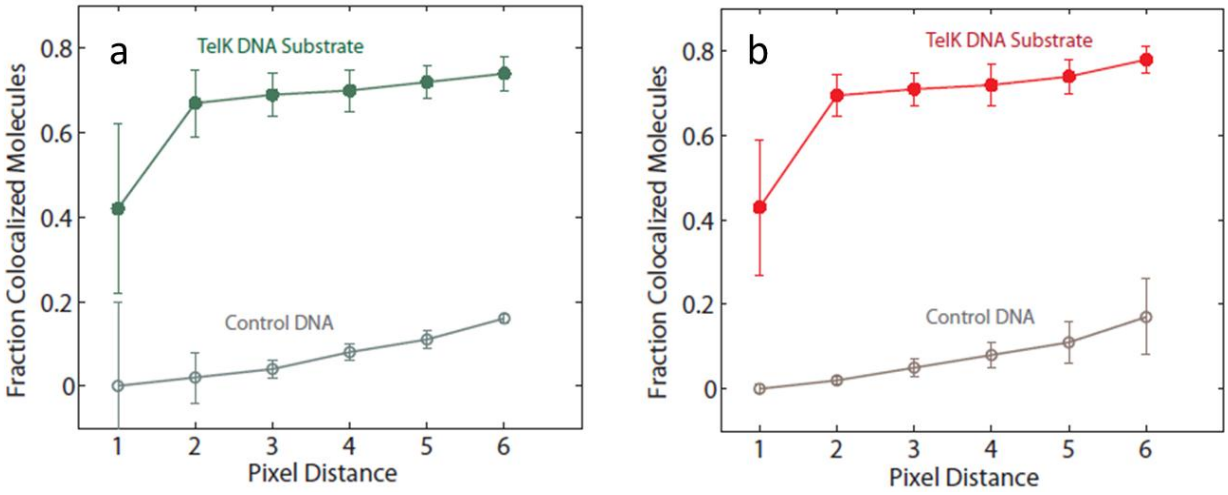

Figure 5-7. Colocalization of Cy3 and Cy5 on our DNA substrate. (a) Fraction of Cy3 molecules colocalized to Cy5 as a function of inter-dye pixel distance for TelK DNA (green) and a control DNA substrate (grey) shows a high degree of colocalization between the Cy3 and Cy5 dyes on our TelK DNA substrate. (b) The same trend is observed for Cy5 molecules colocalized to Cy3 (red) and control DNA (grey).

fluorophore present at a 2-pixel colocalization distance. Our control DNA sample showed low colocalization (< 20%) even at a 6-pixel colocalization distance. The imperfect degree of colocalization for our TelK DNA sample can be attributed to small errors in our mapping files between the Cy3 and Cy5 imaging channels, and to the premature photobleaching or dye damage during DNA synthesis to either Cy3 or Cy5.

5.5 DNA-labeling inhibits hairpin formation by TelK

Next, we tested the ability of TelK to form hairpins on our DNA substrate. Formation of hairpins at the TelK target site cuts the DNA substrate at the center, resulting in two separate DNA strands approximately 80-bp in length. We synthesized a second 159-bp TelK DNA substrate using the same protocol as for our FRET substrate, without the Cy3 and Cy5 FRET pair. This unlabeled DNA substrate was used as a control for TelK activity. We incubated 500 nM of each our unlabeled and labeled DNA substrate with 100 nM TelK, and ran the post-incubation DNA on a 3% agarose gel. As shown in **Figure 5-8**, while TelK is able to cut the unlabeled DNA substrate, incorporation of the Cy3 and Cy5 dyes completely abolishes the ability of TelK to cut DNA. Based on the crystal structure of TelK on its target DNA substrate, the footprint of TelK covers at least 56-bp of duplex DNA, well beyond the TelK target sequence. It is possible that incorporation of bulky cyanine dyes within the footprint of TelK changes the ability of TelK to bind to the DNA such that it blocks the formation of the necessary nucleic acid- amino acid contacts for hairpin catalysis. We also confirmed that TelK is unable to cut our DNA substrate at the single-molecule level in our TIRF instrument by immobilizing our labeled DNA substrate on the surface of our microfluidic chamber as shown in **Figure 5.5**. Next, we flowed in 50 nM, 100 nM, and 300 nM TelK and monitored our sample for the disappearance

of Cy3 which would be indicative of TelK cutting its target sequence. We observed no disappearance of Cy3 spots, indicating a lack of TelK activity. It is likely that the incorporation of bulky cyanine dyes within the TelK binding footprint is responsible for perturbing TelK's interaction with DNA. TelK's sensitivity to the incorporation of organic dyes is unfortunate, since increasing the dye separation beyond the TelK footprint also takes the dyes out of the FRET sensitivity range. Therefore, probing TelK hairpin formation at the single-molecule level will require alternate approaches. In **Chapter 4**, we showed that extending a DNA substrate with the application of small forces inhibited TelK hairpin formation. Here, we show that introducing a FRET pair into the DNA substrate within the TelK footprint can also inhibit hairpin formation. In **Section 5.8**, we discuss the reasons for TelK's sensitivity to changes in its DNA substrate, and

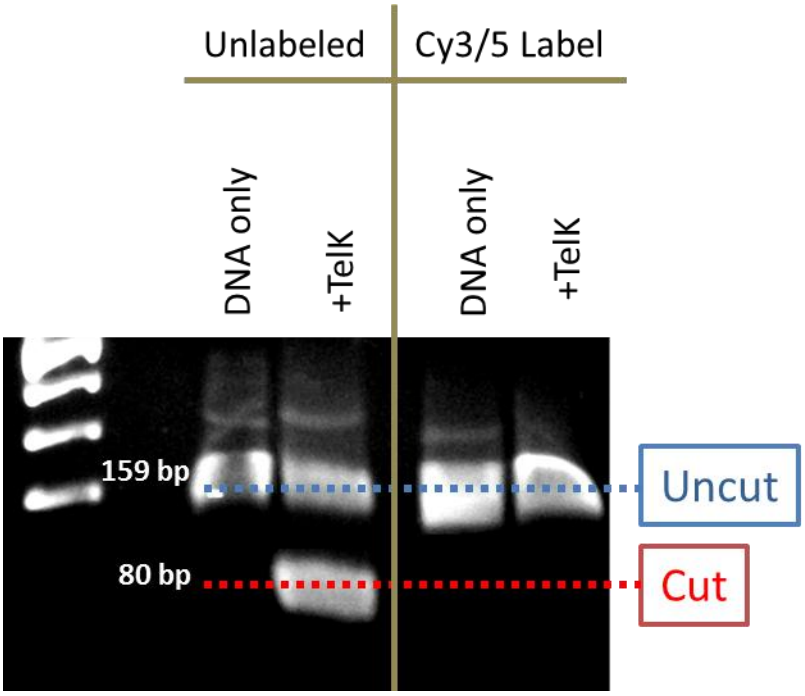

Figure 5-8. FRET DNA substrate cutting by TelK. 50 ng of unlabeled DNA substrate can be cut by 20-nMoles of TelK (2 left lanes). The same quantities of labeled DNA show no cutting by TelK (2 right lanes).

alternate approaches that may be taken to probe hairpin formation by TelK.

5.6 TelK-induced FRET

We monitored our fluorescent signal for instances of FRET. Despite the absence of TelK hairpin formation, we may still be able to capture instances of transient DNA distortion by TelK, as in our optical trap assay in **Chapter 4**. Based on the design of our DNA substrate, we would expect zero FRET when the DNA is fully-extended, and 0.6 FRET if a cruciform structure forms in the central 22-bp inverted repeat sequence. Upon Cy3 excitation with our 532nm laser, we observed mostly uncorrelated fluctuations in Cy3 intensity corresponding to the PIFE signals described above. A small subset (3%) of traces did show anti-correlated Cy3 – Cy5 signals corresponding to ~0.6 FRET. A 0.6 FRET signal corresponds to a 5 nm decrease in dye separation, or a 22-bp shortening of our DNA substrate. Though a 3% FRET population is not sufficient to draw conclusions about TelK-induced DNA dynamics, it is possible that these few traces do provide some preliminary evidence for a cruciform DNA transition state en route to hairpin formation.

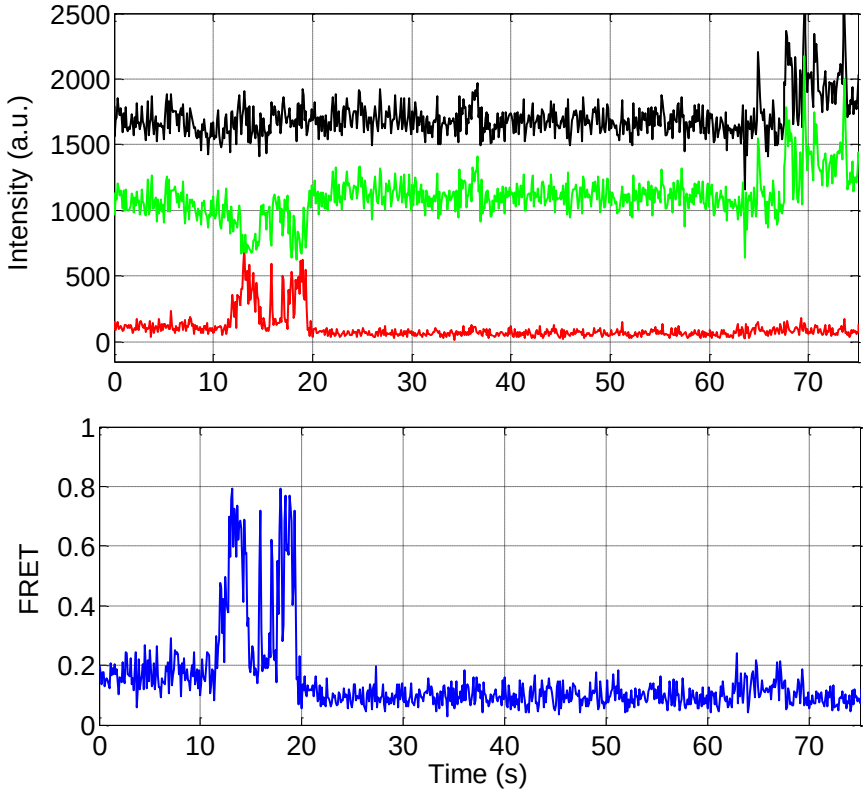

Figure 5-9. TelK FRET trace. (a) DNA- SWNT immobilized on a passivated surface can be hybridized *in situ* with Cy3-labeled complementary DNA (cDNA), and (b) visualized via TIR

5.7 TelK Protein-induced fluorescence enhancement

In the absence of TelK cutting the labeled DNA substrate in bulk, we are unable to probe the full process of hairpin formation with sm-FRET. However, despite a lack of TelK cutting in our optical trap assay in **Chapter 4**, we were still able to observe DNA condensation and use this behavior to elucidate important information about the TelK target search process. Though TelK cannot cut our labeled DNA FRET substrate, we may still be able to learn more about TelK's interaction with its target DNA substrate through alternate fluorescence microscopy approaches.

Protein-induced fluorescence enhancement (PIFE) is an alternative to FRET to monitor the dynamics of proteins in the vicinity of labeled DNA substrates [6]. The sensitivity distance of

PIFE includes the 0-3 nm range, to which FRET is insensitive. Therefore, we can use PIFE as a quantitative measure of protein binding to our surface-immobilized DNA substrate close to the TelK target region. Characterizing PIFE of our DNA substrate in the presence of TelK will tell us if TelK binding to the DNA substrate occurs within a 0-3 nm range of either cyanine dye, or if TelK binding to the DNA clears this distance on either side of each dye. We first monitored the intensity-time traces of the Cy3 label on our surface-immobilized DNA substrates with 532-nm excitation, which showed no noticeable intensity fluctuations (**Figure 5-10a**). This was repeated using 633-nm excitation to monitor Cy5, which showed similarly stable intensity-time traces (data not shown). Next, we introduced 100 nM TelK into our flow channel and monitored the intensity-time traces of the Cy3 molecules via 532-nm excitation (**Figure 5-10b**), and of the Cy5

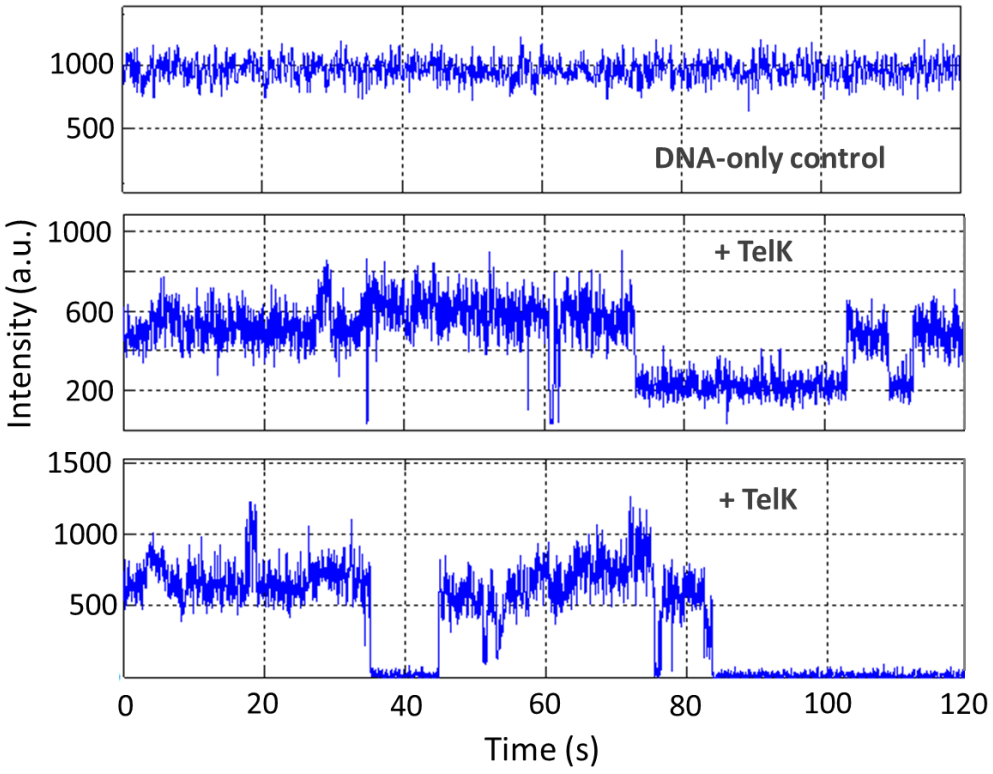

Figure 5-10. Representative PIFE and PIFD traces. (a) Labeled DNA in the absence of TelK shows a steady intensity-time trace for Cy3 fluorescence. (b) Addition of TelK causes multi-state fluctuations in Cy3 and (c) Cy5 intensity.

molecules via 633-nm excitation (**Figure 5-10c**). While the DNA substrate in the absence of TelK showed no PIFE, addition of TelK resulted in significant intensity fluctuations that we attributed to PIFE due to TelK proximity to the dyes. In the absence of TelK, only 4.9% of Cy3 and Cy5 traces showed any intensity fluctuations that resembled PIFE, which can be attributed to dye blinking behavior. However, in the presence of TelK, 86.0% of Cy3 molecules and 81.7% of Cy5 molecules showed PIFE. The PIFE effect persisted for well over 20 minutes for the case of each dye.

Interestingly, while the PIFE effect suggests that protein proximity causes an *increase* in dye intensity, we often observe multi-state intensity fluctuations that both increase and decrease as in **Figure 5-10 b, c**. Recent unpublished results suggest that a protein-induced fluorescence depression (PIFD) effect may also occur for certain protein systems, namely multi-proteins systems that bind as dimers or oligomers in the vicinity of cyanine dyes (personal communication with Helen Hwang). Since our previous studies strongly suggest that TelK can bind as a dimer to both target and non-target DNA, the observance of PIFD in over 80% of our Cy3 and Cy5 traces is not surprising. Unfortunately, PIFD has not yet been characterized to enable quantification of the number of protein units necessary to create the intensity depressions we observe in our assay. It is possible that intensity depressions are being caused by binding of a second TelK monomer after a first has already caused PIFE. It is also possible that intensity depressions are caused by direct binding of single or multiple TelK monomers directly onto the cyanine dyes. Further development of both the PIFE and PIFD phenomena must be undertaken before they can be used to characterize the binding characteristics of multi-protein complexes such as TelK. Nonetheless, our results are useful to confirm that TelK binding to our DNA substrate occurs in the vicinity of the Cy3- and Cy5-labeled target site.

5.8 TelK sensitivity to labeling and force

In **Chapter 4**, we showed that TelK is very sensitive to small forces applied to its DNA substrate. In this chapter, we have shown that that our DNA labeling approach, which places Cy3 and Cy5 dyes 38-bp apart on DNA, inhibits TelK-induced hairpin formation and possibly also de-stabilizes the formation of a cruciform DNA intermediate structure. Because the TelK dimer footprint is 56-bp in length, is possible that changing the structure of DNA by incorporating fluorescent dyes anywhere within the 56-bp footprint could inhibit the formation of DNA hairpins by TelK, and affect the formation of any DNA cruciform transition.

The reasons for TelK sensitivity to such small-scale changes in DNA structure are unclear. Because TelK is responsible for large-scale DNA rearrangements without the input of external energy cofactors, it is possible that TelK is more sensitive to changes in local DNA structure than most proteins. TelK is a protein that has many structural and sequence similarities to the tyrosine recombinase (Y-recombinase) family of proteins. The y-recombinase family of proteins is responsible for performing energy-expensive DNA rearrangements through cutting of both DNA strands allowing for controlled changes in DNA conformation, and finally re-ligation of the DNA strands without the aid of high-energy cofactors such as ATP, much like the process of TelK hairpin formation. Consequently, much ambiguity exists about how proteins in the y-recombinase protein family manage to perform these sterically arduous DNA transformations and obtain 100% conversion of substrate to product as well. The reasons for TelK's heightened sensitivity to changes in its DNA substrate may be due to the unique mechanisms it uses to circumvent a dependence on ATP for catalysis at the DNA target site.

Unfortunately, to probe the DNA transition state with FRET, the dyes must be located at least within 20-bp of each other to produce a measurable FRET signal during the formation of a 22-bp cruciform. Our data seem to suggest that incorporating dyes within the 56-bp TelK footprint greatly alters TelK activity. Therefore, it is unfortunately not possible to accomplish both requirements simultaneously.

An alternate approach will be needed to probe TelK hairpin formation. One possible approach may be to label different TelK subunits, instead of labeling the DNA substrate. If dyes are placed strategically along the TelK surface, we may be able to monitor the internal dynamics of TelK as it undergoes the process of hairpin formation at the single-molecule scale. This can provide insights as to how TelK rearranges its DNA substrate, as we monitor the proximity FRET dyes that flank the TelK catalytic domain throughout the hairpin-forming process. Another approach to more carefully characterize the role of DNA force on TelK hairpin-forming ability would be to use magnetic traps to form DNA tethers. Magnetic traps allow for the application and monitoring of smaller force increments on tethered DNA. A magnetic trapping assay would enable us to determine the precise force at which DNA tethers can no longer be formed by TelK, and give us a better estimate of the energy barrier that inhibits TelK hairpin formation in our optical trap assay. Magnetic traps also provide the ability to apply torsion to our DNA tether. Because TelK shares many similarities to the topology-sensitive topoisomerase and tyrosine recombinase protein families, it would be interesting to determine if TelK activity depends on DNA topology. This latter assay may also provide insights into the reaction pathway of TelK-catalyzed DNA hairpin formation.

5.9 Materials and methods

Tethered particle microscopy

The TPM assay was performed on an objective-type TIRF microscope with 532 nm laser excitation, as described in **Chapter 2**. We incubated fluorescent anti-digoxygenin microspheres (Spherotech, Lake Forest, IL, HFP-0856-5) with 1 nM DNA containing the TelK target site in the center, a biotin on the 5' end, and a digoxigenin at the 3' end. The target DNA substrate for use in our TPM assay was synthesized based on the 2.9-kbp origin pSKN plasmid harboring the TelK target site. Our target-site containing dsDNA substrates were synthesized using a 5'-mono-biotinylated forward and a 5'-mono-digoxigenated reverse PCR primer (Integrated DNA Technologies, Coralville, Iowa) to amplify the desired 3.5 kb sequence of the pSKN. A high fidelity Phusion PCR kit (F-513S, Finnzymes, Woburn, Massachusetts) was used to carry out the PCR amplification. Subsequent DNA purification was performed with a Qiagen PCR purification kit with a 50-µl DNA elution volume. The purity of our DNA product was confirmed by running a 1% agarose gel.

We then constructed a microfluidic chamber formed by a glass slide and a glass coverslip held together with double-sided tape. This chamber was then passivated by flowing in a 33 µM 1:100 solution of BSA and neutravidin in water (Thermo Scientific, Waltham, MA, USA, # 31000). We then introduced our DNA-microsphere solution into our chamber and let this solution incubate for 5 minutes, enabling our biotinylated DNA substrates to stick via biotin-neutravidin interactions. We achieved buffer dexoygenation by adding an oxygen scavenging system (100 nM glucose oxidase, 1.5 mM catalase, 56 mM glucose) to TelK buffer (20 mM Tris-HCl, 50 mM potassium glutamate, 1mM DTT, 0.1 mM EDTA).

We then imaged these surface-immobilized DNA-microsphere complexes using an objective-type TIRF microscope as described in **Chapter 2**. Next, we flowed in 100nM of unlabeled TelK, and recorded the disappearance of fluorescence as a marker for TelK hairpin formation activity at a given DNA molecule position.

TelK FRET substrate synthesis

The DNA substrate used for our FRET assays was synthesized by separately annealing three dsDNA segments, left handle, right handle, and central part, and subsequently ligating them to form the final substrate. All oligonucleotides were purchased from IDT (Integrated DNA Technologies, Coralville, IA).

First, we combined our left handle, right handle, and central part oligos together into three separate 50 µM annealing reactions in T50 buffer (20 mM Tris-HCl, 50 mM NaCl, pH 8.0). Each reaction was heated to 90°C in a heat block and left to cool to room temperature throughout the course of 4 hours. The sequence of the DNA substrates for each of the three segments is as follows:

Left Handle

5- CCCAAGCTCTAGAGTCGACCCGGGTCGACCTGCAGGCATGCAAGCTAGCTTTATCAGCAC -3
+
3- GGGTTCGAGATCTCAGCTGGGCCCAGCTGGACGTCCGTACGTTCGATCGAAATA -5

Right Handle

5- ATAGGATCCACTAGTTCTAGAGCGGCCGCCACCGCGGTGGAGCTCCAGCTTTTG -3
+
3- CACGACTATCCTAGGTGATCAAGATCTCGCCGGCGGTGGCGCCACCTCGAGGTCGAAAAC -5

Central part of ligation:

5- cy3ACAATTGCCCATTATACGCGCGTATAATGGACTATTGTGTGCTG -3
+
3- GTCGTGTGTTAACGGGTAATATGCGCGCATATTACCTGATAACAcy5 -5

Next, we combined all three annealed DNA substrates in a 1:1:1 ratio with a final molar concentration of 1 µM for ligation with T4 DNA ligase (New England Biolabs, Ipswich, MA, Catalog # M0202T). The ligation reaction was stopped by heating to 10 minutes at 65°C and run through a Qiagen PCR purification kit (28104, Qiagen, Valencia, CA, USA) with a 20-µl DNA elution volume. We confirmed the purity and expected length of our product by running it on a 3% agarose gel and staining our substrate with EtBr. The length of our final ligation product ran at a length of 159-bp, as expected.

TIRF Microscopy

All TPM experiments were performed on an objective-type TIRF microscope with 532 nm laser excitation, and all PIFE and FRET data was acquired on a prism-type TIRF microscope with either 532 nm or 633 nm excitation. Data collection and analysis were performed as detailed in **Chapter 2**.

5.10 Acknowledgements

We gratefully acknowledge the guidance provided by Professor Toshio Yanagida's laboratory at Osaka University for guidance in protocol development and for allowing us to use their objective TIRF setup to perform our TPM assays. We would particularly like to thank Komori Tomotaka and Thomas Martin. We are also thankful for the guidance provided by Professor Taekjip Ha's group in the design of the TelK DNA substrate, and in assistance with experimental techniques. We would particularly like to thank Reza Vafabakhsh, Prakrit Jena, and Helen Hwang for assistance with the experimental design presented in this chapter, and to Taekjip Ha and his group for the generosity in allowing us to use the Ha lab TIRF instruments.

5.11 Chapter references

1. Grindley, N.D.F., K.L. Whiteson, and P.A. Rice, *Mechanisms of site-specific recombination.* Annual Review of Biochemistry, 2006. **75**: p. 567-605.
2. Huang, W.M., et al., *Protelomerase uses a topoisomerase IB/Y-recombinase type mechanism to generate DNA hairpin ends.* Journal of Molecular Biology, 2004. **337**(1): p. 77-92.
3. Witz, G., G. Dietler, and A. Stasiak, *Tightening of DNA knots by supercoiling facilitates their unknotting by type II DNA topoisomerases.* Proceedings of the National Academy of Sciences of the United States of America, 2011. **108**(9): p. 3608-3611.
4. Aihara, H., W.M. Huang, and T. Ellenberger, *An interlocked dimer of the protelomerase TelK distorts DNA structure for the formation of hairpin telomeres.* Molecular Cell, 2007. **27**(6): p. 901-913.
5. Ha, T., *Single-molecule fluorescence methods for the study of nucleic acids.* Curr Opin Struct Biol, 2001. **11**(3): p. 287-92.
6. Hwang, H., H. Kim, and S. Myong, *Protein induced fluorescence enhancement as a single molecule assay with short distance sensitivity.* Proc Natl Acad Sci U S A, 2011. **108**(18): p. 7414-8.

Chapter 6. Visualization of bio-nano interactions

Current experimental tools have been unable to probe the structure of biomolecules on the surface of nanomaterials. This chapter outlines the development of a fluorescence microscopy-based platform which allows spatial and temporal resolution of biomolecular structure and activity at this interface. Carbon nanotube-encapsulated nucleic acids, designed to explore sequence-dependent affinity to the nano-surface and bioavailability upon interactions with proteins, are observed via total internal reflection (TIR) microscopy at the single-molecule level. The oligonucleotides are found to demonstrate cooperative exfoliation from the nano-surface with sequence specificity. DNA-protein interactions are measured at the nanotube surface, exhibiting 50% arrest of protein function at a distance of 1-nm. This platform, validated by several example applications, is generally applicable for nano-bio systems to answer questions of toxicity, structure, molecular recognition, and enables incorporation of nanoparticles into DNA-origami structures via self-assembly.

6.1 Biocompatible single-wall carbon nanotubes

The use of nanoparticles such as single-wall carbon nanotubes (SWNT) in biological and medical sciences is a new and promising direction for sensing, therapeutics, and diagnostics [1-4]. However, as with most novel tools in biological and medical research, questions of safety and toxicity are numerous, and often difficult to address or predict [5]. Furthermore, predicting the interactions between nanoparticles and biomolecules is difficult in the absence of well-established precedent experiments.

There are many pros and cons to the use of SWNT for biological applications. Primarily, SWNT emit light in the near-infrared (nIR) window of 800-1600 nm, where tissues and cells are most transparent. However, as is the case with most nanoparticles, SWNT are strongly hydrophobic, a property that makes them incompatible in the aqueous environments of biological

molecules. The large degree of SWNT hydrophobicity gives rise to much of the toxicity associated with SWNT. Clearly, in order to use SWNT for biological applications, their hydrophobicity and toxicity must be both overcome and characterized. To overcome the toxic nature of SWNT, researchers have begun encapsulating SWNT with biologically-friendly molecules to create monodisperse SWNT samples that are nontoxic and water-soluble. Common examples of biopolymers used to encapsulate SWNT include surfactants, lipids, synthetic polymers, and single-stranded DNA (ssDNA) [6-9]. Each biopolymer has unique advantages associated with its use as a dispersion facilitator. Sodium dodecyl sulfate (SDS) encapsulation is quick and reliable, while ssDNA encapsulation efficiency is strongly dependent on ssDNA sequence and length, but this added binding specificity can be exploited to purify SWNTs of different chiralities or diameters [10, 11].

The focus of the final two chapters will be to develop single-molecule assays to probe biomolecule behavior on SWNT surfaces to better understand the mechanism of DNA and protein interactions on ssDNA-solubilized SWNT (DNA-SWNT). We use a standard probe-tip sonication method to encapsulate HiPCO SWNT with several different ssDNA substrates [12]. **Figure 6-1** illustrates the marked difference in SWNT solubility prior to SWNT encapsulation by ssDNA. In this example, we mix HiPCO SWNT with three variants of $(GT)_{15}$ ssDNA: unlabeled $(GT)_{15}$, $(GT)_{15}$ with a 3'-terminal Cy3, and $(GT)_{15}$ with a 3'-terminal Cy5. Though the ssDNA sequences used throughout chapter 6 and 7 vary slightly, the same encapsulation protocol is used throughout.

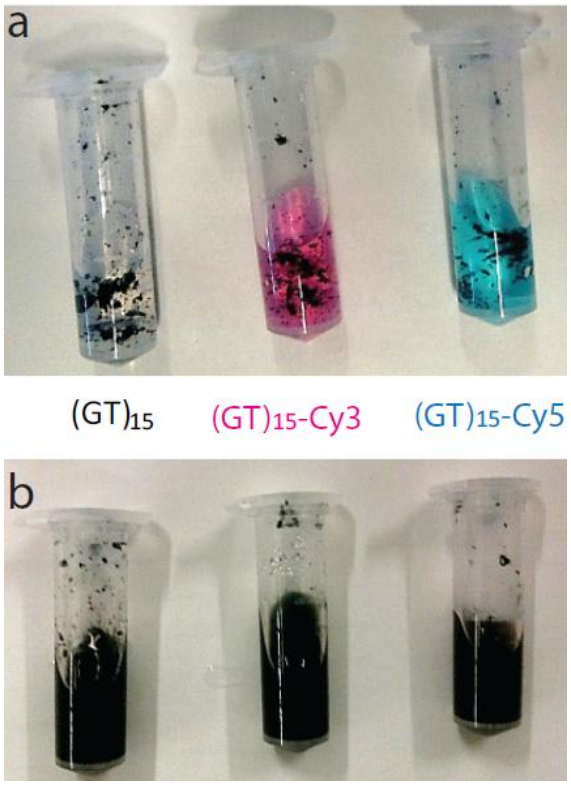

Figure 6-1. Monodispersed ssDNA-wrapped SWNT via sonication. (a) Water-insoluble HiPCO SWNT mixed with a 2:1 mass ratio of DNA:SWNT. From left to right: SWNT with $(GT)_{15}$ (clear), Cy3-labeled $(GT)_{15}$ (pink), and Cy5-labeled $(GT)_{15}$ (blue) ssDNA (b) SWNT become encapsulated with ssDNA and soluble in 100mM NaCl water after 2 minutes of probe-tip sonication at 10W power.

6.2 TIRF-based imaging platform for nano-bio interactions

Although many tools exist to characterize both biomolecules and nanomaterials, these methods are currently unable to give a detailed picture of biomolecular structure at the nano-bio interface [13]. As a result, bioavailability, toxicological effects, and basic molecular structure and conformation of biomolecules on nanoparticles remain unclear and leaves us ill-equipped to predict the interactions of nanomaterials with living organisms and their components [14]. Furthermore, these ambiguities limit the use of biomolecules such as DNA, which is also a

useful nanomaterial, for the integration of nanoparticles in the DNA-templated design of nanostructures.

A common tool to study individual biomolecules and their interactions in vitro and in cell-free environments is single-molecule total internal reflection fluorescence microscopy (sm-TIRF) [15]. Imaging with sm-TIRF combines nanometer spatial resolution and millisecond temporal resolution with the ability to simultaneously detect hundreds of multi-component DNA-protein complexes interacting in a microfluidic chamber. To gain a better understanding of the interactions of proteins and DNA on SWNT surfaces, we developed a sm- TIRF-based platform to study the dynamic behavior of biological molecules in the immediate vicinity of a SWNT. Application of this platform to the study of DNA-SWNT enables us to probe the structure and hybridization potential of ssDNA on a nanotube surface. Currently, it is unclear if the ssDNA used to solubilize SWNT is available for interactions with other biomolecules. If so, does the

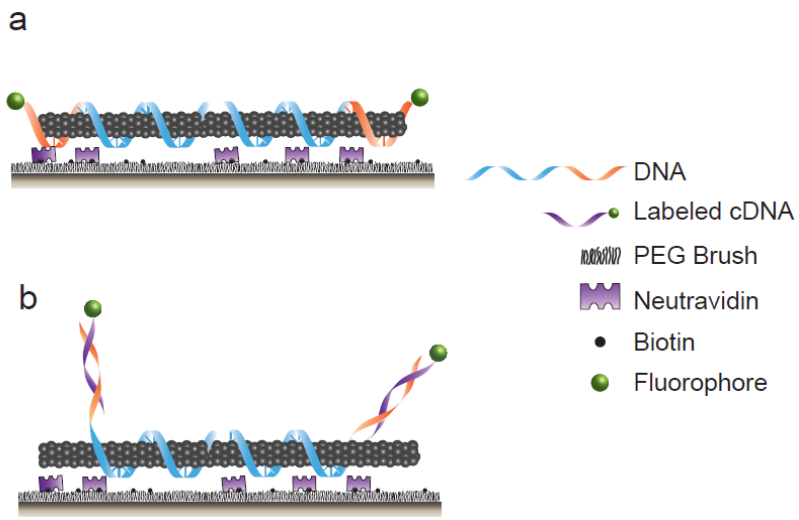

Figure 6-2. Visualization of DNA-SWNT with TIRF. (a) SWNT solubilized with fluorophore-labeled ssDNA is deposited onto the PEG surface via Neutravidin-SWNT nonspecific adhesion (b) fluorophores can be incorporated onto DNA-SWNT for visualization via *in situ* hybridization by a fluorophore-labeled oligonucleotide complementary to the ssDNA wrapping the SWNT.

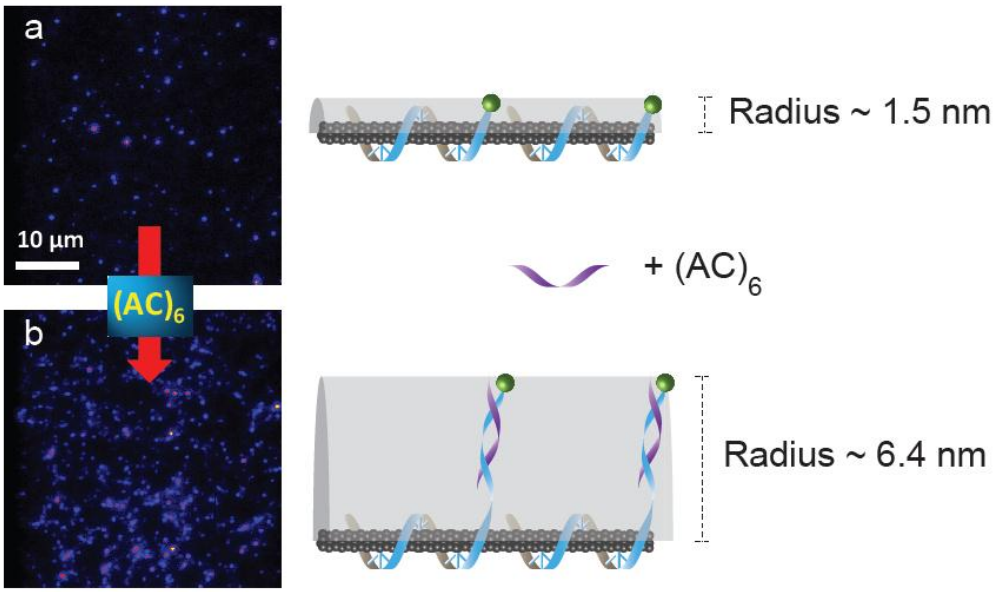

Figure 6-3. Quenching of fluorophores on the SWNT surface. (a) Few fluorescent objects are detected when Cy3-labeled $(GT)_{15}$ ssDNA is used to solubilize SWNT, due to fluorophore proximity to and stacking on the SWNT surface. (b) Hybridizing a strand complementary to $(GT)_{15}$ causes duplex formation and removal of the fluorophore from the SWNT surface by nearly 4-fold. Post-hybridization, many more fluorescent objects are observed due to fluorophore de-quenching.

DNA bioavailability change when it interacts with the SWNT, and if so, to what extent? Questions of SWNT toxicity are also crucial for the design and implementation of DNA-SWNT-based biotechnologies. Unfortunately, much ambiguity remains regarding DNA-SWNT toxicity, particularly at the single-molecule scale. Are DNA-binding proteins able to perform their biological functions on DNA substrates on a SWNT surface? Our TIRF-based platform allows us to probe the activity of proteins at discrete distances from the DNA-SWNT, and helps us determine whether protein-DNA interactions are hindered by the proximity of a SWNT.

DNA-SWNT were immobilized on a PEGylated microfluidic slide surface via nonspecific SWNT-neutravidin interactions (**Figure 6-2**). The SWNT-neutravidin interactions were strong enough to withstand the laminar forces associated with buffer exchanges in the

microfluidic channel, which were necessary to change experimental conditions. This surface-immobilization protocol was used for all DNA-SWNT variants throughout this chapter. In order to visualize surface-immobilized DNA-SWNT with sm-TIRF, the ssDNA on DNA-SWNT was tagged either directly by incorporating a fluorophore into the ssDNA used to solubilize the SWNT (**Figure 6-2 a**), or by hybridizing the ssDNA with a complementary strand (**Figure 6-2 b**) that is terminally labeled with an organic fluorophore. Previous studies have shown that quenching of organic fluorophores occurs as a function of proximity to the surface of SWNT [16], possibly due to the stacking of aromatic cyanine fluorophores onto the planar sp^2-hybridized carbons on the SWNT surface. Our first attempt to visualize SWNT by incorporating a fluorophore directly into the ssDNA enabled us to observe this quenching phenomenon. **Figure 6-2 a** shows only sparse DNA-SWNT fluorescent spots. In an attempt to remove the fluorophore from the quenching radius of the SWNT, we hybridized an unlabeled complementary DNA oligonucleotide to the DNA-SWNT *in situ*: To surface-immobilized $(GT)_{15}$-Cy3 SWNT, we added $(AC)_6$, and observed strong de-quenching of the Cy3 fluorophores as a result of duplex formation at the 3' end of $(GT)_{15}$-Cy3. Because the complementary $(AC)_6$ is not fluorescently labeled, we confirm that our increased fluorescence signal is only due to duplex-mediated de-quenching. We estimate the distance of the fluorophore from the surface of the SWNT to increase from 1.5 nm to 6.4 nm upon hybridization, which de-quenches $(GT)_{15}$-Cy3 by 520% (**Figure 6-3**). Therefore the visualization scheme presented in **Figure 6-2 a** is not optimal for the visualization of DNA-SWNT. We presume that a physical interaction, such as pi-pi stacking, is necessary between the fluorophore and the SWNT for quenching to occur.

To quantify the number of DNA duplexes formed per diffraction-limited fluorescent SWNT spot, we exploited the quenching properties of organic dyes. In this example, we

solubilize SWNT with $(GT)_{15}$-Rnd1 ssDNA, where Rnd1 is a 16-nucleotide extension as detailed in **Materials and Methods**, and deposit these solubilized SWNT onto a PEG slide via nonspecific neutravidin-SWNT interactions by incubating the DNA-SWNT in the microfluidic channel for 15 minutes. Longer incubation times did not lead to more DNA-SWNT surface-immobilization. Each of our experiments included imaging of a control channel in which only neutravidin was deposited onto the PEGylated slide, to compare the emission from surface impurities to our sample. A slide with only these DNA-SWNT deposited onto the PEGylated surface showed a few fluorescent spots, due to surface impurities and inhomogenous coating by the PEG layer (**Figure 6-4 a**). The SWNT become visible only when adding a fluorescently-labeled complementary oligonucleotide (cRnd) to the Rnd extension due to oligonucleotide hybridization and duplex formation (**Figure 6-4 b**). The sm-TIRF image in **Figure 6-4 b** shows a typical field of view, with fluorescent DNA-SWNT ranging in length from ~200 nm (observed as a round diffraction-limited spot) to ~ 1.5 μm in length. This length distribution is consistent with atomic force microscope (AFM) measurements of our DNA-SWNT samples as detailed in the AFM imaging section below. Therefore, by counting the number of cyanine dye photobleaching steps per SWNT spot, we determined the number of duplexes formed per SWNT observed (**Figure 6-4 c**). It is worth noting that the DNA-SWNT visualization approach outlined in **Figure 6-2 b**, visualization via hybridization of a labeled complimentary strand, only enables us to monitor duplexes that successfully form on the SWNT. This method ignores the ssDNA molecules wrapping the SWNT, since the wrapping ssDNA is unlabeled. However, this approach is optimal for studies involving DNA duplexes on SWNT surfaces since it enables us to consider only fully-formed DNA duplexes in our analysis. This approach is more reliable for studies involving DNA duplexes compared with direct labeling of the wrapping ssDNA as outlined in

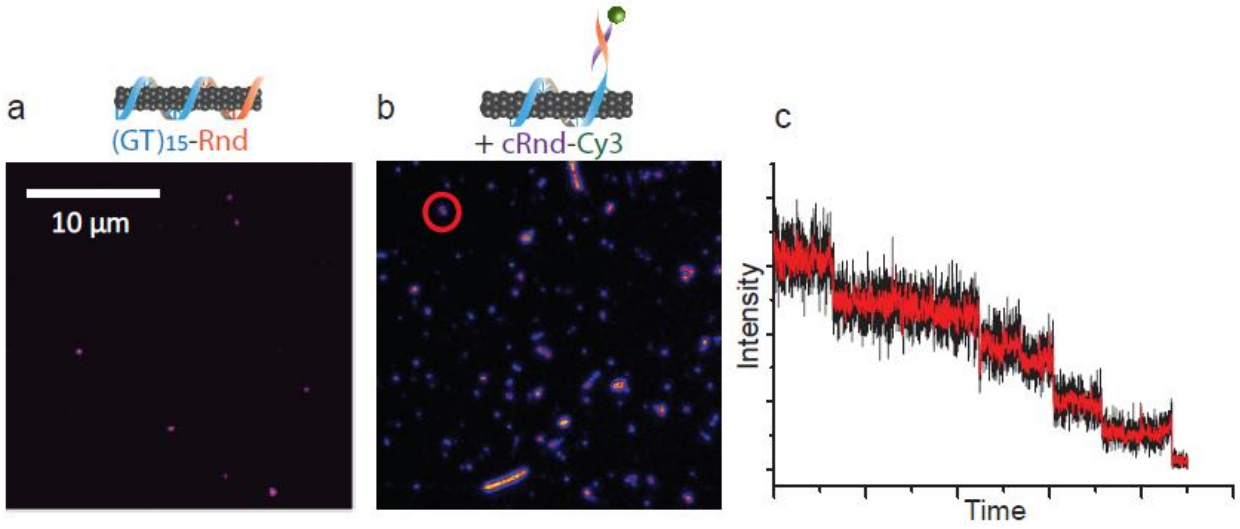

Figure 6-4. Quantification of duplexes per DNA-SWNT. (a) Very few fluorescent spots are observed when imaging $(GT)_{15}$-Rnd SWNT on a passivated surface. (b) Addition of Cy3-cRnd enables visualization of DNA-SWNT via TIR. Cy3 photobleaching steps can be identified in the intensity-time traces of individual spots, and are used to quantify the number of duplexes formed per fluorescent spot.

Figure 6-3a. Direct ssDNA labeling introduces fluorescence quenching into our visual output, therefore we cannot know with certainty if a fluorescent spot is an unquenched fluorophore or a duplex when using direct ssDNA labeling. Since the process of quenching and de-quenching is dynamic and interferes with our ability to quantify changes in fluorescence based on a single parameter such as DNA hybridization (**Section 6.3**) or protein activity on a DNA duplex (**Section 6.5**), we use the visualization scheme presented in **Figure 6-3a** for our studies involving DNA duplexes on a SWNT surface. We use our direct ssDNA labeling visualization scheme for studies involving only the wrapping ssDNA (**Section 6.4**). For both visualization schemes, ur analysis enabled simultaneous monitoring of hundreds of fluorescent DNA-SWNT within a microfluidic channel by combining spot and step counts.

6.3 Cooperative DNA hybridization occurs on a nanotube

Previous studies have shown that the function of biological molecules such as DNA can be significantly altered when they interact with nanoparticles such as SWNT [17,18]. Knowing that it is possible to form DNA duplexes on the surface of a SWNT by hybridizing an oligonucleotide complementary to the ssDNA on the SWNT, we then explored the hybridization behavior of different complementary oligonucleotides to different parts of the ssDNA. First, we explored the sequence-dependence of this hybridization phenomenon. Next we explored the cooperativity of hybridization when oligonucleotides were added to both ends of the ssDNA simultaneously.

We solubilized SWNT with three different wrapping ssDNAs, as described in **Materials and Methods**. These ssDNA strands can be described by the nomenclature $(GT)_{15}$-Rndn, where Rnd is a 16-nucleotide random DNA sequence that has been cyclically permutated n = 1, 2, 3 times to generate three different "Rnd" extensions that contain the same nucleotides but in different order. We subsequently immobilized the DNA-SWNT on our Polyethylene Glycol (PEG)-coated surface and introduced complementary DNA oligonucleotides (cDNA) that have been labeled by a Cy3 or Cy5 fluorescent tag either at the 5' or 3' end of the oligonucleotide. Here, we compared the hybridization efficiency of $c(GT)_{15}$-Cy5 versus cRnd-Cy3 for three different iterations of cRnd. We introduced both c(GT)15-Cy5 and cRnd-Cy3 simultaneously and quantified the number of hybridized cDNA molecules by sequentially imaging Cy3 emission from $c(GT)_{15}$ and Cy5 emission from cRnd. Because each DNA wrapping the SWNT offers one potential binding site for each cDNA oligonucleotide, the observed fluorescence is a direct measure of the hybridization efficiency and is also inversely proportional to the affinity of that DNA segment for the SWNT surface.

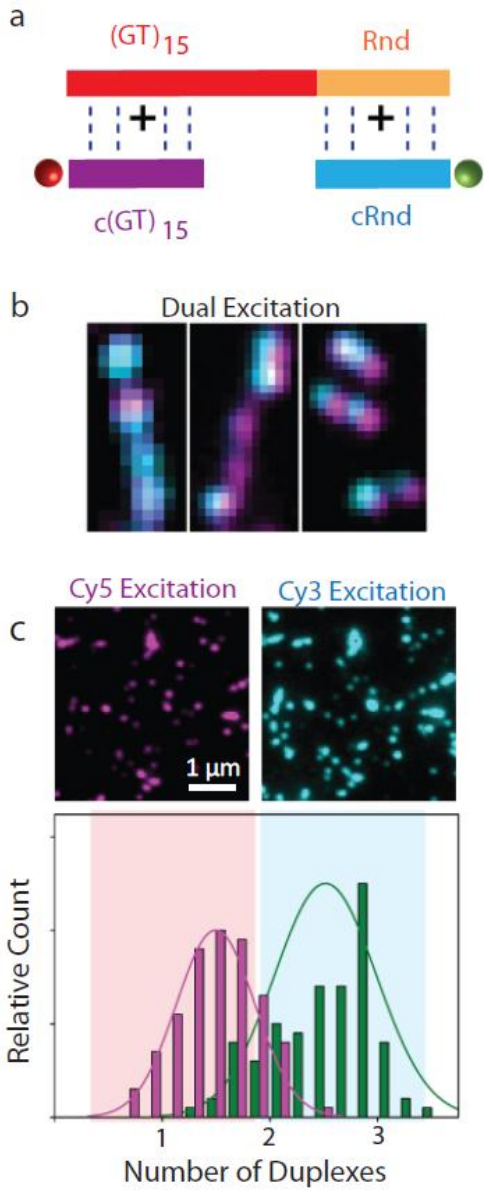

Figure 6-5. Hybridization efficiency on SWNT surface. (a) Schematic of $(GT)_{15}$-Rndn DNA used for SWNT solubilization, and complementary labeled oligonucleotide hybridization partners. (b) Overlay of sm-TIRF image of DNA-SWNT hybridized with both hybridization partners, viewed with Cy3 and Cy5 excitation. (c) Relative count of $c(GT)_{15}$ (purple) and cRnd (green) .

Upon dual imaging, we consistently observed 67% more fluorescence from cRnd1 than from $c(GT)_{15}$, indicating a 67% stronger affinity of $(GT)_{15}$ for the SWNT than Rnd1 since the latter part of the ssDNA is less available for hybridization by a complementary oligonucleotide (**Figure 6-5**). We repeated the same experiment for all three iterations of Rndn and observed a similar hybridization discrepancy between Rndn and $(GT)_{15}$. We hypothesize that the binding affinity of ssDNA to the SWNT surface is dictated by the nucleic acid - SWNT surface interactions that are specific to each sequence. Therefore, the primary determinant of hybridization potential is the binding strength between the DNA and the SWNT. Next, we tested the effect of DNA hybridization as a function of oligonucleotide order of addition. Duplex formation is ordinarily a bimolecular reaction between two complementary strands, but we find the hybridization to different sections of a nanotube-adsorbed DNA substrate to demonstrate positive cooperativity. For a ssDNA sequence used to wrap SWNT with distinct 5'

$(GT)_{15}$ and 3' (Rnd) regions (**Figure 6-6 a**), duplex formation with a Cy3-labeled complementary strand to $(GT)_{15}$, $c(GT)_{15}$, can occur at multiple $(GT)_{15}$ sites along a nanotube. We find that hybridizing to Rnd1 on $(GT)_{15}$-Rnd1 forms an average of 2.3 duplexes per nanotube when only cRnd1 is available for hybridization (**Figure 6-6 b**). However, if complementary nucleotides are available for duplex formation at both ends of the ssDNA strand, then the presence of unlabeled $c(GT)_{15}$ hybridizing to the 5' end at $(GT)_{15}$ significantly increases the probability of duplex formation by cRnd1 at the 3' end, Rnd1 (**Figure 6-6 c**). We detect a 32% increase in the number of Rnd1 duplexes when $c(GT)_{15}$ is hybridizing to nanotube-adsorbed $(GT)_{15}$-Rnd1. This cooperativity is not observed in the absence of the nanotube nor is it due to intrinsic differences in the 5' and 3' end of ssDNA or the specific oligonucleotide sequence used (data not shown). We suggest that this hybridization cooperativity is due to a change in the way the entire ssDNA strand wraps around the SWNT whenever a part of it hybridizes to a complementary oligonucleotide. For instance, binding of $c(GT)_{15}$ to the 5' end of the ssDNA could shift the positions of all the downstream ssDNA bases such that it decreases the stability of the entire ssDNA strand on the SWNT. This would facilitate binding of cRnd1 at the opposite end of the ssDNA strand. Thus, we observe the nanotube to induce allosteric effects during DNA hybridization, thus illustrating how biological processes can be fundamentally altered by interactions with a nanoparticle surface.

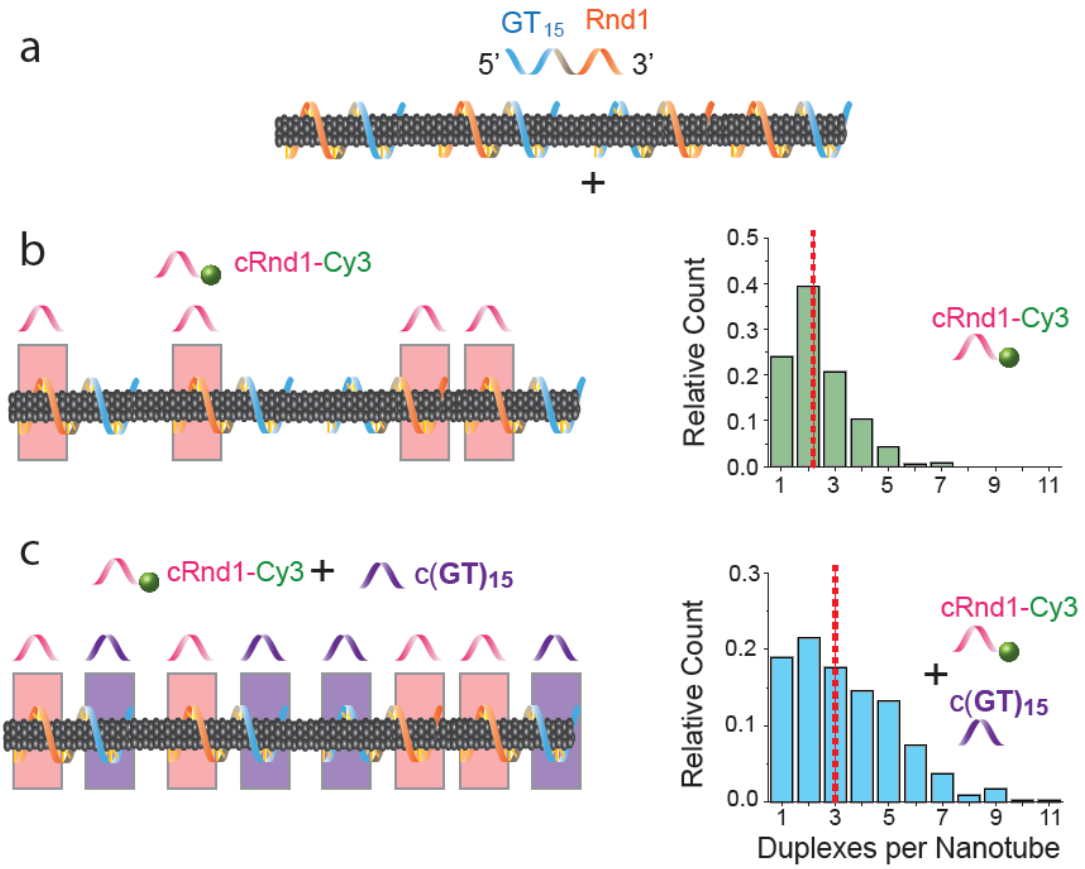

Figure 6-6. Cooperative DNA hybridization on a SWNT surface. (a) $(GT)_{15}$-Rnd1 DNA-SWNT are immobilized on a surface. (b) A Cy3-labeled complement to Rnd1, Cy3-cRnd1, is added to the microfluidic flow chamber and on average 2.3 duplexes form per SWNT. (c) When unlabeled $c(GT)_{15}$ is added at the same time as Cy3-cRnd1, on average 3.1 duplexes form per SWNT, and the distribution of duplexes per SWNT broadens noticeably.

6.4 Nucleotide accessibility on a nanotube probed by S1 Nuclease

A DNA-functionalized nanoparticle is likely to be targeted by nucleases inside a cell, therefore determining the stability of ssDNA used to wrap SWNT in the presence of nucleases is necessary. Previous results on the stability of DNA-nanotube complexes against single-strand nucleases have been inconclusive [19, 20]. Our next experiment resolves these findings by mapping the bioavailability profile of nanotube-bound DNA to S1, a small monomeric nuclease

that non-specifically cleaves ssDNA at the 5' end via nucleotidehydrolase activity, and at the 3' end via phosphohydrolase activity [21]. We prepared ssDNA sequences with Cy3 fluorophore conjugated to an oligonucleotide containing the $(GT)_{15}$ sequence for nanotube-binding and a 20 base random sequence Rnd5. Three variants of SWNT-wrapping DNA were tested for accessibility, where the fluorophore position represented the position along the ssDNA where the accessibility was being probed. **Figure 6-7 a** shows these three variants: 1) A 3' terminal nucleotide on $(GT)_{15}$, tested by $(GT)_{15}$ -Cy3, 2) an internal nucleotide tested by $(GT)_{15}$-Cy3-Rnd, and 3) the 3' terminal end of a random DNA sequence, tested by $(GT)_{15}$-Rnd-Cy3.

We define the accessibility of a nucleotide position by the fractional decrease in fluorescent nanotube density upon oligonucleotide cleavage (**Figure 6-7 b**). We observe a 47% fluorescence reduction due to cleavage of $(GT)_{15}$-Rnd5-Cy3 SWNT. In contrast, the accessibility of the Cy3-labeled 3' terminal nucleotide on $(GT)_{15}$ SWNT is only 18%, indicating that the 3' terminal base is less accessible on $(GT)_{15}$ than on $(GT)_{15}$Rnd5. The accessibility of an internal nucleotide positioned 7 bases from the 3' end of $(GT)_{15}$-Rnd1 SWNT is significantly attenuated at 4.8%, indicating a much stronger protective influence of the nanotube on internally-positioned bases. The distance between the fluorophore and the nanotube, combined with the size of S1 [22] suggests that the nuclease makes physical contact with the nanotube-DNA interface. Combining these results into an accessibility map (**Figure 6-7 c**) indicates that nuclease-induced cleavage of a functionalized nanoparticle can be modulated with the appropriate choice of nucleotide sequence and position observed for DNA hybridization. For applications in which DNA-SWNT are used for *in vivo* imaging or other biomedical applications, these fundamental interactions must be taken into consideration.

6.5 DdeI Activity at the nanotube surface

Protein-DNA interactions are another type of fundamental biological interaction that is often probed in medical and biochemical assays. To extend the use of nanomaterials to probe, target, or otherwise alter these fundamental interactions, the effects of nanoparticle proximity on protein-DNA activity must be better understood. We undertook a series of assays to quantify the behavior of a protein on its DNA substrate, when this DNA substrate was synthesized to be located at a varying distance from the SWNT surface. Nanotubes were encapsulated with an oligonucleotide (GT_{15}-DdeI n bp) containing a Ddel endonuclease target site (CTAAG) when hybridized *in situ* with a Cy3-labeled complementary strand (Cy3-cDdeI-n bp). This protocol

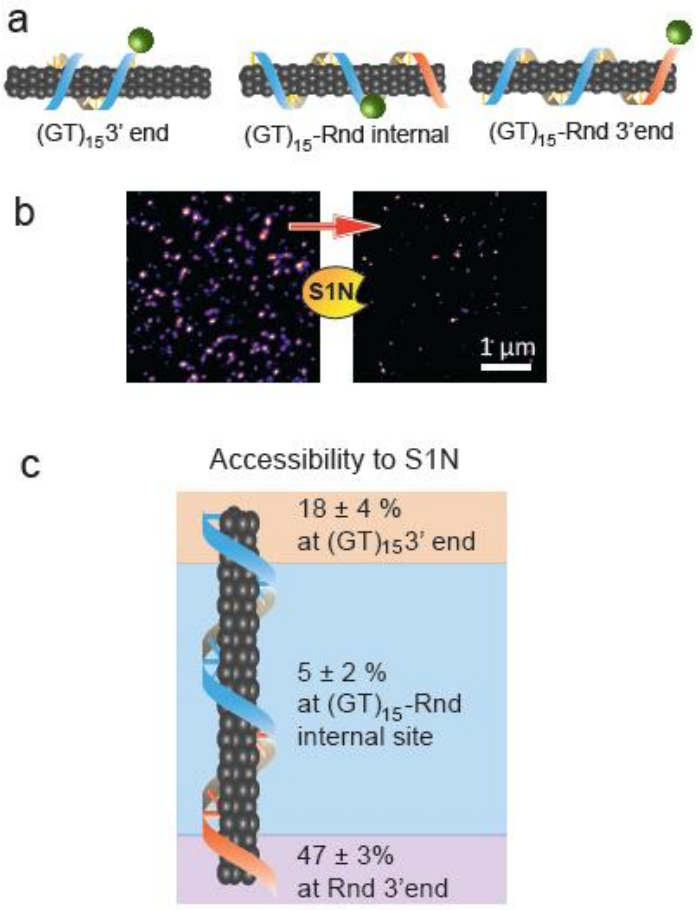

Figure 6-7. S1 Nuclease accessibility to different parts of DNA-SWNT. (a) Schematic of three substrates tested for S1N accessibility – $(GT)_{15}$ 3' end, (GT)15-Rnd internal, and $(GT)_{15}$-Rnd end. (b) TIRF image of S1N activity on $(GT)_{15}$-Rnd 3' end-labeled DNA-SWNT. (c) Summary of S1 accessibility for three tested substrate sites.

allowed us to form duplexes containing the DdeI restriction site n base pairs away from the GT_{15}-nanotube interface with a fluorescent tag at the end of the duplex. Upon incubation with DdeI under standard conditions [23], we observe a decrease in the fluorescent nanotube density due to cleavage of the Cy3-labeled section of DNA downstream from the recognition site (**Figure 6-8 a**). Control assays using DNA duplexes lacking the DdeI target site did not show a decrease in fluorescence after incubation with DdeI. We confirm the presence of the nanotubes themselves by hybridizing the post-reaction complex with a Cy5-labeled complement to GT_{15} (cGT_{15}-Cy5) and recover the initial fluorophore density (data not shown). For nanotubes prepared with DNA sequences of the form $(GT)_{15}$-DdeI-nbp, we quantify the fractional decrease in Cy3-DNA labeled nanotube density after treatment with DdeI for n = 0, 3, 6 and 9 bp (**Figure 6-8 b**). We find that the fraction of duplex DNA target substrate remaining decreases

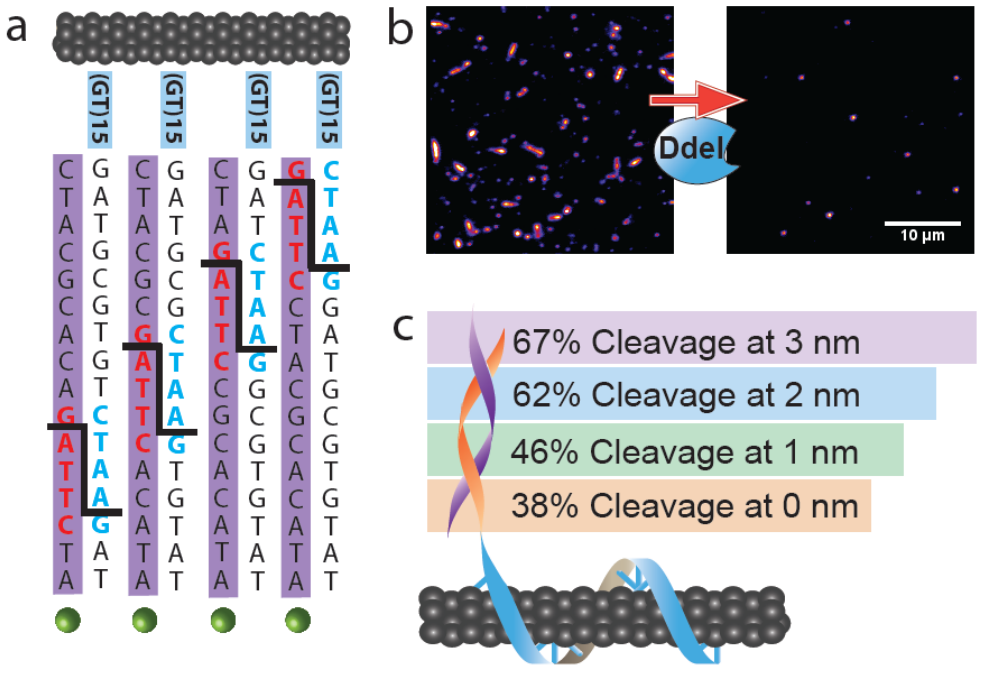

Figure 6-8. DdeI activity at a DNA-SWNT surface. (a) Schematic of the four DdeI DNA-SWNT substrates, with the DdeI target site at 1nm-increments away from the SWNT surface. (b) Representative TIRF image of DdeI activity on DdeI-9 DNA-SWNT. (c) Summary of decreasing DdeI activity on the four DNA-SWNT substrates, as a function of distance from the SWNT surface.

monotonically as a function of increasing distance from the nanotube surface (**Figure 6-8 c**). As this distance dependence is not observed with DNA-only controls (data not shown), we confirm a nanoparticle-induced arrest of protein activity. These results demonstrate that nanoparticle toxicity occurs at a single-molecule level, as the activity of our model protein DdeI decreases as its DNA substrate approaches the surface of a SWNT.

6.6 DNA Origami tethered to DNA-SWNT

Our studies confirm DNA accessibility on the surface of nanoparticles, thereby enabling the use of DNA used for SWNT solubilization for DNA-based nanotechnologies such as DNA origami. DNA origami exploits the exceptional self-assembly properties inherent to DNA base-pairing rules, making DNA a functional nanomaterial in addition to an important biomaterial [24]. DNA accessibility on nanotube surfaces can be utilized to merge the fields of nanoparticle and DNA-based nanomaterial research through sequence-specific hybridization. Recent developments in DNA origami research have provided a foundation for the use of DNA origami in therapeutics and sensing [25, 26], not unlike the use of synthetic nanomaterials in these fields. Therefore, the ability to merge DNA origami nanostructures with functionalized synthetic nanomaterials such as DNA-SWNT can provide an additional approach to the development of nano-scale sensors and therapeutics. We tested our above-described platform for its ability to link DNA-SWNT to DNA origami structures via in-situ hybridization on the surface of our microfluidic chamber.

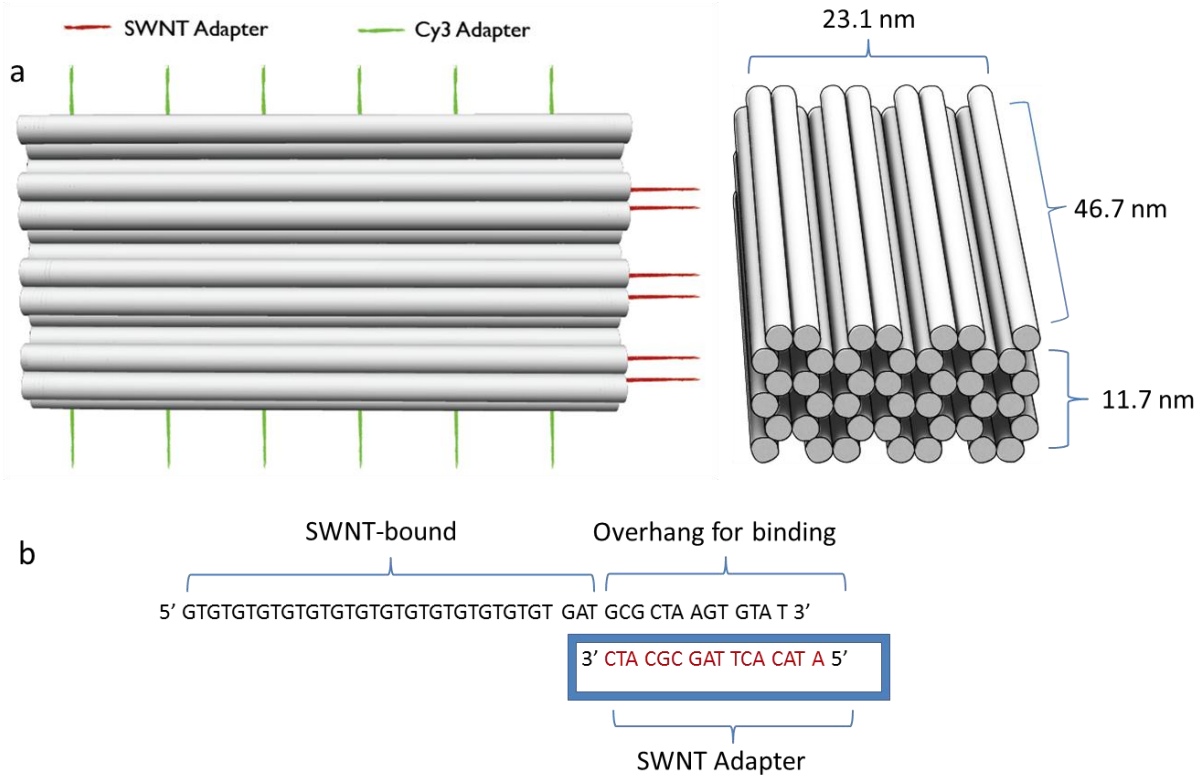

Figure 6-9. DNA Origami substrate design. (a) A 12-barrel DNA origami structure is designed to contain ssDNA adapters to bind Cy3-labeled oligonucleotides, or to bind a complementary ssDNA strand on a DNA-SWNT. (b) Sequence details for origami SWNT adapter binding to the DNA-SWNT overhang for binding.

We designed a 12-barrel DNA origami structure such that it contained two types of ssDNA "adapters" that served as attachment points for complementary DNA hybridization (**Figure 6-9**). Cy3 adapters hang off the side of the origami structure and are available for hybridization by a Cy3-labeled complementary strand that is added after the origami folding. A second set of adapters, the SWNT adapters, hang off the end of the origami barrels and are available for hybridization to DNA-SWNT.

We demonstrate successful linear scaffolding of DNA-origami in a microfluidic flow cell. We show that Cy3-labeled DNA origami can be deposited along the length of a carbon

nanotube via *in situ* complementary DNA hybridization (**Figure 6-10**). Control studies using origami SWNT adapter overhangs that are non-complementary to the ssDNA on the SWNT did not show deposition of DNA origami along the SWNT. This allows us to control the deposition of origami onto a surface-immobilized DNA-SWNT via a fixed attachment point. We have successfully engineered constructs containing protein target sites flanked by DNA-SWNT and origami, in order to assay protein accessibility as a function of proximity to nanostructures. While origami-only structures are susceptible to degradation by endonucleases, origami-DNA-SWNT structures are resistant to such degradation (data not shown). We believe that the size of

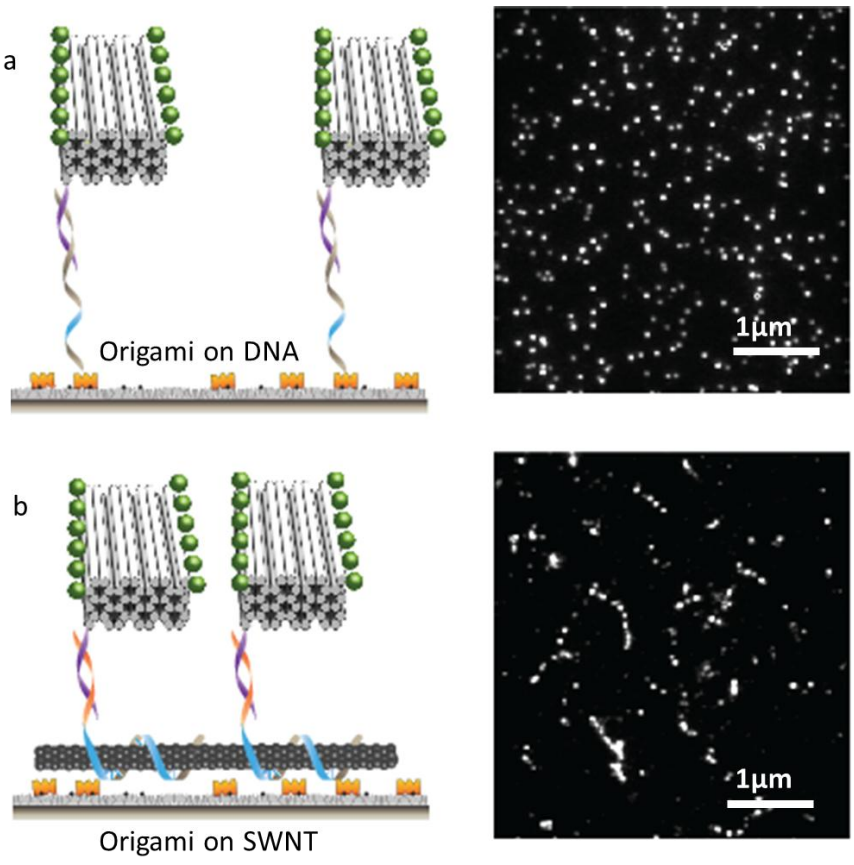

Figure 6-10. Monodispersed ssDNA-wrapped SWNT via sonication. (a) DNA- SWNT immobilized on a passivated surface can be hybridized *in situ* with Cy3-labeled complementary DNA (cDNA), and (b) visualized via TIR

the origami presents a steric barrier for endonuclease access to its target sequence. It is possible that the endonuclease cannot load onto the DNA in the absence of a free DNA end, or that the physical distance between the origami structure and the SWNT is too small for endonucleases to diffuse into. The duplex region between the origami structure and the SWNT surface is 16 bp, or 5.4 nm in length, whereas many small endonucleases have radii in the 2-6nm range, therefore steric inaccessibility is the most likely cause of endonuclease inactivity. This finding provides a promising platform for *in vivo* use of nanotube-DNA origami hybrid nanostructures that are invulnerable to the biochemical defenses of living organisms. Such resistance is crucial for the development of drug delivery nanosystems.

Careful engineering of DNA origami with DNA-SWNT has potential applications for the development of DNA-insulated nanowires, controlled photoactivated release of DNA origami-caged molecules for sm-TIRF, and nanofluidic switches.

6.7 Materials and methods

Buffers and reagents

Sample buffer for fluorescence microscopy: A 50 mM Tris (hydromethyl)aminomethane buffer was used for all experiments described in this chapter. Tris buffer, in conjunction with other imaging buffer components described below, can maintain a stable buffered environment for the study of biomolecules at a pH that is compatiable with maintaining the integrity of the PEG layer (pH >7).

Neutravidin: Neutravidin further reduces non-specific interactions from occurring within the microfluidic channel, while enabling the specific binding of biotinylated DNA substrates or, in our case, DNA-SWNT nonspecific adhesion to the surface. Our experiments use 0.2 mg/mL neutravidin in our standard T50 buffer, which produces DNA-SWNT immobilization for the samples used in the experiments presented in this chapter.

Imaging buffer: Prior to imaging our samples in sm-TIRF, we include a mixture of Glucose Oxidase + Catalase to reduce the concentration of dissolved molecular oxygen (O_2) in our sample chamber buffer. Oxygen has been shown to facilitate the photoactivated degradation of biomolecules when exposed to imaging lasers, and causes faster irreversible photobleaching of organic dyes such as Cy3 and Cy5. Glucose oxidase scavenges oxygen in our buffer by converting glucose into gluconic acid and hydrogen peroxide, thereby decreasing the concentration of dissolved molecular oxygen in our buffers, and enabling longer lifetimes of our organic dyes.

DNA sequence information

DNA oligonucleotides used were purchased from Integrated DNA Technologies (IDT, Coralville, IA).

For Cy3-quenching experiments:

(GT)15+Cy3: 5' GTGTGTGTGTGTGTGTGTGTGTGTGTGTGT Cy3 3'

For DNA-DNA interaction experiments the DNA name and sequences are as follows:

(GT)15+Rnd1: 5’ GTGTGTGTGTGTGTGTGTGTGTGTGTGTGT CTA AGG ATG CGT GTA T 3’

(GT)15+Rnd2: 5’ GTGTGTGTGTGTGTGTGTGTGTGTGTGTGT GAT GCG TGT CTA AGA T 3’

(GT)15+Rnd3: 5’ GTGTGTGTGTGTGTGTGTGTGTGTGTGTGT GAT GCG CTA AGT GTA T 3’

(GT)15+Rnd4: 5’ GTGTGTGTGTGTGTGTGTGTGTGTGTGTGT GAT CTA AGG CGT GTA T 3’

Cy3-cRnd1: 5’ Cy3 ATA CAC GCA TCC TTA G 3’

Cy3-cRnd2: 5’ Cy3 ATC TTA GAC ACG CAT C 3’

Cy3-cRnd3: 5’ Cy3 ATA CAC TTA GCG CAT C 3’

Cy3-cRnd4: 5’ Cy3 ATA CAC GCC TTA GAT C 3’

(GT)15: 5’ GTGTGTGTGTGTGTGTGTGTGTGTGTGT 3’

(GT)30:5’GTGTGTGTGTGTGTGTGTGTGTGTGTGTGTGTGTGTGTGTGTGTGTGTGT GTGTGTGT 3’

Cy5 c(GT)15: 5’ Cy5 TTT TTT CAC ACA CAC AC 3’

Cy3 c(GT)15: 5’ Cy3 TTT TTT CAC ACA CAC AC 3’

For DNA-SWNT and S1 Nuclease studies:

(GT)15+Rnd5+Cy3: 5’ GTGTGTGTGTGTGTGTGTGTGTGTGTGTGT GCG AAT TCA CGG CTA AGC G Cy3 3’

(GT)15+Cy3: 5’ GTGTGTGTGTGTGTGTGTGTGTGTGTGTGT Cy3 3’

(GT)15+Cy3+Rnd1: 5’ GTGTGTGTGTGTGTGTGTGTGTGTGTGTGT GAT GCG /iCy3/ TGT CTA AGA T 3’

For DNA-SWNT and DdeI Restriction Endonuclease studies:

(GT)15+DdeI-9-bp: 5’ GTGTGTGTGTGTGTGTGTGTGTGTGTGTGT GAT GCG TGT CTA AGA T 3’

Cy3-cDdeI-9-bp: 5’ Cy3 ATC TTA GAC ACG CAT C 3’

(GT)15+DdeI-6-bp: 5’ GTGTGTGTGTGTGTGTGTGTGTGTGTGTGT GAT GCG CTA AGT GTA T 3’

Cy3-cDdeI-6-bp: 5’ Cy3 ATA CAC TTA GCG CAT C 3’

(GT)15+DdeI-3-bp: 5’ GTGTGTGTGTGTGTGTGTGTGTGTGTGTGT GAT CTA AGG CGT GTA T 3’

Cy3-cDdeI-3-bp: 5’ Cy3 ATA CAC GCC TTA GAT C 3’

(GT)15+DdeI-0-bp: 5’ GTGTGTGTGTGTGTGTGTGTGTGTGTGTGT CTA AGG ATG CGT GTA T 3’

Cy3 cDdeI-0-bp: 5’ Cy3 ATA CAC GCA TCC TTA G 3’

Control DNA: 5’ Biotin GTGTGTGTGTGTGTGTGTGTGTGTGTGTGT CTA AGG ATG CGT GTA T 3’

Cy3 cDdeI-0-bp: 5’ Cy3 ATA CAC GCA TCC TTA G 3’

DNA-SWNT Preparation

Single-walled carbon nanotubes produced via the HiPCO process were obtained from Rice University. Approximately 0.2 mg DNA was mixed with a w/w excess of SWNT in 800 µL 0.1 N NaCl and ultra-sonicated via probe tip sonicator (Fisher Scientific, Sonic Dismembrator

Model 500, Pittsburg, PA, USA) for two minutes at 10 W in an ice bath. Samples were then centrifuged at 16,000 g for 90 minutes and the supernatant was purified with a Micron YM-100 filter (Millipore, Billerica, MA, USA) to obtain dispersed DNA-SWNT. Samples were resuspended in 20 mM Tris-HCl, 50 mM NaCl, pH 8.0 (T50 buffer) and stored at 4°C. Suspended DNA-SWNT samples are stable for over 5 years.

Slide Preparation and Sample Immobilization

Sample chambers for single-molecule TIRF microscopy were prepared on mPEG-passivated quartz slides with 2% biotin-PEG (21). The PEG surface was coated with 33 nM NeutrAvidin (Thermo, Rockford, IL USA) in 20 mM Tris-HCl, 50 mM NaCl, pH 8.0 (T50) buffer for 10 minutes. DNA-SWNT sample stock concentrations were stored in T50 buffer at 4°C. Dilutions ranging 50 to 500 times of DNA-SWNT stock were incubated on the NeutrAvidin sample for 30 minutes before unbound DNA-SWNT was flushed from the flow chamber with T50. For hybridization in situ, 10 nM fluorophore-labeled complementary DNA in 20 mM Tris-HCl, 200 mM NaCl, pH 8.0 (T200 buffer) was incubated with immobilized DNA-SWNT for ~ 10 minutes before unbound DNA was removed from the slide chamber by washing with T200 buffer twice.

TIRF Microscopy

All fluorescence microscopy experiments of DNA-SWNT were performed on an objective-type TIRF microscope with 532 nm laser excitation or 633 nm laser excitation. Data collection and analysis were performed as detailed in **Chapter 2**.

Data Acquisition

The sm-TIRF data was acquired on an EM-CCD and processed as a stack of 8-bit 512 x 512 pixel grayscale TIFF images, cut in half such that each channel outputs a 512 x 256 region. Each pixel outputs an intensity value ranging from 0 to 255 arbitrary intensity units. To extract regions of interest from the movies representing the fluorescent SWNT, a spot-picking algorithm was employed to detect and identify single molecules. First, a 20-frame intensity average was applied to each movie to reduce the noise intrinsic to our measurements. This averaging makes the resulting image smoother and often eliminates sources of fluorescence from surface impurities, which often photobleach within the first few frames and are averaged out in the 20-frame averaging protocol. Our resulting figure contains diffraction-limited regions of interest corresponding to fluorescent SWNT that are markedly more Gaussian than any single frame, and can be more accurately localized to a point source that is imaged as a 2 x 2 pixel (~140 nm in real-space). We can then identify the location of a fluorescent SWNT and designate the location in each frame of the movie. We can then extract the intensity of each molecule as a function of time from the 512x256 pixel stack that can contain hundreds of molecules.

S1 Nuclease and DdeI Restriction Endonuclease Assay

S1 nuclease (Fermentas, EN0321, Waltham, MA, USA) in 20 mM Tris HCl (pH 7.5), 50 mM NaCl, 0.1 mM ZnCl2 and 50% (v/v) glycerol was diluted 300 times with 6 µL 5X Reaction buffer 200 mM sodium acetate (pH 4.5 at 25°C, 1.5 M NaCl and 10 mM ZnSO4) in 30 µL water for each reaction chamber. Nuclease was left to react with the sample for 15 minutes at room temperature. The reaction was ended by flushing the channel twice with 100 µL T50 buffer. DdeI enzyme (New England Biolabs, R0175S, Ipswich, MA, USA) was diluted 100 fold in

NEBuffer 3 and 50 µL of 1X DdeI was incubated for 15 minutes at room temperature in each flow chamber. The reaction was ended by flushing the channel twice with 100 µL T50 buffer to remove DdeI enzyme.

In Situ Hybridization

DNA-SWNT samples in the microfluidic chamber were incubated with 10 nM complementary ssDNA at room temperature for 10 minutes. Free ssDNA was then removed by flushing the channel twice with 100 µL T50 buffer.

Microfluidic chamber preparation

Quartz slides are drilled to create flow inlets with similar spacing between each inlet. Double sided (3M) tape of ~ 5 mm width and ~ 100 µm thickness is used to bond a coverslip to the slide and form a microfluidic chamber of ~ 40 µL volume. Following the slide surface preparation and immobilization procedure outlined in the Methods section, we immobilize DNA-SWNT at a concentration of DNA-SWNT that gives ~ 300 fluorescent molecules per imaging area. The fluorophores are then imaged with prism-type TIR microscopy (21).

6.8 Acknowledgements

The work presented in this chapter was primarily carried out in Taekjip Ha's research group, in collaboration with Michael Strano's research group. I am thankful for the support and guidance provided by several members of the Ha and Strano research groups. The experimental design, data acquisition, and analysis were performed in collaboration with Dr. Prakrit Jena and Ankur Jain from the Ha group.

6.9 Chapter references

1. Duncan, R. and R. Gaspar, *Nanomedicine(s) under the Microscope.* Molecular Pharmaceutics, 2011. **8**(6): p. 2101-2141.
2. Langer, R. and D.A. Tirrell, *Designing materials for biology and medicine.* Nature, 2004. **428**(6982): p. 487-92.
3. von Maltzahn, G., et al., *Nanoparticles that communicate in vivo to amplify tumour targeting.* Nature Materials, 2011. **10**(7): p. 545-552.
4. Scheinberg, D.A., et al., *Conscripts of the infinite armada: systemic cancer therapy using nanomaterials.* Nature Reviews Clinical Oncology, 2010. **7**(5): p. 266-276.
5. Nel, A., et al., *Toxic potential of materials at the nanolevel.* Science, 2006. **311**(5761): p. 622-7.
6. Hertel, T., et al., *Spectroscopy of single- and double-wall carbon nanotubes in different environments.* Nano Letters, 2005. **5**(3): p. 511-4.
7. Qiao, R. and P.C. Ke, *Lipid-carbon nanotube self-assembly in aqueous solution.* J Am Chem Soc, 2006. **128**(42): p. 13656-7.
8. Chen, J., et al., *Noncovalent engineering of carbon nanotube surfaces by rigid, functional conjugated polymers.* J Am Chem Soc, 2002. **124**(31): p. 9034-5.
9. Heller, D.A., et al., *Optical detection of DNA conformational polymorphism on single-walled carbon nanotubes.* Science, 2006. **311**(5760): p. 508-11.
10. Tu, X., et al., *DNA sequence motifs for structure-specific recognition and separation of carbon nanotubes.* Nature, 2009. **460**(7252): p. 250-3.
11. Heller, D.A., et al., *Concomitant length and diameter separation of single-walled carbon nanotubes.* J Am Chem Soc, 2004. **126**(44): p. 14567-73.
12. Heller, D.A., et al., *Multimodal optical sensing and analyte specificity using single-walled carbon nanotubes.* Nature Nanotechnology, 2009. **4**(2): p. 114-20.
13. Nel, A.E., et al., *Understanding biophysicochemical interactions at the nano-bio interface.* Nature Materials, 2009. **8**(7): p. 543-557.
14. Shvedova, A.A., V.E. Kagan, and B. Fadeel, *Close encounters of the small kind: adverse effects of man-made materials interfacing with the nano-cosmos of biological systems.* Annu Rev Pharmacol Toxicol, 2010. **50**: p. 63-88.
15. Jain, A., et al., *Probing cellular protein complexes using single-molecule pull-down.* Nature, 2011. **473**(7348): p. 484-U322.
16. Yang, R., et al., *Carbon nanotube-quenched fluorescent oligonucleotides: probes that fluoresce upon hybridization.* J Am Chem Soc, 2008. **130**(26): p. 8351-8.
17. Poland, C.A., et al., *Carbon nanotubes introduced into the abdominal cavity of mice show asbestos-like pathogenicity in a pilot study.* Nature Nanotechnology, 2008. **3**(7): p. 423-428.
18. Liu, Z., et al., *Circulation and long-term fate of functionalized, biocompatible single-walled carbon nanotubes in mice probed by Raman spectroscopy.* Proceedings of the National Academy of Sciences of the United States of America, 2008. **105**(5): p. 1410-1415.
19. Moon, H.K., et al., *Effect of nucleases on the cellular internalization of fluorescent labeled DNA-functionalized single-walled carbon nanotubes.* Nano Res., 2008. **1**: p. 351-360.

20. Zheng, M., et al., *DNA-assisted dispersion and separation of carbon nanotubes.* Nature Materials, 2003. **2**(5): p. 338-342.
21. Liu, Z.D., et al., *Carbon nanotube-DNA hybrid used for activity monitoring and inhibitor screening of nuclease.* Analytica Chimica Acta, 2011.
22. Romier, C., et al., *Recognition of single-stranded DNA by nuclease P1: High resolution crystal structures of complexes with substrate analogs.* Proteins: Structure, Function and Genetics, 1998. **32**(4): p. 414-424.
23. Jena, P.V., *Materials and methods are available as supporting material on Science online.*
24. Li, H.Y., J.D. Carter, and T.H. LaBean, *Nanofabrication by DNA self-assembly.* Materials Today, 2009. **12**(5): p. 24-32.
25. Douglas, S.M., I. Bachelet, and G.M. Church, *A logic-gated nanorobot for targeted transport of molecular payloads.* Science, 2012. **335**(6070): p. 831-4.
26. Walsh, A.S., et al., *DNA cage delivery to mammalian cells.* ACS Nano, 2011. **5**(7): p. 5427-32.

Chapter 7. Force study of DNA-nanotube interactions

A single-walled carbon nanotube (SWNT) can form a complex with ssDNA and has great potential for many biological applications. It is thought that ssDNA wraps in a helical pattern along the SWNT, but the exact binding mechanism and associated energies are not well known due to limitations in the instrumentation used to study DNA–SWNT interactions. In this study we present the first use of optical tweezers to investigate the binding mechanism of the DNA-SWNT complex. We found that the ssDNA unwraps in discrete steps of 5 to 10 base pairs from the SWNT at forces of around 20 pN. We also observe a gradual elongation of our DNA-SWNT complex, possibly due to slipping of the ssDNA along the nanotube length. Steered Molecular Dynamics simulations of a similar DNA-SWNT system reproduce the unraveling steps and DNA slipping behavior we observe experimentally. These results vary significantly from previous studies of DNA-graphene interactions, and provide unprecedented resolution of DNA-SWNT interaction modes.

7.1 Biocompatible single wall carbon nanotubes

SWNTs have a large array of biological applications for diagnostic, sensing, or therapeutic tools [1, 2]. However, as outlined in **Chapters 2 and 6**, there are challenges to implementing SWNTs in such applications due to SWNT hydrophobicity and toxicity when introduced into a biological system [3-5]. When SWNTs are combined with single-stranded DNA (ssDNA) and sonicated as detailed in **Chapter 6**, a DNA-SWNT complex is formed that is soluble in water, stable for months [4], and non-toxic to many biological samples [6]. DNA-SWNT have been useful in a variety of applications, yet little is known about their SWNT wrapping mechanism.

A mechanism for DNA-SWNT interactions proposes the bases on a single strand of DNA are held onto the nanotube surface by π-stacking interactions, leaving the negatively charged sugar-phosphate backbone of the DNA available for solvation by water [7]. Yet, it is still unclear

exactly how DNA interacts with the surface of the SWNT, and how tightly it is bound. In order to predict DNA-SWNT interactions to further DNA-SWNT-based applications, a detailed picture of the DNA-SWNT interface is required. Measurements with Atomic Force Microscopy (AFM) suggest that ssDNA wraps the SWNT with a helical pitch of about 14 to 18 nm, depending on the sequence of the DNA and the chirality of the SWNT [3, 8]. However, measurements taken with a Scanning Tunneling Microscope (STM), which has better X-Y resolution, suggest a much tighter wrapping, with a pitch of 3.3 nm for nanotubes of the common chirality (6,5) [9]. This is in better agreement with molecular dynamics simulations, which generally predict pitches of 2 to 8 nm [10]. The binding energy of the DNA to the SWNT has not yet been measured, though molecular dynamics studies estimate an energy barrier of 0.4-4 k_BT per base for horizontal slipping along the nanotube and a total binding energy of 11-25 k_BT per base, depending on the base and the model [10, 11]. The binding energy of ssDNA to graphite which has a planar geometry, unlike the curved surface of a SWNT, was measured with AFM and found to be 8.5-11.3 k_BT depending on the sequence. This corresponds to average peeling forces of 60-85 pN [12].

In this study we present the first use of optical tweezers to measure DNA-SWNT interactions. Optical tweezers are useful for this study because they can be used to manipulate single molecules and measure the resulting forces and displacements on a molecular scale [5]. We use two near-infrared optical tweezers to study three sequences of ssDNA and their interactions with the SWNT they solubilize: $(GT)_{15}$, $(AT)_{15}$, and $(GT)_{30}$. The $(GT)_{15}$ sequence has been shown to be very effective at binding and dispersing many different SWNT chiralities [3]. We chose to probe $(GT)_{30}$ to determine whether ssDNA sequence length had any effect on the SWNT wrapping mechanism, whereas $(AT)_{15}$ was chosen to probe the effect of having one

third fewer hydrogen bond-donating groups within the ssDNA substrate. We compare these sequences with $(AT)_{15}$ to determine the difference in binding energies between the guanine and adenine bases. We choose both $(GT)_{15}$ and $(GT)_{30}$ to investigate the effect of sequence length on binding, as longer ssDNA strands wrap less tightly around SWNTs [13].

7.2 Experimental approach: Forming DNA-SWNT tethers

A 1.4 kb double-stranded DNA (dsDNA) substrate was synthesized to contain one biotin and one digoxigenin modification at either end as described in **Materials and methods**. This DNA "handle" was subsequently incubated with anti-digoxigenin (AD) microspheres such that two of these AD-DNA microspheres could subsequently be held in two optical traps (**Figure 7-1 a**). The AD-DNA trapped microspheres were brought into a neutravidin channel within the experimental microfluidic chamber, which enabled neutravidin to bind to the free biotinylated ends of the dsDNA handles. The neutravidin-ended DNA handles were then used to bind DNA-SWNT that were solubilized using $(GT)_{15}$-T_6-Biotin, $(GT)_{30}$-Biotin, or $(AC)_{15}$-T_6-Biotin, as

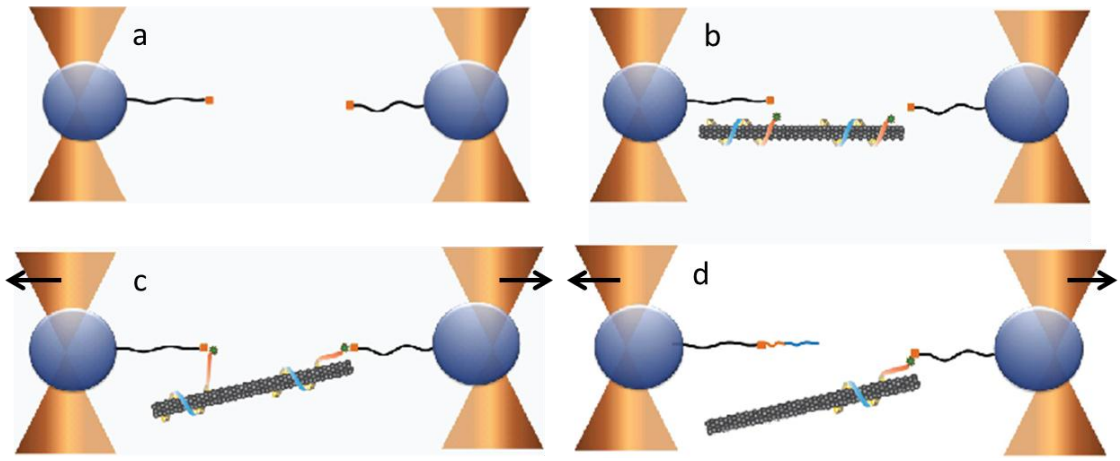

Figure 7-1. Formation of DNA-SWNT tethers. (a) 1.4 kb dsDNA handles are capped with neutravidin to (b) form a tether between two biotinylated ssDNA strands wrapping a SWNT. (c) Moving the traps apart at a constant velocity unwinds the ssDNA from the SWNT. (d) Eventually the ssDNA unravels and the DNA-SWNT tether is lost.

described in **Materials and methods**. The alternating GT or AC sequences were designed to bind to the SWNT surface in a helical manner [14, 15], whereas the T_6 tails were designed to provide a region of ssDNA that binds less readily to the SWNT surface, to facilitate tethering the DNA-SWNT between the dsDNA handles. The neutravidin-ended DNA handles were then brought to an outlet that allowed the controlled release of these biotinylated DNA-SWNT substrates, as detailed in **Materials and methods**. The microspheres were brought into close contact at the exit of the DNA-SWNT outlet, thereby exposing the neutravidin-ended DNA handles to the DNA-SWNT. When two strands of biotinylated ssDNA on a single DNA-SWNT became attached to each of the DNA handles, a DNA-SWNT tether formed between the microspheres (**Figure 7-1 b**). The interaction of the ssDNA wrapping the SWNT was studied by measuring the length vs. the force of each DNA-SWNT tether by moving the traps apart at a speed of 8 nm/s and measuring force and extension at a rate of 100 Hz (**Figure 7-1 c**). These traces were subsequently analyzed as force-extension plots. Each of our DNA-SWNT single tethers simultaneously pulled on two separate biotinylated ssDNA wrapping strands. However, we ensured that each of the data traces included in our analysis was comprised of only a single DNA-SWNT tether, by ensuring that our tether broke in a single step (**Figure 7-1 d**).

7.3 DNA-SWNT pulling curves show ssDNA unraveling events

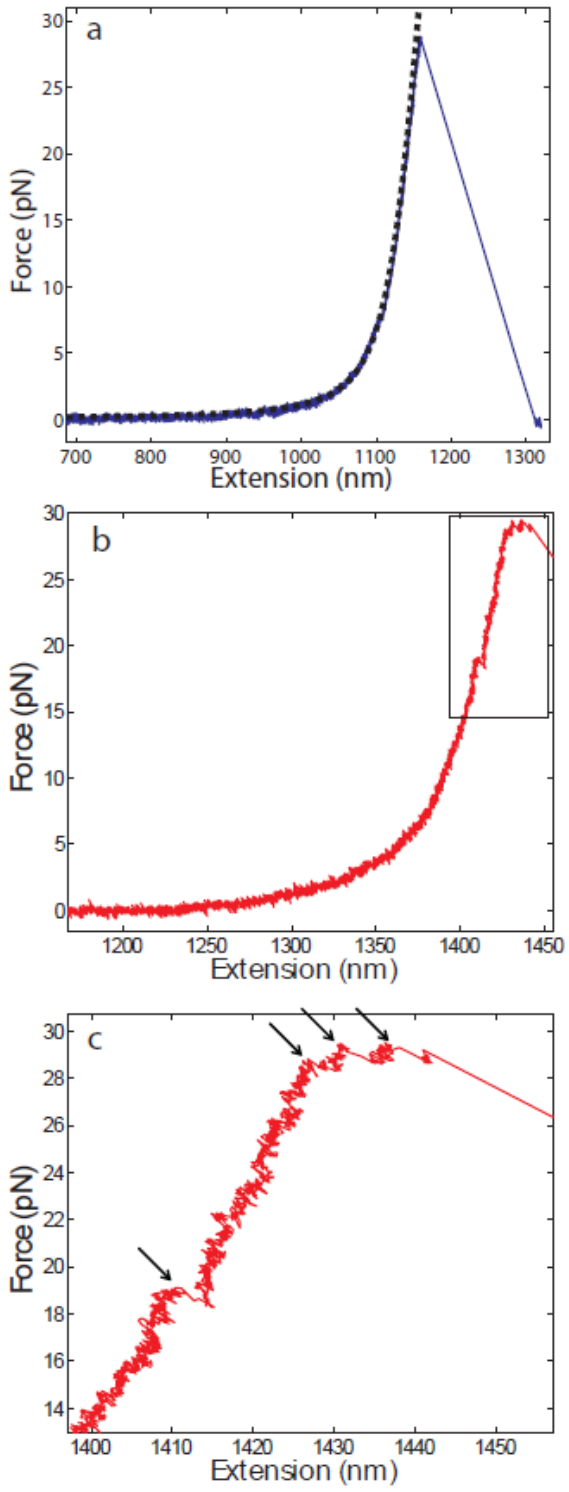

Figure 7-2. Example DNA-SWNT force-extension curve a) Force versus extension plot of dsDNA tether, b) $(GT)_{15}$ DNA-SWNT tether. c) Box represents zoomed in region in b) which has unraveling events marked with arrows.

Force-extension plots of control dsDNA-only tethers show a single upward curve, and are in excellent agreement with the theoretical dsDNA force-extension behavior as predicted by the Worm-like chain model of DNA elasticity [16] (**Figure 7-2 a**). In contrast, a $(GT)_{15}$ DNA-SWNT force-extension curves have contributions from both the dsDNA handles and the DNA-SWNT complex. Thus, $(GT)_{15}$ DNA-SWNT pulling curves show predominantly dsDNA pulling curve behavior, but also show notable deviations from the dsDNA-only pulling curve, particularly prior to tether breakage (**Figure 7-2 b**). Zooming in to the top of the $(GT)_{15}$ force-extension curve, we observe small, abrupt changes in force and extension we identify as steps (**Figure 7-2 c**), which we believe correspond to unraveling of the $(GT)_{15}$ ssDNA from the SWNT right before the tether is lost. These steps are present in over 80% of our tethers for all three DNA-SWNT samples. The forces at which these individual

unraveling events occurred for $(GT)_{15}$ from SWNT were fairly widespread as shown in **Figure 7-3 a**, with an average value of 19 ± 9 pN (mean ± SD). Unraveling event forces for $(GT)_{30}$ and $(AT)_{15}$ were similar, with average ssDNA unbinding force values of 21 ± 11 and 23 ± 10 pN (mean ± SD), respectively. These results differ substantially from DNA-SWNT dissociation force measurements determined previously. For instance, ssDNA was pulled from graphite with an AFM with an average force of 60-85 pN [12], while we find measure forces averaging about 20 pN for all sequences. There are several possible reasons for this discrepancy. The discrepancies in ssDNA unbinding forces found with our optical trap approach compared to AFM measurements can be explained by the different geometries of graphene being probed. In AFM experiments, unbinding of ssDNA from the planar surface of graphite was studied [12]. In contrast, we are measuring the unraveling of ssDNA from the curved SWNT surface. This suggests that ssDNA wraps more loosely around a cylindrical graphene structure, such as a SWNT, than to planar graphene. Furthermore, AFM pulling measurements are typically taken at higher pulling velocities (over 100 nm/s) than optical trap force-extension curves. The rapid pulling of AFM measurements results in force-extension curves that are taken in non-equilibrium conditions, resulting in an over-estimate of the true polymer unbinding force.

The use of optical traps is a novel approach to probe ssDNA-SWNT interactions. Not only do the slower pulling velocities enable a more accurate equilibrium measurement of the ssDNA unbinding force, but the slow pulling velocity and nanometer resolution allow us to probe intermediate states in the ssDNA unbinding process. While the use of AFM to probe ssDNA-graphene interactions can only provide information on bound versus unbound states, since AFM experiments pull off entire strands of ssDNA. In contrast, high-resolution optical

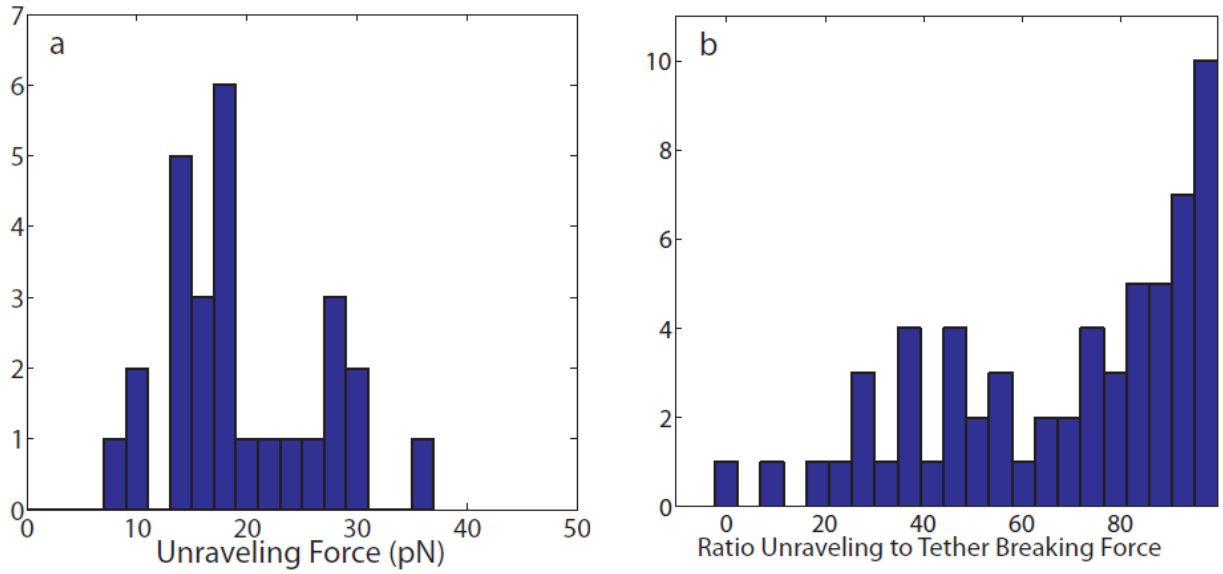

Figure 7-3. DNA-SWNT unraveling and tether breaking forces. (a) Histogram of force at which individual unraveling steps occur. (b) Ratio at which unraveling events occur compared to overall tether breaking force.

traps have the ability to probe the intermediate events such as ssDNA unraveling steps, due to the nanometer-scale resolution of our optical traps.

We next performed an analysis over where these steps are located within the force-extension curve, as a ratio between the force at which the individual step is observed versus the final force (maximum force prior to breakage) to which all of our $(GT)_{15}$ DNA-SWNT tethers were pulled. This analysis provides insights into the DNA-SWNT unraveling mechanism. **Figure 7-3 b** shows that, as expected, ssDNA unraveling events are more likely to occur moments before the tether breaks, as opposed to occurring consistently during the course of the entire force-extension curve. We observe similar behaviors for our two other DNA-SWNT samples, $(GT)_{30}$ and $(AT)_{15}$. This suggests that the mechanism of ssDNA unraveling from a SWNT through the application of a constant pulling velocity involves a stably-bound DNA-SWNT complex for the majority of the pulling trajectory, followed by one or more ssDNA unraveling events leading to the dissociation of the entire DNA-SWNT.

Previous studies have been inconclusive regarding the helical structure of ssDNA along a SWNT, primarily because this helical structure has not been probed directly. AFM imaging measurements, scanning tunneling microscopy assays, and molecular dynamics simulations have suggested helical pitches anywhere from 2.2 nm to over 18 nm [3, 8, 10], proposing unraveling step sizes within this range per ssDNA half-turn. We performed a step-size analysis to determine the unraveling step size of the ssDNA from the SWNT. As shown in **Figure 7-4**, for $(GT)_{15}$, we observe a Gaussian distribution for the unraveling step size, with an average value of 7.1 ± 0.7 nm (mean ± SE). Given that the DNA-SWNT complex has a diameter of 2-3 nm and a pitch of 2-8 nm, this corresponds to a release of roughly one fifth to one full ssDNA turn at a time. In a few rare instances, we also observe negative extension step-sizes that correspond to ssDNA re-wrapping events. Similar distributions and values are observed for $(GT)_{30}$ and $(AT)_{15}$, with

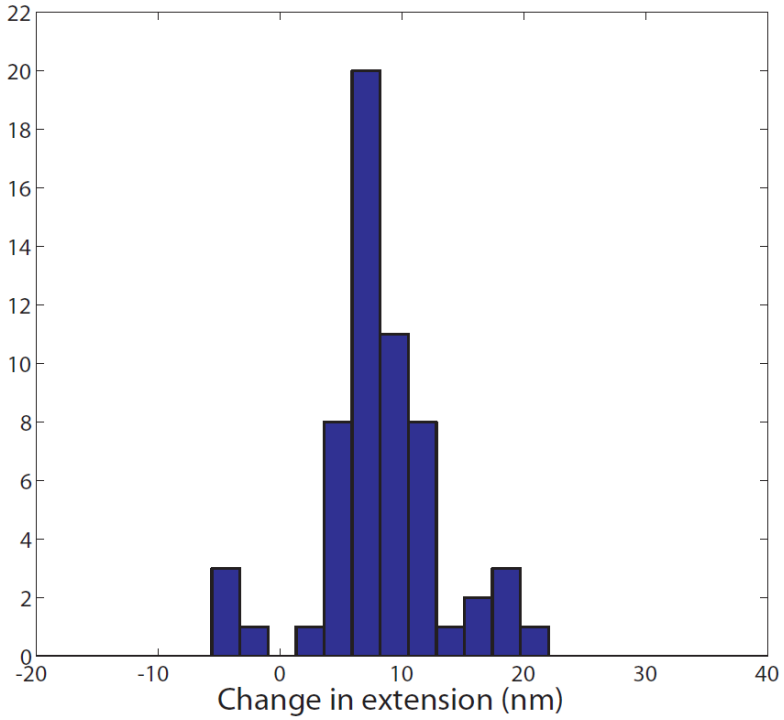

Figure 7-4. DNA-SWNT step size extension change. Change in extension for all $(GT)_{15}$ ssDNA unraveling events from SWNT. Complete dissociation of ssDNA from the SWNT are not included in this analysis.

average ssDNA unraveling step size values of 6.0 ± 2.0 and 7.9 ± 0.9 nm (mean ± SE), respectively.

Another noteworthy result from our DNA-SWNT tether breaking force analysis and step-size analysis is the similarity in both the breaking force and the step-size between our three samples. We found no difference in unraveling step-size or unbinding forces for different sequences and lengths of ssDNA. This suggests that $(GT)_{15}$, $(GT)_{30}$, and $(AT)_{15}$ wrap SWNT with comparable binding strengths and similar pitches despite what has been previously suggested in the literature [14, 17]. It is also possible that ssDNA binding to SWNT is a dynamic process instead of adopting a stable binding conformation. If this is the case, it is possible that slipping along the SWNT occurs for all three sequences, and that the dynamic or transient nature of ssDNA-SWNT binding overshadows any inherent differences in binding due to sequence or length differences.

7.4 Contributions to DNA-SWNT pulling curve

Each DNA-SWNT pulling curve has three main potential contributions: 1) The ssDNA unraveling from the SWNT, 2) the 1.4 kb dsDNA handles 3) the length of the SWNT, which will depend on the re-orientation of the SWNT as it aligns with the pulling direction of the tether. It is unlikely that the SWNT stretching contributes to the DNA-SWNT pulling curve, due to the large persistence length of SWNT [18]. Our ultimate goal is to remove the dsDNA handle and SWNT length contributions from the force-extension curves, leaving only the one contribution we wish to study: the ssDNA unraveling from the SWNT.

We devised an analysis scheme to remove the contribution of the 1.4 kb dsDNA handles stretching. Removal of the 1.4 kb dsDNA handle contribution was accomplished by subtracting

the force-extension curve of 1.4 kb DNA as predicted by the Worm-Like Chain model of polymer elasticity [16]. Next, we aimed to remove the SWNT length contribution. However, removing the SWNT length contribution was not straightforward for two reasons. First, our DNA-SWNT sample is not of uniform SWNT length. Second, the SWNT will need to re-orient itself with the pulling direction of the tether before it can contribute its full length to the force-extension curve. We will address each of these points prior to removing the SWNT length contribution from the force-extension curve.

The process of SWNT wrapping by ssDNA involves probe-tip sonication of the DNA + SWNT solution for 2 minutes at 10 W, as described in **Materials and methods**. This sonication process breaks SWNT into smaller SWNT, creating a DNA-SWNT length distribution with an average DNA-SWNT length of ~ 300nm. In **Figure 7-5 a**, we show an AFM image of our $(GT)_{15}$ DNA-SWNT sample. These AFM images were analyzed to obtain a length distribution of our DNA-SWNT sample in **Figure 7-5 b**. Because we know the length of our dsDNA handles to

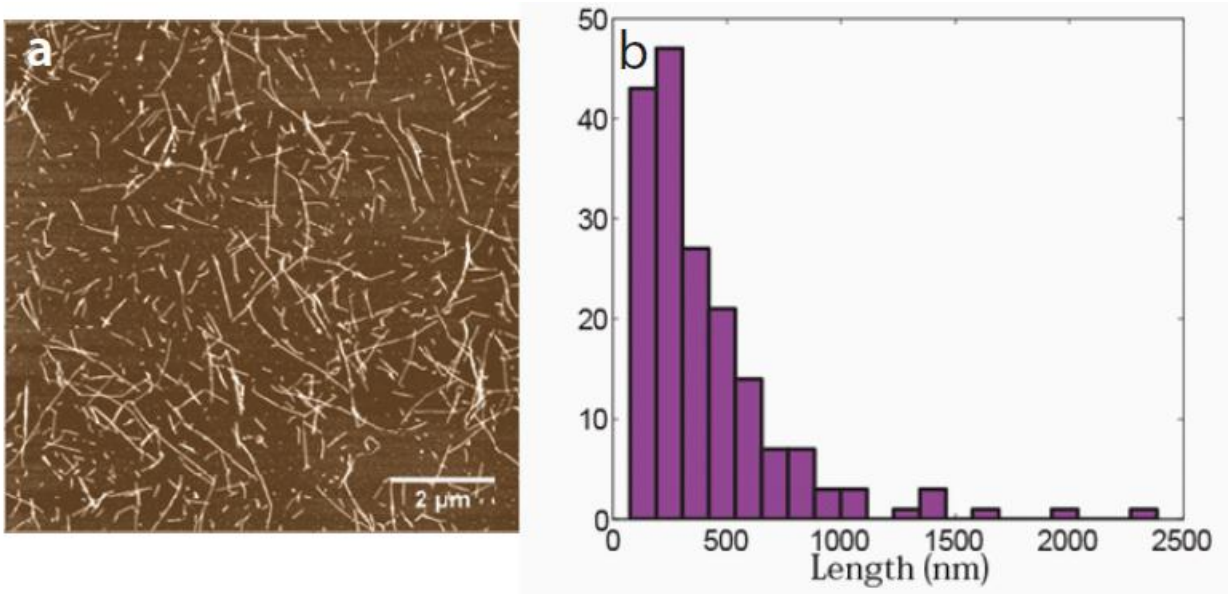

Figure 7-5. AFM scan and length analysis of $(GT)_{15}$ DNA-SWNT. (a) An AFM scan of our $(GT)_{15}$ DNA-SWNT sample and the (b) corresponding length distribution of the AFM-imaged DNA-SWNT.

be 1.4 kb each, or 2.8 kb of total dsDNA contribution, subtracting this length from a tether in which the SWNT is aligned with the direction of pulling would allow us to determine the length contributed by the tethered DNA-SWNT at a given force. However, we must first determine the dynamics of the DNA-SWNT reorientation.

We determined the rotational contribution of the DNA-SWNT as it rearranges in 3D space to align with the direction to which the tether is being pulled, by modeling the SWNT as a rotating rod. This SWNT rod is assumed to make an angle Θ with the direction of tether pulling with a fixed point of rotation halfway between the two points at which it is tethered by the dsDNA handles. This rod experiences a force, F, applied by our optical trap that aligns the SWNT to its equilibrium position in the direction of the applied force.

$$z = d\cos(\Theta)\, e^{-\Omega\cos(\Theta)/k_b T}$$

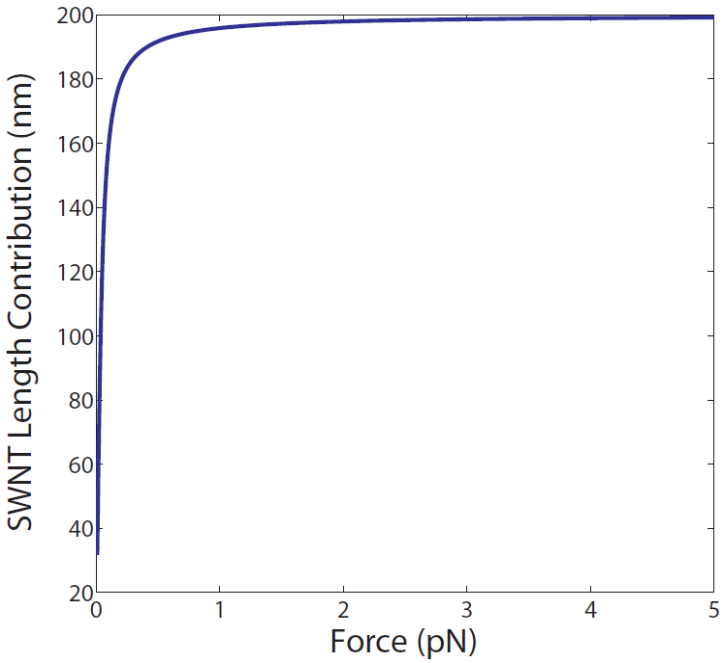

Figure 7-6 Rotational contribution of SWNT to DNA-SWNT pulling curve. The length of the DNA-SWNT tethered between our two dsDNA handles is calculated by subtracting the contribution of the dsDNA handles from the fully-extended length of the DNA-SWNT tether.

In the above equation, z represents the horizontal component of the SWNT along the direction of tether pulling. When the SWNT is fully aligned in the direction of pulling, z will equal the actual tethered length of the SWNT. The SWNT will undergo rotation until it reaches an equilibrium position that aligns it with the force vector when $\Theta = 0$. For a SWNT length of 300 nm, we found that the SWNT is almost entirely aligned in the direction of the applied force very low forces (**Figure 7-6**). At 1 pN, the SWNT is 98% aligned in the direction of applied force, contributing a length of 294 nm to the pulling curve out of its 300 nm total length. Therefore, to remove the SWNT length contribution from our force-extension curves, we do so at 1pN of tension, where we assume that the SWNT length contribution to the force-extension curve is equal to the physical length of the SWNT. It is important to note that it is not possible to know where along the length of the SWNT the tethering occurs, therefore, the distance between the attachment points on a DNA-SWNT tether (DNA-SWNT tethering length) will be less than or equal to the physical length of the tethered DNA-SWNT.

We calculated the DNA-SWNT tethering length for our tethers by removing the dsDNA handle contribution at 1pN of force. A histogram of this DNA-SWNT tethering length is shown in **Figure 7-7**. The average DNA-SWNT tethering length was found to be 522 ± 20 nm (mean ± SE) with a wide length distribution that falls well within the range of the DNA-SWNT lengths determined by our AFM measurements. As expected, we observe slightly shorter DNA-SWNT tethering lengths in our optical trap than the actual DNA-SWNT length distribution as determined by AFM.

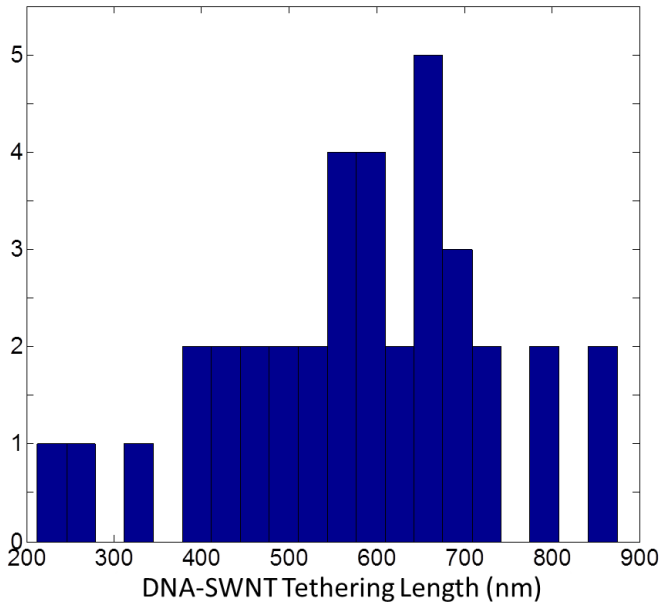

Figure 7-7 DNA-SWNT tethering length. The length of the DNA-SWNT tethered between our two dsDNA handles is calculated by subtracting the contribution of the dsDNA handles from the fully-extended length of the DNA-SWNT tether.

7.5 ssDNA slipping and unraveling

The ability to determine the DNA-SWNT tethering lengths for each tether enables us to remove this DNA-SWNT length contribution from the pulling curve, along with the contribution of the dsDNA handles. Plotting the resulting force-extension curve leaves us with only the

contribution from the DNA-SWNT section of the tether, and the behavior associated with ssDNA dissociating from the SWNT as force is applied. We expected these DNA-SWNT only force-extension curves to collapse around zero extension at all forces with small steps deviating from zero extension representing ssDNA unraveling from the SWNT. While we do observe these unraveling events, most of our DNA-SWNT force-extension curves do not collapse at zero extension. As shown in **Figure 7-8**, DNA-SWNT pulling curves for which the tethered SWNT was determined to have a short tethering length (< 400nm, blue curve) are similar to the curve we would expect when removing the dsDNA + SWNT length contributions. However, most of the data does not collapse around zero force – only tethers for short (< 400nm) DNA-SWNT do. Tethers formed with longer DNA-SWNT deviate from our expected zero-force curves more so

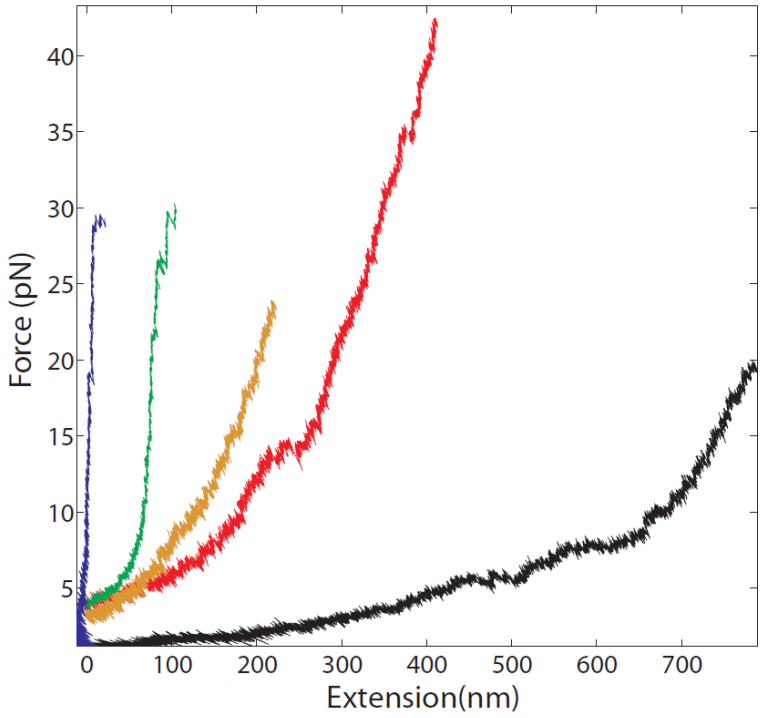

Figure 7-8. DNA-SWNT only contribution to force-extension curve. DNA-SWNT pulling curves with contributions from the dsDNA handles and the SWNT lengths removed. Slopes of the pulling curves with only the DNA-SWNT contribution vary depending on the length of the SWNT tethered. Representative force-extension curves are shown for tethered SWNT in the < 400 nm (blue), 400-800 nm (green), 800-1200 nm (orange), 1200-1600 nm (red), and > 1600 nm (black) length ranges.

than tethers formed with shorter DNA-SWNT. For instance, as shown in **Figure 7-8**, tethers formed with 400-800 nm SWNT (green), 800-1200nm SWNT (orange), 1200-1600nm SWNT (red), or >1600nm SWNT (black) have increasingly large deviations from the expected zero-force curve as shown by their increasingly shallower slopes. Having removed the contribution of the dsDNA handles and the SWNT length from the force-extension curve, the reason for this deviation must be rooted in the dynamics of the DNA-SWNT part of the tether.

Another possible explanation for a change in the force-extension curve slopes is slipping of the ssDNA along the SWNT as the DNA-SWNT complex is pulled. The potential contribution of ssDNA slipping along the SWNT is likely due to the small energy barrier to ssDNA slipping on the SWNT surface compared to the larger energy barrier associated with ssDNA unbinding. Though no experimental studies to date have directly probed ssDNA unraveling or slipping on SWNT, several similar studies have probed the binding energies of individual nucleotides [19] or polynucleic acid chains on graphene sheets. Pulling ssDNA off a graphene sheet via AFM predicts a binding energy per nucleotide of 2.1 – 4.5 k_BT [19], which is around the same size as the predicted energy barrier for ssDNA slipping on graphene structures [20]. However, it is generally thought that ssDNA-graphene interactions may be more stable than ssDNA-nanotube interactions due to the curvature of carbon nanotubes. This curvature causes the sp^2-hybridized carbon atoms on the rolled-up sheet of graphene to be, on average, further from the DNA bases [19]. This lower stability between the ssDNA and SWNT will contribute to a lower ssDNA binding energy, and a lower energy barrier for ssDNA slipping as well. Gowtham *et al.* use VASP molecular modeling to predict the binding energy of individual DNA bases to a sheet of graphene versus a SWNT. For each of the four DNA bases, the binding energy of that DNA base to a carbon nanotube is lower than the binding energy of that same base to a sheet of graphene,

presumably due to the curvature of the SWNT [21]. The curvature of the SWNT surface may also contribute to a lower energy barrier to ssDNA slipping along the length of the SWNT, since the energy barrier for the ssDNA to move between adjacent isoenergetic binding sites on the SWNT surface is predicted to be lower on a curved surface. Therefore, while prior AFM measurements of ssDNA binding to graphene have not reported a slipping component to ssDNA unbinding, it is possible that the curved surface of a cylindrical carbon nanostructure such as a SWNT enables slipping to be a main contribution to the process of ssDNA unbinding from a SWNT.

7.6 DNA-SWNT steered molecular dynamics

In collaboration with the Schulten computational biophysics group, we applied steered molecular dynamics (SMD) to study the structure of ssDNA wrapped around a SWNT with a constant force applied to one end of the ssDNA. We constructed a system comprising a (5,10)-

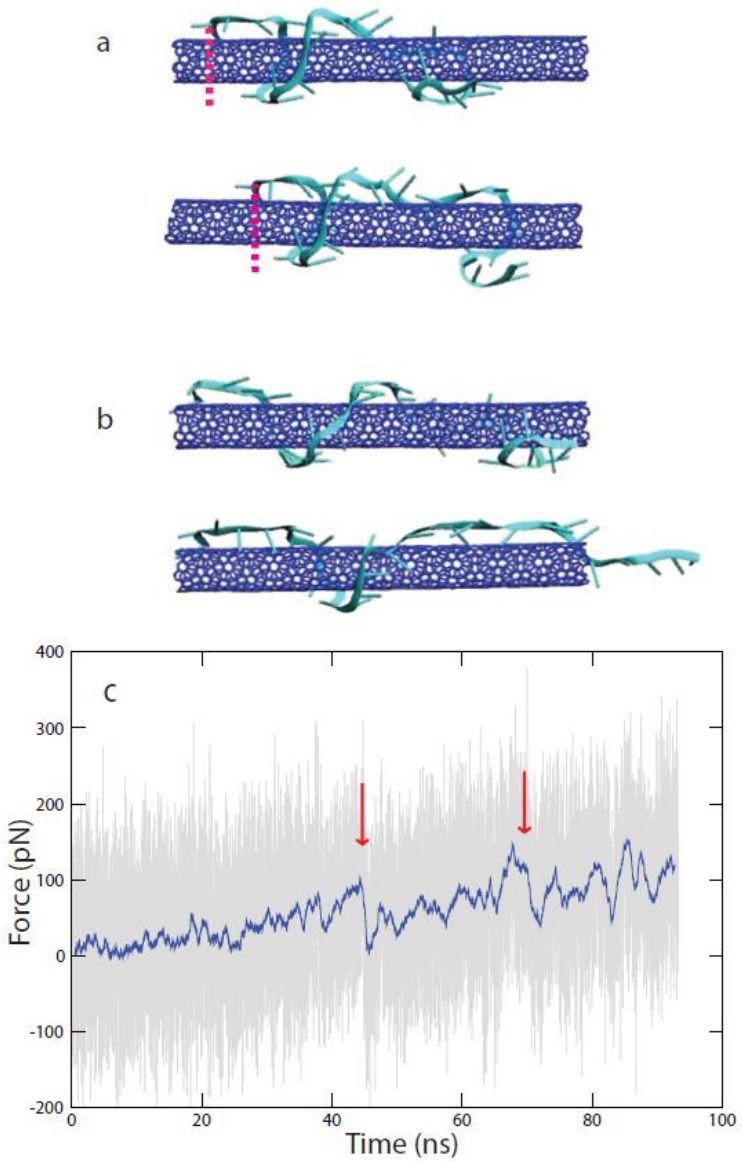

Figure 7-9. Molecular dynamics simulation of (GT)15 ssDNA unraveling from a (5,10)-SWNT. (a) Lateral motion of the SWNT within the helical structure of the ssDNA is observed between 0 ns and 10 ns, relative to the fixed ssDNA 3' end denoted by a dashed magenta line. (b) A sudden unraveling of a half-turn of the ssDNA is observed between 65 ns and 72 ns and (c) a corresponding force drop is observed in the force-time trajectory. Two such events are highlighted by red arrows.

SWNT wrapped with $(GT)_{15}$-T_6 ssDNA, and fixed the 5' end of the ssDNA in space. The application of a constant 1 angstrom/ns pulling velocity to the 3' end of the ssDNA in a direction along the SWNT length allowed for the unraveling dynamics of the system to be probed throughout the course of the 90 ns simulation. Unraveling snapshots at 0 ns, 10 ns, 65 ns, and 72 ns are shown in **Figure 7-9**. The simulation confirms two phenomena that we believe to have observed in our optical trap pulling assays. First, we observe sudden step-wise unraveling of a half-turn of the ssDNA between 65 ns and 72 ns. Plotting the force-time trace of this SMD trajectory shows force steps during half-turn unraveling events similar to the force-drop steps we observe in our force-extension curves while pulling DNA-SWNT with our optical trap. However, we also observe significant lateral motion of the SWNT with respect to the wrapping ssDNA. This lateral motion occurs throughout the course of the simulation, but is most apparent when the SWNT is still mostly wrapped by the ssDNA between 0 ns and 10 ns. For instance, in **Figure 7-9 a**, a red dashed line marks the position of the tethered end of the ssDNA at t = 0 and t = 10 ns, and the lateral movement of the SWNT relative to the tethered ssDNA end is apparent. This lateral motion is observed continuously throughout the course of the SMD simulation. This suggests that, when pulling on two separate ssDNA strands using fixed attachment points as in our optical trap assay, lateral motion of the SWNT can occur readily and ssDNA slipping is likely to occur throughout the course of the pulling curve in our experiments. The shallower force-extension curves that we observe experimentally could be due to the slipping of ssDNA along the length of the SWNT. This phenomenon may occur more noticeably on longer SWNT, as we observe in our optical trap pulling experiments. It follows that slipping would occur more readily on longer tethered SWNT than on shorter tethered SWNT, since longer SWNT would provide a longer length over which the ssDNA could slide.

In **Figure 7-9b**, we highlight an unraveling event of roughly a half-turn of ssDNA from the SWNT surface. This unraveling event corresponds to a sudden drop in the force-time plot of the pulling trajectory between t = 65 and t = 72 ns. This force drop is highlighted by the second red arrow in **Figure 7-9 c**. These steps are qualitatively similar to the force drops that accompany our optical trap force-extension curves prior to tether breakage, however, the pulling velocity of our SMD simulation is approximately 8 orders of magnitude higher than in our optical trap. Therefore, while we cannot compare the magnitude of the force steps quantitatively, the force steps that accompany the unraveling events observed in the SMD support our hypothesis that force-extension steps in our optical trap pulling curves corresponds to unraveling of the ssDNA from the SWNT.

7.7 DNA-SWNT unraveling model

Many questions remain regarding the mechanism of ssDNA unraveling from SWNT. Techniques such as AFM and STM that have been commonly used to determine the interactions of DNA with carbon nanostructures have been limited in their ability to explore the details of DNA interactions with carbon nanostructures. Sub-events leading to the dissociation of DNA from the nanostructure surface have been hidden below the resolution limit of these techniques. Additionally, cylindrical nanostructures such as SWNT have been notoriously difficult to study using these techniques – their unique cylindrical geometry hinders surface-immobilization, which is required for the study of DNA-nanostructure unbinding mechanisms using AFM and STM. Our optical trap approach to the study of ssDNA unraveling from SWNT provides a novel approach to the study of surface-decoupled DNA-SWNT. Our results provide a detailed look into the mechanism of ssDNA unbinding from a carbon nanotube with a resolution that enables us to directly observe unwrapping and slipping events.

Based on our experimental force-extension curves and our SMD simulations, we propose that the mechanism of ssDNA unbinding from SWNT is comprised of two primary contributions: ssDNA unwrapping in half-turn intervals, and ssDNA slipping along the SWNT length. Our optical trap experiments show clear steps in force-extension curves of ssDNA pulled from a SWNT surface. These steps are within the size range predicted to be characteristic of ssDNA unraveling in half-turn intervals prior to ssDNA unbinding from the cylindrical SWNT structure [3, 8, 10]. The forces at which these events occur are lower than the forces for ssDNA unbinding from similar nanostructures such as graphene, as predicted by previous studies [21]. SMD results support our experimental observations. Although SMD pulling of ssDNA was performed at a much faster rate than our optical trap pulling experiments, previous studies have found that the loading rate has no effect on the unbinding behavior of ssDNA pulling from graphite using AFM [22]. Therefore, our experimental results can be qualitatively compared to our SMD trajectories. Our results provide a clear and more detailed study of the mechanisms responsible for ssDNA-SWNT interactions, which can facilitate the design and implementation of DNA-solubilized SWNT across many emerging fields.

7.8 Materials and methods

Synthesis of dsDNA handles

Our dsDNA tethers were synthesized using a 5'-mono-biotinylated forward and a 5'-mono-digoxigenated reverse PCR primer (Integrated DNA Technologies, Coralville, Iowa) to amplify the desired 1.4 kb sequence of the pBR322 E. coli plasmid (Fermentas, Glen Burnie, Maryland). A high fidelity Phusion PCR kit (F-513S, Finnzymes, Wburn, Massachusetts) was

used to carry out the PCR amplification. Subsequent DNA purification was performed with a Qiagen PCR purification kit with a 50 µl DNA elution volume. An identical protocol was followed for the synthesis of dual-biotinylated DNA tethers, replacing the reverse primer above with a 5'-mono-biotinylated PCR primer with the same sequence.

Preparation of Anti-digoxigenin coated microscpheres

100 µL of 1.4% w/v 1.0µm protein G microspheres from Polyscience were washed with filtered (0.2µm) 0.2M Triethanol amine (TEA), pH 8.2 (the microspheres were combined with 200 µL TEA, centrifuged at 7.5krpm for 1min, and the supernatant removed). This process was repeated twice. 10 µL of Anti-DIG polyclonal sheep antibody from Roche and 200 µL TEA were added to the microspheres and vortexed for 30min. The microspheres were then washed three times to remove excess antibodies (the microspheres were combined with 200 µL of filtered (0.2µm) Phosphate Buffered Saline, pH 7.0 (PBS), centrifuged at 7.5 krpm for 1min, and the supernatant removed). The microspheres were stored in 200 µL PBS at 4°C.

Buffers and channel conditions

Anti-DIG microsphere channel: 10 ng of a solution of 1.4-kb dsDNA handles was incubated with ~0.86 µm diameter Anti-DIG microsphere. This suspension was allowed to incubate at room temperature for ~1hr. The suspension was combined with 1 mL T50 buffer, 20 µL filtered (0.2 µm) 25% glucose, 10 µL Bovine Serum Albumen (BSA), and 2 µL gloxy [23] (added within a few minutes prior to trapping).

Neutravidin channel: 1 mL of T50 buffer was combined with 10 µL filtered (0.2µm) Neutravidin, 20 µL of 25% filtered (0.2 µm) glucose, 10 µL BSA, and 2 µL gloxy (added within a few minutes prior to trapping).

Buffer channel: 1 mL of T50 buffer was combined with 20 µL of 25% filtered (0.2 µm) glucose, 10 µL BSA, and 2 µL gloxy (added within a few minutes prior to trapping).

DNA-SWNT channel: 1 mL of T50 buffer was combined with 10 µL of DNA-SWNT solution, 20 µL of 25% filtered (0.2 µm) glucose, 10 µL BSA, and 2 µL gloxy (added within a few minutes prior to trapping).

DNA-SWNT tether formation

Polystyrene microspheres coated in anti-digoxigenin were incubated with 1.4 kb dsDNA that had digoxigenin on one end and biotin on the other. The digoxigenin on the dsDNA strand bound to the anti-digoxigenin coating the AD microsphere to serve as a dsDNA "handle." One AD-dsDNA microsphere was trapped in each beam of the dual optical trap setup. The microspheres were then maneuvered into buffer containing neutravidin, which bound to the biotin on the ends of the dsDNA handles. The microspheres were then brought to another channel containing only buffer, and brought to an outlet that controlled the release of the DNA-SWNT complex. The ssDNA wrapping the SWNT was biotinylated at the 5' end which was free to bind to the neutravidin on the dsDNA handles to form a tether (Figure 1). Because the DNA-SWNT was coated in ssDNA, the dsDNA attachment points could occur anywhere along the nanotube, which itself could vary in length from 200nm to 2000nm.

Preparation of solubilized DNA-SWNT

Approximately 1 mg of SWNT synthesized by the HiPCO process was combined with 10 µL of DNA (either $(GT)_{15}$-T_6-biotin, $(AT)_{15}$-T_6-biotin, or $(GT)_{30}$-T_6-biotin sequence) in an eppendorf tube. 800 µL of 100nM NaCl was added to this mixture, the tube was placed on ice, and sonicated with a probe-tip sonicator for 2 min at 10 W. The insoluble mixture of SWNTs was observed to change to a homogenous solution following sonication as described previously [4]. To remove excess SWNTs from solution, the suspension was centrifuged for 90 min at 16,000g; the supernatant was removed and filtered on a millipore micron centrifugation filter device (Ultracel YM-100) using 200 µL aliquots of filtered (0.2 µm) T50 buffer. This solution was stored at 4°C in T50 buffer.

Experimental setup

A chamber with four compartments was prepared as described in Materials and Methods and depicted in **Figure 7-10**. Two Anti-DIG microspheres were captured (one in each trap) at position 1, then moved through the Neutravidin channel to position 2, allowing the Neutravidin to bind to the biotin on the dsDNA "handles" attached to the microspheres. At position 2, the microspheres were tested for their ability to form DNA-only tethers. In over 500 microsphere pairs, we never observed DNA-only tethers, suggesting that all terminal biotin sites had a neutravidin molecule bound. The microspheres were then moved through the opening between the two middle chambers to position 3 in the buffer-only channel. The two microspheres were then moved to position 4, at the exit of the capillary serving as the outlet point for DNA-SWNT using a flow of 100 µL/hour in the DNA-SWNT channel. At position 4, tethers were formed by bringing the microspheres close together, allowing the Neutravidin on each of the microspheres to bind to the biotin at the end of the ssDNA on the DNA-SWNT. After a tether had been

formed, the microspheres were pulled apart until the tether had broken, and a force-extension curve was plotted. Only single tethers were considered. A single tether is identified by a single peak in the force-extension curve that returns to zero in a single breaking step.

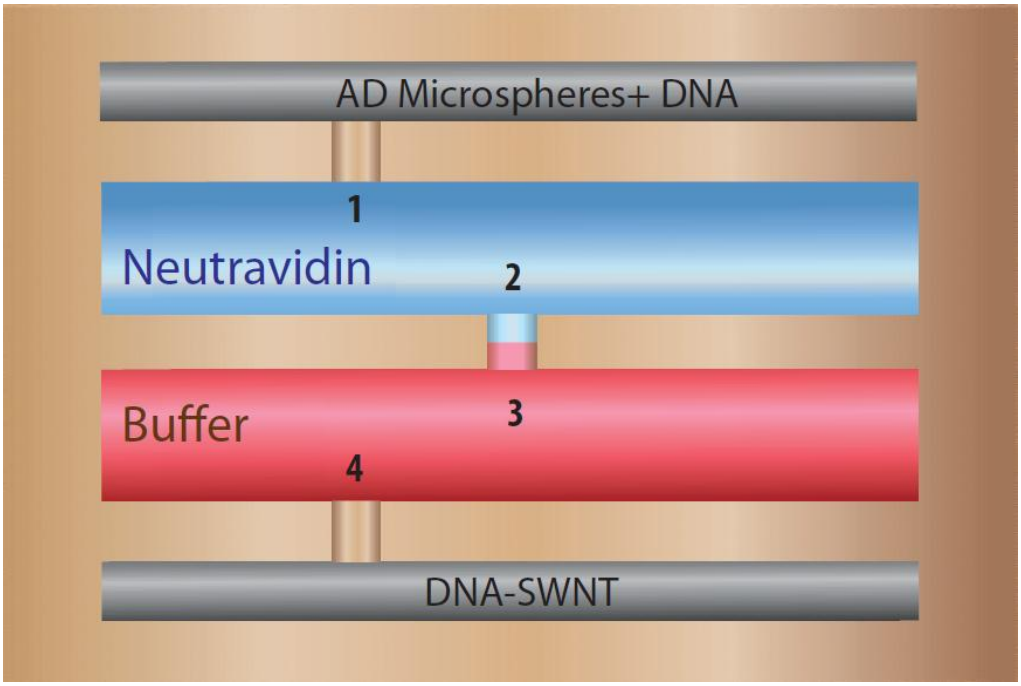

Figure 7-10. Optical trap chamber layout. Two AD microspheres coated with dsDNA handles are trapped at position 1. Next, they are moved through the neutravidin channel where the biotin-ended dsDNA handles are coated with a neutravidin molecule. At position 2, we ensure that tethering cannot occur for the dsDNA handles only. We next move to position 3 followed by 4, where we expose our microspheres to DNA-SWNT. Formation of a tether occurs at position 4, once a DNA-SWNT binds to two dsDNA handles.

AFM Imaging of DNA-SWNT

The method for preparing the AFM samples followed a previously established protocol [15]. Briefly, AFM samples were prepared by depositing $(GT)_{15}$ DNA-SWNT on freshly cleaved mica. Dry AFM measurements were made by first exposing the mica surface to 1 M MgCl2 for 60 seconds, rinsing with DI water, and drying with ultrapure nitrogen before depositing $(GT)_{15}$ DNA-SWNT solution at a concentration of 5-10 mg/L in 100 mM Tris pH 7.5. We then exposed

the surface to nanotube solution for 15 seconds, rinsed with DI water and dried with ultrapure nitrogen.

Dual optical trap setup

The optical tweezers apparatus used for the experiments presented in this chapter has been described elsewhere [24, 25], and briefly in **Chapter 3**.

Steered molecular dynamics

A DNA-SWNT system consisting of a (5,10)-SWNT wrapped with $(GT)_{15}$ ssDNA was placed in a water box with 50 nM NaCl to match our experimental buffer conditions. An all-atom steered molecular dynamics simulation was performed by fixing the 3' end of the $(GT)_{15}$ DNA at a reference coordinate within the water box, whereas the rest of the system was allowed to move freely. The 5' end of the $(GT)_{15}$ DNA was pulled along the axis of the SWNT with a pulling velocity of 1 angstrom/ns.

7.9 Acknowledgements

I gratefully acknowledge Elana Urbach and Brian Silver for their dedication to this project as summer REU participants. I would also like to acknowledge Prof. Klaus Schulten's theoretical and computational biology group, particularly Dr. Xueqing Zou and Chaitanya Sathe for helpful discussions regarding the work presented in this chapter. Dr. Xueqing Zou was instrumental in assembling and running the SMD simulations to match our experimental setup.

7.10 Chapter references

1. Langer, R. and D.A. Tirrell, *Designing materials for biology and medicine.* Nature, 2004. **428**(6982): p. 487-92.
2. Sinha, N. and J.T. Yeow, *Carbon nanotubes for biomedical applications.* IEEE Trans Nanobioscience, 2005. **4**(2): p. 180-95.
3. Zheng, M., et al., *Structure-based carbon nanotube sorting by sequence-dependent DNA assembly.* Science, 2003. **302**(5650): p. 1545-8.
4. Zheng, M., et al., *DNA-assisted dispersion and separation of carbon nanotubes.* Nat Mater, 2003. **2**(5): p. 338-42.
5. Moffitt, J.R., et al., *Recent advances in optical tweezers.* Annu Rev Biochem, 2008. **77**: p. 205-28.
6. Liu, Z., et al., *Circulation and long-term fate of functionalized, biocompatible single-walled carbon nanotubes in mice probed by Raman spectroscopy.* Proc Natl Acad Sci U S A, 2008. **105**(5): p. 1410-5.
7. Manohar, S., *DNA--Carbon Nanotube Interactions.* 2010.
8. Campbell, J.F., et al., *Atomic force microscopy studies of DNA-wrapped carbon nanotube structure and binding to quantum dots.* J Am Chem Soc, 2008. **130**(32): p. 10648-55.
9. Yarotski, D.A., et al., *Scanning tunneling microscopy of DNA-wrapped carbon nanotubes.* Nano Lett, 2009. **9**(1): p. 12-7.
10. Johnson, R.R., A.T. Johnson, and M.L. Klein, *Probing the structure of DNA-carbon nanotube hybrids with molecular dynamics.* Nano Lett, 2008. **8**(1): p. 69-75.
11. Gowtham, S., et al., *First-principles study of physisorption of nucleic acid bases on small-diameter carbon nanotubes.* Nanotechnology, 2008. **19**(12): p. 125701.
12. Manohar, S., et al., *Peeling single-stranded DNA from graphite surface to determine oligonucleotide binding energy by force spectroscopy.* Nano Lett, 2008. **8**(12): p. 4365-72.
13. Yang, Q.H., et al., *Loosening the DNA wrapping around single-walled carbon nanotubes by increasing the strand length.* Nanotechnology, 2009. **20**(19): p. 195603.
14. Zhang, J.Q., et al., *Single Molecule Detection of Nitric Oxide Enabled by d(AT)(15) DNA Adsorbed to Near Infrared Fluorescent Single-Walled Carbon Nanotubes.* Journal of the American Chemical Society, 2011. **133**(3): p. 567-581.
15. Jin, H., et al., *Divalent ion and thermally induced DNA conformational polymorphism on single-walled carbon nanotubes.* Macromolecules, 2007. **40**(18): p. 6731-6739.
16. C. Bustamante, J.F.M., E. D. Siggia, and S. Smith, *Entropic elasticity of lambda-phage DNA.* Science, 1994. **265**: p. 1599-1600.
17. Jin, H., et al., *Size-Dependent Cellular Uptake and Expulsion of Single-Walled Carbon Nanotubes: Single Particle Tracking and a Generic Uptake Model for Nanoparticles.* ACS Nano, 2009. **3**(1): p. 149-158.
18. Fakhri, N., et al., *Diameter-dependent bending dynamics of single-walled carbon nanotubes in liquids.* Proc Natl Acad Sci U S A, 2009. **106**(34): p. 14219-23.
19. Gowtham, S., et al., *First-principles study of physisorption of nucleic acid bases on small-diameter carbon nanotubes.* Nanotechnology, 2008. **19**(12).
20. Johnson, R.R., A.T. Johnson, and M.L. Klein, *Probing the structure of DNA-carbon nanotube hybrids with molecular dynamics.* Nano Letters, 2008. **8**(1): p. 69-75.

21. Manohar, S., et al., *Peeling single-stranded DNA from graphite surface to determine oligonucleotide binding energy by force spectroscopy.* Nano Letters, 2008. **8**(12): p. 4365-72.
22. Zhang, Y.H., et al., *Direct measurements of the interaction between pyrene and graphite in aqueous media by single molecule force spectroscopy: Understanding the pi-pi interactions.* Langmuir, 2007. **23**(15): p. 7911-7915.
23. Markita P. Landry, P.M.M., Zhi Qi and Yann R. Chemla, *Characterization of Photoactivated Singlet Oxygen Damage in Single-Molecule Optical Trap Experiments.* Biophysical Journal, 2009. **97**(8).
24. Moffitt, J.R., Y.R.Chemla, D. Ixhaky, and C. Bustamante, *Differential detection of dual traps improves the spatial resolution of optical tweezers.* Proc Natl Acad Sci U S A, 2006.
25. Bustamante, C., Y. R. Chemla, and J. R. Moffitt, *Single-Molecule Techniques: A Laboratory Manual.* 2008.

Chapter 8. Summary and Concluding Remarks

Advances in life science research have reached a new scale. The ability to query biological interactions at their fundamental size scales provides us with a more thorough understanding of the mechanisms responsible for behavior on the macro scale. However, as with most new scientific approaches, care must be taken to ensure that the integrity of our samples is not compromised. Once reliable protocols are established for single-molecule techniques, these approaches can be powerful in decoding the intricacies of life at the nano-scale. Through our work with protein-DNA target search processes, we have shown that single-molecule techniques are particularly powerful when several are used to probe the same process in a complementary manner. We have also shown that single-molecule techniques can provide unprecedented detail in probing the interface between biological molecules and nanoparticles. Such results exemplify the power of single-molecule techniques to answer fundamental questions about how biological molecules interact with each other, and with synthetic nanomaterials.

8.1 Photodamage induced by single-molecule instrumentation

Recent advances in physics and optics have made it possible to isolate these bio-molecules individually and study their properties on a single-molecule scale. While single-molecule techniques have provided scientists with a much more comprehensive picture of how biological molecules function, little work has been done to identify and understand the causes and effects of the photo-induced damage that may occur from the interaction of the bio-molecules being studied, and the lasers being used to study them. After all, lasers are a coherent source of photons that carry energy which could easily photodamage bio-molecules directly or indirectly, and are a central part of virtually all single-molecule instruments. Optical traps, which typically use a 1064-nm wavelength laser, focus this laser light down to a diffraction-limited spot, resulting in a local photon

flux that is extremely large and potentially hazardous to biological molecule integrity [1]. Near infrared lasers were chosen for optical trapping due to the fact that this wavelength of infrared light is "invisible" to most biological samples. However, our work has uncovered that "invisible" doesn't always mean "harmless".

Characterization of the optical trap-induced photodamage presented in **Chapter 3** of this thesis was initially motivated by an experimental annoyance that caused our DNA tethers to become prematurely unstable, limiting our observation time window. Exploring the cause of this DNA tether instability unearthed consequences that entailed more than a mere experimental frustration. We found that our optical trap damages our DNA substrate via a reaction involving the transfer of energy from the laser to oxygen dissolved in our buffer. This creates a reactive form of oxygen known as singlet oxygen, and in turn singlet oxygen damages DNA by reacting unfavorably with DNA bases. The consequences of this photodamage are particularly deleterious for single molecule experiments. In bulk, the occasional damage of a few molecules will be obscured by the very phenomenon — averaging over large numbers of molecules — that gives single-molecule science its advantage. However, the damage of a molecule in a single molecule experiment can lead to data that reflects the behavior of the damaged molecule, instead of providing insight about the naturally occurring biological system, and leading scientists to draw incorrect conclusions.

Most single-molecule techniques employ the use of lasers to extract information from these biological systems: Optical traps use near-infrared lasers to immobilize and measure the sample, whereas fluorescence microscopy techniques such as fluorescence resonance energy transfer (FRET), total internal reflection fluorescence (TIRF)

microscopy, Stimulated Emission Depletion (STED) microscopy, and fluorescence correlation spectroscopy (FCS) (to name but a few) use visible wavelengths to excite fluorescent modifications on the sample, and some of these techniques use various combinations of these approaches for single molecule studies [2-5]. However, little has been done to characterize the potentially photodamaging effects of these techniques. Many of the efforts made to reduce sample photodamage have been motivated by, and have focused on, stabilizing the molecules providing the signal of interest [6-9]. These studies have focused on characterizing the adverse effects single-molecule instruments can have on the biological molecules, and have found that these effects can be harmful to biological samples [10, 11]. Many of these techniques differ in wavelength, intensity, and require different chemical composition of the buffers. All of these variables can potentially affect the photodamage that occurs as a result of the interaction of the sample with the experimental approach.

It is unfortunate that, decades after the implementation of optical traps for *in vitro* single-molecule biology experiments, inquiries about the effects of photodamage to tethered DNA systems have only begun. Hopefully, in the future, the development of novel scientific techniques and instrumentation will always be carried out in parallel to efforts which ensure that the implementation of these techniques will produce reliable results.

8.2 TelK as a model for protein target search

Protein-DNA interactions are essential to many vital cellular processes, many of which require a protein to identify a particular DNA sequence for activity. Bulk studies

[12, 13], and more recently, single-molecule studies [14-19] revealed the mechanism(s) by which monomeric proteins identify their target sites. While these studies helped address fundamental questions about target-search rates as they relate to target-site catalysis, most sequence-specific proteins in the cell do not act singularly. To address the more relevant but also more complex questions of how target-search occurs for dimer-active proteins, we provide experimental and theoretical evidence for an alternate target-search mechanism for this subset of cellular proteins in **Chapter 4** of this thesis. This work provides a model for target search by proteins that are monomers in solution but dimers at the target site.

Our work has also uncovered elements of target-search by dimer-active proteins that had yet to be addressed in the literature. For instance, we observe transient dimerization events that occur along non-target DNA that are accompanied by protein immobilization and DNA condensation. Our work shows that these non-target dimerization events, which are in direct kinetic competition with the process of target-site identification, do not inhibit target-finding at biologically relevant concentrations. Accompanying molecular dynamics (MD) simulations provide molecular-scale details for why these interactions occur, and confirm our experimentally-based predictions for the behavior of a TelK monomer with DNA, or a TelK monomer with another TelK monomer. However, our results cause other questions about protein-DNA interactions to surface. For example, proteins are thought to use a 1D scanning mechanism as their primary recognition sequence- finding mechanism. The currently accepted model for protein 1D search mechanisms suggests that proteins are able to bind "loosely" to DNA in order to scan DNA in 1-D thereby restricting the search region of the protein to a line in lieu of a volume. When the protein identifies its correct recognition sequence along the DNA backbone, *only* then are the electrostatic interactions maximized between the protein surface and the DNA nucleotides, and the protein adopts a "tightly"

bound state on the DNA, often changing the DNA conformation [17]. Is this restriction lifted in the case of dimer-active proteins? Monomer-active proteins only need to concern themselves with finding their DNA target sequences, whereas dimer-active proteins must contain the ability to be selective towards a particular target site but also a second protein binding partner. Perhaps this added protein-protein requirement for activity decreases the ability of dimer-active proteins to selectively adopt a tightly-bound conformation on a particular DNA target sequence. This would result in the non-target DNA condensation events we observe, as TelK monomers encounter each other prematurely on DNA.

It would be useful to study other dimer-active protein families to see if their target-search mechanisms are similar to what we observe with TelK. Such studies would provide a better understanding of structure-function relationships of proteins and their interactions with DNA. The currently accepted model for protein target-search relies on the exclusivity of "tight" binding at the target site to restrict catalysis solely to the target site [17]. In the absence of this tight-binding exclusivity, as is the case for TelK, target-site catalysis must be regulated by alternate mechanisms. As has been previously suggested [20], dimer-active proteins may bend DNA to "test" their compatibility with that particular DNA sequence via protein-DNA and protein-protein interactions. Studies have shown that many dimer or oligomer- functional proteins control against premature cleavage at incorrect DNA sites by "tucking away" key catalytic protein residues until the protein has correctly bound to and optimally distorted the DNA target sequence [21, 22]. Dimer- and oligomer-active proteins may use this mechanism to maximize their electrostatic contacts with the DNA. A physically protected catalytic protein residue would therefore only be available via physical distortion of the DNA substrate by the protein. Although distortions will occur along non-target DNA sequences, catalysis will only occur at the correct sequence. As has been previously

suggested for certain SSPs [23], TelK's ability to bend DNA may help TelK find its target site by maximizing the sampling of local DNA sequences through DNA-bending.

Lastly, questions of structure-function relationships as they contribute to target-search mechanisms may depend on the energy-dependence of the protein. Many questions remain with regards to the functioning of proteins which, like TelK, are independent from energy cofactors. TelK is responsible for performing energy-expensive DNA rearrangements through cutting of the DNA backbone allowing for controlled changes in DNA conformation, and finally re-ligation of the DNA strands. The process of hairpin formation is performed without the aid of high-energy cofactors such as ATP. Because there is no net loss or gain of nucleotides during the modification of DNA structure or topology, it is unclear how type tyrosine recombinases (Y-recombinases) and IB topoisomerases drive their isoenergetic reactions unidirectionally when theory would predict a 50-50 ratio of substrate and product in the absence of a driving factor such as ATP. It is possible that electrostatically induced DNA twisting or bending at the DNA target site may help stabilize the protein-DNA complex and drive the overall reaction forward. It has also been hypothesized that protein-protein interactions and distortions resulting from these interactions may play a crucial role in making protein catalysis unidirectional [24].

While our work represents an important advancement in understanding protein-DNA target search mechanisms and target-site specificity, much work remains to be done to elucidate trends in structure-function relationships for the target-search mechanisms of different protein families. The diverse functions, reaction pathways, energy sources, functional units, and other such parameters of cellular proteins will undoubtedly require an equally diverse set of parameters to fully characterize the target search behavior of sequence-specific proteins beyond the currently accepted model.

Additionally, the mechanistic details of hairpin formation by TelK remain poorly understood. It is possible that TelK induces a cruciform intermediate structure on its DNA structure [25], although the TelK-DNA crystal structure suggests such a large deformation is unlikely to fit into the TelK catalytic pocket [26]. Our approach to studying this intermediate structure with FRET was unsuccessful due to abolition of TelK hairpin-forming activity with the introduction of a FRET dye pair on our DNA substrate. In **Chapter 5**, we discuss alternate approaches to studying the process of DNA hairpin formation by TelK.

8.3 Applications of nanotechnology

Nanomaterials have various potential biological applications due to their unique optical, chemical, and mechanical properties, including their use as sensors, imaging agents, and drug carriers. A significant number of theoretical and experimental studies have focused on DNA-nanoparticle interactions *in vitro*, particularly in the context of DNA-nanopore single-molecule sequencing [27, 28]. However, to use nanomaterials *in vivo* for therapeutic or sensing applications, nanomaterials must often first be passivated or functionalized with biomolecules to reduce the toxic potential of the nanomaterial. For this reason, there have been many efforts to study bio-nano interactions using chromatography, transmission electron microscopy, atomic force microscopy, and near-infrared microscopy [29-33]. However, these techniques are unable to resolve many details of biomolecular interactions at nano-scales, and are unable to provide details of bio-nano interactions at their fundamental length scales. As a result, researchers wishing to develop sensors or therapeutics often resort to using search libraries and biomolecule arrays to develop technologies based on a "black box" understanding of nanoparticle- biomolecule interactions.

As a result, many questions remain about biological interactions at a nanosurface, including how certain biological molecules such as DNA assemble on nano-surfaces, how the electronic properties of nanoparticles affect and are affected by biomolecules, and the possible toxicological effects of nanomaterials [34-37]. The work presented in this thesis focuses on understanding this "bio-nano" interface between biomolecules and nanoparticles. We focus on single-walled carbon nanotubes (SWNTs), and their interactions with proteins and DNA. SWNTs have various potential biological applications due to their unique optical, chemical, and mechanical properties, as sensors of biological activity. However, their biocompatibility is a topic of continuous investigation due to their strong hydrophobicity leading to incompatibility with the aqueous environments preferred by most living systems [34, 38, 39].

Though SWNTs tend to form insoluble aggregates due to this hydrophobicity, sonicating single-stranded DNA (ssDNA) with SWNTs forms a ss-DNA wrapped DNA-SWNT complex that is soluble in water [40]. This DNA-SWNT complex can be uptaken by mammalian cells via endocytosis, and does not appear to be toxic to these cells. However, the rational design of nanomaterials intended for in vivo use requires a thorough understanding of the DNA-nanotube surface itself, as well as the activity of biomolecules at this nanoscale interface. It is not sufficient to establish that SWNT transition from lethal to harmless in a cell when wrapped with ssDNA. Although DNA has been used extensively to manipulate, characterize, purify, and encapsulate SWNT, the process by which DNA interacts with SWNT is poorly defined [29, 40, 41]. Work must also be undertaken to characterize what particular interactions lead to these changes in toxicity.

In this thesis, we characterized several fundamental interactions between DNA, proteins, and SWNT. In **Chapter 6**, we applied fluorescence microscopy to the study of DNA-SWNT for sub-diffraction limited monitoring of biological processes with microscopes

that are becoming increasingly conventional and inexpensive [42, 43]. By using visible TIRF microscopy to study DNA-SWNT, we were able to probe the dynamic behavior of biological molecules in the immediate vicinity of a nanomaterial. We found that both DNA-DNA and protein-DNA interactions were highly modulated by their interactions with SWNT, and predictably dependent on their distance from the SWNT surface. Both of these results strongly suggest that the behaviors of biological systems can be altered at the scale of a single-molecule in the vicinity of a nanoparticle. These single-molecule results can further our understanding of the molecular-scale mechanisms responsible for the toxic effects of SWNT in cells and organisms. Extending the use of our fluorescently-labeled DNA-SWNT platform *in vivo* is one potential downstream application of our technique, and can provide a technology to advance the detection of biological interactions in living systems.

To further characterize the mechanism by which ssDNA wraps around a nanotube to form a DNA-SWNT complex, we also studied the unraveling and unbinding mechanism of ssDNA from the surface of a SWNT. In **Chapter 7**, we used a high-resolution optical trap to pull ssDNA off a DNA-SWNT complex. By monitoring the force-extension behavior of the DNA, we were able to show that ssDNA unbinding involves discrete unraveling steps preceding full unraveling. Our force-extension curves also suggest that ssDNA slipping along the SWNT contributes to the unbinding process. Steered molecular dynamics (SMD) simulations of pulling ssDNA from a SWNT were performed to complement our optical trap experiments. The SMD results successfully reproduced force drop steps in the force-time trajectory of the SMD, similar to the small steps we presumed to be unraveling events in the optical trap. Our 90-ns SMD trajectory produced distinct force drops which coincide with the trajectory's ssDNA unraveling events. Our SMD simulation also showed that the ssDNA slips along the SWNT throughout the entire trajectory, as suggested by our optical trap results. Our combined optical trap and SMD results provide insights into the dynamics of

DNA-SWNT unraveling, while our optical trap DNA-SWNT pulling approach provides an accurate measure of the forces associated with DNA-SWNT unraveling and unbinding. The findings presented in this work can serve to advance the development of technologies based on biomolecule-nanoparticle interactions. For instance, our findings may enable the use of DNA-SWNT in the development of technologies based on DNA self-assembly. DNA is a polymer with the unique property of sequence-specific molecular recognition, which has given rise to fields such as DNA self-assembly and DNA origami that exploit this property to synthesize self-assembling nanostructures. The discovery and characterization of DNA accessibility on DNA-SWNT provided in this work provides a fundamental platform for future applications in a variety of DNA-based research areas, including — but not limited to — *in vivo* protein sensors, label-free detection of biological interactions, drug delivery, as well as applications to synthetic DNA-based technologies such as DNA-SWNT nanowires, DNA-SWNT self-assembly, and DNA-SWNT-based DNA origami.

8.4 Chapter references

1. Neuman, K.C. and S.M. Block, *Optical trapping*. Rev Sci Instrum, 2004. **75**(9): p. 2787-809.
2. Roy, R., S. Hohng, and T. Ha, *A practical guide to single-molecule FRET*. Nature Methods, 2008. **5**(6): p. 507-16.
3. Selvin, P.R. and T. Ha, *Single-molecule techniques: a laboratory manual*. 2008, Cold Spring Harbor, New York: John Inglis.
4. Leung, B.O. and K.C. Chou, *Review of super-resolution fluorescence microscopy for biology*. Appl Spectrosc, 2011. **65**(9): p. 967-80.
5. Tian, Y., M.M. Martinez, and D. Pappas, *Fluorescence correlation spectroscopy: a review of biochemical and microfluidic applications.* Appl Spectrosc, 2011. **65**(4): p. 115A-124A.
6. Rasnik, I., S.A. McKinney, and T. Ha, *Nonblinking and long-lasting single-molecule fluorescence imaging*. Nature Methods, 2006. **3**(11): p. 891-3.
7. Hohng, S. and T. Ha, *Near-complete suppression of quantum dot blinking in ambient conditions.* J Am Chem Soc, 2004. **126**(5): p. 1324-5.
8. Borejdo, J., et al., *Reduction of photobleaching and photodamage in single molecule detection: observing single actin monomer in skeletal myofibrils.* J Biomed Opt, 2008. **13**(3): p. 034021.
9. Swoboda, M., et al., *Enzymatic Oxygen Scavenging for Photostability without pH Drop in Single-Molecule Experiments.* ACS Nano, 2012. **6**(7): p. 6364-9.
10. Tycon, M.A., et al., *Quantification of dye-mediated photodamage during single-molecule DNA imaging.* Anal Biochem, 2012. **426**(1): p. 13-21.
11. Neuman, K.C., et al., *Characterization of photodamage to Escherichia coli in optical traps.* Biophys J, 1999. **77**(5): p. 2856-63.
12. Ptashne, M., *Specific binding of the lambda phage repressor to lambda DNA.* Nature, 1967. **214**(5085): p. 232-4.
13. Gilbert, W. and B. Muller-Hill, *The lac operator is DNA.* Proc Natl Acad Sci U S A, 1967. **58**(6): p. 2415-21.
14. Halford, S.E., *An end to 40 years of mistakes in DNA-protein association kinetics?* Biochem Soc Trans, 2009. **37**(Pt 2): p. 343-8.
15. Gowers, D.M., G.G. Wilson, and S.E. Halford, *Measurement of the contributions of 1D and 3D pathways to the translocation of a protein along DNA.* Proc Natl Acad Sci U S A, 2005. **102**(44): p. 15883-8.
16. Gorman, J. and E.C. Greene, *Visualizing one-dimensional diffusion of proteins along DNA.* Nat Struct Mol Biol, 2008. **15**(8): p. 768-74.
17. Halford, S.E. and J.F. Marko, *How do site-specific DNA-binding proteins find their targets?* Nucleic Acids Research, 2004. **32**(10): p. 3040-3052.
18. Hilario, J. and S.C. Kowalczykowski, *Visualizing protein-DNA interactions at the single-molecule level.* Curr Opin Chem Biol, 2010. **14**(1): p. 15-22.
19. Koslover, E.F., M.A. Diaz de la Rosa, and A.J. Spakowitz, *Theoretical and computational modeling of target-site search kinetics in vitro and in vivo.* Biophys J, 2011. **101**(4): p. 856-65.

20. Erie, D.A., et al., *DNA Bending by Cro Protein in Specific and Nonspecific Complexes - Implications for Protein Site Recognition and Specificity.* Science, 1994. **266**(5190): p. 1562-1566.
21. Guo, F., D.N. Gopaul, and G.D. van Duyne, *Structure of Cre recombinase complexed with DNA in a site-specific recombination synapse.* Nature, 1997. **389**(6646): p. 40-6.
22. Gopaul, D.N., F. Guo, and G.D. Van Duyne, *Structure of the Holliday junction intermediate in Cre-loxP site-specific recombination.* EMBO J, 1998. **17**(14): p. 4175-87.
23. Grove, A., et al., *Localized DNA flexibility contributes to target site selection by DNA-bending proteins.* Journal of Molecular Biology, 1996. **260**(2): p. 120-5.
24. Grindley, N.D.F., K.L. Whiteson, and P.A. Rice, *Mechanisms of site-specific recombination.* Annual Review of Biochemistry, 2006. **75**: p. 567-605.
25. Huang, W.M., et al., *Protelomerase uses a topoisomerase IB/Y-recombinase type mechanism to generate DNA hairpin ends.* Journal of Molecular Biology, 2004. **337**(1): p. 77-92.
26. Aihara, H., W.M. Huang, and T. Ellenberger, *An interlocked dimer of the protelomerase TelK distorts DNA structure for the formation of hairpin telomeres.* Molecular Cell, 2007. **27**(6): p. 901-913.
27. Clarke, J., et al., *Continuous base identification for single-molecule nanopore DNA sequencing.* Nat Nanotechnol, 2009. **4**(4): p. 265-70.
28. Wells, D.B., et al., *Assessing graphene nanopores for sequencing DNA.* Nano Lett, 2012. **12**(8): p. 4117-23.
29. Tu, X., et al., *DNA sequence motifs for structure-specific recognition and separation of carbon nanotubes.* Nature, 2009. **460**(7252): p. 250-3.
30. Malik, S., et al., *Physical chemical characterization of DNA-SWNT suspensions and associated composites.* Composites Science and Technology, 2007. **67**(5): p. 916-921.
31. Campbell, J.F., et al., *Atomic force microscopy studies of DNA-wrapped carbon nanotube structure and binding to quantum dots.* J Am Chem Soc, 2008. **130**(32): p. 10648-55.
32. Manohar, S., et al., *Peeling single-stranded DNA from graphite surface to determine oligonucleotide binding energy by force spectroscopy.* Nano Lett, 2008. **8**(12): p. 4365-72.
33. Heller, D.A., et al., *Multimodal optical sensing and analyte specificity using single-walled carbon nanotubes.* Nature Nanotechnology, 2009. **4**(2): p. 114-20.
34. Sayes, C.M., et al., *Functionalization density dependence of single-walled carbon nanotubes cytotoxicity in vitro.* Toxicol Lett, 2006. **161**(2): p. 135-42.
35. Nel, A., et al., *Toxic potential of materials at the nanolevel.* Science, 2006. **311**(5761): p. 622-7.
36. Balbus, J.M., et al., *Meeting report: hazard assessment for nanoparticles--report from an interdisciplinary workshop.* Environ Health Perspect, 2007. **115**(11): p. 1654-9.
37. Zhang, L.W., et al., *Biological interactions of quantum dot nanoparticles in skin and in human epidermal keratinocytes.* Toxicol Appl Pharmacol, 2008. **228**(2): p. 200-11.

38. Colvin, V.L., *The potential environmental impact of engineered nanomaterials.* Nat Biotechnol, 2003. **21**(10): p. 1166-70.
39. Tkach, A.V., et al., *Direct effects of carbon nanotubes on dendritic cells induce immune suppression upon pulmonary exposure.* ACS Nano, 2011. **5**(7): p. 5755-62.
40. Heller, D.A., et al., *Optical detection of DNA conformational polymorphism on single-walled carbon nanotubes.* Science, 2006. **311**(5760): p. 508-11.
41. Roxbury, D., et al., *Recognition ability of DNA for carbon nanotubes correlates with their binding affinity.* Langmuir, 2011. **27**(13): p. 8282-93.
42. Yildiz, A., et al., *Myosin V walks hand-over-hand: single fluorophore imaging with 1.5-nm localization.* Science, 2003. **300**(5628): p. 2061-5.
43. Selvin, P.R. and T. Ha, eds. *Single-molecule techniques: a laboratory manual*. 2008, John Inglis: Cold Spring Harbor, New York.